Electrons in Nanostructures

coherent manipulation and counting statistics

Flindt, Christian

Publication date:
2007

Document Version
Publisher's PDF, also known as Version of record

Electrons in Nanostructures
– coherent manipulation and counting statistics

Christian Flindt

Ph.D. Thesis
August 2007

Electrons in Nanostructures
– coherent manipulation and counting statistics
Ph.D. Thesis, Technical University of Denmark

Christian Flindt
MIC – Department of Micro and Nanotechnology
DTU – Building 345 east
DK-2800 Kgs. Lyngby
Denmark
E-mail: cf@mic.dtu.dk
Web: http://www.mic.dtu.dk

Front cover: Part of a charge stability diagram
Back cover: The author giving a presentation

Document typeset in LaTeX 2_ε

Abstract

This thesis concerns theoretical aspects of electrons in man-made nanostructures. Advances in nanofabrication technology during recent decades have made it possible to produce electrical devices on the nano-scale, whose functionality is determined by the quantum mechanical nature of a single or a few electrons. Such few-electron devices are expected to form the building blocks of future electrical circuits and it is thus necessary to develop a thorough theoretical understanding of the physics of electrons in nanostructures. Regarding applications there is a particular interest in the possibilities offered by the quantum mechanical behavior of electrons when it comes to information processing. This branch of research is also concerned with fundamental questions in physics.

Besides an introduction to the above-mentioned subjects, the thesis contains a number of contributions to the fields of coherent electron manipulation and the statistical description of electron transport through nanodevices. The physics of the electrons are described with a combination of numerical methods, developed and applied in the thesis, and more analytical approaches, which are also discussed. The thesis contains a study of the interaction between the spins of electrons and proposals for novel methods of confining and manipulating electrons in nanostructures. Moreover, a novel coupling mechanism between electron spins and light in the form of photons is described, which could find applications in quantum-based communication. The statistical description of electron transport through nanostructures is based on rate equations, and the primary contribution of the thesis in that respect is the development of a method that allows for the calculation of the distribution of electrons passing through a device. The method is illustrated with applications to two nano-electromechanical systems and is finally extended such that it also takes into account possible memory effects in the transport.

Resumé

Denne afhandling omhandler teoretiske aspekter af elektroner i menneskeskabte nanostrukturer. De seneste årtiers udvikling af nanofabrikationsteknikker har muliggjort, at man i dag kan fremstille elektriske komponenter på nanometerskala, hvis funktionalitet er bestemt af enkelte eller få elektroners kvantemekaniske natur. Sådanne få-elektron-komponenter forventes at danne byggestenene i fremtidens elektriske kredsløb, og det er derfor nødvendigt med en dybtgående teoretisk forståelse af elektroners fysik i nanostrukturer. Med henblik på anvendelser er der især interesse omkring de muligheder, elektroners kvantemekaniske opførelse giver i forbindelse med informationsbehandling. Denne gren af forskningen berører også fundamentale spørgsmål i fysikken.

Udover en introduktion til de ovennævnte emner indeholder afhandlingen en række bidrag til områderne omhandlende kohærent manipulering af elektroner i nanostrukturer samt den statistiske beskrivelse af elektrontransport gennem nanokomponenter. Beskrivelsen af elektronernes fysik er baseret på en kombination af numeriske metoder, der udvikles og anvendes i afhandlingen, og mere analytiske tilgange, der ligeledes beskrives. Afhandlingen indeholder et studie af vekselvirkningen mellem elektroners spin samt forslag til nye metoder til at fastholde og manipulere elektron-spin i nanostrukturer. Herudover beskrives en ny koblingsmekanisme mellem elektroners spin og lys i form af fotoner, der vil kunne finde anvendelse i kvante-baseret kommunikation. Den statistiske beskrivelse af elektrontransport gennem nanostrukturer baserer sig på rate-ligninger, og afhandlingens primære bidrag er i den forbindelse udviklingen af en metode, hvormed fordelingen af elektroner, der passerer igennem en komponent, kan beregnes. Metoden illustreres ved anvendelse på to nano-elektromekaniske systemer, og til slut udvides metoden så den også omfatter eventuelle hukommelseseffekter i transporten.

Preface

Meine Herren, rechnen wir!
Gentlemen, let's compute!
Gottfried Leibniz (1646-1716)

The present thesis is submitted in candidacy for the Ph.D. degree at Technical University of Denmark. The thesis describes the work that I carried out in the period August 15, 2004 to August 15, 2007 supervised by Professor Antti-Pekka Jauho, MIC – Department of Micro and Nanotechnology, Technical University of Denmark, and co-supervised by Associate Professor Karsten Flensberg, Nano-Science Center, University of Copenhagen.

First of all, I would like to thank both my supervisors for their continuous support and willingness to always letting me pursue my own interests. Together they have provided a fruitful scientific environment in which I was free to make my own decisions (and make my own mistakes). This has given me the opportunity and possibility to engage myself in and start up several projects and collaborations with a number of excellent scientists. In particular, I would like to thank Alessandro Braggio, Andrea Donarini, Mikhail D. Lukin, N. Asger Mortensen, Tomáš Novotný, Jesper Pedersen, Thomas G. Pedersen, Anders S. Sørensen, and Jacob M. Taylor for their collaboration. I would like also to thank Professor Tobias Brandes, Professor Daniel Loss, and Professor Jesper Mørk for serving on the evaluation committee of my thesis.

Support from NorFa, Otto Mønsted Fonden, and the Denmark-America Foundation is kindly acknowledged, together with my Ph.D. stipend financed by Technical University of Denmark. I am also thankful to the Lukin Group at Department of Physics, Harvard University, for hosting me during a six months visit in the fall 2006. Moreover, I would like to thank the numerous people I have encountered and interacted with as part of my Ph.D. studies, including fellow soccer players, office mates, other group members, and many more. Finally, I would like to thank my friends, family, and girlfriend, for their support during the last three years.

Christian Flindt
Kgs. Lyngby
August 15, 2007

List of publications

[**A**] T. Novotný, A. Donarini, **C. Flindt**, and A.-P. Jauho, 'Shot Noise of a Quantum Shuttle', Phys. Rev. Lett. **92**, 248302 (2004)

[**B**] **C. Flindt**, T. Novotný, and A.-P. Jauho, 'Current noise in a vibrating quantum dot array', Phys. Rev. B **70**, 205334 (2004)

[**C**] A.-P. Jauho, T. Novotný, A. Donarini, and **C. Flindt**, 'Modelling of Quantum Electromechanical Systems', J. Comput. Electron. **3**, 367 (2004)

[**D**] **C. Flindt**, T. Novotný, and A.-P. Jauho, 'Full counting statistics of nano-electromechanical systems', Europhys. Lett. **69**, 475 (2005)

[**E**] A.-P. Jauho, A. Donarini, **C. Flindt**, and T. Novotný, 'Open problems in noise in NEMS', AIP Conf. Proc. **800**, 56 (2005)

[**F**] **C. Flindt**, T. Novotný, and A.-P. Jauho, 'Noise and Bistabilities in Quantum Shuttles', AIP Conf. Proc. **780**, 442 (2005)

[**G**] **C. Flindt**, T. Novotný, and A.-P. Jauho, 'Current noise spectrum of a quantum shuttle', Physica E **29**, 411 (2005)

[**H**] A.-P. Jauho, **C. Flindt**, T. Novotný, and A. Donarini, 'Current and Current Fluctuations in Quantum Shuttles', Phys. Fluids **17**, 100613 (2005)

[**I**] **C. Flindt**, N. A. Mortensen, and A.-P. Jauho, 'Quantum Computing via Defect States in Two-Dimensional Anti-Dot Lattices', Nano Lett. **5**, 2515 (2005)

[**J**] **C. Flindt**, A. S. Sørensen, and K. Flensberg, 'Spin-Orbit Mediated Control of Spin Qubits', Phys. Rev. Lett. **97**, 240501 (2006)

[**K**] **C. Flindt**, A. S. Sørensen, and K. Flensberg, 'Spin-orbit induced spin-qubit control in nanowires', J. Phys.: Conf. Ser. **61**, 302 (2007)

[**L**] J. Pedersen, **C. Flindt**, N. A. Mortensen, and A.-P. Jauho, 'Quantum information processing using designed defect states in 2D anti-dot lattices', AIP Conf. Proc. **893**, 821 (2007)

[**M**] **C. Flindt**, A. S. Sørensen, M. D. Lukin, and J. M. Taylor, 'Spin-Photon Entangling Diode', Phys. Rev. Lett. **98**, 240501 (2007)

[**N**] **C. Flindt**, A. Braggio, and T. Novotný, 'Non-Markovian dynamics in the theory of full counting statistics', AIP Conf. Proc. **922**, 531 (2007)

[**O**] J. Pedersen, **C. Flindt**, N. A. Mortensen, and A.-P. Jauho, 'Failure of standard approximations of the exchange coupling in nanostructures', Phys. Rev. B **76**, 125323 (2007)

[**P**] J. Pedersen, **C. Flindt**, N. A. Mortensen, and A.-P. Jauho, 'Designed defects in 2D antidot lattices for quantum information processing', to appear in Physica E

[**Q**] A. Braggio, **C. Flindt**, and T. Novotný, 'Non-Markovian signatures in the current noise of a charge qubit', to appear in Physica E

[**R**] J. Pedersen, **C. Flindt**, N. A. Mortensen, and A.-P. Jauho, 'Spin qubits in antidot lattices', submitted to Phys. Rev. B

[**S**] T. G. Pedersen, **C. Flindt**, J. Pedersen, N. A. Mortensen, A.-P. Jauho, K. Pedersen, 'Graphene Antidot Lattices – Designed Defects and Spin Qubits', submitted to Phys. Rev. Lett.

Papers **D**, **F**, **G**, **I**, **J**, **K**, **M**, **N**, **O**, and **R** are included in this thesis.

Contents

Chapter 1

Introduction

The field of solid state physics has reached a level of sophistication where it is now possible to detect and manipulate single electrons in man-made nanostructures. This has opened up a variety of possibilities for observing and exploiting quantum mechanical behavior of individual electrons in solid-state structures, which is interesting not only from a fundamental physics point of view, but also offers intriguing technological pathways to novel nano-sized semiconductor devices whose functionality is based on the quantum mechanical behavior of single electrons inside the devices. With the continuous miniaturization that electronic devices are currently undergoing, the possibility of fabricating such quantum mechanical single-electron devices in a not so far future does not seem unrealistic.

In order to progress towards that goal it is, however, necessary to develop a thorough understanding of the physics governing electrons in nano-scale devices. Relevant questions to address concern the ability to manipulate single electrons and the extraction of information about the intrinsic electronic processes in these devices from measurements of the flow of electrons passing through them. This requires detailed theoretical descriptions of the electrons in the envisioned devices and their interactions with the environment, combined with thorough experimental investigations. While solid state and condensed matter physics have typically been formulated in a many-body language, the ability to isolate single electrons in a solid-state structure has added several new ingredients which for many years have been studied in another field of physics, namely quantum optics. Here, quantum coherent processes involving only a few photons are routinely investigated, and many of these ideas and concepts can now be transferred to the solid-state, where electrons then play the roles of the photons.

Due to the well-developed, industrial semiconductor technology that has already proven successful in the fabrication of large-scale integrated electronic

circuits, there is good reason to believe that solid state physics may provide suitable systems and architectures for studies and applications of coherent and controlled dynamics of many electrons. This is, in particular, interesting in relation to the discovery that quantum mechanics can be a highly useful resource in the processing of information, enabling a remarkable speed-up to certain computational problems with algorithms that are based on the laws of quantum mechanics rather than on classical physics, as conventional algorithms. The implementation of quantum hardware exploiting these concepts is consequently an important milestone in physics and in the engineering sciences.

1.1 This thesis

This thesis contains of number of theoretical studies and proposals related to various aspects of electrons in nanostructures. The two main lines of investigation concern coherent manipulation of confined electrons spins and the theory of full counting statistics applied to transport through nano-scale devices. Besides the introductory and concluding chapters, the thesis contains three main chapters, Chapters 2, 3, and 4. Moreover, a number of published or submitted papers have been included at the end of the thesis. Since most of these papers assume that the reader has a fairly good knowledge of the specific fields related to these papers, one goal with the thesis is to provide the reader with sufficient background knowledge needed in order to understand the included papers. This includes not only the theory related to the different fields touched upon, but also some considerations concerning the experimental aspects of the fields, including the current experimental status. Altogether, this is meant to put the included papers into a broader context, and, hopefully, clarify the motivation behind each of the works. It is also my hope that the thesis will be useful to other graduate students and researchers entering these fields, and the thesis reflects in many ways my own efforts in getting acquainted with the fields studied throughout the thesis. I have consequently focused on giving the type of introduction to the various fields that I would have found useful when I began with the research work described in the following. Below, I give a brief overview of the contents of the thesis.

Chapter 2 gives a brief introduction to various types of quantum dots, or artificial atoms, which are small man-made confining regions in a solid state system, where electrons can be trapped. The strong correlations between electrons in quantum dots due to their mutual Coulomb interaction are discussed, which among other phenomena leads to Coulomb blockade. Al-

though the exposition given here only scratches the surface of this vast topic, the essentials needed to understand the following chapters and the included papers are given. In the following section, the field of nanoelectromechanical systems (NEMS) is introduced, and two models of so-called nano-scale charge shuttles are described. These models have already been described and studied in previous works, and here only the main features of the two models and previously obtained results are summarized. The two systems are studied in further detail in Chapter 4. The last section of Chapter 2 concerns a novel proposal for trapping of electrons in designed defects in an otherwise periodic potential modulation of a two-dimensional electron gas.

Chapter 3 concerns the spins of confined electrons, in particular, when considered as possible candidates for information storage and processing in a future solid-state quantum computer. First, a brief introduction to quantum computing is given, and again, without being exhaustive, this section provides the reader with the necessary background knowledge needed for the following sections and the included papers. Next, the exchange coupling between electron spins in coupled quantum dots in introduced. The exchange coupling has been promoted as a controllable interaction in a future solid-state quantum computer. The origin of the interaction is discussed and various approaches to the evaluation of the coupling strength are described. Several standard approximations are benchmarked against numerically exact results. In the following section the strong spin-orbit coupling in, e.g., InAs nanowires is proposed as a general means to coherent manipulation of electron spins in quantum dots. Finally, a proposal for an optoelectronic device that would provide a quantum optical interface to electron spins trapped in quantum dots is described. Here, information is shared between an emitted photon and electron spins trapped in the device, in such a way that emitted photons can be used to connect remote devices.

Chapter 4 deals with full counting statistics (FCS) within a rate equation formulation. FCS describes the stochastic propagation of electrons through nano-scale devices and is introduced at the beginning of the chapter with a few simple examples that illustrate the central concepts of the theory. Next, a general approach to the calculation of the cumulants of the current through a nano-scale device is presented and applied to the charge shuttle systems introduced in Chapter 2. It is shown how the first three cumulants can be used to identify a mechanical bistability and how the finite-frequency noise may reveal frequency shifts and internal energy scales. While the systems considered so far in the chapter are memoryless or Markovian, two approaches to the calculation of current cumulants for non-Markovian systems are presented and applied to two simple models. It is argued that it may be difficult to distinguish between signatures in the FCS due to quantum coherence and

classical, non-Markovian dynamics, respectively.

Finally, Chapter 5 contains a summary of the thesis and an outlook describing possible future directions.

The included papers at the end of the thesis have each been assigned a letter in the List of Publications which will be used, when I refer to one of these works. Other works referred to in the thesis, not authored or co-authored by me, have been numbered and the corresponding references can be found in the Bibliography. I sometimes refer to a paper from the List of Publications which has not been included in the thesis, and in that case I clearly state together with the reference that the paper is not included. According to ministerial orders, joint author statements describing my share of each included publication must be signed by all co-authors and submitted together with the thesis. Although it is not mandatory, I have chosen also to include these statements in the thesis together with the included papers, since I feel that they give a clear picture of my contribution to each of the works.

Throughout the remainder of the thesis I shall be using "we" rather than "I". This is not because we prefer to refer to ourselves in plural, but "we" in this context should be thought of as the author *and* the reader, and also the many collaborators without whom much of the work presented in this thesis would not have been possible.

Chapter 2

Quantum Dots

Advances in micro and nanofabrication techniques have made it possible to fabricate structures on sub-micron scales that confine electrons to nano-scale regions in a solid-state environment [1, 2, 3]. Such structures are commonly referred to as quantum dots, or as artificial atoms due to the quantized orbital level-structure that arises due to the tight confinement of the electrons, resembling real atoms. Quantum dots provide a unique, man-made platform for experimental studies of few-electron systems with a high degree of control of the various parameters defining the "atom", and with a variety of experimental methods for probing the system electronically or optically. As electronic devices have decreased dramatically in size over the last decades and seemingly continue to do so, it is also highly likely that quantum dots will form an important building block in future nano-scale electronics with applications in digital and analog circuitry, metrological standards, sensors, light-emitting diodes (LEDs) and also quantum information processing [4]. Understanding the physics of quantum dots is consequently an important scientific task with promising applications in future technologies.

Quantum dots come in a large variety of shapes, sizes, materials, and functionality, depending on their fabrication. One prominent type are the so-called gate-defined quantum dots consisting of a electrostatic, confining potential, created by metallic gate electrodes, in which electrons can be trapped. Typically, the gate electrodes are fabricated using electron-beam lithography on top of a heterostructure with a two-dimensional electron gas (2DEG) trapped at the interface between two semiconductor materials [1, 5, 6, 7, 8], e.g., GaAs and $Ga_{1-x}Al_xAs$. More recently, quantum dots have been defined along semiconductor nanowires [9, 10, 11, 12] or carbon nanotubes [13, 14] by placing them across grids of metallic gate electrodes. The size of a gate-defined quantum dot is roughly determined by the spacing between the gate-electrodes, which is typically on the order of a few hundred nanometers. Since

the voltages applied to the gate electrodes are experimentally controllable, gate-defined quantum dots allow for a high degree of tunability of tunnel barriers, occupation numbers, etc.

Self-assembled quantum dots provide a complementary approach to confinement of charges in the solid-state [15]. Such quantum dots can be fabricated using a combination of molecular-beam-epitaxy (MBE) growth techniques and strain-driven self-assembly, also known as the Stranski-Krastanov process. Here, the difference between the lattice constants of two semiconductor materials drives the formation of small islands during the growth process. If the island material has a smaller band gap than the surrounding material, a quantum dot is formed at the location of the island. In contrast to gate-defined quantum dots, self-assembled quantum dots do not only confine electrons, but also holes due to the band gap differences between the quantum dot material and the surrounding material, and they are consequently optically active and addressable [16, 17, 18, 19]. Moreover, self-assembled quantum dots are usually smaller than their gate-defined counterparts, with typical dimensions in the range 10-50 nm. On the other hand, the tunability offered by gate-defined quantum dots is less pronounced, when it comes to the self-assembled quantum dots. Finally, we mention that optically active quantum dots can also be fabricated inside nanowires by varying the wire material during growth. This approach was used in Ref. [9], where two tunneling barriers of InP were introduced during the growth process of InAs nanowires with diameters of 50 nm. By changing the barrier distance between 10 nm and 100 nm, the size of the quantum dot inside the nanowires could be varied. In Ref. [20] a quantum dot was grown inside a nanowire between n and p doped regions, such that electrons and holes could be injected into the quantum dot region with subsequent electron-hole recombination followed by light emission.

2.1 Coulomb blockade

While the quantized energy spectrum plays an important role in the understanding of quantum dots, another important constituent are the strong interactions and correlations among charged particles confined to sub-micrometer dimensions. In such systems Coulomb interactions are responsible for a large variety of charge dynamics and effects, and in particular, the phenomenon of Coulomb blockade is important in order to understand the physics of quantum dots that are weakly coupled to surrounding electrodes. In this section we discuss the effects of Coulomb blockade on the charging dynamics of single quantum dots and tunnel-coupled quantum dots and introduce the concept

of charge stability diagrams which provide a convenient means to visualize the stable charge configurations as function of various experimentally controllable parameters.

We start by considering a so-called single-electron transistor (SET) consisting of a small island, a metallic dot, coupled via tunnel junctions to source and drain electrodes and capacitively coupled to a gate voltage V_G that can be controlled externally. The island is weakly coupled to the electrodes, such that the number of electrons on the island is a good quantum number. Within the effective capacitance model the charging energy of the island with n electrons reads [5]

$$E_{\rm ch}(n, n_G) = \frac{e^2}{2C}(n - n_G)^2, \tag{2.1}$$

where C is the total capacitance of the island (i.e. the sum of the capacitances associated with the two junctions and the gate electrode), while n_G is proportional to V_G. The magnitude of the charging energy is set by the capacitance entering the pre-factor $e^2/2C$, which we denote by U. With capacitances in the range from fF to aF the charging energy lies in the range from sub-meV to eV.

The charging energy strongly influences electron transport through the island. In order to understand this effect, and in particular, how the electron flow through the SET can be controlled by the gate potential V_G, it is customary to plot the parabolas defined in Eq. (2.1) for fixed values of the occupation number n [5]. A number of these parabolas are shown in Fig. 2.1. For different values of n_G one can read off the electron number n corresponding to the lowest energy state. It is seen that for $n_G = n + 1/2$, the charge states n and $n + 1$ are energetically degenerate, such that the island can switch between having n and $n + 1$ electrons, thereby allowing current to flow through the island, one electron at a time, even at low bias-voltages. Away from these so-called degeneracy points (marked by circles) the low-bias conductance is suppressed, which is known as Coulomb blockade. In the following when we use the concept of "an additional electron", we are referring to the one electron that enters and leaves the island, when the occupation number switches from n to $n+1$ and back again. From the above discussion the notion of a single-electron transistor becomes clear: The device allows for electrostatic control of the single-electron flow in a way which is similar to the functionality of a conventional transistor.

We next consider the charging dynamics of a tunnel-coupled double quantum dot modeled as two single-particle levels with energies ε_L and ε_R, respectively, and tunnel-coupling τ. The quadratic part of the Hamiltonian of

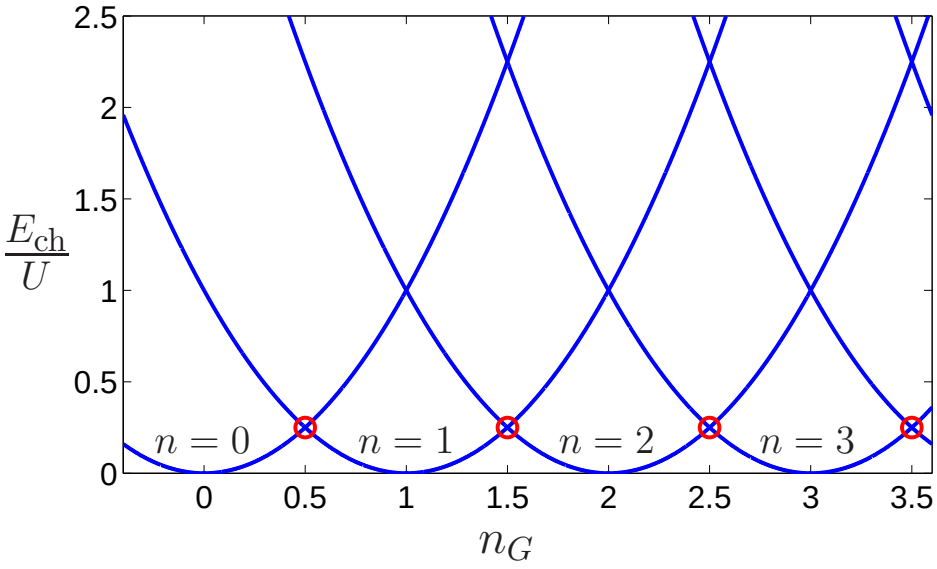

Figure 2.1: The charging energy $E_{\mathrm{ch}}(n, n_G) = U(n - n_G)^2$ with $U = e^2/2C$. For different integer values of the electron number n of the island, we plot the charging energy as function of the gate-controlled parameter n_G. For a fixed value of n_G we can read off the electron number n corresponding to the state with lowest energy. The circles mark points where states with electron numbers n and $n + 1$ are energetically degenerate. A similar figure can be found in Ref. [5].

the double quantum dot reads

$$H_0 = \varepsilon_L \hat{n}_L + \varepsilon_R \hat{n}_R + \tau(c_L^\dagger c_R + c_R^\dagger c_L), \tag{2.2}$$

where $c_{L(R)}^\dagger$ creates an electron on the left (right) dot, and the tunnel matrix element τ has been assumed to be real. The spin degree of freedom is a central subject in the following chapter, and for now we just include the spin-degeneracy of the two levels by allowing them to be doubly occupied, such that the occupation number operators $\hat{n}_\alpha$, $\alpha = L, R$, have eigenvalues 0, 1, and 2. For the Coulomb interaction between electrons on the double quantum dot we use a simple model reading

$$\hat{H}_{\text{ch}} = U_{LL}(\hat{n}_L - n_L)^2 + U_{RR}(\hat{n}_R - n_R)^2 + U_{LR}(\hat{n}_L - n_L)(\hat{n}_R - n_R), \tag{2.3}$$

where U_{LL} and U_{RR} denote the interaction strengths for electrons on the same dot, while the last term in the Hamiltonian accounts for long-range Coulomb interactions between electrons on different quantum dots with strength U_{LR}. Again we assume that n_L and n_R can be controlled by adjusting the local gating of the quantum dots. From a computational point of view, it is worth noticing that the full Hamiltonian of the double quantum dot $H_{DQD} = H_0 + \hat{H}_{\text{ch}}$ can be written as a direct sum (i.e. on block form) of Hamiltonians corresponding to different numbers of electrons on the double quantum dot, i.e., $H_{DQD} = \bigoplus_{i=0}^{4} H_{DQD}^{(i)}$, where $H_{DQD}^{(n)}$ is the Hamiltonian of the double quantum dot with n electrons.

The double quantum dot is assumed to be tunnel-coupled to a left and a right electrode, described as reservoirs of non-interacting electrons kept at chemical potentials μ_L and μ_R, respectively. Electrons may tunnel between the left lead and the left quantum dot, and the right lead and the right quantum dot. The Hamiltonian of the full system is

$$\hat{H} = H_{DQD} + H_T + H_L + H_R, \tag{2.4}$$

where $H_{L(R)}$ is the Hamiltonian of the left (right) lead, while H_T is a standard tunneling Hamiltonian, describing the tunnel coupling to the leads. In the following, we assume that the coupling to the leads is so weak that the double quantum dot is well-described by a probability distribution $P(\alpha_n)$ for the double quantum dot to be in the many-particle eigenstate $|\alpha_n\rangle$ with n electrons. Transitions between different eigenstates that differ in occupation number by one occur due to tunneling of single electrons between the leads and the double quantum dot and can be described using Fermi's Golden rule rates, treating the tunneling Hamiltonian H_T as the perturbation (the details of such calculations can be found in Ref. [21]).

With the Fermi's Golden rule transition rates at hand, the equation of motion for $P(\alpha_n)$ reads

$$\frac{d}{dt}P(\alpha_n) = -\sum_{\beta,m=n\pm1}\Gamma_{\beta_m\leftarrow\alpha_n}P(\alpha_n) + \sum_{\beta,m=n\pm1}\Gamma_{\alpha_n\leftarrow\beta_m}P(\beta_m), \tag{2.5}$$

which in matrix form can be written

$$\frac{d}{dt}\mathbf{P} = \mathbf{M}\mathbf{P}, \tag{2.6}$$

where $\mathbf{P}$ is a vector containing the probabilities $P(\alpha_n)$ and $\mathbf{M}$ is a matrix containing the transitions rates from Eq. (2.5). Equations like Eqs. (2.5) and (2.6) are referred to as rate or Master equations. The solution of Eq. (2.6) formally reads $\mathbf{P}(t) = e^{\mathbf{M}(t-t_0)}\mathbf{P}(t_0)$ with the stationary solution given by the long-t limit, i.e., $\mathbf{P}^{\rm stat} = \lim_{t\to\infty} e^{\mathbf{M}(t-t_0)}\mathbf{P}(t_0)$. Assuming that the stationary solution is unique [i.e. independent of the initial condition $\mathbf{P}(t_0)$], it may also be found as the normalized solution to the matrix equation $\mathbf{M}\mathbf{P}^{\rm stat} = 0$, which typically can be solved numerically. Using this approach we can calculate numerically the stationary probability distribution $P^{\rm stat}(\alpha_n)$ of the double quantum dot as function as various parameters, e.g., the single-particle energy levels, the bias across the double dot, etc. Having found the stationary state, we can in principle also calculate the current through the system, which we, however, refrain from doing in this chapter.

From the probability distribution $P^{\rm stat}(\alpha_n)$ we have access to the stable charge configurations of the two quantum dots, which we can visualize using a charge stability diagram [2, 3]. In Fig. 2.2 we show a numerically calculated charge stability diagram for the double quantum dot described above. Here, we have introduced two gate voltages V_L and V_R that shift n_L and n_R, respectively, assuming simple linear relations reading $V_L = U_{LL}n_L$ and $V_R = U_{RR}n_R$. As these voltages are changed, the stationary mean occupations of the two dots $(m_L, m_R) = (\langle\hat{n}_L\rangle, \langle\hat{n}_R\rangle)$ change, and the quasi-hexagonal, so-called honeycomb structure appears. For the shown charge stability diagram, we have taken the single-particle levels to be identical and zero, i.e., $\varepsilon_L = \varepsilon_R = 0$, and we have assumed that no bias is applied between the left and right electrodes. Also, a constant tunneling density of states $\Gamma_\alpha \equiv 2\pi|t_\alpha|^2\mathcal{D}_\alpha$, $\alpha = L, R$, has been assumed, where $t_{L(R)}$ is the tunnel-coupling from the left (right) quantum dot to states in the left (right) lead with density of states $\mathcal{D}_{L(R)}$, and we have assumed that the coupling to the leads is symmetric, i.e., $\Gamma_L = \Gamma_R$ (for finding the stationary state, only the ratio of the two rates matters, not their magnitude, although it has already in the weak coupling limit been assumed that the level-broadening due to these rates is negligible compared to the smearing due to the temperature).

In experiments similar charge stability diagrams can be mapped out by monitoring the current through a quantum point close to the double quantum dot. If the quantum point contact is tuned close to a conductance step, the current through it is highly sensitive to the number of charges on the nearby double quantum dot [2, 3]. This approach to charge sensing also opens up the possibility of real-time counting of electrons propagating through the double dot [22], which will be the subject of Chapter 4. From the charge stability diagram many of the parameters entering the model described above can be extracted, including the tunnel coupling, which gives rise to hybridized single-particle states and corresponding curvature of the boundaries between different charge stability regions [2, 3]. For the shown charge stability diagram a relatively large tunnel coupling has been used (see the figure caption for the used parameters), and the curvature is clearly seen in the honeycomb diagram. The temperature can be seen in the smearing of the transitions between different charge stability regions.

Although that we in this section do not perform any calculations of transport through the double dot, the charge stability diagram still provides us with information about when we can expect low-bias transport to occur. Similarly to the charging energy parabolas shown in Fig. 2.1, we can locate degeneracy points, where three charge stability configurations of the form (m_L, m_R), (m_L+1, m_R), and (m_L, m_R+1), are equally possible [for example $(0,0)$, $(1,0)$, and $(0,1)$, as indicated by a circle in Fig. 2.2]. At such a triple point, single electrons can propagate through the double quantum dot, taking it through the sequence $(m_L, m_R) \to (m_L+1, m_R) \to (m_L, m_R+1) \to (m_L, m_R)$, where we have assumed that the electron enters the left quantum dot from the left lead and leaves the right dot via the right lead. Without Coulomb interaction between the two dots, it may also be possible to find points, where four charge stability configurations of the form (m_L, m_R), (m_L+1, m_R), (m_L, m_R+1), and (m_L+1, m_R+1), are equally possible and all participate in transport. Finally, we note that the charge stability configuration $(1,1)$ offers a unique experimental setting for studies of the interactions between two (fairly) well-isolated electrons. In the models presented here, the spin degrees of freedom were not included, but the study of spin-spin interactions between two trapped electrons will be a central theme in the following chapter.

2.2 Mechanical vibrations

In the previous section we considered conventional Coulomb blockade quantum dots, where mainly the electronic degrees of freedom are of interest.

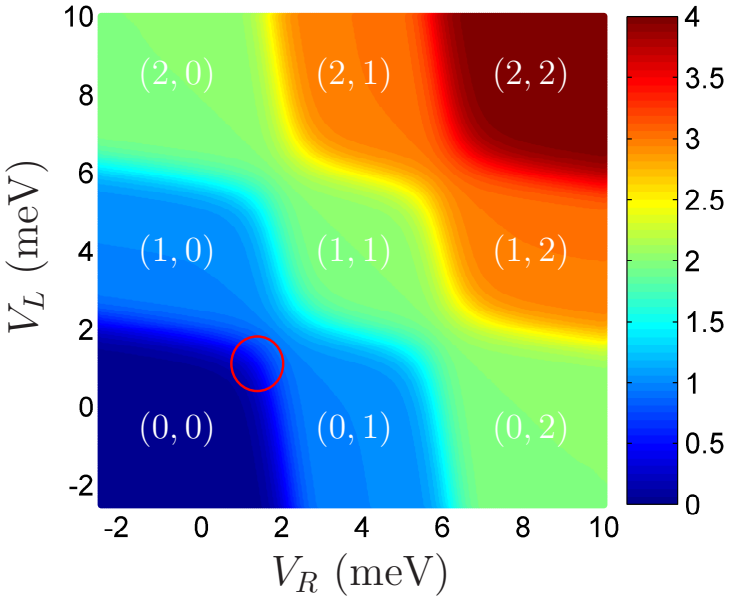

Figure 2.2: Charge stability diagram of two tunnel-coupled quantum dots. For a given setting of the gate voltages V_L and V_R we can read off the stable charge configuration of the double quantum dot, where the notation (m_L, m_R) denotes the mean number of electrons on the left and right quantum dot, respectively. The strengths of the Coulomb interaction on each of the quantum dots are $U_{LL} = U_{RR} = 4$ meV, while the strength of the inter-dot Coulomb interaction is $U_{LR} = 1$ meV. The tunnel-coupling between the dots is $\tau = 1$ meV, giving rise to the clear curvature of the boundaries between different charge stability regions. The smearing of the boundaries is due to a finite temperature of the leads, here $k_B T = 0.5$ meV (or $T \simeq 6$ K). A triple-point, where low-bias transport is allowed, is marked by the circle. The scale-bar denotes the total number of electrons on the two quantum dots.

In the field of nano-electromechanical systems (NEMS) electron transport is combined with mechanical vibrations, adding an extra degree of complexity on top of the quantum dot physics already described. Typically, the mechanical degrees of freedom are provided by a nano-to-micrometer size cantilever or pillar or by a molecule trapped between the source and drain electrodes. The mechanical degrees of freedom may couple capacitively to the electronic degrees of freedom as in the experiment reported in Ref. [23], where a superconducting single-electron transistor (SSET) was used as a sensitive probe of the position of a doubly clamped nano-resonator. In Ref. [24] measured conductance steps were associated with vibration-assisted electron tunneling through a C_{60} molecule, whose mechanical degrees of freedom were assumed quantized. Nano-electromechanical systems with quantized vibrations form a subfield of NEMS, which has been coined quantum electromechanical systems or QEMS [25].

An interesting type of NEMS (or QEMS), which will be our main focus in the following, is the so-called charge shuttle, originally proposed in Ref. [26]. In this proposal a nano-sized metallic island is imagined to be trapped in a soft matrix between source and drain electrodes. The system is operated close to a degeneracy point in the Coulomb blockade regime, where electrons propagate one-by-one through the system. If the applied bias is sufficiently large, an electromechanical instability occurs, and the system goes from the standard tunneling regime to the so-called shuttling regime, where the grain is driven into mechanical oscillations back and forth between the electrodes: When an electron tunnels from the source onto the metallic grain, the electric field between the leads drives the grain towards the drain electrode, where the electron is then released, the grain returns towards its equilibrium position, and the process repeats. The system displays an interesting interplay between electronic and mechanical degrees of freedom, since the flow of electrons drives the oscillations of the grain, which, in turn, affects the electron tunneling processes via the exponential dependence of the tunneling probability on the position of the grain. In terms of applications, the system is interesting, since it is expected to provide a highly well-defined, low-noise charge flow with an average current given by the electron charge e and the oscillator frequency ω_0, i.e., $I = e\omega_0/2\pi$.

The shuttling instability has not yet been demonstrated experimentally on the nano-scale, although progress towards that goal has been reported [27, 28]. In Ref. [28] an integer number of electrons were transported between source and drain electrodes via the tip of a vibrating silicon nano-pillar. The mechanical oscillations were, however, not driven by a pure DC-bias across the tip, and the Coulomb blockade regime was not reached. On the theoretical side, a series of works have dealt with various aspects of nano-

scale charge shuttling. For example, spin transport in shuttle systems was considered in Refs. [29, 30, 31], noise properties and counting statistics of a classical and an AC-driven shuttle in Refs. [32, 33, 34, 35], and shuttling of Cooper pairs in Refs. [36, 37, 38]. A first-principles calculation of a molecular shuttle system was reported in Ref. [39], and also more exotic phenomena, like Kondo shuttling [40], have been discussed.

An important question relates to the mechanical motion in nano-sized shuttle systems: How does a shuttle system behave, when its dimensions are so small that the vibrational degrees of freedom become quantized? In the experiment described in Ref. [41] a nanomechanical resonator was cooled towards the quantum mechanical ground state, indicating that the idea of a *quantum* shuttle, where the mechanical motion is quantized, may be experimentally reachable. This idea has been discussed theoretically in Refs. [42, 43, 44, 45], and we shall here mainly focus on the models of charge transport through quantum shuttles developed in Refs. [42, 43].

Both of these models are described by many-particle Hamiltonians of the form

$$\begin{aligned}\hat{H} =& \hat{H}_{\rm elec} + \hat{H}_{\rm osc} + \hat{H}_{\rm bath} + \hat{H}_{\rm leads} \\ &+ \hat{H}_{\rm elec-osc} + \hat{H}_{\rm osc-bath} + \hat{H}_{\rm elec-leads},\end{aligned} \tag{2.7}$$

where the first line contains the Hamiltonians of the various subsystems – the electronic states of the quantum shuttle, $\hat{H}_{\rm elec}$, the mechanical oscillator, $\hat{H}_{\rm osc}$, an external heat bath providing mechanical dissipation, $\hat{H}_{\rm bath}$, and the source and drain electrodes, $\hat{H}_{\rm leads}$ – while the second line describes their mutual couplings and interactions. The two models mainly differ in their electronic level structure, $\hat{H}_{\rm elec}$, and the electro-mechanical coupling, $\hat{H}_{\rm elec-osc}$. While both systems are operated in the Coulomb blockade regime such that only a single additional electron may enter the device, the model considered in Ref. [42] consists of an array of three coherently coupled quantum dots, where only the central quantum dot has a mechanical degree of freedom. In contrast, the model considered in Ref. [43] consists of a single mechanically vibrating quantum dot coupled to left and right electrodes. Although, the former model was the first proposal for a charge shuttle with quantized mechanical degrees of freedom, we shall refer to it as a vibrating quantum dot array, since the coherent coupling to the additional quantum dots both complicates and enriches the physics beyond standard "shuttle physics". Instead we refer to the second model consisting of a single vibrating quantum dot as a quantum shuttle.

In both models, the mechanical oscillations are described by a harmonic oscillator with mass m and frequency ω_0, i.e., $\hat{H}_{\rm osc} = \hat{p}^2/2m + m\omega_0^2\hat{x}^2/2$.

The systems are tunnel-coupled to source (left) and drain (right) electrodes, which are treated as reservoirs of non-interacting fermions kept at chemical potentials μ_L and μ_R, respectively, and mechanical dissipation is provided by a generic heat bath at temperature T consisting of harmonic oscillators that couple linearly to the position of the oscillating dot. For the quantum shuttle only a single electronic state with energy ε_0 is considered and the coupling to the harmonic oscillator is provided by the electric field E between the electrodes, such that [43]

$$\hat{H}_{\rm elec}^{\rm shut} + \hat{H}_{\rm elec-osc}^{\rm shut} = (\varepsilon_0 - eE\hat{x})c_0^\dagger c_0. \tag{2.8}$$

The oscillator affects the electronic tunnel-coupling to the leads via exponential dependencies of the effective tunneling rates on the position $\hat{x}$. The system is shown schematically in Fig. 2.3. In the model of the vibrating quantum dot array three electronic states, $|L\rangle$, $|C\rangle$, and $|R\rangle$, are tunnel-coupled in series, such that [42, 46]

$$\hat{H}_{\rm elec}^{\rm array} + \hat{H}_{\rm elec-osc}^{\rm array} = \begin{pmatrix} \varepsilon_b/2 & t_L(\hat{x}) & 0 \\ t_L(\hat{x}) & -\varepsilon_b\hat{x}/2x_0 & t_R(\hat{x}) \\ 0 & t_R(\hat{x}) & -\varepsilon_b/2 \end{pmatrix}, \tag{2.9}$$

where we for the electronic degrees of freedom have used a matrix representation in the basis consisting of $|L\rangle$, $|C\rangle$, and $|R\rangle$. The tunnel-couplings between the quantum dots depend exponentially on the position of the oscillator, i.e., $t_L(\hat{x}) = \tau_L e^{-\alpha(\hat{x}+x_0)}$, $t_R(\hat{x}) = \tau_R e^{\alpha(\hat{x}-x_0)}$, where it has been assumed that the outer dots are positioned at $\pm x_0$ (not the characteristics oscillator length here) and α denotes the inverse tunneling length, while the position of the central dot is denoted $\hat{x}$. In this model the electron flow drives the oscillator via the energy difference ε_b between the outer dots, referred to as the device bias. The coupling to the leads does not depend on the oscillator. The vibrating quantum dot array is shown schematically in Fig. 2.4.

Calculating the transport characteristics of these models is a highly non-trivial, non-equilibrium, many-particle problem, which has no simple solution. Combining many-body correlations with broadening of levels due to the coupling to continua of states, e.g., the leads, under non-equilibrium conditions forms a core problem in quantum transport theory [21, 47]. In one approach, the leads and the heat bath are traced out, and an equation of motion, a so-called generalized Master equation, for the reduced density matrix $\hat{\rho}(t)$ of the electronic states and the oscillator can be derived. Such derivations are still highly complicated and the resulting equations are typically only valid in certain parameter ranges and under certain assumptions. In Ref. [48] Gurvitz and Prager devised a systematic approach to microscopic

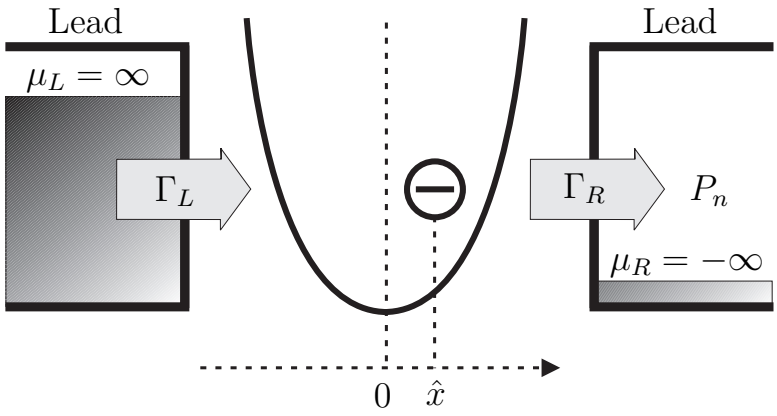

Figure 2.3: Illustration of the quantum shuttle. A high bias drives electrons through the quantum dot, causing the shuttle instability to occur. The injection of electrons from the left lead and the ejection of electrons via the right lead depend on the position $\hat{x}$ of the quantum dot. The mechanical vibrations are damped with rate γ due to a surrounding heat bath. The probability of having collected n electrons during the time span t is denoted $P_n(t)$ and is a central object in characterizing transport through the shuttle, which will be one of the subjects of Chapter 4. Figure from Paper **D**.

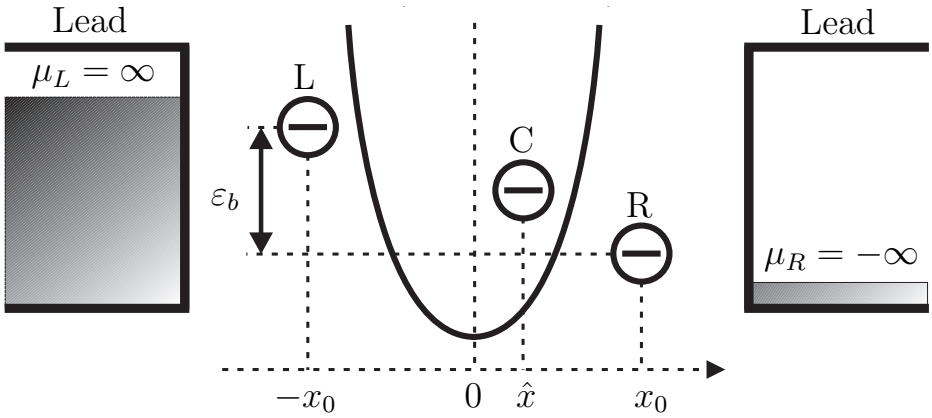

Figure 2.4: Illustration of the vibrating quantum dot array. A high bias drives electrons through the array whose outer quantum dots are dealigned by the device bias ε_b. The central quantum dot can vibrate mechanically, and thereby modify the tunnel-coupling to the outer quantum dots that are assumed to be static at positions $\pm x_0$. The mechanical vibrations of the central quantum dot are damped with rate γ due to a surrounding heat bath. Figure from Paper **B** (not included).

derivations of generalized Master equations in the contexts of quantum transport taking as starting point a many-particle Hamiltonian. The method was applied to a number of few-state systems, and the resulting generalized Master equations were shown only to hold, if the electronic states lie well within the bias window, such that the width of the states due to the coupling to the leads does not extend outside the bias window. This we refer to as the high-bias limit. Moreover, a constant tunneling density of states was assumed, such that injection of electrons from the left lead end ejection via the right lead can be described by single rates Γ_L and Γ_R, respectively.

The approach by Gurvitz and Prager was also applied in Refs. [42, 43] to describe transport through the quantum dot array and the quantum shuttle, respectively, and here we just quote the resulting equations. For a thorough account of their derivation we refer to Ref. [49]. In both cases, the generalized Master equation takes the form

$$\mathcal{L}\hat{\rho}(t) = (\mathcal{L}_{\rm coh} + \mathcal{L}_{\rm driv} + \mathcal{L}_{\rm damp})\hat{\rho}(t), \tag{2.10}$$

where the Liouvillean $\mathcal{L}$ consists of $\mathcal{L}_{\rm coh}$, containing the coherent dynamics of the system, if it were isolated, $\mathcal{L}_{\rm driv}$, describing the coupling to the leads and the injection and ejection of electrons, and the damping kernel $\mathcal{L}_{\rm damp}\hat{\rho}(t)$ accounting for dissipation due to the heat bath. The coherent part has the form $\mathcal{L}_{\rm coh}\hat{\rho}(t) = -i[\hat{H}_{\rm elec} + \hat{H}_{\rm osc} + \hat{H}_{\rm elec-osc}, \hat{\rho}(t)]$ (with $\hbar = 1$). For the quantum shuttle the driving part reads for the electronic diagonal elements [43]

$$\begin{aligned}
\mathcal{L}^{\rm shut}_{\rm driv}\hat{\rho}_{00} &= -\frac{\Gamma_L}{2}(e^{-\frac{2\hat{x}}{\lambda}}\hat{\rho}_{00} + \hat{\rho}_{00}e^{-\frac{2\hat{x}}{\lambda}}) + \Gamma_R e^{\frac{\hat{x}}{\lambda}}\hat{\rho}_{11}e^{\frac{\hat{x}}{\lambda}}, \\
\mathcal{L}^{\rm shut}_{\rm driv}\hat{\rho}_{11} &= -\frac{\Gamma_R}{2}(e^{\frac{2\hat{x}}{\lambda}}\hat{\rho}_{11} + \hat{\rho}_{11}e^{\frac{2\hat{x}}{\lambda}}) + \Gamma_L e^{-\frac{\hat{x}}{\lambda}}\hat{\rho}_{00}e^{\frac{-\hat{x}}{\lambda}},
\end{aligned} \tag{2.11}$$

where λ is the tunneling length entering the exponential position dependence of the tunnel rates. For the quantum dot array, the driving term can be written

$$\mathcal{L}^{\rm array}_{\rm driv}\hat{\rho} = \begin{pmatrix} \Gamma_R\hat{\rho}_{RR} - \Gamma_L\hat{\rho}_{00} & 0 & 0 & 0 \\ 0 & \Gamma_L\hat{\rho}_{00} & 0 & -\frac{1}{2}\Gamma_R\hat{\rho}_{LR} \\ 0 & 0 & 0 & -\frac{1}{2}\Gamma_R\hat{\rho}_{CR} \\ 0 & -\frac{1}{2}\Gamma_R\hat{\rho}_{RL} & -\frac{1}{2}\Gamma_R\hat{\rho}_{RC} & -\Gamma_R\hat{\rho}_{RR} \end{pmatrix}, \tag{2.12}$$

where $\hat{\rho}_{ij} \equiv \langle i|\hat{\rho}|j\rangle$ is the electronic matrix element of $\hat{\rho}(t)$ between the electronic states $|i\rangle$ and $|j\rangle$, $i, j = 0, L, C, R$. Note that these matrix elements are still operators in the oscillator space. Finally, the damping $\mathcal{L}_{\rm damp}$ can take different forms, which we will not discuss in further detail here, since

the exact form does not play a significant role, as long as the damping is sufficiently weak. Importantly, however, the damping kernel contains a rate γ at which the oscillator is damped and a temperature T which, via the Bose-Einstein distribution, defines the mean occupation number of the oscillator at thermal equilibrium. We note that the high-bias assumption effectively means that the source and drain electrodes can be considered as completely filled and empty Fermi seas, respectively, and the temperature of the electron reservoirs consequently drops out of the problem.

In Refs. [42, 43] the mean current through the quantum shuttle and the quantum dot array was calculated numerically as function of the damping γ and the device bias ε_b, respectively. In particular, for the quantum shuttle charge-resolved Wigner phase space distributions of the oscillator led to an easy identification of a cross-over from a standard sequential tunneling picture to the shuttling regime with decreasing damping [43]. In the shuttling regime, a clear correlation between the motion of the oscillator and the charge state could be seen and the mean current saturated to a value which is consistent with the expected shuttle current given by the electron charge and the oscillator frequency. In Ref. [42], peaks in the mean current were identified at values of the device bias close to integer multiplies of the oscillator frequency, strongly indicating the occurrence of electro-mechanical resonances and vibration-assisted transport through the array.

While the Wigner phase space distributions provide a convenient, theoretical means to visualize and investigate the dynamics of the mechanical degrees of freedom, such phase-space distributions may not be easily experimentally accessible. As an alternative way of probing and investing the systems we consequently went beyond studies of the mean current and considered in Papers **A** and **B** (not included) the current fluctuations or the noise of the systems, which is a quantity that is more routinely measured in experiments [50]. Calculating the current noise of systems described by generalized Master equations of the form given in Eq. (2.10) is, however, a non-trivial technical challenge which we had to address. In Chapter 4 we describe in further detail the set of tools (and extensions thereof) we developed in this effort. Most interestingly, we found numerically that both systems in certain parameter regimes exhibit a large noise enhancement, which we tentatively attributed to an electro-mechanical bistability leading to a slow switching between two current channels, also known as telegraph noise [50]. This claim was further substantiated and supported in Papers **D** and **F** and is also discussed in more detail in Chapter 4. Finally, we mention that while generalized Master equations of the form given in Eq. (2.10) are clearly local in time and thus Markovian, another more general and interesting class of equations are those with a memory-kernel, so-called non-Markovian general-

ized Master equations, which constitute another important topic in Chapter 4.

2.3 Defect states

At the beginning of this chapter we introduced a series of conventional methods to confine electrons in man-made solid-state structures on the nano-scale. All of these approaches have successfully been demonstrated in numerous experiments, and each have their individual advantages in terms of quantum dot tunability, optical activity, etc. In order to devise a readily scalable procedure that would allow for the fabrication of a large number of coupled, localized electronic states, we explored in Paper **I** an idea to create "artificial" band structures and band gaps, in which localized electronic states can reside, very much in the spirit of the principles exploited in photonic crystals [51, 52] and photonic crystal fibers [53].[1] Although the exact origin of the potential modulation is not essential or crucial for the idea presented in the following, we were inspired by almost two decades of semiconductor fabrication of so-called antidot lattices [54, 55, 56, 57, 58]. These structures typically consist of a semiconductor heterostructure interface hosting a two-dimensional electron gas (2DEG). Using a conducting atomic force microscope (AFM) tip the heterostructure is locally oxidized, leading to a depletion of the underlying 2DEG. Such a depletion region, which can be on the order of 100 nm or less in diameter, is referred to as an antidot, and a periodic pattern of antidots is commonly known as an antidot lattice. While perfectly periodic antidot lattices have been the subject of numerous experimental studies, antidot lattices containing "defects", i.e., missing antidots, have not yet been considered, and the main goal of Paper **I** was exactly to consider designed defects in antidot lattices and, in particular, the formation of bound states, which we shall refer to as defect states, at the location of the missing antidots.

We thus consider a simple model of a two-dimensional electron gas residing at a semiconductor heterostructure interface with a periodic potential modulation. The electrons are treated in the effective mass approximation, obeying the standard quadratic dispersion relation $\varepsilon_{\mathbf{k}} = (\hbar\mathbf{k})^2/2m^*$ in absence of the potential modulation, where m^* is the effective electron mass determined by the host material (e.g. $m^* = 0.067m_e$ for GaAs). In the effective mass approximation the two-dimensional single-electron Schrödinger

[1] Of course, the idea behind photonic band gaps etc. might originally have been inspired by similar concepts in solid-state physics, and in that sense we are "stealing" it back.

equation then reads

$$\left[-\frac{\hbar^2}{2m^*}\nabla^2 + \sum_i V(\mathbf{r}-\mathbf{R}_i)\right]\psi_n(\mathbf{r}) = E_n\psi_n(\mathbf{r}), \tag{2.13}$$

where the sum runs over the positions $\mathbf{R}_i$ of the anti-dots. Each antidot is modeled as a circular potential barrier of height V_0 and diameter d, i.e., $V(\mathbf{r}) = V_0$ for $|\mathbf{r}| < d/2$ and zero otherwise. We consider the lattice of anti-dots to be hexagonal with a center-to-center distance between the antidots denoted Λ, commonly referred to as the pitch in the field of photonic crystal fibers. The lattice is shown schematically in the left inset of Fig. 2.5, where the Wigner-Seitz cell is also indicated in gray. Moreover, we consider states residing energetically well below the barrier height V_0, such that penetration of the electron wave functions into the antidots can be neglected, i.e., $\psi_n(\mathbf{r}) = 0$ in the anti-dots. The assumption is not crucial, as long as V_0 is larger than the other energy scales that we consider, but it simplifies our calculations in the following by reducing Eq. (2.13) to

$$-\Lambda^2\nabla^2\psi_n(\mathrm{r}) = \varepsilon_n\psi_n(\mathrm{r}), \tag{2.14}$$

where we have introduced the dimensionless eigenenergies $\varepsilon_n = \frac{2m^*\Lambda^2 E_n}{\hbar^2}$.

The periodicity imposed by the antidot lattice can be used to construct an eigenbasis corresponding to Eq. (2.14). In particular, it can be seen from Fig. 2.14 that eigenstates can be chosen which are left invariant, up to a phase factor, under translation by the distance Λ in the directions $\mathbf{a}_1 = (1, 0)$ and $\mathbf{a}_2 = (1, \sqrt{3})/2$. These are, of course, the Bloch states $\psi_{\mathbf{n},\mathbf{k}}(\mathbf{r})$ which fulfill the translational constraint $\psi_{\mathbf{n},\mathbf{k}}(\mathbf{r} - \mathbf{R_n}) = e^{-i\mathbf{k}\cdot\mathbf{R_n}}\psi_{\mathbf{n},\mathbf{k}}(\mathbf{r})$, where $\mathbf{R_n} = \Lambda(n_1\mathbf{a}_1 + n_2\mathbf{a}_2)$ with $n_1, n_2 \in \mathbb{Z}$. This observation allows us to calculate the effective band structure due to the antidot lattice by solving Eq. (2.14) on the finite-size domain defined by the Wigner-Seitz cell with periodic boundary conditions. Such numerical calculations are easily implemented and carried out using commercially available finite-element packages. In Fig. 2.5 we show results of band structure calculations for the high-symmetry axes illustrated in the right inset, where the first Brillouin zone can be seen. A number of band gaps have clearly appeared due to the periodic potential modulation, and in the following we shall consider the lowest-lying gap, indicated with ϑ_{eff}, in more detail. We note that Ref. [59] and Papers **P**, **Q** (both not included), and **R** contain more elaborate, numerical band structure and density-of-states calculations.

As already mentioned, the appearance of band gaps opens up the possibility of creating localized states, residing inside the band gaps, by introducing designed "defects" in the lattice, i.e., leaving out one or several antidots in the

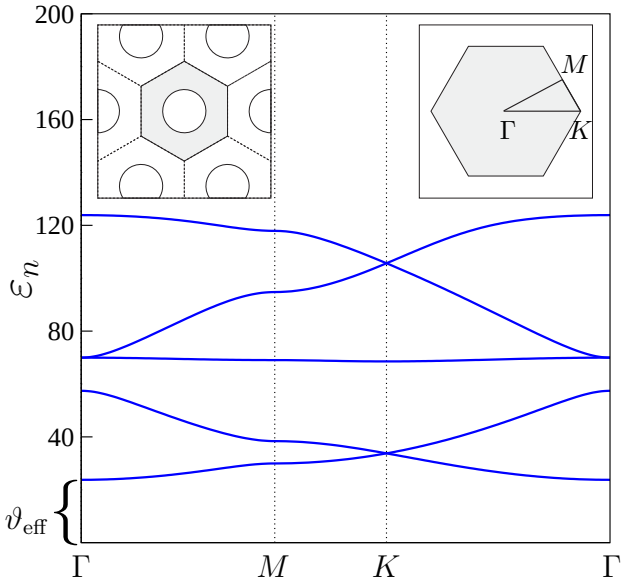

Figure 2.5: Band structure of a periodic antidot lattice. Results were obtained by solving numerically the single-particle Schrödinger equation with periodic boundary conditions on the boundaries of the Wigner-Seitz cell shown with gray in the left inset and assuming that the wavefunction vanishes inside the antidots indicated with circles. The band structure in shown along the high-symmetry axes indicated on the first Brillouin zone shown in the right inset. Results were obtained with $d/\Lambda = 0.5$. The dimensionless energies are $\varepsilon_n = 2m^*\Lambda^2 E_n/\hbar^2$ with $\hbar^2/2m \approx 0.6$ eVnm^2 for GaAs. With $\Lambda \simeq 100$ nm, the gap ϑ_{eff} is on the order of 2 meV. Figure from Paper **I**.

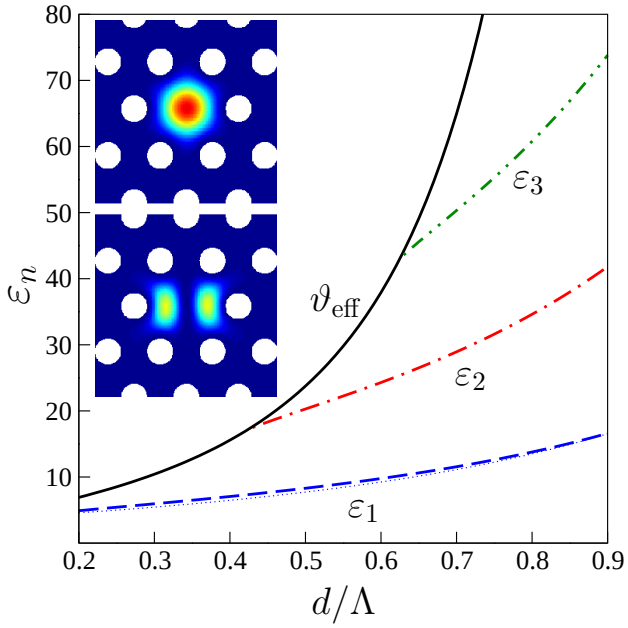

Figure 2.6: Energy spectrum of a single defect. The energy of three (localized) defect states are shown as function of the ratio d/Λ together with the gap height $\vartheta_{\rm eff}$ (full line), giving an upper limit to the existence of bound states. The thin dotted line is a semi-analytic expression for the first level derived in Paper **I**. The inset shows the absolute square of the localized eigenfunctions corresponding to the first (upper panel) and the second (lower) panel eigenenergies at $d/\Lambda = 0.5$. The dimensionless energies are $\varepsilon_n = 2m^*\Lambda^2 E_n/\hbar^2$ with $\hbar^2/2m \approx 0.6$ eVnm^2 for GaAs. Figure from Paper **I**.

structure. As an example of such defect states we consider an antidot lattice with a single defect. The level-structure corresponding to this configuration of antidots can again be found using finite-element methods by solving the single-particle Schrödinger equation on a large super-cell, containing many antidots surrounding the defect, and assuming that eigenfunctions vanish far from the defect. In Fig. 2.6 we show the energy spectrum for a single defect as function of the ratio d/Λ. Together with the position of the eigenenergies we show the height of the effective potential (or gap height) $\vartheta_{\rm eff}$ surrounding the defect, giving an upper limit to the existence of localized states (in the first gap). It is interesting to note, that the number of localized states can be controlled via the ratio d/Λ, and in particular, it is seen that only a single localized state forms, if $d/\Lambda < 0.42$. The insets show the absolute square of two localized states formed for $d/\Lambda = 0.5$.

Two neighboring defects may lead to a level-structure which resembles that of conventional tunnel-coupled quantum dots. Also in the present case, bonding and anti-bonding states form, which are energetically split by twice the tunnel-coupling, i.e., $\Delta\varepsilon = 2\tau$. From the energy-spectrum of the coupled defect states we can thus find the tunnel-coupling τ, which is shown in Fig. 2.7 as function of the width w of a constriction separating the two defects. This could for example be implemented using a split-gate geometry as indicated on the figure, and the width could be controlled by changing the applied voltages on the gate electrodes making up the split-gate. The inset shows snap shots of coherent oscillations of an electron initially localized in the left defect, resembling similar charge dynamics observed in tunnel-coupled quantum dots, e.g., in the isolated silicon double-dot structure described in Ref. [60].

Based on the principles outlined above, anti-dot lattices may provide a convenient experimental platform for studies of electron dynamics in several tunnel-coupled defect states. From an experimental point of view it should, in principle, not present any significant extra effort to fabricate several coupled defect states, once two coupled states have successfully been implemented in an antidot lattice. Coherent transport through arrays of tunnel-coupled quantum dots has been studied in Refs. [61, 62], where a highly precise tuning of the tunnel couplings between neighboring quantum dots in a linear array was suggested as a means to obtain complete population transfer from one end of the array to the other. As an alternative approach to coherent charge transfer between spatially well-separated electronic levels, which does not reply on a precise tuning of tunnel couplings, we have recently explored an idea based on resonant coupling of two distant defect states in an antidot lattice inspired by related ideas for transverse light guiding in optical fibers [63, 64]. The mechanism behind the resonant coupling is described in Ref. [59] and Paper **R**.

Finally, we discuss the importance of the length scale Λ which via the relation $E_n = \hbar^2\varepsilon_n/2m^*\Lambda^2$ determines the actual eigenenergies E_n by relating them to the dimensionless eigenenergies ε_n. Clearly, smaller values of Λ lead to tighter confinement of the defect states and corresponding larger (actual) level-splittings, which should be compared to the other energy scales of the system, e.g., temperature. While it might not be conceivable to fabricate antidot lattices with values of Λ much below 100 nm using local oxidation techniques, one could alternatively imagine creating tighter confinements by pattering a sheet of graphene with a lattice of holes and use that as an antidot lattice structure in which designed defects can be introduced. Sheets of graphene can now be routinely fabricated [65, 66, 67] and with available electron beam techniques it should be possible to make holes with a radius

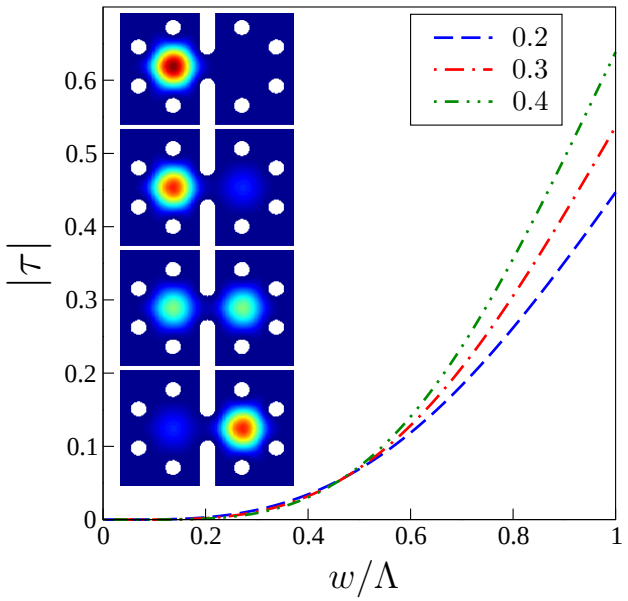

Figure 2.7: Tunnel coupling as function of constriction width. Two single-level defects are tunnel-coupled via a split-gate geometry as indicated on the insets, showing the time evolution of a particle initialized in the right defect (upper inset). The absolute square of the wavefunction is shown. The width w of the constriction is assumed to be controllable using the voltages applied to the gate electrodes indicated on the insets. The three curves correspond to different values of the ratio d/Λ, while the time-evolution was carried out with $d/\Lambda = 0.4$ and $w/\Lambda = 0.6$. The dimensionless tunnel coupling is defined as $|\tau| = 2m^*\Lambda^2|t|/\hbar^2$ with $\hbar^2/2m \approx 0.6$ eVnm^2 for GaAs. With $\Lambda \simeq 100$ nm the oscillation period is $T \simeq 0.3$ ns. Figure from Paper **I**.

corresponding to a few lattice constants of graphene ($a_{\text{latt}} \simeq 0.246$ nm). With such small structures, the band gaps would be on the order of 1 eV, making graphene antidot lattices an interesting candidate system for coherent electron and electron spin manipulation. As proposed in Ref. [68] graphene may be a suitable material for coherent spin manipulation and quantum information processing due to the low spin-orbit coupling in graphene and because the predominant carbon isotope ^{12}C has zero nuclear spin and consequently no hyperfine interaction with the electron spin. Very recently, we have considered defect states in graphene antidot lattices as a possible platform for quantum information processing with electron spins. This proposal in described in Paper **S** (not included). The next chapter deals with electrons spins in tunnel-coupled quantum dots as a resource for quantum information processing in the solid-state.

Chapter 3

Spin Physics

The electrons internal[1] contribution to its angular momentum, the *spin*, has for decades been a physical quantity of immense interest and research, partially due to its potential applications in future technologies. For example, within the field of spintronics, the spin of the electron plays a role similar to that of the electron charge in conventional electronics. Rather than controlling the flow of electron charge through a device, the aim is to develop devices whose functionality is determined by the flow of spin polarized currents. In a different field, solid-state quantum computing, the electron spin is considered as a promising candidate for quantum information storage and manipulation, since the electron spin provides a natural two-level system that could serve as a quantum bit, a *qubit*, in a future solid-state architecture for quantum information processing. While the field of spintronics is often concerned with large numbers of spins, spin based quantum information processing deals with the manipulation and control of just a single or a small number of electron spins.

In this chapter the emphasis lies on the use of the electron spin as a carrier of information in a future device for quantum information processing in the solid-state. We first give a very brief introduction to quantum computing, including the criteria needed to be addressed for a physical implementation, and we discuss the current experimental status of quantum computing with electron spins in quantum dots. We then consider the exchange coupling between electron spins in tunnel coupled quantum dots, which forms an important building block for spin based quantum computing. In particular, we discuss the origin of the coupling and various approaches for calculating the coupling strength. The two last sections are devoted to two proposals for novel approaches to spin manipulation and quantum optical interfacing of

[1] By internal we here mean independent of the orbital degrees of freedom.

quantum dot systems. In the first proposal we consider the spin-orbit coupling in a one-dimensional geometry, e.g., a nanowire, as a general means to manipulate and couple electron spins in gate-defined double quantum dots. In the second proposal we consider an opto-electrical device for electrical generation of single photons that are entangled with the spin states of the electrons in a double quantum dot.

3.1 Quantum computing

Conventional, or classical, computers are based on information storage in bits that can take the values 0 or 1. This approach to information storage and processing has already been demonstrated to be extremely successful from a technology point of view, when combined with digital electronics based on discrete voltage levels. It may, however, be fruitful to challenge this approach, and ask what possible advantages could be gained, if the individual bits of a computer were replaced by quantum mechanical bits, or *qubits*, that would exploit the full Hilbert space spanned by two quantum states $|0\rangle$ and $|1\rangle$, corresponding to the classical bit 0 and 1, respectively. Rather than just being in the state $|0\rangle$ *or* $|1\rangle$, the state of such a qubit would in general be of the form

$$|\Psi\rangle = a|0\rangle + b|1\rangle, \tag{3.1}$$

with $|a|^2 + |b|^2 = 1$. Such thoughts were first articulated by R. P. Feynman [69, 70] and D. Deutsch [71] in the mid-eighties, and it was subsequently realized that qubits indeed would make it possible to construct certain quantum algorithms that would out-speed the corresponding classical algorithms. Most prominent are Shor's algorithm for prime number factorization [72] and Grover's search algorithm [73]. Even if only a few quantum algorithms to date have been constructed and shown superior to their classical counterparts, there may be good belief to think that quantum computers can provide speed-up to a much larger class of computational problems. At least, one could argue that it probably would be more surprising if it turned out that the algorithms developed so far were the only ones where quantum mechanics proved helpful, and from a more "variational" point of view, one can follow D. P. DiVincenzo in the claim that a quantum computer must be as least as good as a classical computer [74]: Since classical physics follows as a special case of quantum mechanics, there are no tasks that a classical computer can solve more efficiently than a quantum computer.

In the following we will not be concerned with the question of which types of problems could possibly be solved on a quantum computer. Instead we discuss the necessary conditions that must to be met in order to physically

implement a future device for quantum information processing. Five requirements have been formulated by D. P. DiVincenzo, which we quote from Ref. [74]:

1. A scalable physical system with well characterized qubits.
2. The ability to initialize the state of the qubits to a simple fiducial state, such as $|000\ldots\rangle$.
3. Long relevant decoherence times; much longer than the gate operation time.
4. A "universal" set of quantum gates.
5. A qubit-specific measurement capability.

Criteria 3 states that the time that a quantum bit can be kept in a quantum mechanical superposition of the form given in Eq. (3.1) before it via interactions with its environment reduces to a statistical mixture with a density matrix reading $\hat{\rho} = |a|^2|0\rangle\langle 0| + |b|^2|1\rangle\langle 1|$, should be much longer than the typical time of an operation on the qubit. Since quantum algorithms consist of a series of unitary operations on the qubits, it should be possible to implement any operation on the qubits as stated in criteria 4, but in most physical systems it may not be obvious how to implement a given desired interaction among the qubits. It has, however, been shown that any operation can be constructed from a *universal* set of quantum gates consisting of all *single*-qubit operations and a single *two*-qubit operation known as the controlled-NOT, or CNOT, gate [75]. The CNOT gate operates on a two-qubit state $|i,j\rangle$ as $U_{\mathrm{CNOT}}|i,j\rangle = |i, i\oplus j\rangle$ with $i,j = 0,1$ and $i\oplus j \equiv i+j-2ij$. The CNOT gate flips the second qubit conditioned on the state of the first. It is interesting to consider the application of the CNOT gate to a two-qubit state, where the first qubit is in the state $(|0\rangle + |1\rangle)/\sqrt{2}$ and the second is in the state $|0\rangle$,

$$U_{\mathrm{CNOT}} \frac{1}{\sqrt{2}} \left(|0\rangle_1 + |1\rangle_1\right) |0\rangle_2 = \frac{1}{\sqrt{2}} \left(|0\rangle_1|0\rangle_2 + |1\rangle_1|1\rangle_2\right). \tag{3.2}$$

As can be seen, the CNOT leads to a two-qubit state, which cannot be written as a product of single-qubit states, also known as an *entangled* state. The ability to generate entanglement between different qubits is thus a cornerstone in any physical implementation of a quantum computer according to DiVincenzos criteria. In many possible realizations of a quantum computer it may not be straightforward to implement the CNOT gate, but other

two-qubit operations also suffice, as long as they, with the use of single-qubit operations, can be transformed into the CNOT gate.

Having outlined the requirements for a future quantum computer, we next turn to an actual physical system. Already, a variety of systems from different fields of physics have been promoted and studied theoretically and experimentally. Candidate systems include trapped ion systems [76, 77], implementations based on nuclear magnetic resonance [78, 79, 80], nuclear spins of donor atoms in doped silicon devices [81], superconducting systems [82, 83], and nitrogen-vacancy (NV) centers in diamond [84, 85]. Here, we shall focus on a particular proposal from the solid-state, namely the spins of electrons trapped in gate-defined quantum dots [86, 87]. In this proposal, pioneered by D. Loss and D. P. DiVincenzo, the relatively well-isolated spin of an electron provides a natural two-level system in which a qubit can be encoded by defining, e.g., $|\downarrow\rangle \equiv |0\rangle$ and $|\uparrow\rangle \equiv |1\rangle$. The electron spins are envisioned to be trapped in gate-defined quantum dots as the ones described in the previous chapter, and in particular, two-qubit operations between spins in tunnel coupled quantum dots are carried out by electrically pulsing the exchange interaction between them [87]. The exchange interaction will be the subject of the following section, but for now we note that the Hamiltonian describing the exchange interaction between two electron spins $\boldsymbol{\sigma}_1$ and $\boldsymbol{\sigma}_2$ takes the form $\mathcal{H} = J\boldsymbol{\sigma}_1 \cdot \boldsymbol{\sigma}_2$ which can be used to implement the so-called square-root of swap operation, $\sqrt{\text{SWAP}}$, which via single-qubit operations can be mapped onto the CNOT gate [86]. The proposal is of particular interest in relation to DiVincenzos first criteria concerning scalability, since it is based on semiconductor technology which has already proven to be highly scalable when it comes to conventional computers.

Since the idea of using electron spins in gate-defined quantum dots for quantum computing was first proposed in 1998, a series of experiments have been addressing each of DiVincenzos criteria. Single-spin rotations using electron spin resonance (ESR) have thus been experimentally demonstrated (see Section 3.3) [88], as well as electrostatic control of the exchange coupling in a double quantum dot [6] and single-shot read-out of a single electron spin [89]. The main decoherence mechanism has proven to be the hyperfine coupling of the electron spin to nuclear spins in the host material [6, 86, 87] and ongoing experimental activities are consequently aimed at implementing the same ideas and concepts in materials, which in contrast to GaAs, have zero nuclear spin. Among such materials, two promising candidates are silicon [60] and graphene [68]. While criteria 2-5 essentially may be considered fulfilled, criteria 1 concerning scalability still remains experimentally unaddressed, but, as already mentioned, the success of semiconductor technology within conventional information processing makes it reasonable to believe

that an implementation of a large number of coupled quantum dots may be within experimental reach, and theoretical work towards that goal is already in progress [90].

Before finishing this section we briefly mention DiVincenzos additional criteria for the physical implementation of quantum communication, i.e., the transmission of intact qubits over a long distance. This would be desirable for, e.g., quantum cryptography and quantum key distribution [91, 92]. The additional requirements read [74]

6. The ability to interconvert stationary and flying qubits,

where flying qubits typically mean optical photons which, for example, can carry quantum information in the two light polarizations, and

7. The ability to faithfully transmit flying qubits between specified locations.

Concerning criteria 6, we propose in Section 3.4 a semiconductor device that would allow for emission of single photons that are frequency-entangled with the spin states of a double quantum dot. Before doing so, however, we start by considering in detail the exchange coupling between two electron spins in a double quantum dot.

3.2 Exchange interaction

As we saw in Chapter 2 tunnel-coupled double quantum dots can be tuned into a charge regime, where only a single electron occupies each of the two quantum dots. In this charge regime the spin and charge dynamics can be described by a *spin-independent* two-particle Hamiltonian of the form

$$H(\mathbf{r}_1, \mathbf{r}_2) = h(\mathbf{r}_1) + h(\mathbf{r}_2) + C(|\mathbf{r}_1 - \mathbf{r}_2|), \tag{3.3}$$

where the single-particle Hamiltonians read $h(\mathbf{r}) = \frac{[\mathbf{p}+e\mathbf{A}(\mathbf{r})]^2}{2m} + V(\mathbf{r})$, while $C(|\mathbf{r}_1 - \mathbf{r}_2|) = \frac{e^2}{4\pi\varepsilon_r\varepsilon_0|\mathbf{r}_1-\mathbf{r}_2|}$ is the Coulomb interaction between the two electrons. Since we are considering tunnel-coupled quantum dots, the external potential $V(\mathbf{r})$ has a double-well shape, while the dimensionality of the problem depends on the type of quantum dots considered [here, we consider two dimensions, i.e., $\mathbf{r} = (x, y)$]. The vector potential $\mathbf{A}(\mathbf{r})$ is chosen corresponding to a possible, applied magnetic field $\mathbf{B}$, i.e., $\mathbf{B} = \nabla \times \mathbf{A}$.[2] As we shall see,

[2]The Zeeman shift due to the magnetic field has been omitted in the Hamiltonian, but is trivial to include in final total energy calculations.

the Pauli principle leads to an effective interaction between the spin degrees of freedom, even though the problem defined by Eq. (3.3) at first glance does not seem to concern the spins [93].

The Pauli principle states that the total wavefunction $\Psi_{\sigma_1,\sigma_2}(\mathbf{r}_1,\mathbf{r}_2)$ describing two fermions must change sign under interchange of the particles, i.e., $\Psi_{\sigma_1,\sigma_2}(\mathbf{r}_1,\mathbf{r}_2) = -\Psi_{\sigma_2,\sigma_1}(\mathbf{r}_2,\mathbf{r}_1)$. In a second quantized description this is ensured by the anti-commutation relation of the creation operators that reads $\{\hat{c}^\dagger_{\alpha\sigma},\hat{c}^\dagger_{\beta\sigma'}\} = \hat{c}^\dagger_{\alpha\sigma}\hat{c}^\dagger_{\beta\sigma'} + \hat{c}^\dagger_{\beta,\sigma'}\hat{c}^\dagger_{\alpha,\sigma} = 0$, where $\hat{c}^\dagger_{\alpha\sigma}$, $\alpha = L,R$, creates an electron with spin $\sigma =\uparrow,\downarrow$ in the ground state of the left ($\alpha = L$) or right ($\alpha = R$) quantum dot. Assuming first that the two quantum dots are well-separated, such that tunnel coupling and Coulomb interaction between the two dots may be neglected, the ground state of the two-particle system is four-fold degenerate, and the ground state manifold may be spanned by the spin-singlet state

$$\frac{1}{\sqrt{2}}\left(\hat{c}^\dagger_{L\uparrow}\hat{c}^\dagger_{R\downarrow} - \hat{c}^\dagger_{L\downarrow}\hat{c}^\dagger_{R\uparrow}\right)|0\rangle \quad\leftrightarrow\quad \Psi^{(0)}_S(\mathbf{r}_1,\mathbf{r}_2)\otimes\frac{1}{\sqrt{2}}\left(|\uparrow\rangle_1|\downarrow\rangle_2 - |\downarrow\rangle_1|\uparrow\rangle_2\right)$$

and the spin-triplet states

$$\begin{aligned}
\hat{c}^\dagger_{L\uparrow}\hat{c}^\dagger_{R\uparrow}|0\rangle &\quad\leftrightarrow\quad \Psi^{(0)}_A(\mathbf{r}_1,\mathbf{r}_2)\otimes|\uparrow\rangle_1|\uparrow\rangle_2,\\
\frac{1}{\sqrt{2}}\left(\hat{c}^\dagger_{L\uparrow}\hat{c}^\dagger_{R\downarrow} + \hat{c}^\dagger_{L\downarrow}\hat{c}^\dagger_{R\uparrow}\right)|0\rangle &\quad\leftrightarrow\quad \Psi^{(0)}_A(\mathbf{r}_1,\mathbf{r}_2)\otimes\frac{1}{\sqrt{2}}\left(|\uparrow\rangle_1|\downarrow\rangle_2 + |\downarrow\rangle_1|\uparrow\rangle_2\right),\\
\hat{c}^\dagger_{L\downarrow}\hat{c}^\dagger_{R\downarrow}|0\rangle &\quad\leftrightarrow\quad \Psi^{(0)}_A(\mathbf{r}_1,\mathbf{r}_2)\otimes|\downarrow\rangle_1|\downarrow\rangle_2.
\end{aligned}$$

In the right column we have included the real-space representation of the two-particle states with $\Psi^{(0)}_{S/A}(\mathbf{r}_1,\mathbf{r}_2) \equiv \left[\psi_L(\mathbf{r}_1)\psi_R(\mathbf{r}_2) \pm \psi_R(\mathbf{r}_1)\psi_L(\mathbf{r}_2)\right]/\sqrt{2}$ being (anti-)symmetric combinations of the orbital groundstate wavefunctions $\psi_{L/R}(\mathbf{r})$ of the (isolated) left and right dots, respectively.[3] It is important to notice that the orbital part, $\Psi^{(0)}_S$, of the spin-singlet state is symmetric, while the spin-triplet states have an anti-symmetric orbital part, $\Psi^{(0)}_A$. If the two quantum dots are moved closer together tunnel coupling and Coulomb interactions become important, and the *non-interacting* orbital wavefunctions $\Psi^{(0)}_S$ and $\Psi^{(0)}_A$ given in terms of Slater permanents and determinants, respectively, are no longer eigenfunctions of the Hamiltonian in Eq. (3.3). Instead, the eigenvalue problem $H\Psi_{S/A} = \varepsilon_{S/A}\Psi_{S/A}$ must be solved. The splitting $J_V(\mathbf{B}) \equiv \varepsilon_A - \varepsilon_S$ of the two groundstates energies, corresponding to symmetric and anti-symmetric orbital wavefunctions, respectively, generally

[3]Here, we have not allowed for linear combinations of the single particle states ψ_L and ψ_R, since this would lead to doubly occupied dots, which would be energetically unfavorable.

depends on the shape of the confining potential V and the applied magnetic field $\mathbf{B}$. As we shall shortly see the *exchange* energy $J_V(\mathbf{B})$ determines the strength of an effective spin-spin interaction.

Since the Pauli principle intimately links the symmetries of the spin and the orbital parts, it is possible to think of the splitting $J_V(\mathbf{B})$ between the *orbital* groundstate eigenfunctions as a splitting between the spin states instead [93]. The mapping between orbital and spin degrees of freedom can be constructed by considering the square of the operator of the total spin $\boldsymbol{\sigma} = \boldsymbol{\sigma}_1 + \boldsymbol{\sigma}_2$ of the two electrons, $\boldsymbol{\sigma}^2 = \boldsymbol{\sigma}_1^2 + \boldsymbol{\sigma}_2^2 + 2\boldsymbol{\sigma}_1 \cdot \boldsymbol{\sigma}_2$. We note that $\boldsymbol{\sigma}^2$ has eigenvalues $s(s+1)$ corresponding to states with total spin s, and thus $\boldsymbol{\sigma}_i^2 = 1/2(1/2+1) = 3/4$, $i = 1, 2$ (since the electrons have spin $s_i = 1/2$). Consequently, the operator $\boldsymbol{\sigma}_1 \cdot \boldsymbol{\sigma}_2$ has eigenvalues $s(s+1)/2 - 3/4$, i.e., $-3/4$ for the singlet state ($s = 0$) and $1/4$ for the triplet states ($s = 1$). Using these observation, we construct the operator $(\varepsilon_S + 3\varepsilon_A)/4 + (\varepsilon_A - \varepsilon_S)\boldsymbol{\sigma}_1 \cdot \boldsymbol{\sigma}_2$, which exactly has the eigenvalues ε_S for the singlet state and ε_A for the triplet states, respectively. If we omit the common energy term $(\varepsilon_S + 3\varepsilon_A)/4$, we may then think of the splitting $J_V(\mathbf{B})$ as arising from an effective interaction in spin space described by the Hamiltonian

$$\mathcal{H} = J_V(\mathbf{B})\boldsymbol{\sigma}_1 \cdot \boldsymbol{\sigma}_2. \tag{3.4}$$

This is the well-known Heisenberg Hamiltonian. The mapping onto (or restriction to) the 4-dimensional spin space is strictly speaking only valid, when the two (symmetric and antisymmetric) orbital groundstates are energetically well-separated from the rest of the energy spectrum, such that the higher-lying states can be excluded, making a low-energy description, as Eq. (3.4) is, reasonable. It is worth noticing that the strength $J_V(\mathbf{B})$ of the interaction between the spins depends on the confining potential $V(\mathbf{r})$ and the magnetic field $\mathbf{B}$ via the *orbital* (or charge) degrees of freedom, and the exchange interaction thus provides a convenient way of controlling electrostatically the magnetic interaction. This is in particular relevant when considering gate-defined quantum dots, where the external potential $V(\mathbf{r})$ can be controlled with the gate electrodes.

Evaluating the interaction strength $J_V(\mathbf{B})$, given a confining potential $V(\mathbf{r})$ and an applied magnetic field $\mathbf{B}$, is in general non-trivial and has been a topic of intense research, since the first treatment of the Helium molecule by W. Heitler and F. London [94]. In the Heitler–London approximation the exchange coupling is simply evaluated as

$$J_V^{\mathrm{HL}}(\mathbf{B}) = \langle \Psi_A^{(0)} | H | \Psi_A^{(0)} \rangle - \langle \Psi_S^{(0)} | H | \Psi_S^{(0)} \rangle, \tag{3.5}$$

where $|\Psi_S^{(0)}\rangle$ and $|\Psi_A^{(0)}\rangle$ are the non-interacting two-particle orbital wavefunctions introduced above, and H is the full two-particle Hamiltonian given in

Eq. (3.3). While the Heitler–London approximation may be a simple estimate of the exchange coupling, it is often useful to get a rough idea of the qualitative features of the coupling strength, and for simple model potentials it may even be possible to obtain closed-form analytic expressions where various parameter dependencies can be clearly identified [87, 95]. The range of validity of the Heitler–London approximation is, however, not immediately clear. One can show that the singlet-state without magnetic field is always the ground state and consequently, $J_V(\mathbf{B} = 0) \geq 0$ [93, 96]. This criterion was used in Ref. [97] to test the Heitler–London approximation. While the criterion may reveal, when the Heitler–London breaks down by predicting a negative exchange coupling at zero magnetic field, it cannot, on the other hand, tell, if positive exchange coupling predictions are correct. Additionally, the criterion is not applicable with finite magnetic fields. A more quantitative test was provided in Ref. [98], where Heitler-London results were compared with numerically exact results obtained for weakly tunnel-coupled quantum dots as function of the magnetic field. The results show that the Heitler–London approximation for the chosen parameters predicts at too low exchange coupling.

The Heitler–London approximation can be improved by choosing different single-particle wavefunctions as recently suggested in Ref. [99], or, more conventionally, by including doubly occupied singlet states, i.e., two-particle states, where both electrons are occupying the same orbital quantum dot state (which is only allowed for the spin singlet). The latter approach is known as the Hund–Mulliken approximation [87]. If inter-dot Coulomb interactions are negligible and the tunnel-coupling t between the two quantum dots much smaller than the onsite Coulomb interaction U, the Hund–Mulliken approximation leads to the standard Hubbard expression $J_V^H(\mathbf{B}) = 4t^2/U$. Obviously, the Hubbard expression cannot explain that the exchange coupling can become negative with finite magnetic fields, since $J_V^H(\mathbf{B}) \geq 0$, and the inter-dot Coulomb interaction has to been included in order to account for this behavior [87]. As already briefly mentioned above, numerical methods constitute an alternative approach to exchange coupling calculations. Numerically exact results can for example be obtained by expanding the full two-particle Hamiltonian in Eq. (3.3) in a suitable two-particle basis and diagonalizing numerically the resulting matrix representation of the Hamiltonian [98, 100, 101, 102, 103, 104]. In contrast to the various approximations introduced above, the numerical results can in principle be considered exact, if a sufficiently large number of basis states are used. On the other hand, the advantages provided by closed-form analytic expressions in terms of clear parameter dependencies are not immediately available.

In order to test the various approximative schemes we developed in connection with Paper **O** a numerically exact finite-element method inspired by Ref. [105], where exchange coupling calculations using an expansion in two-dimensional Gaussian wavefunctions were reported. Our method was implemented using a commercially available finite-element solver providing a convenient platform for exchange coupling calculations. The details of the method and the implementation are given in Paper **O** and, in particular, Ref. [59]. The method is best suited for systems with a substantial wavefunction overlap between the two quantum dots, which is also the regime that from an experimental point of view would be most interesting: As the overlap is reduced, e.g., by an increase of the distance between the quantum dots, the exchange coupling falls off dramatically, making it vanishing for any practical point of view. Our aim was thus to provide a stringent test of the various standard approximations by comparing them to numerically exact results for quantum dots with a large overlap. As an illustrative example, we considered the double-dot potential

$$V(\mathbf{r}) = \frac{m\omega_0^2}{2}\left[\min\{(x-d)^2,(x+d)^2\} + y^2\right]. \tag{3.6}$$

for values of the inter-dot distance d comparable to the characteristic oscillator length $r_0 \equiv \sqrt{\hbar/m\omega_0}$. A figure showing the potential can be found in Paper **O**. While this potential might be a very crude approximation of the actual potential inside a realistic double quantum dot, it has the main features one would expect from a double-dot potential (two potential wells separated by a tunnel barrier) and is as such useful for benchmark calculations as the ones presented here.

In Figs. 3.1 and 3.2 we show comparisons of the standard approximations with numerical results for the exchange coupling as function of inter-dot distance and magnetic field, respectively. Without magnetic field, the Hubbard approximation gives fairly reasonable predictions of the exchange coupling as function of inter-dot distance, while most of the other approximations fail. In contrast, the extended Hubbard approximation, which also includes inter-dot Coulomb interactions, seems better at predicting the exchange coupling at finite magnetic fields. The results are discussed in further detail in Paper **O**, where also the one-dimensional case is considered. In general, the results show that approximative calculations of the exchange coupling in quantum dots with large wavefunction overlap is highly non-trivial, and great care should be taken when the standard approximations are applied. In Paper **R** we applied our numerical method to calculate the exchange coupling between electron spins in tunnel coupled defect states in the antidot lattice geometry introduced in Section 2.3.

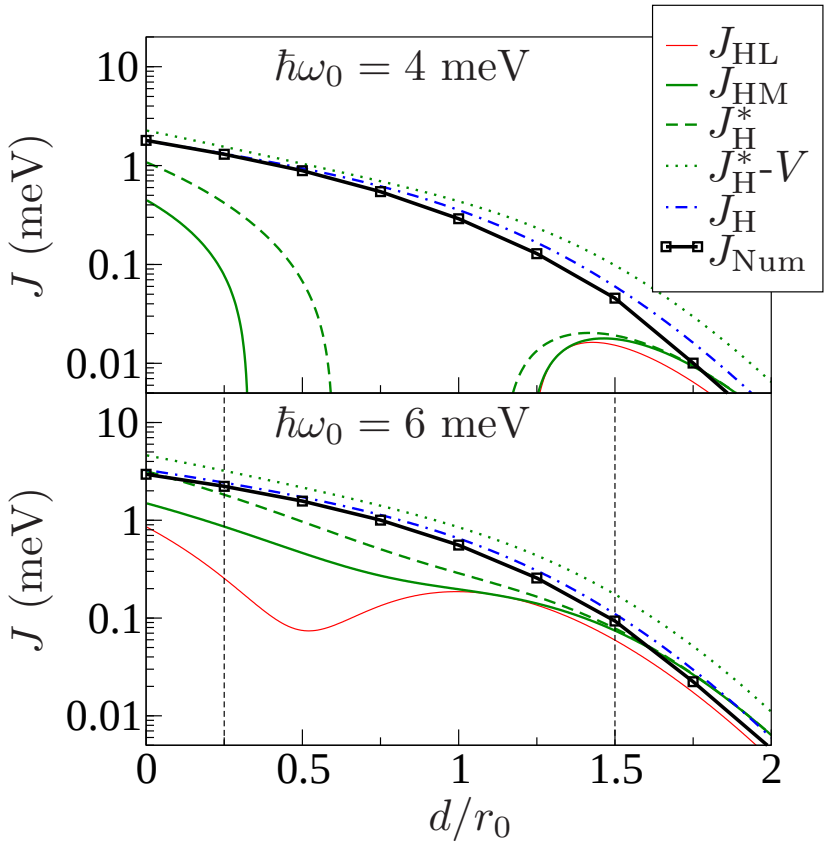

Figure 3.1: Exchange coupling in a two-dimensional double quantum dot. The exchange coupling J is calculated numerically as function of the inter-dot distance d with different confinement energies $\hbar\omega_0$. The characteristic oscillator length is $r_0 \equiv \sqrt{\hbar/m\omega_0}$. For comparison we show results obtained with the following approximations: Heitler–London (J_{HL}), Hund–Mulliken (J_{HM}), extended Hubbard (J^*_H and $J^*_H - V$), and Hubbard (J_H) – see Paper **O** for details. The vertical lines correspond to the values of d for which the magnetic field dependence is shown in Fig. 3.2. Figure from Paper **O**.

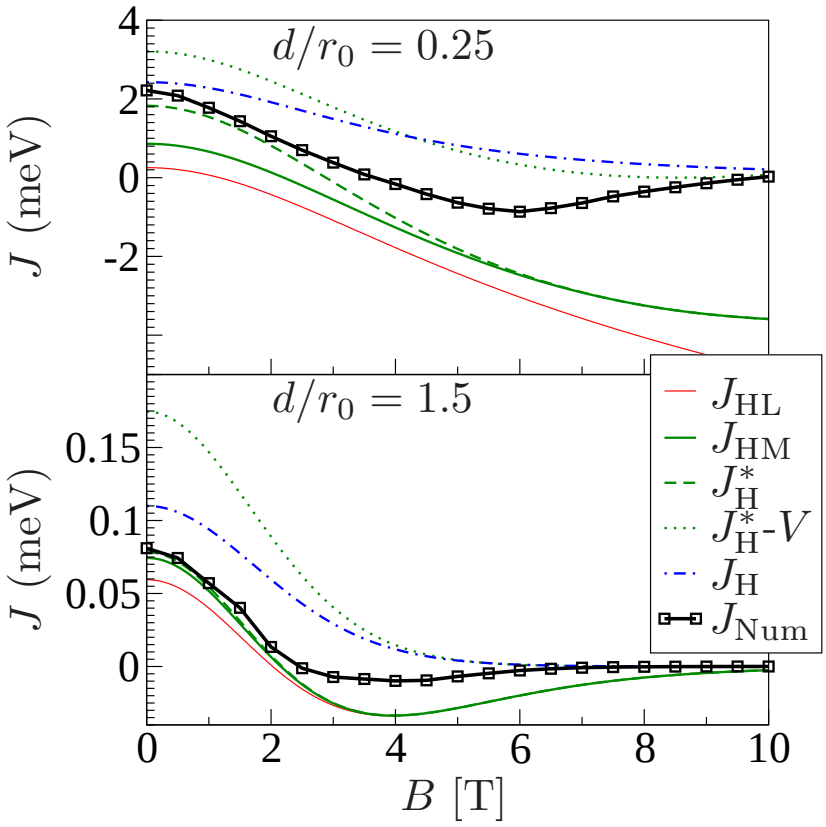

Figure 3.2: Exchange coupling in a two-dimensional double quantum dot in a perpendicular magnetic field. The exchange coupling J is calculated numerically as function of the magnetic field strength B with $\hbar\omega_0 = 6$ meV, and $d/r_0 = 0.25, 1.5$, where $r_0 \equiv \sqrt{\hbar/m\omega_0}$. The electron g^*-factor does not enter in these calculations, since the exchange coupling is a purely orbital effect. For comparison we show results obtained with the following approximations: Heitler–London (J_{HL}), Hund–Mulliken (J_{HM}), extended Hubbard (J^*_H and $J^*_H - V$), and Hubbard (J_H) – see Paper **O** for details. Figure from Paper **O**.

3.3 Spin-orbit coupling

In the previous section we introduced the exchange coupling and discussed various methods for calculating the coupling strength $J_V(\mathbf{B})$. As we pointed out, the exchange coupling provides a convenient way of electrostatically controlling the magnetic interaction between electron spins in gate-defined quantum dots. Herein lies, however, also a potential source of erroneous quantum gate operations due to random fluctuations in the electrostatic environment that change the external potential $V(\mathbf{r})$, e.g., fluctuations in the gate electrodes or movements of nearby trapped charges. Such electrostatic fluctuations in the surroundings change the exchange interaction in an uncontrollable way, thereby reducing the ability to carry out a desired two-qubit operation on the spins. This scenario was studied in Ref. [95], where it was found that charge fluctuations may present a serious challenge for the use of the exchange coupling for two-qubit operations in large-scale quantum computing architectures. As an alternative approach to spin manipulation, which potentially could be less susceptible to such fluctuations, we explored in paper **J** the possibility of using the spin-orbit coupling in nanostructures. Although it has previously been suggested that the spin-orbit coupling could play a role in coherent electron manipulation [106, 107, 108], the spin-orbit coupling is typically considered to be an undesired effect, since it couples the spin to the orbital (or charge) degrees of freedom, which couple more strongly to the environment than the spin itself [109, 110]. In Paper **J** we took the ideas of exploiting the spin-orbit coupling further and proposed to use the spin-orbit coupling as a general means to control and manipulate trapped electron spins. In this section we discuss our proposal.

The spin-orbit is a relativistic effect which arises when a charged particle travels through a static electric field: In the rest-frame of the particle, the electric field is transformed into a magnetic field which couples to the spin. In a solid electrons may experience an electric field from the charged atoms in the crystal lattice of the material giving rise to a coupling between the spin and the orbital degrees of freedom [3]. This microscopic effect should be included in the detailed description of electrons in a solid, e.g., at the level of band structure calculations, but as often in solid-state physics simpler models may suffice and capture the essential physics. As an example, one could mention the effective-mass approximation, where all band structure effects are collected in an effective mass entering the free-electron picture. Similarly, simple, effective descriptions of the spin-orbit coupling exist that capture the effects of the solid-state material and its crystal structure. Two prominent examples are the Rashba [111, 112] and Dresselhaus [113] couplings that describe the spin-orbit coupling of electron spins in two-dimensional quantum

dots due to lack of crystal lattice symmetry [3]. Here, we refrain from going into a deeper discussion of the underlying microscopic theory, and in the following we employ a simple model of the spin-orbit coupling in a one-dimensional system.

As a promising candidate system for an experimental implementation of our idea, we consider InAs nanowires with a gate-defined double quantum dot along the length of the wire. The setup is shown schematically in Fig. 3.3. Successful fabrication and electrostatic control of the external potential within such a nanowire were reported in Ref. [10]. The choice of material is interesting, since InAs has a large electron g^*-factor and spin-orbit coupling, which would enhance the effects that we describe in the following. In Ref. [10] the few-electron regime of the double quantum was not reached, but in a subsequent experimental study with a further optimized design, control of the electron number down to the last electron was reported [114]. We consider the two-electron regime and model the one-dimensional system with the Hamiltonian

$$H(x_1, x_2) = h(x_1) + h(x_2) + C(|x_1 - x_2|) \tag{3.7}$$

where $C(|x_1 - x_2|) = \frac{e^2}{4\pi\varepsilon_r\varepsilon_0|x_1-x_2|}$ is the Coulomb interaction between the two electrons and the single-particle Hamiltonians read

$$h(x) = \frac{p_x^2}{2m} + V(x) + \frac{1}{2}g^*\mu_B B\sigma^z + \alpha p_x\sigma^y. \tag{3.8}$$

Compared to the Hamiltonian given in Eq. (3.3), we have in the single-particle Hamiltonians included the Zeeman term $\frac{1}{2}g^*\mu_B B\sigma^z$ and a phenomenological spin-orbit coupling of the form $\alpha p_x\sigma^y$. Here, we have assumed that the motion of the electron generates an effective magnetic field which is linear in the momentum p_x of the electron along the nanowire, which defines the x-axis in the orbital space. The effective magnetic field due to the spin-orbit coupling defines a direction in spin space which we (freely) denote by y. The external magnetic field is applied in a perpendicular direction, which we choose to denote by z. Finally, the spin-orbit coupling contains the parameter α which quantifies the coupling strength. The external potential $V(x)$ is defined by a number of perpendicular gate electrodes along the nanowire as illustrated in Fig. 3.3. The vector potential corresponding to the external magnetic field is chosen such that it has no component in the x-direction and consequently does not enter the single-particle Hamiltonians in Eq. (3.8).

In order to understand the effect of the spin-orbit term we start by considering only the single-particle Hamiltonian given by Eq. (3.8). First, we note that in the absence of an external magnetic field, an electron traveling

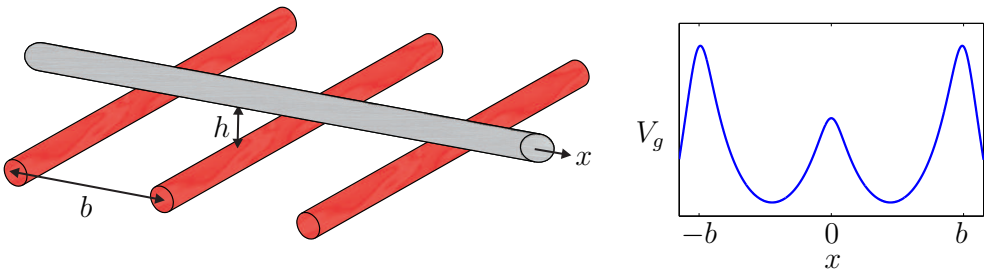

Figure 3.3: InAs nanowire across three gate electrodes. The three gate electrodes, positioned at $x = -b, 0, b$ with a distance h to the nanowire, are used to define a double-dot potential inside the nanowire. A representative curve of the potential along the nanowire is shown to the right. In the experiment reported in Ref. [10] the spacing between the electrodes was $b = 210$ nm and the distance to the nanowire was $h = 25$ nm (two more gate electrodes used in the experiment are not shown here). Figure from Paper **J**.

along the x-axis, with spin initially pointing along the z-axis or x-axis, will have its spin flipped after a distance of $\pi l_{\rm so}/2$,[4] where we have introduced the spin-orbit length $l_{\rm so} = \hbar/m\alpha$. It is interesting to note that this does not depend on the speed at which the charge is traveling, but only the traversed length. At the time when Paper **J** was published the exact values of the electron g^*-factor and the spin-orbit length $l_{\rm so}$ for confined electrons in InAs nanowires were not known, and we used $|g^*| = 14$ and $\hbar\alpha = 30$ meVnm or $l_{\rm so} = 94$ nm with $m = 0.027m_e$, inspired by numbers of the same order found in the literature for two-dimensional electron gases [115, 116] and unconfined electrons in InAs nanowires [11]. In the following we still use these values, although a recent experimental study of the spin-orbit coupling in InAs nanowires reported a spin-orbit length of $l_{\rm so} \simeq 127$ nm and an effective g^*-factor $|g^*| \simeq 8 \pm 1$ [114]. For the Coulomb interaction in InAs, we use $\varepsilon_r = 15.15$.

The spin-orbit coupling allows an efficient way of flipping the spin of an electron using fast variations of the external potential. This idea is described in detail in Papers **J** and **K** and here we give a physical picture of the proposed mechanism. In order to simplify matters, we consider a single electron confined by the harmonic potential $V(x) = m\omega_0[x - \bar{x}(t)]^2/2$, where we assume that the equilibrium position $\bar{x}(t)$ can be controlled with the gate

[4]Using a simple 'back-of-an-envelope' calculation we find that $e^{i\alpha p_x \sigma^y \Delta t/\hbar} = i\sigma^y$, if $\alpha p_x \Delta t/\hbar = l_{\Delta t}/l_{\rm so} = \pi/2$, where $l_{\Delta t}$ is the distance that the electrons travels during time Δt and $l_{\rm so} \equiv \hbar/m\alpha$. We thus find $l_{\Delta t} = \pi l_{\rm so}/2$.

electrodes. We denote the characteristic oscillator length by $l_0 \equiv \sqrt{\hbar/m\omega_0}$. First of all, we assume that we can change the equilibrium position $\bar{x}(t)$ on a time-scale which is fast compared to the one associated with the Zeeman splitting of the spin states. At the same time, we need the change to be slow compared to the time scale associated with the level splitting of the orbital degrees of freedom. These criteria we can express as $|g^*\mu_B B/\hbar| \ll |\dot{x}_0(t)/l_{\rm so}|$ and $|\dot{x}_0(t)/l_0| \ll \omega_0$, or simply $|g^*\mu_B B/\hbar| \ll |\dot{x}_0(t)/l_0| \ll \omega_0$, if we assume that the oscillator length and the spin-orbit length are comparable, i.e., $l_{\rm so} \simeq l_0$.[5] The first criterium allows us to neglect the precession of the spin due to the magnetic field, while the effective magnetic field arising from the spin-orbit coupling is "turned on" during a translation of the equilibrium position $\bar{x}(t)$. The second criterium ensures that the electron stays in the orbital ground state without being excited to higher-lying orbital states during the translation (in more technical terms, we assume that the translation is adiabatic with respect to the orbital degrees of freedom). Within these assumptions our scheme for flipping the spin reads:

1. Translation of $\bar{x}(t)$ by a distance of $\pi l_{\rm so}/4$. This rotates the spin around the y-axis, down into the xy-plane, pointing along the x-axis.

2. Free evolution of the spin in the external B-field for a period of $T = \hbar\pi/g^*\mu_B B$. This rotates the spin by an angle of π around the z-axis, such that it ends up pointing in the negative-x direction.

3. Translation of $\bar{x}(t)$ back to the initial position. This rotates the spin around the y-axis by an angle of $\pi/2$, such that the spin ends up in the state $|\downarrow\rangle$.

The trajectory on the Bloch sphere of a spin, initialized in the state $|\uparrow\rangle$, during this procedure is shown in Fig. 3.4. In Paper **J** the total spin flip time was estimated to be below 1 ns. During the spin-flip operation the electron is translated back and forth by the distance $\pi l_{\rm so}/4 = 74$ nm. If such a large translation cannot be obtained with the given gate configuration, one can instead construct more complex manipulation schemes which, on the cost of higher complexity, would need shorter translations. For example, if one only translates the electron by the distance $\pi l_{\rm so}/8 = 37$ nm during the steps

[5] In these expressions we should in principle take into account the fact that the spin states here are actually, in a quantum optical language, dressed states of spin *and* orbital degrees of freedom due to the spin-orbit coupling. The Zeeman energies of the states are renormalized by the spin-orbit coupling, leading to an effective g^*-factor reading $g^* e^{-(l_0/l_{\rm so})^2}$, which should be used in these inequalities. This is described in Papers **J** and **K**.

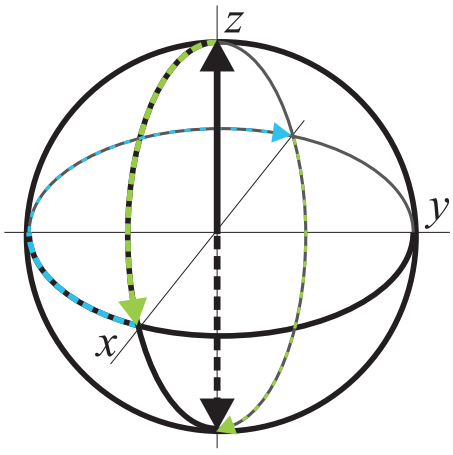

Figure 3.4: Spin flip on the Bloch sphere. The spin is initially pointing north (thick arrow). The three dashed lines are the rotations of the spin during the spin flip scheme. Rotations around the y-axis are due to the spin-orbit coupling (steps 1 and 3), while the rotation in the x-y plane are due to the externally applied magnetic field (step 2). Figure from Paper **K**.

1-3, the spin would end up pointing in the negative-x direction. Such an operation could consequently replace steps 1-2 in the full spin-flip rotation described above. With the principles outline here, it is, in general, possible to construct manipulation schemes, that would allow the spin to reach any point on the Bloch sphere. Finally, we note that in order to carry out a more quantitative description of the scheme, it is convenient to work in a rest frame that follows the spin-orbit induced rotation of the spin as discussed in Paper **K**.

It is worth comparing our method to more conventional schemes for spin flipping, which typically rely on the principle of electron spin resonance (ESR). In ESR, a time-dependent magnetic field is applied perpendicularly to the Zeeman field which defines the z direction. If the time-dependent field is rotating with a frequency that is resonant with the Zeeman splitting, the rotation exactly cancels the effect of the static field. This conclusion is most easily reached using a frame that follows the rotating magnetic field [117]. The spin will then precess around the direction of the time-dependent field, making a spin-flip possible. The frequency of the precession is given by the magnitude of the time-dependent field. If the involved g^*-factor and Zeeman fields are large, it can, however, be an experimental challenge to produce sufficiently fast oscillating magnetic fields. Nevertheless, such ESR driven oscillations of an electron spin in a quantum dot have been experimentally realized [88]. ESR driven spin rotation where a time-varying effective magnetic field is obtained using a combination of time-varying electric fields and the spin-orbit coupling have also been suggested in Refs. [118, 119], and this was very recently demonstrated in the experiment described in Ref. [120]. Compared to these schemes, our proposal does not rely on any resonance condition.

We now return to the two-particle Hamiltonian in Eq. (3.7) and present the results for the effective spin-spin coupling arising due to the spin-orbit coupling. It is not surprising that the spin-orbit coupling in combination with the Coulomb interaction between the two electrons can give rise to an effective spin-spin coupling: The spin-orbit coupling couples the spins of the individual electrons to the orbital degrees of freedom of the respective electrons, which in turn are coupled due to the Coulomb interaction. We first develop a simple model of the electrostatic potential generated by the three gate electrodes, modeling each of the electrodes as infinitely long line charges with charge densities λ_l, λ_c, and λ_r for the left, central, and right electrodes, respectively. With these assumptions, the electrostatic potential along the nanowire reads

$$V_g(x) = V_e(x+b,\beta_l) + V_e(x,\beta_c) + V_e(x-b,1), \tag{3.9}$$

with $V_e(x,\beta) = -\beta\hbar\omega_g \ln[(x^2+h^2)/x_g^2]$, where we have introduced $\beta_{l(c)} \equiv \lambda_{l(c)}/\lambda_r$, $\hbar\omega_g \equiv e\lambda_r/4\pi\varepsilon_0\varepsilon_r$, and $x_g \equiv \sqrt{\hbar/m\omega_g}$. A representative plot of the potential is shown in Fig. 3.3. The model potential allows us to characterize the sensitivity of the spin-spin coupling to fluctuations in the charge densities. However, before doing so, we first approximate the two potential wells with two harmonic oscillator potentials with frequency ω_0 displaced by the distance d. This approximation allows us to calculate analytically the strength of the effective spin-spin interaction. The results presented below are only valid to second order in the magnetic field and to lowest order in the Coulomb interaction, which we expand using $1/|x_2-x_1| \simeq 1/d - \delta/d^2 + \delta^2/d^3$, where we have assumed that $d \gg \delta \equiv (x_2-\bar{x}_2)-(x_1-\bar{x}_1)$. The result is, however, correct to all orders in the spin-orbit coupling α.

In Papers **J** and **K** we presented two different derivations of the effective spin Hamiltonian and here we just quote the final result,

$$\mathcal{H} = \tau\sigma_1^x\sigma_2^x + \frac{1}{2}\tilde{g}^*\mu_B B(\sigma_1^z+\sigma_2^z), \tag{3.10}$$

where

$$\tau = -\frac{e^2}{4\pi\varepsilon_0\varepsilon_r}\frac{2l_0^4(\tilde{g}^*\mu_B B)^2}{l_{\rm so}^2(\hbar\omega_0)^2 d^3} \tag{3.11}$$

and the renormalized g^*-factor is $\tilde{g}^* = g^* e^{-(l_0/l_{\rm so})^2}$, as already mentioned. We note, that the above result was reproduced in Ref. [121], where a thorough analysis of the spin-orbit induced spin-spin coupling between two two-dimensional quantum dots was presented. The analytic result can be benchmarked against numerically exact results obtained from the low-energy spectrum of the two-particle Hamiltonian in Eq. (3.7). Compared to the previous section, where we studied the exchange coupling between electrons in

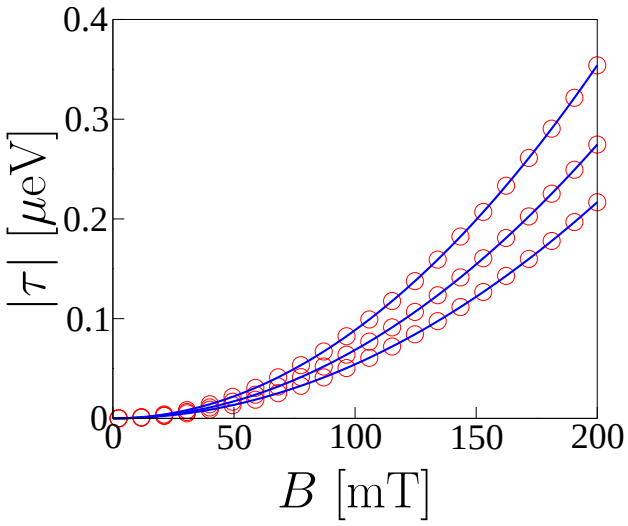

Figure 3.5: Spin-spin coupling as function of magnetic field. Numerical results are shown with circles, while full lines correspond to the analytic expression in Eq. (3.11). Parameters are $\hbar\omega_g = 1$ meV ($x_g = 53$ nm), $h = 0.5x_g$, $b = 10x_g$, $\beta_l = 1$, $\beta_c = 0.6$ (upper circles), 0.7, 0.8 (lower circles). Corresponding to the three values of β_c we have used $\hbar\omega_0 = 0.39$, 0.40, 0.42 meV and $d = 8.3x_g$, $8.7x_g$, $9.1x_g$. Figure from Paper **J**.

two two-dimensional quantum dots, the present problem is computationally cheaper due to the lower dimensionality. For the results shown in the following, we have used a simple discretization of the two-particle Hamiltonian on a real-space grid, with the number of grid points being on the order 100-500, leading to a sparse matrix representation from which it is feasible, with conventional numerical methods, to extract the low-energy spectrum.

In Fig. 3.5 we show the strength of the coupling as function of the magnetic field. The numerical results, shown with circles, confirm the parabolic dependence on the magnetic field. For the given parameters the spin-orbit induced coupling is on the order of μeV, which is much larger than the exchange coupling at the same inter-dot distance, however, smaller than the exchange coupling for quantum dots with a large overlap as those considered in the previous section and in Paper **O**. Although, it may not be possible to control the strength of the spin-orbit coupling experimentally, the dependence of the spin-spin coupling on the spin-orbit coupling is interesting due to the competing effects of the spin-orbit coupling as it enters via the spin-orbit length in the denominator, giving rise to a parabolic dependence on α, and the renormalized g^*-factor that leads to an exponential dependence on the

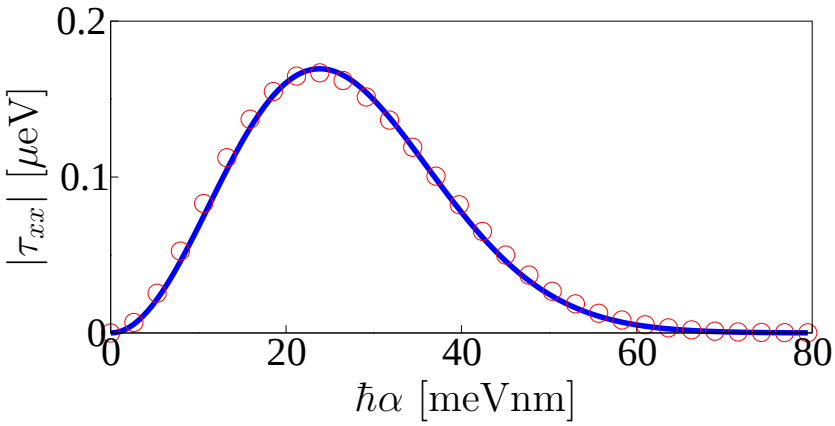

Figure 3.6: Spin-spin coupling as function of the spin-orbit coupling. Numerical results are shown with circles, while full lines correspond to the analytic expression in Eq. (3.11). The spin-spin coupling is denoted τ_{xx} in this figure, while the spin-orbit coupling is denoted α. Parameters are $B = 160$ mT, $\hbar\omega_0 = 0.4$ meV ($l_0 = 80$ nm) and $d = 750$ nm. Figure from Paper **K**.

spin-orbit coupling. These two effects are clearly seen in Fig. 3.6, where the spin-spin coupling is shown as function of the spin-orbit coupling α. For low values of α the parabolic dependence is dominating, while the exponential suppression prevails for larger values. When the oscillator length is much longer than the spin-orbit length, the orbital ground state averaging leads to a vanishing effective g^*-factor.

As previously mentioned, it has been argued that the exchange coupling is sensitive to fluctuations in the electrostatic environment [95], and it is thus relevant to study the corresponding sensitivity of the spin-orbit induced coupling. Following Ref. [95] we characterize the sensitivity of the spin-spin coupling to slow fluctuations in the electrostatic environment by calculating numerically $\partial\tau/\partial\beta_{c/l}$. Our numerical results also contain the contributions from the exchange coupling J, which we may extract by setting the spin-orbit coupling to zero, and thereby compare quantitatively the two coupling mechanisms. In Fig. 3.7 we show the strengths of the two coupling mechanisms as function of the charge density on the central electrode, parameterized by β_c, which determines the height of the barrier separating the electrons. We also show $|(1/\tau)\partial\tau/\partial\beta_c|$, $|(1/J)\partial J/\partial\beta_c|$, and $|(1/\tau)\partial E_z/\partial\beta_c|$, where $E_z = g^*\mu_B B e^{-(l_0/l_{\rm so})^2}$ is the renormalized Zeeman splitting. The figure clearly shows that $|(1/\tau)\partial\tau/\partial\beta_c| \ll |(1/J)\partial J/\partial\beta_c|$, which we interpret as a smaller sensitivity of the spin-orbit induced coupling, compared with

the exchange coupling, to electrostatic fluctuations in the central electrode. Here, we have only compared the two coupling mechanisms for well-separated quantum dots, which is not necessarily the optimal operational regime for the exchange coupling, which is most effective for quantum dots with a large overlap as discussed in the previous section. In Paper **J** we also studied the sensitivity of the two coupling mechanisms to fluctuations in the charge densities of the outer electrodes, for which we found that the two coupling mechanisms are, to a good degree, equally sensitive.

Figure 3.7 shows that the renormalized Zeeman splitting it highly sensitive to gate fluctuations. This is not surprising, considering the exponential dependence on the oscillator length. For controlled, coherent evolution, it is, however, problematic with energetically fluctuating levels, and in the present case, the problem could potentially be circumvented by only encoding a single qubit (rather than two) in the spin pair as suggested in Ref. [122], and experimentally implemented in Ref. [6]. Here, the qubit states $|0\rangle$ and $|1\rangle$ are represented by the spin singlet state $(|\uparrow\downarrow\rangle + |\downarrow\uparrow\rangle)/\sqrt{2}$ and the unpolarized spin triplet state $(|\uparrow\downarrow\rangle - |\downarrow\uparrow\rangle)/\sqrt{2}$, which (in contrast to the polarized spin triplets $|\uparrow\uparrow\rangle$ and $|\downarrow\downarrow\rangle$) do not couple to homogenous magnetic fields, or changes of the renormalized Zeeman energy due to electrostatic fluctuations in case of the spin-orbit coupling.

3.4 Spin-photon entanglement

In the previous sections we have been focusing on two-electron systems in gate-defined quantum dots, and, in particular, various mechanisms for manipulating their spins and having them interact. While such two-electron systems could be important as building blocks in a future solid-state quantum computing architecture, another important task concerns the interaction between different computational units over long distances, which would be desirable for quantum communication purposes. In order to achieve this goal it is generally believed that it would be necessary to interface spin qubit systems with quantum optical systems, such that quantum information can be transferred, converted, or shared between the stationary qubits (the electron spins) and flying qubits, typically optical photons. In Paper **M** we consequently proposed and analyzed a novel semi-conductor device that would allow for electrically controlled generation of single photons that are entangled with the spins of a two-electron system in a double quantum dot. By interfering outgoing photons from two distant devices on a beam-splitter, it would be possible to generate entanglement between the spin states in the two devices. In this section we describe and analyze our proposal.

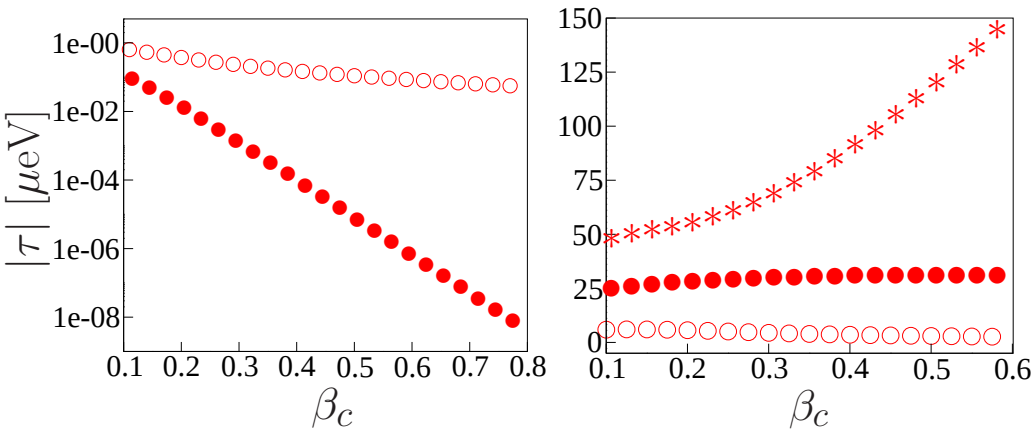

Figure 3.7: Sensitivity to gate fluctuations. The left figure shows numerical calculations of the spin-orbit induced coupling τ (open circles) and the exchange coupling J (filled circles) as functions of the charge density on the central electrode parameterized by β_c. The right figure shows $|(1/\tau)\partial\tau/\partial\beta_c|$ (open circles), $|(1/J)\partial J/\partial\beta_c|$ (filled circles), and $|(1/\tau)\partial E_z/\partial\beta_c|$ (stars), where $E_z = g^*\mu_B B e^{-(l_0/l_{so})^2}$ is the renormalized Zeeman splitting. Parameters are $\hbar\omega_g = 1$ meV ($x_g = 53$ nm), $\beta_l = 1$, $h = 0.5x_g$, $b = 10x_g$, and $B = 40$ mT (left figure), 80 mT (right figure). Figures from Paper **J**.

The system that we have in mind consists of a *p*-*i*-*n* diode structure with two tunnel-coupled quantum dots in the intrinsic region. A possible realization could be a nanowire similar to those fabricated and experimentally studied in Ref. [20] which reports on single, optically active quantum dots grown inside nanowires between p and n doped regions. In our proposal, the single quantum dot would be replaced by a double quantum dot as illustrated in Fig. 3.8, where the envisioned structure is shown schematically together with a band edge diagram. As discussed in Chapter 2 such a structure can be fabricated by varying the semiconductor material used in the growth process such that n and p doped regions can be introduced and tunneling barriers can be defined in order to create confinement in the intrinsic region. As illustrated in the figure, these types of structures do not only confine electrons, but also holes, and the basic idea of our approach is to control the injection of single electrons and holes into the double quantum dot by adjusting the bias across the intrinsic region and the voltages applied to a local gate electrode close to one of the quantum dots. This would allow us to create a metastable electron-hole complex that recombines under the emission of a photon that is frequency-entangled with the spin states of the final-state electrons.

In order to devise a suitable injection scheme we consider the charge stability diagram of the device, which we calculate numerically following the procedure outlined in the previous chapter. The n and p doped regions are modeled as Fermi seas of non-interacting electrons and holes kept at chemical potentials $\mu_n = \mu_n^0 + eV/2$ and $\mu_p = \mu_p^0 - eV/2$, respectively, where μ_n^0 and μ_p^0 are given by the doping levels of the n and p regions, and V is the voltage difference between the two Fermi seas. The two charge reservoirs are assumed to be weakly tunnel-coupled to the double quantum dot, which we model with the many-particle Hamiltonian

$$\hat{H}_{DQD} = \hat{H}_{ee}^{l} + \hat{H}_{ee}^{r} + \hat{H}_{hh}^{r} + \hat{H}_{eh}^{r} + \hat{H}_{\tau} + \hat{H}_{F}, \tag{3.12}$$

describing Coulomb interactions between different charges, tunnel coupling of the two quantum dots, and the shift of the levels in the right quantum dot due to the local gate electrode F indicated in Fig. 3.8. For the Coulomb repulsion between similar particles on the same quantum dot we use a simple model reading $\hat{H}_{qq}^{s} = U_{qq}\hat{n}_q^s(\hat{n}_q^s - 1)/2$, where $\hat{n}_q^s$ is the number operator of particles on the left ($s = l$) or right ($s = r$) quantum dot with charge $q = e, h$. In order for the scheme that we describe in the following to work ideally, we assume that the hole states of the left quantum dot remain unoccupied, which could occur due to substantial band-gap differences (0.1 eV or more) between the two quantum dots, arising, e.g., from strain and dot size differences. For the Coulomb attraction between electrons and hole in the right quantum dot we use $\hat{H}_{eh}^{r} = -U_{eh}\hat{n}_e^r\hat{n}_h^r$. Tunneling of electrons between the quantum dots

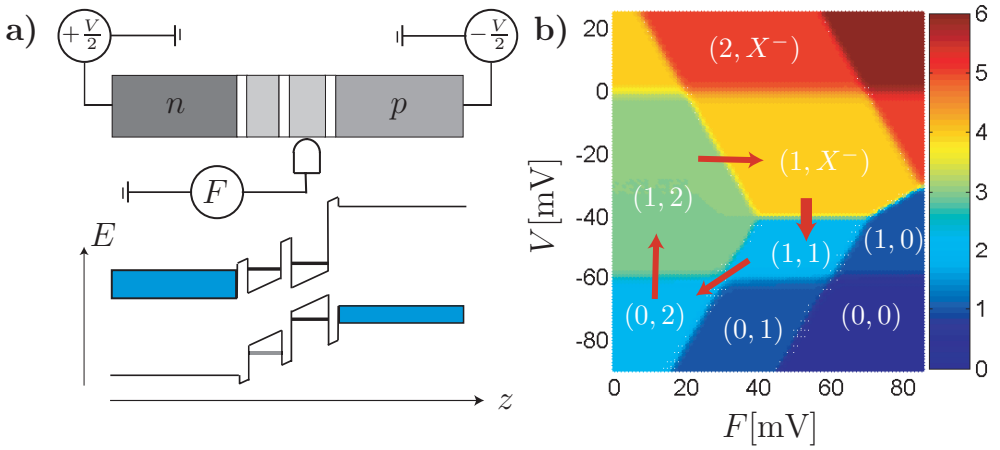

Figure 3.8: Schematic nanowire diode structure, band edge diagram, and charge stability diagram. (a) The diode structure consists of an optically active double quantum dot sandwiched between n and p doped regions. (b) Numerically calculated charge stability diagram. The scale-bar denotes the total number of charges on the double-dot, while the labeling (n, m) corresponds to a configuration with n electrons on the left quantum dot, and m electrons on the right quantum dot, but no holes. The symbol X^- denotes a negatively charged exciton consisting of two electrons and one hole. Arrows correspond to the charging sequence described in the text. Parameters are $U_{ee} = 30$ meV, $U_{hh} = 50$ meV, $U_{eh} = 40$ meV, $\tau = 1$ meV, and identical tunnel couplings to the leads being much smaller than the temperature $T = 4$ K. The values of μ_n^0 and μ_p^0 were used to fix the occupations of the quantum dots at $V, F = 0$. Figure from Paper **M**.

with tunnel coupling τ is contained in the term $\hat{H}_\tau$, while $\hat{H}_F = -eF(\hat{n}_h^r - \hat{n}_e^r)$ incorporates the shift of the electron and hole states in the right quantum dot due to the local gate electrode F. No electrostatic cross-talk between the quantum dots is included. In Fig. 3.8 we show the resulting charge stability diagram, where the total number of charges on the double quantum dot is given as function of the bias across the device V and the local gate F. With a given setting of V and F the system tends towards the corresponding stable charge configuration indicated on the diagram. The notation is explained in the figure caption.

While the main features of the charge stability diagram are determined by the charge degrees of freedom due to the strong Coulomb interaction, the charges, of course, also carry spin with them. Conduction band electrons in conventional semiconductors are often well-described as free electrons with an effective mass m^* and spin $\sigma = \pm 1/2$. The valence band electrons (or holes), on the other hand, have a more complicated band and pseudo-spin structure. Typically, the hole band structure of bulk semiconductors consists of three bands, namely, the split-off, the heavy-hole, and the light-hole bands (the last two bands deriving their names from the corresponding effective masses) [123]. The hole states can be characterized by the *total* angular momentum, containing contributions from the orbital and the spin degrees of freedom. In particular, the light and heavy holes have total angular momentum 3/2 with corresponding projections $\pm 1/2$ for the light holes and $\pm 3/2$ for the heavy holes [123]. In confined geometries, injected holes are predominately of heavy-hole character [123], and we consequently only consider heavy-holes with (pseudo-)spin $\Sigma = \pm 3/2$. In the following, heavy holes are created in the right quantum dot with the operator $\hat{d}^\dagger_{r,\Sigma}$, while electrons in the left and right quantum dots are created by $\hat{c}^\dagger_{l,\sigma}$ and $\hat{c}^\dagger_{r,\sigma}$, respectively. The system is considered to be in a so-called Faraday configuration where both the applied magnetic field B and the direction of the emitted light lie along the growth axis (the z-axis in Fig. 3.8) [123].

The charging sequence now consists of the following steps:

1. The system is initialized in the charge configuration $(0, 2)$ in the lower-left corner of the charge stability diagram. Due to the tight confinement, the two electrons will pair up in a spin singlet configuration, which we write as $|0, 2S\rangle = \hat{c}^\dagger_{r,\uparrow}\hat{c}^\dagger_{r,\downarrow}|0\rangle$.

2. By increasing the bias, an extra electron is injected into the left quantum dot. We assume for now that the injected electron has spin $\sigma = \uparrow$, such that the state of the system is $|1\uparrow, 2S\rangle = \hat{c}^\dagger_{l,\uparrow}|0, 2S\rangle$.

3. By control of the local gate F we move to the charge stability region

$(1, X^-)$, and assume for now that the injected hole has spin $\Sigma = \Downarrow$. This brings us to the meta-stable state $|1\uparrow, X^-_{S,\Downarrow}\rangle = \hat{d}^\dagger_{r,\Downarrow}|1\uparrow, 2S\rangle$.

With the system in the meta-stable state $|1\uparrow, X^-_{S,\Downarrow}\rangle$, electron-hole recombination is expected to take place under emission of a single left-hand circularly polarized photon with a frequency on the order of the band gap (typically on the order of 1 eV) [123]. Since the final state $|1\uparrow, 1\downarrow\rangle = d_{r\Downarrow}c_{r,\uparrow}|1\uparrow, X^-_{S,\Downarrow}\rangle$ is different from the (meta-)stable charge configuration $(1, X^-)$ for the given setting of V and F, refilling by an electron and a hole is expected, leading to emission of more than one photon. Therefore, we rapidly (compared to the decay rate) move to the regime, where $(1, 1)$ is the stable charge configuration, such that the fourth step of the sequence is

4. We rapidly change the bias V in order for electron-hole recombination to take place in the charge stability region (1,1), leaving us with the final state $|1\uparrow, 1\downarrow\rangle = d_{r\Downarrow}c_{r,\uparrow}|1\uparrow, X^-_{S,\Downarrow}\rangle$ upon photon emission.

At the end of the sequence, the system can be reinitialized by returning to the $(0, 2)$ charge stability region, and the sequence can be repeated. In Fig. 3.8 the full cycle is indicated with arrows on the charge stability diagram. In particular, the rapid move from $(1, X^-)$ to $(1, 1)$ is indicated with a thick arrow. We note that the spin of the heavy-hole determines the polarization of the emitted photon [123], allowing us to polarization filter photons that may have been emitted with the injected hole in the wrong spin state (in step 3). The spin of the injected electron must be dealt with separately and we return to this question below. A diagram showing the possible final states depending on the initial electron and hole spins can be found in Paper **M**.

It is important to notice that the envisioned final state of the two electrons is a superposition of the unpolarized singlet and triplet energy eigenstates, i.e.,

$$|1\uparrow, 1\downarrow\rangle = \frac{1}{\sqrt{2}}\left(|(1,1)S\rangle + |(1,1)T_0\rangle\right), \tag{3.13}$$

where $|(1,1)S\rangle = \frac{1}{\sqrt{2}}\left(\hat{c}^\dagger_{l\uparrow}\hat{c}^\dagger_{r\downarrow} - c^\dagger_{l\downarrow}c^\dagger_{r\uparrow}\right)|0\rangle$ and $|(1,1)T_0\rangle = \frac{1}{\sqrt{2}}\left(\hat{c}^\dagger_{l\uparrow}\hat{c}^\dagger_{r\downarrow} + c^\dagger_{l\downarrow}c^\dagger_{r\uparrow}\right)|0\rangle$, which with finite tunnel-coupling are split by the exchange energy J as discussed at the beginning of this chapter. These states have been, as already mentioned in the previous section, shown to provide a single robust qubit [6]. The emitted photon will thus be frequency-entangled with the spin states of the remaining electrons, such that the combined state of the electron spins and the photon field reads

$$|\Phi\rangle = \frac{1}{\sqrt{2}}\left[|(1,1)S\rangle \otimes \hat{\xi}^\dagger(\omega_S)|0\rangle + |(1,1)T_0\rangle \otimes \hat{\xi}^\dagger(\omega_{T_0})|0\rangle\right], \tag{3.14}$$

where we have assumed equal branching ratios for the two decay paths, the difference between the photon frequencies is $|\omega_{T_0} - \omega_S| = |J|$, and $\hat{\xi}^\dagger(\omega)$ creates a photon with frequency ω. The exact shape of the photon wavepackage can be found within standard Wigner-Weißkopf theory for spontaneous photon emission [124]. Here, the probability amplitude for being in the excited state, denoted $c_e(t)$, decays exponentially, i.e.,

$$\dot{c}_e(t) = -\left(\frac{\gamma_S}{2} + \frac{\gamma_{T_0}}{2}\right) c_e(t) = -\frac{\gamma}{2} c_e(t), \tag{3.15}$$

where γ_S and γ_{T_0} are the spontaneous decay rates for decaying into the singlet and (unpolarized) triplet states, respectively, and where we have introduced their sum $\gamma = \gamma_S + \gamma_{T_0}$. The assumption of equal branching ratios corresponds to taking $\gamma_S = \gamma_{T_0}$. Above we have assumed that the final state charge configuration $(1,1)$ is reached via electron-hole recombination. Non-radiative decay can, however, also occur, if the electron-hole pair, rather than recombining, tunnels back into the electron and hole reservoirs. Corresponding to this process, we introduce a rate Γ_o, which should also enter the total rate γ, i.e., $\gamma \to \gamma + \Gamma_o$.

The (total) decay rate γ gives rise to a Lorentzian broadening of the photon frequency, such that the photon creation operator in a one-dimensional model takes the form $\hat{\xi}^\dagger(\omega) = \sum_k \xi(\omega, k)\hat{a}_k^\dagger$, where $\hat{a}_k^\dagger$ creates photons of mode k, and the wavepacket amplitude reads [124]

$$\xi(\omega, k) = \frac{1}{\sqrt{2\pi}} \frac{\sqrt{\gamma} e^{-ikz_0}}{(\omega_k - \omega) + i\gamma/2}. \tag{3.16}$$

In order for the entanglement to be detectable it is necessary that photons corresponding to different spin states are distinguishable, corresponding to their overlap $|\mathcal{J}|^2 \equiv \left|\sum_k \xi(\omega_S, k)\xi^*(\omega_{T_0}, k)\right|^2 = \frac{\gamma^2}{\gamma^2 + (\omega_{T_0} - \omega_S)^2}$ being smaller than unity. With the exchange coupling $J = \omega_{T_0} - \omega_S$ reaching values on the order of meVs and the decay rate being in the GHz regime (corresponding to μeVs), we have $J \gg \gamma$, and thus $\mathcal{J} \simeq 0$.

The spin-photon entanglement can be used for probabilistic spin-spin entanglement between distant double quantum dots using approaches similar to those suggested for atomic systems [125]. We consequently consider the beam splitter setup depicted in Fig. 3.9. Here, two photons emitted from two distant nanowire structures are interfered on a 50/50 beamsplitter and subsequently detected at the shown detectors. The probability for detecting the two photons at *different* detectors reads $P(1_L, 1_R) = (1 - |\mathcal{J}|^2)/1$, where $\mathcal{J}$ is the overlap of the wavepacket amplitudes of the two photons [126]. For identical photons $|\mathcal{J}| = 1$, which leads to so-called Hong-Ou-Mandel bunching: The photons are with certainty detected in the *same* detector. This is,

of course, very different from fermions that instead would anti-bunch and go to different detectors. On the other hand, if the photons are distinguishable, $\mathcal{J} = 0$, they do not interfere, and with probability 1/2 they are detected at different detectors, consistent with the expected result for uncorrelated particles. Using these principles, we can now consider two spin-photon pairs prepared in a entangled state of the form given in Eq. (3.14). The two photons are again interfered on the beam splitter, and if the outgoing photons are subsequently detected at *different* detectors, the detected photons must have different frequencies, and consequently correspond to different spin states in the two nanowire structures. From the input-output relations of the beam splitter it follows that the entangled state of the spins in the spatially separated nanowires reads

$$|\Psi_{L,R}\rangle = \frac{1}{\sqrt{2}}\left[|(1,1)S\rangle_L|(1,1)T_0\rangle_R - |(1,1)T_0\rangle_L|(1,1)S\rangle_R\right], \tag{3.17}$$

conditioned on photon detection in different detectors. Here, the subscripts correspond to the left (L) and right (R) device depicted in Fig. 3.9. The probability of detecting the photons at different detectors reads $\eta^2 \times 1/2 \times 1/2$, where η is the combined single photon emission and detection probability, and the two factors of 1/2 correspond to the probability of the two photons being in different states (one corresponding to the spin singlet and the other to the spin triplet), and the probability, in that case, to detect the photons at different detectors, respectively. Entanglement is thus not generated on demand, but only probabilistically. However, if photon emission and detection do not lead to entanglement generation, the charging sequence and accompanying photon emission can be repeated until entanglement has been generated.

In the above scenario, ideal conditions were considered, under which photon detection at different detectors leads to entanglement generation of the spin states. In reality, however, photon detection at different detectors could also occur for other reasons, for example, a time delay between photon emissions from the two devices would lead to different arrival times at the beam splitter, preventing the photons from interfering. Such an error process could lead to detection at different detectors without entanglement generation, and would thus reduce the fidelity of the entanglement procedure. Other error processes include wrong electron spin preparation in step 2 of the charging sequence and different energy levels in the two nanowire devices, leading to different photon frequencies. The effects of such error processes can be quantified by calculating the fidelity defined as $\mathcal{F} \equiv \langle\Psi_{L,R}|\hat{\rho}_s|\Psi_{L,R}\rangle$, where $|\Psi_{L,R}\rangle$ is the desired spin state defined in Eq. (3.14) and $\hat{\rho}_s$ is the reduced density matrix of the spin states, taking into account these error processes.

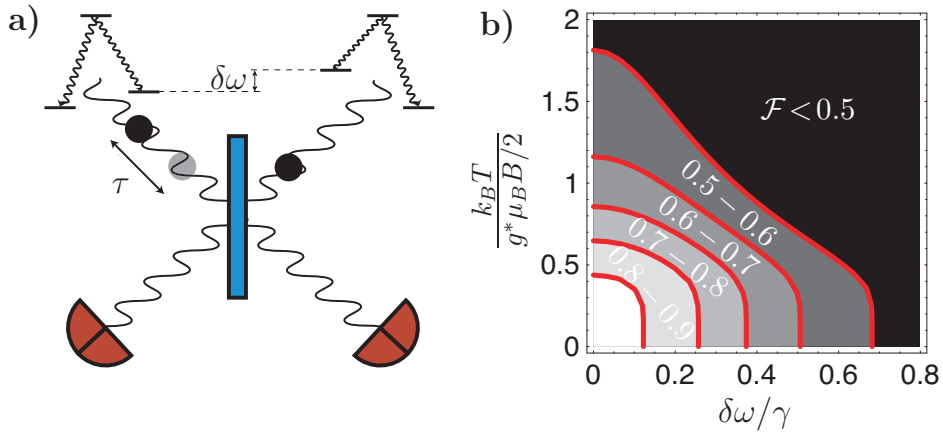

Figure 3.9: Beam splitter setup and entanglement fidelity. (a) Photons from a left and a right device are interfered on a 50/50 beam splitter and subsequently detected at the two detectors. Detections at different detectors leads, in the ideal case, to entanglement between the spin states of the two distant devices. (b) Entanglement fidelity $\mathcal{F}$ as function of the electron reservoir temperature T over Zeeman splitting and the ratio of the energy mismatch $\delta\omega$ and the decay rate γ. The average delay time between the arrival of the two photons was $\bar{\tau} = 0.03\gamma^{-1}$. In the white region $\mathcal{F} > 0.9$. Figure from Paper **M**.

A calculation of the fidelity is given in Paper **M**, and the result is shown in Fig. 3.9. We note that entanglement generated with less than unity fidelity is still useful for quantum computing and communication, as protocols exist for entanglement purification, if only the entanglement can be generated with fidelity larger than 1/2 [127, 128]. From Fig. 3.9 we see that it is possible to generate entanglement with a high fidelity, if the temperature of the electron reservoir is small compared to the Zeeman energy and the difference $\delta\omega$ in frequency of, say, the photons emitted from the two devices corresponding to singlet spin states, is small compared with the total decay rate γ.

Chapter 4

Counting Statistics

The flow of electrons through nano-scale devices is in general a stochastic process, and the number of transferred charges in a given time interval can at best be described by a probability distribution. The study of this probability distribution and its moments or cumulants has been motivated by the expectation that it potentially may contain more information about the intrinsic transport processes in a nano-scale system than the average current or conductance. While this has been a topic of intense theoretical research (see for example Refs. [129, 130, 131] and references therein), only recently experimental studies of real-time counting of electrons have appeared [22, 132, 133, 134, 135]. In these experiments, a quantum point contact close to one or two quantum dots was used as a sensitive real-time probe of the number of charges on the dot(s), making it possible to detect single electrons as they propagated through the dot(s).

In this chapter we introduce the basic concepts of full counting statistics (FCS), the stochastic theory of charge transfer through mesoscopic systems. We consider a number of simple examples that help us develop an intuitive understanding of the theory and allow us to introduce some of the key concepts in FCS. Roughly speaking, the theory of FCS can be divided into two branches: One branch, which was pioneered by L. S. Levitov and G. B. Lesovik [136, 137], is based on scattering theory, relevant for non-interacting particles propagating through open quantum dots, quantum point contacts, etc. The other branch, developed by D. A. Bagrets and Yu. V. Nazarov [138], describes charge transport using rate equations, which may be relevant for systems, where particle interactions are so strong, that a single-particle description is no longer valid. This is for example the case, when considering electron transport through Coulomb blockade quantum dots, which will be our main focus. In the rate equation approach, the number of transferred charges is considered to be a *classical* stochastic variable. This, in turn,

makes the theory applicable to systems well outside the field of mesoscopic physics.[1] Here, we first consider the FCS of memoryless or Markovian systems, before we proceed with a more general theory that also takes into account non-Markovian effects.

4.1 Current fluctuations

Our first goal is to introduce the concept of cumulants and the cumulant generating function. This is most easily done by considering a concrete example. We thus consider particles transmitted through a barrier with rate Γ starting at $t = 0$. The probability of having transmitted n particles at time t is denoted $P_n(t)$. The probabilities obey the equation of motion

$$\frac{d}{dt}P_n(t) = \Gamma\left[P_{n-1}(t) - P_n(t)\right] \tag{4.1}$$

with solution

$$P_n(t) = \Gamma\int_0^t d\tau e^{-\Gamma(t-\tau)}P_{n-1}(\tau) + e^{-\Gamma t}P_n(t=0). \tag{4.2}$$

Since $P_{n<0}(t) = 0$ and $P_n(t=0) = \delta_{n,0}$, we readily find the expression

$$P_n(t) = \frac{(\Gamma t)^n}{n!}e^{-\Gamma t}, t > 0, n = 0, 1, 2, \ldots, \tag{4.3}$$

which is the well-known Poisson distribution. The probabilities peak [$\dot{P}_n(t_n) = 0$] at $t = t_n = n/\Gamma$ with peak heights $P_n(t_n) = e^{-n}n^n/n!$. In Fig. 4.1 we show the probability distribution $P_n(t)$ at different times t.

Rather than the probabilities $P_n(t)$, it is often more convenient to consider the cumulant generating function $\mathcal{S}(\chi, t)$ which we now define as follows[2]

$$e^{S(\mathcal{S}(\chi,t)} \equiv P_\chi(t) = \sum_n P_n(t)e^{in\chi}. \tag{4.4}$$

From the cumulant generating function the m'th cumulant of the number of transmitted charges $\langle\langle n^m\rangle\rangle$(t), $m = 1, 2, \ldots$ is obtained by differentiating with respect to the *counting field* χ at zero, i.e.,

$$\langle\langle n^m\rangle\rangle(t) = \left.\frac{\partial^m\mathcal{S}(\chi,t)}{\partial(i\chi)^m}\right|_{\chi\to 0}. \tag{4.5}$$

[1] As suggested in Ref. [139] one could think of people entering and leaving a night club, and it is not difficult to develop similar ideas of airplanes taking off and landing in an airport.

[2] We note that our convention differs in sign compared to the one often encountered in the literature [131].

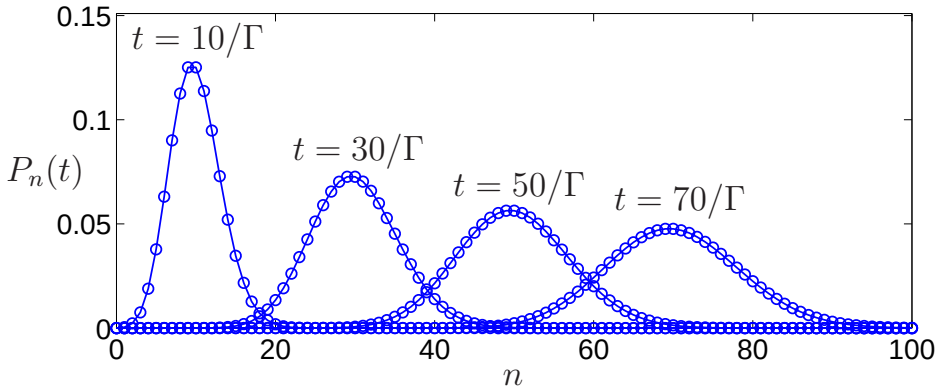

Figure 4.1: Poisson process. The Poisson distribution $P_n(t) = (\Gamma t)^n e^{-\Gamma t}/n!$ is shown at different points of time. The lines serve as guides to the eye.

By inspection it is easily seen that

$$\begin{aligned}
\langle\langle n^1 \rangle\rangle &= \langle n \rangle, \\
\langle\langle n^2 \rangle\rangle &= \langle (n - \langle n \rangle)^2 \rangle, \\
\langle\langle n^3 \rangle\rangle &= \langle (n - \langle n \rangle)^3 \rangle, \\
\langle\langle n^4 \rangle\rangle &= \langle (n - \langle n \rangle)^4 \rangle - 3\langle (n - \langle n \rangle)^2 \rangle^2.
\end{aligned} \tag{4.6}$$

Here, single brackets denote averaging with respect to the probability distribution $P_n(t)$, i.e., $\langle f(n) \rangle(t) = \sum_n f(n) P_n(t)$. The second (variance) and third (skewness) cumulants are identical to the second and third central moments, respectively, while the fourth (kurtosis) and higher order cumulants in general are different from the corresponding central moments.

For the Poisson process described by Eq. (4.3) we find

$$e^{\mathcal{S}_p(\chi,t)} = e^{-\Gamma t} \sum_{n=0}^{\infty} \frac{(\Gamma t e^{i\chi})^n}{n!} = e^{-\Gamma(1-e^{i\chi})t} \tag{4.7}$$

or

$$\mathcal{S}_p(\chi, t) = \Gamma(e^{i\chi} - 1)t. \tag{4.8}$$

From $\mathcal{S}_p(\chi, t)$ we see that all cumulants of a Poisson process are identical and given as $\langle\langle n^m \rangle\rangle_p(t) = \Gamma t$, $m = 1, 2, \ldots$. If we normalize cumulants with respect to the first cumulant, we find for a Poisson process $\langle\langle n^m \rangle\rangle_p / \langle\langle n^1 \rangle\rangle_p = 1$. This is often referred to as the Poissonian limit. In Fig. 4.1 it can be seen, how the average number of transferred charges $\langle\langle n^1 \rangle\rangle(t)$ and the variance of the distribution $\langle\langle n^2 \rangle\rangle(t)$ grow linearly with time.

It is instructive to compare the results for a Poisson process with those of a deterministic process, where particle transfers occur at fixed times $\tau_1 < \tau_2 < \tau_3 < \ldots$. For such a process we have $P_n(t) = \theta(t - \tau_n) - \theta(t - \tau_{n+1})$, where $\theta(t)$ is the Heaviside step function. The probabilities fulfill $P_n(t)P_{n'}(t) = \delta_{n,n'}P_n(t)$ leading to the property $\langle n^m \rangle_d = \langle n \rangle_d^m$, where the subscript denotes deterministic, and for the first three cumulants we thereby find $\langle\langle n \rangle\rangle_d(t) = \sum_n \theta(t - \tau_n)$ and $\langle\langle n^2 \rangle\rangle_d(t) = \langle\langle n^3 \rangle\rangle_d(t) = 0$. A deterministic process thus has zero variance and skewness.

For the Poisson process we saw that the cumulants grow linearly in time. For example, for the average number of charges $\langle\langle n \rangle\rangle(t) = \Gamma t$, and it is natural to consider Γ as the mean current of charges. This leads us to the definition of current cumulants

$$\langle\langle I^m \rangle\rangle = \frac{d}{dt}\langle\langle n^m \rangle\rangle(t)\Big|_{t\to\infty}, m = 1, 2, 3, \ldots, \tag{4.9}$$

where the limit $t \to \infty$ ensures that steady-state has been reached. The first current cumulant $\langle\langle I^1 \rangle\rangle$ is obviously the mean current, while the second cumulant can be related to current-current correlations within the system: If we consider transport through a system, where the current across a barrier, connected to, say, a right lead, can be described by an operator $\hat{I} = \frac{d}{dt}\hat{N}_R$, where $\hat{N}_R$ is the operator of charges in the right lead, the current-current correlator in steady-state is defined as $C_{II}(t) = \langle\{\hat{I}(t), \hat{I}(0)\}\rangle/2 - \langle\hat{I}(0)\rangle^2$, where the curly brackets denote an anti-commutator. The current noise spectrum is then the Fourier transform of $C_{II}(t)$, i.e.,

$$S_{II}(\omega) = \int_{-\infty}^{\infty} dt C_{II}(t) e^{i\omega t}. \tag{4.10}$$

As discussed in Papers **B** (not included) and **G**, the zero-frequency noise $S_{II}(0)$ can be related to the second cumulant as

$$S_{II}(0) = \langle\langle I^2 \rangle\rangle = \frac{d}{dt}\left[\langle n^2 \rangle - \langle n \rangle^2\right]\Big|_{t\to\infty}. \tag{4.11}$$

This result suggests an interpretation of the zero-frequency noise as an effective charge-diffusion coefficient [see e.g. Ref. [140] and Paper **B** (not included)]: The zero-frequency noise determines the speed at which the variance of the distribution grows.

Above, we did not include the electric charge q of the transferred (quasi-) particles in the definition of the current operator. However, if the charge were included, a measurement of the ratio of the first two cumulants, the so-called Fano factor F, would reveal the effective charge of (quasi-) particles

transmitted with a Poissonian statistics, i.e., $F_p = q$ [141]. This principle has been used in experiments on Cooper pair transport, where a doubling of the Fano factor was observed, i.e., $F_p = 2$ [142], and in experiments in the fractional quantum Hall regime, where Fano factors of 1/3 and 1/5 were measured [143, 144, 145]. Throughout this chapter we will use the convention $q = 1$ and $\hbar = 1$.

In general, the second cumulant of the current can be related to the frequency dependence of the current-current correlator via the MacDonald formula [146]

$$S_{II}(\omega) = \omega \int_0^\infty dt \sin(\omega t) \frac{d}{dt} \left[\langle n^2 \rangle - \langle n \rangle^2 \right], \tag{4.12}$$

Here, it is important that the product $\omega \sin(\omega t)$ is considered as a distribution given by the expression

$$\omega \sin(\omega t) \to \left[\omega \sin(\omega t) + \eta \cos(\omega t) \right] e^{-\eta t}, \eta \to 0, \tag{4.13}$$

ensuring that the zero-frequency limit [given by Eq. (4.11)] is obtained for $\omega \to 0$, where MacDonalds formula seemingly would yield zero otherwise. This is discussed in further detail in Paper **G**. In general, the zero-frequency noise is conserved throughout a system [see e.g. Paper **B** (not included)], implying that the zero-frequency noise measured in one of the two leads in a standard transport setup, in principle, should be the same as the zero-frequency noise at any barrier throughout the system. For measurements of the finite-frequency noise it is, on the other hand, important also to include displacement currents and corresponding noise contributions. Such contributions may be included via the Ramo-Shockley theorem as described in Refs. [129, 147] and Paper **G**.

Having introduced the concept of current cumulants, we next consider a simple example of how they can be calculated: We consider a transport setup where single particles are injected into and leaving a system with rates Γ_L and Γ_R, respectively, such that the system at each particle transfer event switches between the states 0 and 1. This is a relevant description when considering electron transport through a single, weakly coupled Coulomb blockade quantum dot operated close to a degeneracy point as described in Chapter 2. We describe the system by the probability vector $\mathbf{p}_n(t) = [p_n(0,t), p_n(1,t)]^T$ containing the probabilities $p_n(i,t)$, that the system at time t is in the state $i = 0, 1$, while n charges have been transported through the system. The time evolution of $\mathbf{p}_n(t)$ is given by a Markovian equation of motion reading

$$\frac{d}{dt}\mathbf{p}_n(t) = \begin{pmatrix} -\Gamma_L & 0 \\ \Gamma_L & -\Gamma_R \end{pmatrix} \mathbf{p}_n(t) + \begin{pmatrix} 0 & \Gamma_R \\ 0 & 0 \end{pmatrix} \mathbf{p}_{n-1}(t). \tag{4.14}$$

The counting field χ is introduced via the Fourier transformation $\mathbf{p}_\chi = \sum_n \mathbf{p}_n e^{in\chi}$, under which Eq. (4.14) translates to

$$\frac{d}{dt}\mathbf{p}_\chi(t) = \mathcal{W}(\chi)\mathbf{p}_\chi(t). \tag{4.15}$$

with

$$\mathcal{W}(\chi) = \begin{pmatrix} -\Gamma_L & e^{i\chi}\Gamma_R \\ \Gamma_L & -\Gamma_R \end{pmatrix}. \tag{4.16}$$

Although, it is possible to study the charge transport statistics of this model in its Markovian formulation, we choose for illustrative purposes to "complicate" matters by tracing out the two states of the quantum dot, and instead study the resulting *non-Markovian* dynamics of the probability distribution $P_n(t) \equiv p_n(0,t) + p_n(1,t)$, whose equation of motion (in Fourier space) reads[3]

$$\frac{d}{dt}P_\chi(t) = \Gamma_R(e^{i\chi} - 1)p_\chi(1,t). \tag{4.17}$$

We note that $\frac{d}{dt}p_\chi(1,t) = \Gamma_L p_\chi(0,t) - \Gamma_R p_\chi(1,t) = \Gamma_L[P_\chi(t) - p_\chi(1,t)] - \Gamma_R p_\chi(1,t)$ with solution

$$p_\chi(1,t) = \Gamma_L \int_0^t d\tau e^{-(\Gamma_L+\Gamma_R)(t-\tau)}P_\chi(\tau) + e^{-(\Gamma_L+\Gamma_R)t}p_\chi(1,t=0), \tag{4.18}$$

leading us to the non-Markovian equation of motion for $P_\chi(t)$,

$$\begin{aligned}\frac{d}{dt}P_\chi(t) =& \Gamma_L\Gamma_R(e^{i\chi}-1)\int_0^t d\tau e^{-(\Gamma_L+\Gamma_R)(t-\tau)}P_\chi(\tau) \\ &+ \Gamma_R(e^{i\chi}-1)e^{-(\Gamma_L+\Gamma_R)t}p_\chi(1,t=0).\end{aligned} \tag{4.19}$$

In Laplace space, defined by $P_\chi(z) = \int_0^\infty dt P_\chi(t)e^{-zt}$, Eq. (4.19) becomes an algebraic equation which we can solve for $P_\chi(z)$,

$$zP_\chi(z) - P_\chi(t=0) = \Lambda_0(z,\chi)\left[P_\chi(z) + \frac{1}{\Gamma_L}p_\chi(1,t=0)\right], \tag{4.20}$$

having introduced

$$\Lambda_0(z,\chi) = \frac{\Gamma_L\Gamma_R(e^{i\chi}-1)}{z+\Gamma_L+\Gamma_R}. \tag{4.21}$$

We assume that we start counting charges at $t = 0$ and that the system at that time has reached steady-state, such that $P_\chi(t=0) = 1$ and $p_\chi(1, t = 0) = \Gamma_L/(\Gamma_L + \Gamma_R)$. We thereby find

$$P_\chi(z) = \frac{1}{z - \Lambda_0(z,\chi)}\left[1 + \frac{\Lambda_0(z,\chi)}{\Gamma_L+\Gamma_R}\right]. \tag{4.22}$$

[3]For comparison Eq. (4.1) reads $\frac{d}{dt}P_\chi(t) = \Gamma(e^{i\chi}-1)P_\chi(t)$ in Fourier space.

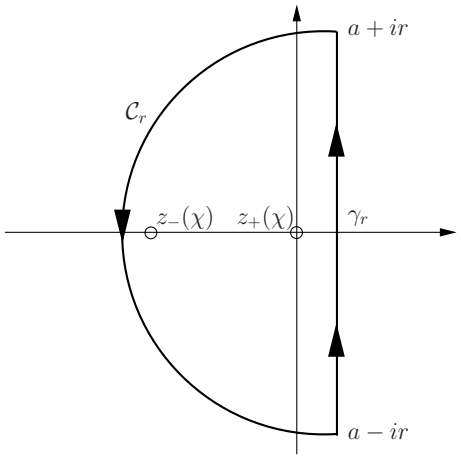

Figure 4.2: Complex contour for integration. The line segment γ_r extends from $a-ir$ to $a+ir$, $a, r > 0$, while $\mathcal{C}_r$ is a half-circle connecting the same points as illustrated. The closed contour $\mathcal{C}_r \cup \gamma_r$ is used for $r \to \infty$.

We return to the time domain by an inverse Laplace transformation given by the so-called Bromwich integral [148]

$$P_\chi(t) = \frac{1}{2\pi i}\int_{a-i\infty}^{a+i\infty} dz \frac{e^{zt}}{z-\Lambda_0(\chi,z)}\left[1+\frac{\Lambda_0(z,\chi)}{\Gamma_L+\Gamma_R}\right], \tag{4.23}$$

where a is a positive number sufficiently large for $P_\chi(t)e^{-at}$ to be integrable. The integral can be carried out by closing the contour and using residue theory. The poles of the integrand are given by the solution to the equation

$$z - \Lambda_0(z,\chi) = 0 \tag{4.24}$$

or

$$(\Gamma_L + z)(\Gamma_R + z) - \Gamma_L\Gamma_R e^{i\chi} = 0, \tag{4.25}$$

which has the solutions

$$z_\pm(\chi) = -\frac{\Gamma_L+\Gamma_R}{2} \pm \sqrt{\left(\frac{\Gamma_L+\Gamma_R}{2}\right)^2 + \Gamma_L\Gamma_R(e^{i\chi}-1)}. \tag{4.26}$$

With straightforward algebra we then find

$$P_\chi(t) = \frac{1}{2\pi i}\oint dz \frac{z+\Gamma_L+\Gamma_R+\Lambda_0(0,\chi)}{[z-z_+(\chi)][z-z_-(\chi)]}e^{zt}, \tag{4.27}$$

where the closed contour for $t > 0$ is shown in Fig. 4.2 together with the two poles. In the limit $r \to \infty$, the contribution from the integral along $\mathcal{C}_r$ vanishes as the integrand goes to zero.

We first consider the zero-frequency current cumulants given by the long-t behavior of $\mathcal{S}(\chi,t)$. Evaluating the complex contour integral using residue

theory, we see that the long-t behavior of $P_\chi(t)$ is governed by the pole with the smallest real part (since the contribution from each pole is damped as $e^{\alpha t}$, where α is the real part of the corresponding pole), and consequently

$$P_\chi(t) = e^{\mathcal{S}(\chi,t)} \to C(\chi)e^{z_+(\chi)t} \tag{4.28}$$

for $t \to \infty$, where $C(\chi)$ is a time-independent function of the counting field. We have thus found the important result that the cumulant generating function in the long-t limit approaches $z_+(\chi)t$ asymptotically, i.e.,

$$\mathcal{S}(\chi, t) \to z_+(\chi)t. \tag{4.29}$$

Although, we have only obtained this result for the given example it holds at a more general level as we will now discuss. First, it is important to notice that the two poles $z_+(\chi)$ and $z_-(\chi)$ were found by solving Eq. (4.25), which is seen also to be the characteristic equation for the matrix $\mathcal{W}(\chi)$ defined in Eq. (4.16). The two poles are consequently eigenvalues corresponding to this matrix, and, in particular, $z_+(\chi)$, which is the eigenvalue that develops adiabatically with χ from the zero-eigenvalue of $\mathcal{W}(0)$, i.e., $z_+(0) = 0$, determines the cumulant generating function in the long-t limit. In Ref. [138] and Paper **D** this statement was shown to hold in general for Markovian (generalized) Master equations of the form given in Eq. (4.15) with *any* number of states.

From a formal point of view this is an important result, however, it does not tell us *how* to determine the χ-dependence of this eigenvalue when the matrix $\mathcal{W}(\chi)$ is of large dimensions. This may be the case, for example, when considering the quantum electromechanical systems introduced in Section 2.2. For these systems, the quantized mechanical vibrations are included in the (generalized) Master equations which are consequently of very large (in principle, infinite) dimensions, corresponding to the dimensionality of the oscillator Hilbert space. The technical question of how to determine the χ-dependence of the zero-eigenvalue is the subject of the following section.

The example considered above also provides us with an important result for systems with *non-Markovian* dynamics whose equations of motion in Fourier and Laplace space read $P_\chi(z) = [z - \mathcal{W}(z, \chi)]^{-1}P_\chi(t = 0)$. In Ref. [149] it was shown that Eq. (4.24) holds for this kind of non-Markovian equations, where $\Lambda_0(z, \chi)$ is then the eigenvalue of $\mathcal{W}(z, \chi)$ that develops adiabatically from the zero-eigenvalue with χ, i.e., $\Lambda_0(0, z) = 0$, and the appropriate solution of Eq. (4.24), denoted $z^*(\chi)$ is the one that goes to zero with χ going to zero, i.e., $z^*(0) = 0$. Again, this is mostly a formal result, and the question of how to find the current cumulants in the non-Markovian case will be the subject of later sections in this chapter.

After these remarks, we return to the calculation of the current cumulants for the given example. Combining Eqs. (4.26) and (4.29) we find the

well-known results [129, 132, 150] for the current, noise, and higher order cumulants

$$\begin{aligned}\langle\langle I^1\rangle\rangle =& \frac{\Gamma_L\Gamma_R}{\Gamma_L+\Gamma_R},\\ \frac{\langle\langle I^2\rangle\rangle}{\langle\langle I^1\rangle\rangle} =& \frac{\Gamma_L^2+\Gamma_R^2}{(\Gamma_L+\Gamma_R)^2} = \frac{1}{2}(1+a^2),\\ \frac{\langle\langle I^3\rangle\rangle}{\langle\langle I^1\rangle\rangle} =& \frac{1}{4}(1+3a^4),\\ \frac{\langle\langle I^4\rangle\rangle}{\langle\langle I^1\rangle\rangle} =& \frac{1}{8}(1+a^2-9a^4+15a^6),\end{aligned} \tag{4.30}$$

where we as in Ref. [132] have introduced the *asymmetry* $a = (\Gamma_L - \Gamma_R)/(\Gamma_L + \Gamma_R)$. Although these results are well-known, the derivation presented here, based on a non-Markovian equation obtained by tracing out the two charge states, is non-standard and possibly new. We note that the results for the zero-frequency cumulants are not dependent on the choice of initial conditions but only on the pole (or eigenvalue) $z_+(\chi)$.

The finite-frequency cumulants, on the other hand, depend on the choice of initial condition and the full set of poles. In the following, we consider the frequency dependence of the second cumulant found from the full solution for $P_\chi(t)$, again assuming that the system at $t = 0$ has reached steady-state. Evaluating the expression in Eq. (4.27) using residue theory, we then find for $t \geq 0$

$$P_\chi(t) = \frac{\left[\Gamma_L+\Gamma_R+\Lambda_0(\chi,0)\right]\left[e^{z_+(\chi)t}-e^{z_-(\chi)t}\right] + z_+(\chi)e^{z_+(\chi)t} - z_-(\chi)e^{z_-(\chi)t}}{z_+(\chi)-z_-(\chi)}, \tag{4.31}$$

from which we can find the t-dependence of the second cumulant $\langle\langle n^2\rangle\rangle(t) = \langle n^2\rangle(t) - \langle n\rangle^2(t)$ by differentiating with respect to the counting field χ at zero [in this context, it may be more appropriate to refer to the second cumulant as the second (central) moment, since it is found from $P_\chi(t)$, which generates moments and not cumulants as $S(t,\chi)$]. The expression for $\langle\langle n^2\rangle\rangle(t)$ is rather lengthy and is not shown here. However, having found $\langle\langle n^2\rangle\rangle(t)$ we may calculate the finite-frequency current-current correlation function using MacDonald's formula given by Eq. (4.12). Carrying out the integration is rather cumbersome and we just quote the final result

$$\frac{S(\omega)}{\langle\langle I^1\rangle\rangle} = 1 - \frac{2\Gamma_L\Gamma_R}{(\Gamma_L+\Gamma_R)^2+\omega^2}. \tag{4.32}$$

This result is also known from the literature [129], but again the derivation presented here is non-standard and illuminating for the general approach to the calculation of finite-frequency current fluctuations.

4.2 Markovian dynamics

In this section we consider the technical question of how to calculate the current cumulants given an n-resolved Markovian (generalized) Master equation of the form

$$\frac{d}{dt}\hat{\rho}_n(t) = \sum_{n'=-\infty}^{\infty} \mathcal{W}(n-n')\hat{\rho}_{n'}(t), \tag{4.33}$$

where n denotes the number of transferred charges at time t. Similarly to the examples considered in the previous section, we introduce the counting field χ via the Fourier transformation $\hat{\rho}_\chi(t) = \sum_{n=-\infty}^{\infty} \hat{\rho}_n(t)e^{in\chi}$ yielding

$$\frac{d}{dt}\hat{\rho}_\chi(t) = \mathcal{W}(\chi)\hat{\rho}_\chi(t). \tag{4.34}$$

As discussed in the previous section the cumulant generating function $\mathcal{S}(\chi,t)$ in the long-t limit is given as $\mathcal{S}(\chi,t) \to t\Lambda_0(\chi)$, where $\Lambda_0(\chi)$ now denotes the eigenvalue of $\mathcal{W}(\chi)$ that develops adiabatically from 0 with χ ($z_+(\chi)$ in the previous section). If $\mathcal{W}(\chi)$ is of large dimensions (> 5) it may be highly non-trivial to determine the χ-dependence of $\Lambda_0(\chi)$ around $\chi = 0$ and non-standard approaches must be developed. In order to find the m'th order cumulant we Taylor expand $\Lambda_0(\chi)$ to m'th order in χ around $\chi = 0$. This we do using Brillouin-Wigner perturbation theory as shown in the following.

We first write

$$\mathcal{W}(\chi) = \mathcal{W} + \overline{\mathcal{W}}(\chi), \tag{4.35}$$

having defined $\mathcal{W} \equiv \mathcal{W}(0)$ and $\overline{\mathcal{W}}(\chi) \equiv \mathcal{W}(\chi) - \mathcal{W}$. Moreover, we will be using the short hand notation $\mathcal{W}' \equiv \partial_\chi \mathcal{W}(\chi)|_{\chi\to 0}$ and similarly for higher order derivatives. We also define the two projectors $\mathcal{P} = \mathcal{P}^2 = |0\rangle\!\rangle\langle\!\langle\tilde{0}|$ and $\mathcal{Q} = \mathcal{Q}^2 = 1 - \mathcal{P}$, obeying the relations $\mathcal{P}\mathcal{W} = \mathcal{W}\mathcal{P} = 0$ and $\mathcal{Q}\mathcal{W} = \mathcal{W}\mathcal{Q} = \mathcal{W}$. Here, we have introduced right and left eigenvectors of $\mathcal{W}$, a corresponding bra(c)ket notation, and an inner product,

$$\hat{\rho}^{\rm stat} \leftrightarrow |0\rangle\!\rangle,\ \langle\!\langle\tilde{0}| \leftrightarrow \hat{1},\ \langle\!\langle\tilde{0}|0\rangle\!\rangle = {\rm Tr}(\hat{1}^\dagger\hat{\rho}^{\rm stat}) = 1. \tag{4.36}$$

Finally, the pseudoinverse, defined as $\mathcal{R}(\Lambda) \equiv \mathcal{Q}[\mathcal{W}-\Lambda]^{-1}\mathcal{Q}$, will be of great importance.

The Brillouin-Wigner perturbation theory allows us to express $\Lambda_0(\chi)$ exclusively in terms of the left and right nullvectors $\langle\!\langle\tilde{0}|$ and $|0\rangle\!\rangle$, the pseudoinverse $\mathcal{R}(\Lambda)$ and the perturbation $\overline{\mathcal{W}}(\chi)$. Following Ref. [117] we start by deriving a formal expression for $\Lambda_0(\chi)$ given by the eigenvalue problem

$$\mathcal{W}(\chi)|0(\chi)\rangle\!\rangle = [\mathcal{W} + \overline{\mathcal{W}}(\chi)]|0(\chi)\rangle\!\rangle = \Lambda_0(\chi)|0(\chi)\rangle\!\rangle. \tag{4.37}$$

By choosing the normalization $\langle\langle\tilde{0}|0(\chi)\rangle\rangle = 1$, it follows easily that

$$\langle\langle\tilde{0}|[\Lambda_0(\chi) - \mathcal{W}]|0(\chi)\rangle\rangle = \Lambda_0(\chi) = \langle\langle\tilde{0}|\overline{\mathcal{W}}(\chi)|0(\chi)\rangle\rangle \tag{4.38}$$

and

$$|0(\chi)\rangle\rangle = |0\rangle\rangle + \mathcal{Q}|0(\chi)\rangle\rangle. \tag{4.39}$$

Moreover, we get from Eq. (4.37)

$$\mathcal{Q}[\Lambda_0(\chi) - \mathcal{W}]|0(\chi)\rangle\rangle = \mathcal{Q}\overline{\mathcal{W}}(\chi)|0(\chi)\rangle\rangle, \tag{4.40}$$

and using that $\mathcal{W}$ and $\mathcal{Q}$ commute, we find

$$\begin{aligned} \mathcal{Q}|0(\chi)\rangle\rangle &= \mathcal{Q}[\Lambda_0(\chi) - \mathcal{W}]^{-1}\mathcal{Q}\overline{\mathcal{W}}(\chi)|0(\chi)\rangle\rangle \\ &= -\mathcal{R}[\Lambda_0(\chi)]\overline{\mathcal{W}}(\chi)|0(\chi)\rangle\rangle, \end{aligned} \tag{4.41}$$

having recognized the pseudoinverse $\mathcal{R}$. Inserting this expression for $\mathcal{Q}|0(\chi)\rangle\rangle$ into Eq. (4.39), we get

$$|0(\chi)\rangle\rangle = |0\rangle\rangle - \mathcal{R}[\Lambda_0(\chi)]\overline{\mathcal{W}}(\chi)|0(\chi)\rangle\rangle, \tag{4.42}$$

which by iteration leads to

$$\begin{aligned} |0(\chi)\rangle\rangle &= \sum_{n=0}^{\infty}\left[-\mathcal{R}[\Lambda_0(\chi)]\overline{\mathcal{W}}(\chi)\right]^n|0\rangle\rangle \\ &= \left[1 + \mathcal{R}[\Lambda_0(\chi)]\overline{\mathcal{W}}(\chi)\right]^{-1}|0\rangle\rangle \end{aligned} \tag{4.43}$$

and finally, from Eq. (4.38), the formal expression for $\Lambda_0(\chi)$

$$\begin{aligned} \Lambda_0(\chi) &= \langle\langle\tilde{0}|\overline{\mathcal{W}}(\chi)|0(\chi)\rangle\rangle \\ &= \langle\langle\tilde{0}|\overline{\mathcal{W}}(\chi)\sum_{n=0}^{\infty}\left[-\mathcal{R}[\Lambda_0(\chi)]\overline{\mathcal{W}}(\chi)\right]^n|0\rangle\rangle \\ &= \langle\langle\tilde{0}|\overline{\mathcal{W}}(\chi)\left[1 + \mathcal{R}[\Lambda_0(\chi)]\overline{\mathcal{W}}(\chi)\right]^{-1}|0\rangle\rangle, \end{aligned} \tag{4.44}$$

which forms the starting point of our perturbative calculation of the current cumulants.

In order to calculate the first three current cumulants we expand Eq. (4.44) to third order in χ using

$$\overline{\mathcal{W}}(\chi) = \overline{\mathcal{W}}'\chi + \frac{1}{2!}\overline{\mathcal{W}}''\chi^2 + \frac{1}{3!}\overline{\mathcal{W}}'''\chi^3 + \ldots, \tag{4.45}$$

and similarly for $\mathcal{R}[\Lambda_0(\chi)]$ (using the short hand notation $\mathcal{R}' \equiv \partial_\chi \mathcal{R}[\Lambda_0(\chi)]|_{\chi\to 0}$, etc.). Notice that $\overline{\mathcal{W}}(0) = 0$ (according to the definition). Ordering terms according to the order of χ we find

$$\begin{aligned}\Lambda_0(\chi) = &\left[\langle\!\langle\tilde{0}|\overline{\mathcal{W}}'|0\rangle\!\rangle\right]\chi + \frac{1}{2!}\left[\langle\!\langle\tilde{0}|\overline{\mathcal{W}}''|0\rangle\!\rangle - 2\langle\!\langle\tilde{0}|\overline{\mathcal{W}}'\mathcal{R}\overline{\mathcal{W}}'|0\rangle\!\rangle\right]\chi^2 \\ &+ \frac{1}{3!}\Big[\langle\!\langle\tilde{0}|\overline{\mathcal{W}}'''|0\rangle\!\rangle - 3\langle\!\langle\tilde{0}|\overline{\mathcal{W}}''\mathcal{R}\overline{\mathcal{W}}' + \overline{\mathcal{W}}'\mathcal{R}\overline{\mathcal{W}}''|0\rangle\!\rangle \\ &-6\langle\!\langle\tilde{0}|\overline{\mathcal{W}}'\mathcal{R}'\overline{\mathcal{W}}'|0\rangle\!\rangle + 6\langle\!\langle\tilde{0}|\overline{\mathcal{W}}'\mathcal{R}\overline{\mathcal{W}}'\mathcal{R}\overline{\mathcal{W}}'|0\rangle\!\rangle\Big]\chi^3 + \ldots\end{aligned} \tag{4.46}$$

From this expansion we can identify the first three current cumulants:

$$\begin{aligned}\langle\!\langle I^1\rangle\!\rangle_m =& \langle\!\langle\tilde{0}|\overline{\mathcal{W}}'|0\rangle\!\rangle/i, \\ \langle\!\langle I^2\rangle\!\rangle_m =& \left[\langle\!\langle\tilde{0}|\overline{\mathcal{W}}''|0\rangle\!\rangle - 2\langle\!\langle\tilde{0}|\overline{\mathcal{W}}'\mathcal{R}\overline{\mathcal{W}}'|0\rangle\!\rangle\right]/i^2, \\ \langle\!\langle I^3\rangle\!\rangle_m =& \Big[\langle\!\langle\tilde{0}|\overline{\mathcal{W}}'''|0\rangle\!\rangle - 3\langle\!\langle\tilde{0}|\overline{\mathcal{W}}''\mathcal{R}\overline{\mathcal{W}}' + \overline{\mathcal{W}}'\mathcal{R}\overline{\mathcal{W}}''|0\rangle\!\rangle \\ &-6\langle\!\langle\tilde{0}|\overline{\mathcal{W}}'\mathcal{R}(\mathcal{R}\overline{\mathcal{W}}'\mathcal{P} - \overline{\mathcal{W}}'\mathcal{R})\overline{\mathcal{W}}'|0\rangle\!\rangle\Big]/i^3.\end{aligned} \tag{4.47}$$

In the last line we have used $\mathcal{R}' = \mathcal{R}^2\partial_\chi\Lambda_0(\chi)|_{\chi=0} = \mathcal{R}^2\langle\!\langle\tilde{0}|\overline{\mathcal{W}}'|0\rangle\!\rangle$ and simplified the expression by reintroducing the projector $\mathcal{P}$. Above, we have added the subscript m, since the expressions are valid for systems with Markovian dynamics. The procedure for calculating the cumulants is straightforward to extend to higher orders, e.g., using Mathematica. For example, the fourth order cumulant reads

$$\begin{aligned}\langle\!\langle I^4\rangle\!\rangle_m = &\Big[\langle\!\langle\tilde{0}|\overline{\mathcal{W}}''''|0\rangle\!\rangle - 6\langle\!\langle\tilde{0}|\overline{\mathcal{W}}''\mathcal{R}\overline{\mathcal{W}}''|0\rangle\!\rangle - 4\langle\!\langle\tilde{0}|\overline{\mathcal{W}}'''\mathcal{R}\overline{\mathcal{W}}' + \overline{\mathcal{W}}'\mathcal{R}\overline{\mathcal{W}}'''|0\rangle\!\rangle \\ &- 12\langle\!\langle\tilde{0}|\overline{\mathcal{W}}''\mathcal{R}(\mathcal{R}\overline{\mathcal{W}}'\mathcal{P} - \overline{\mathcal{W}}'\mathcal{R})\overline{\mathcal{W}}'|0\rangle\!\rangle \\ &- 12\langle\!\langle\tilde{0}|\overline{\mathcal{W}}'\mathcal{R}(\mathcal{R}\overline{\mathcal{W}}''\mathcal{P} - \overline{\mathcal{W}}''\mathcal{R})\overline{\mathcal{W}}'|0\rangle\!\rangle \\ &- 12\langle\!\langle\tilde{0}|\overline{\mathcal{W}}'\mathcal{R}(\mathcal{R}\overline{\mathcal{W}}'\mathcal{P} - \overline{\mathcal{W}}'\mathcal{R})\overline{\mathcal{W}}''|0\rangle\!\rangle \\ &- 24\langle\!\langle\tilde{0}|\overline{\mathcal{W}}'\mathcal{R}\Big(\mathcal{R}^2\overline{\mathcal{W}}'\mathcal{P}\overline{\mathcal{W}}'\mathcal{P} - \mathcal{R}\overline{\mathcal{W}}'\mathcal{P}\overline{\mathcal{W}}'\mathcal{R} \\ &-\overline{\mathcal{W}}'\mathcal{R}^2\overline{\mathcal{W}}'\mathcal{P} - \mathcal{R}\overline{\mathcal{W}}'\mathcal{R}\overline{\mathcal{W}}'\mathcal{P} + \overline{\mathcal{W}}'\mathcal{R}\overline{\mathcal{W}}'\mathcal{R}\Big)\overline{\mathcal{W}}'|0\rangle\!\rangle\Big]/i^4.\end{aligned} \tag{4.48}$$

The expressions for the higher order cumulants are increasingly lengthy and we do not show them here.

In order to calculate the cumulants given the above expressions, one needs to determine the (normalized) right eigenvector $|0\rangle\!\rangle \leftrightarrow \hat{\rho}^{\rm stat}$ by solving the

matrix problem $\mathcal{W}\hat{\rho}^{\rm stat} = 0$. Even for (very) large systems, and consequently (very) large matrices $\mathcal{W}$ (say, of size $10^4 \times 10^4$), $\hat{\rho}^{\rm stat}$ can be found using available numerical techniques [151, 152]. On the other hand, it is not necessary to find the pseudoinverse $\mathcal{R} = \mathcal{Q}\mathcal{W}^{-1}\mathcal{Q}$ explicitly. It is only necessary to solve matrix equations of the form $|x\rangle\!\rangle = \mathcal{Q}\mathcal{W}^{-1}\mathcal{Q}|b\rangle\!\rangle \Rightarrow \mathcal{W}|x\rangle\!\rangle = \mathcal{Q}|b\rangle\!\rangle$, where $|b\rangle\!\rangle$ is given by the problem at hand. The matrix equation has (infinitely many) solutions, since $\mathcal{Q}|b\rangle\!\rangle$ lies in the space spanned by $\mathcal{Q}$, where $\mathcal{W}$ is non-singular. Even for (very) large matrices, a solution, $|x'\rangle\!\rangle$, can be found using available iterative methods as described in Ref. [152] and Paper **B** (not included). Having found a solution $|x'\rangle\!\rangle$, the particular and unique solution $|x\rangle\!\rangle$ is obtained by application of $\mathcal{Q}$, i.e., $|x\rangle\!\rangle = \mathcal{Q}|x'\rangle\!\rangle$. In this process, it was not necessary to determine $\mathcal{R}$ explicitly.

In Paper **D** we calculated numerically the first three current cumulants of the quantum shuttle introduced in section 2.2. For this model, we may write the perturbation $\overline{\mathcal{W}}(\chi)$ as

$$\overline{\mathcal{W}}(\chi) = (e^{i\chi} - 1)\mathcal{I}_+ + (e^{-i\chi} - 1)\mathcal{I}_-. \tag{4.49}$$

Here $\mathcal{I}_{+/-}$ is the current (super-)operator describing single electron transfer events across a junction in the forward/backward direction. The net current across the junction is given by their difference, i.e., $\mathcal{I} \equiv \mathcal{I}_+ - \mathcal{I}_-$, while their sum is denoted $\mathcal{J} \equiv \mathcal{I}_+ + \mathcal{I}_-$. Combining Eqs. (4.47) and (4.49) we find the expressions

$$\begin{aligned}
\langle\!\langle I^1 \rangle\!\rangle =& \langle\!\langle \tilde{0}|\mathcal{I}|0\rangle\!\rangle, \\
\langle\!\langle I^2 \rangle\!\rangle =& \langle\!\langle \tilde{0}|\mathcal{J}|0\rangle\!\rangle - 2\langle\!\langle \tilde{0}|\mathcal{I}\mathcal{R}\mathcal{I}|0\rangle\!\rangle, \\
\langle\!\langle I^3 \rangle\!\rangle =& \langle\!\langle \tilde{0}|\mathcal{I}|0\rangle\!\rangle - 3\langle\!\langle \tilde{0}|\mathcal{J}\mathcal{R}\mathcal{I} + \mathcal{I}\mathcal{R}\mathcal{J}|0\rangle\!\rangle - 6\langle\!\langle \tilde{0}|\mathcal{I}\mathcal{R}(\mathcal{R}\mathcal{I}\mathcal{P} - \mathcal{I}\mathcal{R})\mathcal{I}|0\rangle\!\rangle,
\end{aligned} \tag{4.50}$$

which were also reported in Paper **D**. In Paper **D** these expressions were derived using Rayleigh-Schrödinger perturbation theory, which, however, is very cumbersome to extend beyond the first three current cumulants, unlike the Brillouin-Wigner approach presented here.

In Paper **G** we extended the result for the second cumulant to finite-frequency current-current correlations. Using the MacDonald formula we found, for uni-directional current given by the current (super-)operator $\mathcal{I}_+$, the expression

$$S(\omega) = \langle\!\langle \tilde{0}|\mathcal{I}_+|0\rangle\!\rangle - 2\mathrm{Re}\left[\langle\!\langle \tilde{0}|\mathcal{I}_+\mathcal{R}(-i\omega)\mathcal{I}_+|0\rangle\!\rangle\right], \tag{4.51}$$

where $\mathcal{R}(-i\omega) = \mathcal{Q}[\mathcal{W} + i\omega]^{-1}\mathcal{Q}$.[4]

[4]Note that a different definition of the pseudoinverse was used in Paper **G**.

The study of the FCS of the quantum shuttle was, as already mentioned in Section 2.2, motivated by a giant enhancement of the Fano factor ($F \simeq 100 \gg 1$) found in Paper **A** (not included). Here, the large noise enhancement together with plots of the Wigner phase space distribution of the mechanical oscillator was taken as an indication that the system in certain parameter regimes exhibits a mechanical bistability with slow fluctuations between two oscillator amplitudes leading to random telegraph noise in the charge transfer process. A similar switching phenomenon was found and referred to as the "whistle effect" in Ref. [153], where the noise of a quantum dot system in the cotunneling regime was considered. In a simple model of this behavior, the system is considered as switching between two oscillator-amplitude states, denoted 1 and 2 in the following, with rates $\Gamma_{1\leftarrow 2}$ and $\Gamma_{2\leftarrow 1}$, respectively, and corresponding mean currents I_1 and I_2, respectively, associated with each of the two states. If the switching rates, $\Gamma_{1\leftarrow 2}$ and $\Gamma_{2\leftarrow 1}$, are much slower than the typical charge transfer rates, given by I_1 and I_2, the first three cumulants read [154, 155]

$$\begin{aligned}
\langle\langle I^1 \rangle\rangle &= \frac{I_1\Gamma_{1\leftarrow 2} + I_2\Gamma_{2\leftarrow 1}}{\Gamma_{2\leftarrow 1} + \Gamma_{1\leftarrow 2}} \ , \\
\langle\langle I^2 \rangle\rangle &= 2(I_1 - I_2)^2 \frac{\Gamma_{1\leftarrow 2}\Gamma_{2\leftarrow 1}}{(\Gamma_{1\leftarrow 2} + \Gamma_{2\leftarrow 1})^3} \ , \\
\langle\langle I^3 \rangle\rangle &= 6(I_1 - I_2)^3 \frac{\Gamma_{1\leftarrow 2}\Gamma_{2\leftarrow 1}(\Gamma_{2\leftarrow 1} - \Gamma_{1\leftarrow 2})}{(\Gamma_{1\leftarrow 2} + \Gamma_{2\leftarrow 1})^5} \ ,
\end{aligned} \tag{4.52}$$

or for the third cumulant

$$\langle\langle I^3 \rangle\rangle = 3\langle\langle I^2 \rangle\rangle^2 \frac{(I_1 + I_2)/2 - \langle\langle I^1 \rangle\rangle}{(I_2 - \langle\langle I^1 \rangle\rangle)(\langle\langle I^1 \rangle\rangle - I_1)}. \tag{4.53}$$

Equation (4.53) provides a necessary condition for the occurrence of a bistability. Thus, by calculating numerically the first three current cumulants as function of a chosen control parameter, one can check if Eq. (4.53) is fulfilled and, if so, obtain good reason to believe that the system is going through a bistability as the control parameter is varied. From Eq. (4.52) it is also evident that the second cumulant diverges as $1/\Gamma$ for comparable switching rates $\Gamma_{1\leftarrow 2} \simeq \Gamma_{2\leftarrow 1} \simeq \Gamma$, which would explain the giant enhancement of the noise found in the quantum shuttle.

For the quantum shuttle, the two states (or current channels), 1 and 2, could be identified from the Wigner phase space distribution of the oscillator. For large dampings, the low-amplitude state, corresponding to an almost static quantum dot, is dominating, and the corresponding current, denoted I_1, can be found from a simple two-state picture, which is confirmed by the

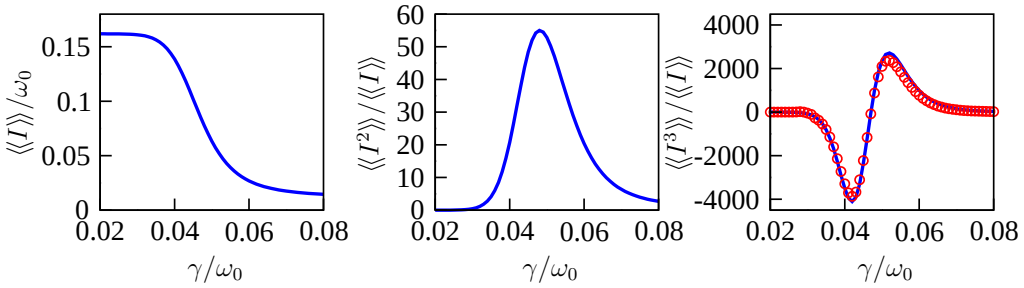

Figure 4.3: First three current cumulants of the quantum shuttle as function of the damping γ. Full lines show numerical results, while circles correspond to Eq. (4.53). Parameters are $\Gamma_L = \Gamma_R = 0.01\omega_0$, $\lambda = 1.5x_0$, $d = eE/m\omega_0^2 = 0.5x_0$, $x_0 = \sqrt{\hbar/m\omega_0}$. Figure from Paper **F**.

corresponding results for the zero-frequency noise. For low dampings, the large-amplitude state dominates, and from charge-resolved Wigner phase distributions it can be seen that single electrons are being transported from the source to the drain electrode with clear correlations between the momentum of the oscillator and the charge-state of the dot. In this so-called shuttling regime, the current, denoted I_2, is expected to be qf, where $f = \omega_0/2\pi$ is the frequency of the oscillations, and q is the charge of the transferred particles (the oscillator frequency is discussed further in connection with the finite-frequency noise). Since charges are transported in an orderly manner, the zero-frequency noise is close to 0.

In Fig. 4.3 we show numerical results for the first three cumulants as function of damping. Together with the third cumulant we show Eq. (4.53) using the numerical results for the first two cumulants. The good agreement between Eq. (4.53) and the numerical results for the third cumulant strongly supports the claim that the system in the region with large noise enhancement is bistable, switching slowly between the two current channels. While it may be very difficult to monitor or measure the phase space distribution of a nano-scale oscillator in an experiment, the first three cumulants may, on the other hand, provide experimentally accessible quantities that could be used to detect a bistability in the transport through a nano-scale device. At the same time, it is not immediately clear, if the same knowledge concerning the internal dynamics of the system can be obtained by just considering the mean current or conductance, and this example thus provides a clear case, where useful information can be extracted from the first few cumulants.

The bistability can also be detected in the finite-frequency noise. Here,

the frequency-dependent Fano factor takes the Lorentzian form [49, 50]

$$F(\omega) = \frac{S(\omega)}{\langle\langle I^1 \rangle\rangle} = \frac{2}{\langle\langle I^1 \rangle\rangle} \frac{\Gamma_{1\leftarrow 2}\Gamma_{2\leftarrow 1}}{\Gamma_{1\leftarrow 2} + \Gamma_{2\leftarrow 1}} \frac{(I_1 - I_2)^2}{(\Gamma_{1\leftarrow 2} + \Gamma_{2\leftarrow 1})^2 + \omega^2}, \tag{4.54}$$

which again can be compared to the numerical results. The switching rates $\Gamma_{1\leftarrow 2}$ and $\Gamma_{2\leftarrow 1}$ are in this case needed, and they can be extracted from the numerical results for the first two cumulants using the analytic expression given in Eq. (4.52). In Papers **F** and **G** the switching rates as function of damping and the agreement between Eq. (4.54) and the numerical results for the finite-frequency noise in the bistable regime, respectively, can be found. From the rates shown in Paper **F**, a clear crossover between the two current channels can be identified.

In general, the finite-frequency noise can reveal information about the internal energy scales of the system [129]. In Paper **G** we therefore calculated the finite-frequency current noise of the quantum shuttle over a range of frequencies comparable with the oscillator frequency ω_0 [in contrast, we only considered the low-frequency regime $\omega \ll \omega_0$, when studying the bistability, since the switching behavior, according to Eq. (4.54), is visible in the low-frequency noise spectrum around frequencies comparable to the (slow) switching rates]. In these calculations contributions due to displacement currents are included via the Ramo-Shockley theorem. The results are shown in Fig. 4.4. Three resonances (or peaks) at finite frequencies are seen, and, in particular, it is interesting to observe that the first peak appears slightly above $\omega = \omega_0$. In Ref. [156] the finite-frequency current noise of a single-electron transistor capacitively coupled to a classical resonator was calculated and peaks in the current noise at the frequency of the resonator were identified. Following these lines, we take the position of the peak slightly above $\omega = \omega_0$ as signature of a renormalization of the oscillator frequency, such that oscillations occur with the frequency $1.03\omega_0$, being the position of the first peak. This would imply that the current in the shuttling regime should read $1.03\omega_0/2\pi = 0.164\omega_0$ and not $\omega_0/2\pi = 0.159\omega_0$. Numerically, the value $0.164\omega_0$ is found for the current, strongly supporting the suggested frequency renormalization.

The methods described above and the expressions given in Eqs. (4.50) and (4.51) are applicable to a large class of systems, including recent studies of transport through single molecules [157, 158] and nano-resonators coupled to normal [159] or superconducting [160] single-electron transistors.[5] In Paper

[5] During a visit to the group of Lecture Andrew D. Armour at University of Nottingham, a similar bistability occurring in a superconducting single-electron transistor coupled to a nano-resonator was identified in numerical results for the third cumulant and the finite-frequency noise obtained using the methods described here.

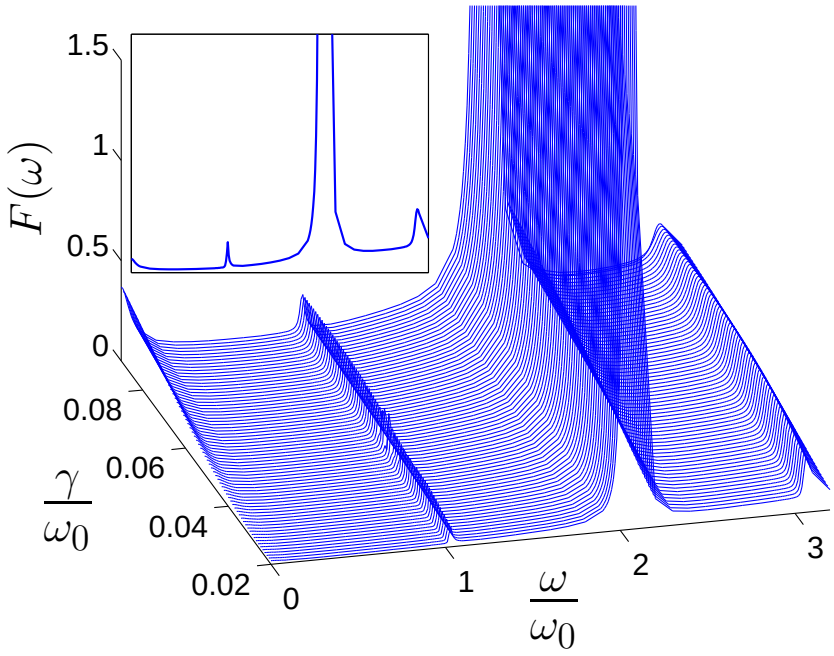

Figure 4.4: Finite-frequency noise spectrum of the quantum shuttle. The frequency-dependent Fano factor $F(\omega) = S_{II}(\omega)/\langle\langle I^1 \rangle\rangle$ is shown for different values of the damping γ. Other parameters are $\Gamma_L = \Gamma_R = 0.05\omega_0$, $\lambda = x_0$, $d = eE/m\omega_0^2 = 0.5x_0$, $x_0 = \sqrt{\hbar/m\omega_0}$. The inset shows a representative curve ($\gamma = 0.05\omega_0$). Figure from Paper **G**.

F we used them to study transport through the vibrating quantum dot array described in Section 2.2. In Paper **B** (not included) a giant enhancement of the noise was found in certain parameter regimes, and by comparing Eqs. (4.53) and (4.54) with numerical results for the third cumulant and the finite-frequency noise, we could again ascribe the enhancement to a slow switching process. The details of this switching process are described in Paper **F**.

As already mentioned, the finite-frequency noise may be used to probe the internal energy scales of a system. In the noise spectrum of the quantum shuttle we found clear signatures of the oscillator frequency, and it is relevant to search for similar signatures of coherent couplings within a system, e.g., between the electronic states of coupled quantum dots. In Fig. 4.5 we show numerical results for the noise spectrum of the vibrating quantum dot array in a frequency range around the oscillator frequency ω_0. The overall structure of the noise spectrum can be explained using a two-state picture with highly asymmetric rates and the corresponding expression for the finite-frequency noise given in Eq. (4.32) (leading to the dashed curve). However, a series of tiny signatures are also observed. These signatures occur at the Bohr frequencies, i.e., the level splittings, of the isolated array and oscillator system, which are marked by arrows in the figure. Again, it is not immediately clear, if calculations or measurements of just the mean current or conduction could reveal these internal energy scales in a similar manner. We note that, recently, similar noise calculations were used to identify vibrational coherences in a nano-electromechanical system [161].

4.3 Non-Markovian dynamics

We now turn to the question of how to determine the current cumulants given a non-Markovian (generalized) Master equation of the form

$$\frac{d}{dt}\hat{\rho}_n(t) = \sum_{n'=-\infty}^{\infty} \int_0^t dt' \mathcal{W}(n-n', t-t')\hat{\rho}_{n'}(t'), \tag{4.55}$$

which in Laplace ($t \to z$) and Fourier space ($n \to \chi$) translates to

$$z\hat{\rho}_\chi(z) - \hat{\rho}_\chi(t=0) = \mathcal{W}(\chi, z)\hat{\rho}_\chi(z). \tag{4.56}$$

As already discussed in Section 4.1, the cumulant generating function is in the long-t limit given as $\mathcal{S}(\chi, t) \to z^*(\chi)t$, where $z^*(\chi)$ is the solution to the equation

$$z^* - \Lambda_0(\chi, z^*) = 0 \tag{4.57}$$

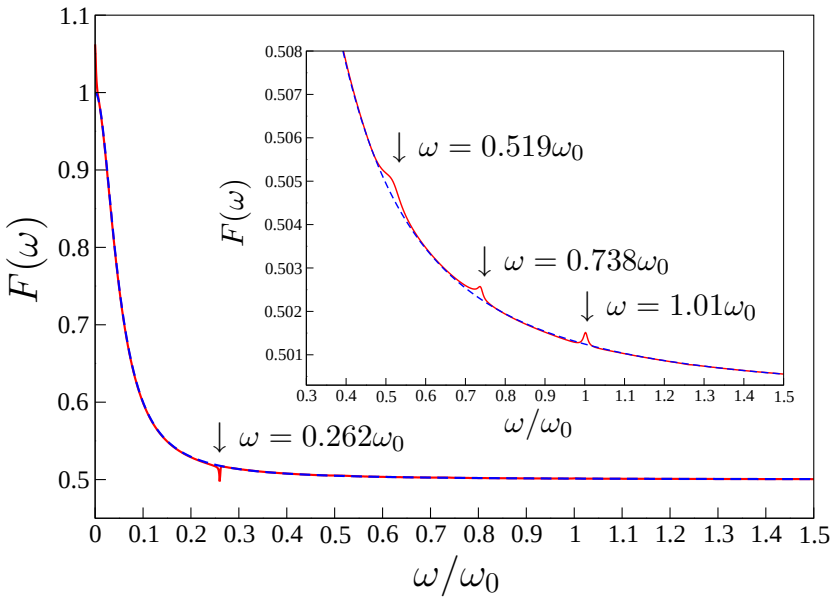

Figure 4.5: Finite-frequency noise spectrum of the vibrating quantum dot array. Numerical results for the frequency-dependent Fano factor $F(\omega) = S_{II}(\omega)/\langle\langle I^1 \rangle\rangle$ are shown with a full line, while the dashed line corresponds to Eq. (4.32) with highly asymmetric rates, where the largest rate is given by $\Gamma_L = \Gamma_R$ of the full model. The Bohr frequencies of the isolated system are shown with arrows that correspond well with the observed signatures in the full noise spectrum. Parameters are $\Gamma_L = \Gamma_R = 0.05\omega_0$, $\gamma = 0.0125\omega_0$, $\varepsilon = 0.5\omega_0$, $\tau_L = \tau_R = 0.5\omega_0$, $\alpha = 0.4\sqrt{2m\omega_0/\hbar}$, $x_0 = 5\sqrt{\hbar/2m\omega_0}$.

that goes to zero with χ going to zero, i.e., $z^*(0) = 0$. Here, $\Lambda_0(\chi, z)$ is the eigenvalue of $\mathcal{W}(\chi, z)$ that develops adiabatically from the zero-eigenvalue with χ, i.e., $\Lambda_0(0, z) = 0$.

In order to determine $z^*(\chi)$ we again apply Brillouin-Wigner perturbation theory. The formal expression given in Eq. (4.44) is still valid, provided that $\mathcal{R}[\Lambda_0(\chi)]$ and $\overline{\mathcal{W}}(\chi)$ are replaced by $\mathcal{R}[\Lambda_0(\chi, z)]$ and $\overline{\mathcal{W}}(\chi, z) = \mathcal{W}(\chi, z) - \overline{\mathcal{W}}(0, 0)$, respectively,

$$\Lambda_0(\chi, z) = \langle\!\langle \tilde{0}|\overline{\mathcal{W}}(\chi, z)\left[1 + \mathcal{R}[\Lambda_0(\chi, z)]\overline{\mathcal{W}}(\chi, z)\right]^{-1}|0\rangle\!\rangle. \tag{4.58}$$

We now expand this formal expression in χ *and* z, which combined with Eq. (4.57) and an expansion of $z^*(\chi)$ in χ, i.e., $z^*(\chi) = \langle\!\langle I^1\rangle\!\rangle(i\chi) + \frac{1}{2!}\langle\!\langle I^2\rangle\!\rangle(i\chi)^2 + \frac{1}{3!}\langle\!\langle I^3\rangle\!\rangle(i\chi)^3 + \ldots$, allows us to solve for the current cumulants. The details of this procedure are not given here, and we just quote the final results for the first three current cumulants

$$\begin{aligned}
\langle\!\langle I^1\rangle\!\rangle =& \langle\!\langle I^1\rangle\!\rangle_m, \\
\langle\!\langle I^2\rangle\!\rangle =& \langle\!\langle I^2\rangle\!\rangle_m - 2i\langle\!\langle I^1\rangle\!\rangle_m \left(\langle\!\langle \tilde{0}|\dot{\overline{\mathcal{W}}}'|0\rangle\!\rangle - \langle\!\langle \tilde{0}|\overline{\mathcal{W}}'\mathcal{R}\dot{\overline{\mathcal{W}}}|0\rangle\!\rangle\right), \\
\langle\!\langle I^3\rangle\!\rangle =& \langle\!\langle I^3\rangle\!\rangle_m - \frac{3\langle\!\langle I^2\rangle\!\rangle}{2\langle\!\langle I^1\rangle\!\rangle_m}\left(\langle\!\langle I^2\rangle\!\rangle_m - \langle\!\langle I^2\rangle\!\rangle\right) \\
& - 3\langle\!\langle I^1\rangle\!\rangle_m \Big(\langle\!\langle \tilde{0}|\dot{\overline{\mathcal{W}}}'' - 2\dot{\overline{\mathcal{W}}}'\mathcal{R}\overline{\mathcal{W}}' - \overline{\mathcal{W}}''\mathcal{R}\dot{\overline{\mathcal{W}}} \\
& -2\overline{\mathcal{W}}'\mathcal{R}(\mathcal{R}\dot{\overline{\mathcal{W}}}\mathcal{P}\overline{\mathcal{W}}' - \overline{\mathcal{W}}'\mathcal{R}\dot{\overline{\mathcal{W}}} - \dot{\overline{\mathcal{W}}}\mathcal{R}\overline{\mathcal{W}}' + \dot{\overline{\mathcal{W}}}')|0\rangle\!\rangle\Big). \\
& - 3i\langle\!\langle I^1\rangle\!\rangle_m^2 \left(\langle\!\langle \tilde{0}|\ddot{\overline{\mathcal{W}}}' - \overline{\mathcal{W}}'\mathcal{R}\ddot{\overline{\mathcal{W}}} - 2\dot{\overline{\mathcal{W}}}'\mathcal{R}\dot{\overline{\mathcal{W}}} + 2\overline{\mathcal{W}}'\mathcal{R}\dot{\overline{\mathcal{W}}}\mathcal{R}\dot{\overline{\mathcal{W}}}|0\rangle\!\rangle\right),
\end{aligned} \tag{4.59}$$

where we have introduced the shorthand notation $\dot{\overline{\mathcal{W}}} \equiv \partial_z \mathcal{W}(\chi, z)|_{\chi, z\to 0}$, etc, used $\mathcal{R}' = \mathcal{R}^2\partial_\chi\Lambda_0(\chi, z)|_{\chi,z=0} = \mathcal{R}^2\langle\!\langle \tilde{0}|\overline{\mathcal{W}}'|0\rangle\!\rangle$ and $\dot{\mathcal{R}} = \mathcal{R}^2\partial_z\Lambda_0(\chi, z)|_{\chi,z=0} = 0$, and reintroduced the projector $\mathcal{P}$ in order to simplify the expressions. In the above expressions, the terms with subscript m correspond to the ones given in Eq. (4.47) for Markovian dynamics [obtained from $\overline{\mathcal{W}}(z = 0, \chi)$]. It is interesting to note that the mean current is not sensitive to non-Markovian effects, while higher order cumulants are. We have not attempted to derive an expression for the fourth (or higher) order cumulant, although it is in principle possible, however, cumbersome.

The expressions above are again generally applicable to a large class of systems, in particular, of course, those with non-Markovian dynamics. Here, we illustrate the developed formalism by considering a transport model of

current research interest [162]. The model describes coherent charge transport of electrons through two coupled single-level quantum dots given by the Hamiltonian

$$\hat{H} = \hat{H}_S + \hat{H}_T + \hat{H}_{\text{leads}}, \tag{4.60}$$

where $\hat{H}_S = \sum_{\alpha=L,R} \varepsilon_\alpha c_\alpha^\dagger c_\alpha + \Omega(c_L^\dagger c_R + c_R^\dagger c_L)$ is the Hamiltonian of the levels of the left (L) and right (R) quantum dot with energies ε_L and ε_R, respectively, coherently coupled with tunneling matrix element Ω (assumed to be real). Here, we have not included any Coulomb interaction between the dots, but this would be straightforward to introduce (see below), and in particular, if double-occupancies of the system are excluded, the model can be mapped onto an effective pseudo-spin description [147, 163]. The double quantum dot is tunnel-coupled to left (L) and right (R) leads via the tunnel-Hamiltonian $\hat{H}_T = \sum_{k_\alpha,\alpha=L,R}(V_{k_\alpha}\hat{c}_{k_\alpha}^\dagger c_\alpha + \text{h.c.})$, with both leads described as non-interacting fermions, i.e., $\hat{H}_\alpha = \sum_{k_\alpha}(\varepsilon_{k\alpha} - \mu_\alpha)\hat{c}_{k_\alpha}^\dagger \hat{c}_{k_\alpha}, \alpha = L, R$, where we above have defined $\hat{H}_{\text{leads}} = \sum_{\alpha=L,R} \hat{H}_\alpha$.

Following Refs. [48, 162, 164] charge transport through the system can be described by a Markovian (generalized) master equation of the form $\frac{d}{dt}\hat{\rho}_\chi(t) = \mathcal{W}(\chi)\hat{\rho}_\chi(t)$, where $\hat{\rho} = (\rho_{00}, \rho_{10}, \rho_{01}, \rho_{11}, \text{Re}[\rho_{10,01}], \text{Im}[\rho_{10,01}])^T$ contains the Fourier transform of the four diagonal elements ρ_{ij} of the reduced density matrix of the double quantum dot, with $i, j = 0, 1$ denoting the number of charges on the left and right dot, respectively, and the real and imaginary parts of the off-diagonal matrix element $\rho_{10,01}$. The operator $\mathcal{W}(\chi)$ in matrix notation reads

$$\mathcal{W}(\chi) = \begin{pmatrix} -\Gamma_L & 0 & \Gamma_R e^{i\chi} & 0 & 0 & 0 \\ \Gamma_L & 0 & 0 & \Gamma_R e^{i\chi} & 0 & 2\Omega \\ 0 & 0 & -2\Gamma & 0 & 0 & -2\Omega \\ 0 & 0 & \Gamma_L & -\Gamma_R & 0 & 0 \\ 0 & 0 & 0 & 0 & -\Gamma & -\varepsilon \\ 0 & -\Omega & \Omega & 0 & \varepsilon & -\Gamma \end{pmatrix} \tag{4.61}$$

with $\Gamma \equiv (\Gamma_L + \Gamma_R)/2$ and $\varepsilon = \varepsilon_L - \varepsilon_R$. The rates are given by the tunneling density of states, i.e., $\Gamma_\alpha = 2\pi \sum_k |V_{k_\alpha}|^2 \delta(\epsilon - \varepsilon_{k\alpha})$, $\alpha = L, R$, which are assumed to be constants. The counting field χ has been introduced in the off-diagonal elements that correspond to tunnel processes which change the number of electrons collected in the right lead by one. The equation above is only valid, if the applied bias $\mu_L - \mu_R$ is much larger than any of the other above-mentioned energy scales [48].

Rather than calculating the current cumulants of the model using the Markovian description given by Eq. (4.61) (which was done in Ref. [162]), we trace out the off-diagonal elements in order to find an effective equation

of motion for the diagonal elements of the reduced density matrix. First, we note that the last two rows of $\mathcal{W}(\chi)$ constitute two coupled linear inhomogeneous differential equations reading

$$\frac{d}{dt}\begin{pmatrix}\mathrm{Re}[\rho_{10,01}]\\ \mathrm{Im}[\rho_{10,01}]\end{pmatrix} = \begin{pmatrix}-\Gamma & -\varepsilon\\ \varepsilon & -\Gamma\end{pmatrix}\begin{pmatrix}\mathrm{Re}[\rho_{10,01}]\\ \mathrm{Im}[\rho_{10,01}]\end{pmatrix} + \begin{pmatrix}0 & 0\\ -\Omega & \Omega\end{pmatrix}\begin{pmatrix}\rho_{10}\\ \rho_{01}\end{pmatrix}. \quad (4.62)$$

By an appropriate change of basis the two differential equations can be decoupled, and having solved the resulting equations, we may return to the original basis, thereby constructing the real and imaginary parts of the off-diagonal matrix element. Following this procedure we find for the imaginary part

$$\mathrm{Im}[\rho_{10,01}](t) = \frac{1}{2\Omega}\int_0^t dt' \Gamma_\Omega(t-t')[\rho_{01}(t') - \rho_{10}(t')], \quad (4.63)$$

where we have defined

$$\Gamma_\Omega(t) = 2\Omega^2 \mathrm{Re}\left[e^{i(\Delta\varepsilon + i\Gamma)t}\right]. \quad (4.64)$$

For the initial condition we have assumed $\mathrm{Im}[\rho_{10,01}](t=0) = 0$, which, however, does not play a role for the zero-frequency cumulants. We will not be needing the real part $\mathrm{Re}[\rho_{10,01}](t)$ in the following. Laplace transforming Eq. (4.63) we find

$$\mathrm{Im}[\rho_{10,01}](z) = \frac{1}{2\Omega}\Gamma_\Omega(z)[\rho_{01}(z) - \rho_{10}(z)], \quad (4.65)$$

where

$$\Gamma_\Omega(z) = \frac{2\Omega^2}{\Gamma + z} L[\varepsilon, 2(\Gamma + z)], \quad (4.66)$$

with $L[x,y] \equiv [1 + (2x/y)^2]^{-1}$. We note that $\Gamma_\Omega(z=0)$ corresponds to the Fermi's golden rule rate for incoherent tunneling found in Ref. [162].

Combining Eqs. (4.61) and (4.65) we find a Laplace transformed equation of motion for the vector $\tilde{\rho} = (\rho_{00}, \rho_{10}, \rho_{01}, \rho_{11})^T$, containing the four diagonal elements, of the form $z\tilde{\rho}_\chi(z) - \tilde{\rho}_\chi^{\mathrm{in}} = \mathcal{W}(\chi, z)\tilde{\rho}_\chi(z)$ with

$$\mathcal{W}(\chi, z) = \begin{pmatrix}-\Gamma_L & 0 & \Gamma_R e^{i\chi} & 0\\ \Gamma_L & -\Gamma_\Omega(z) & \Gamma_\Omega(z) & \Gamma_R e^{i\chi}\\ 0 & \Gamma_\Omega(z) & -[2\Gamma + \Gamma_\Omega(z)] & 0\\ 0 & 0 & \Gamma_L & -\Gamma_R\end{pmatrix}. \quad (4.67)$$

We see that the dynamics is now effectively non-Markovian, having traced out parts of the system. With the matrix $\mathcal{W}(\chi, z)$ at hand we may calculate the first three current cumulants using Eq. (4.59), and, in particular,

we can compare results with and without the non-Markovian contributions [corresponding to the full χ- and z-dependence of $\mathcal{W}(\chi, z)$ and $\mathcal{W}(\chi, z = 0)$, respectively].

In Fig. 4.6 we show calculations of the first three current cumulants as a function of the energy dealignment ε. We note that we obtain the same results when calculating the current cumulants using the expressions given in Eq. (4.47) applied to the model in its Markovian version as it is given in Eq. (4.61). With dashed lines we show the current cumulants obtained without the non-Markovian corrections. These results correspond to the current cumulants one obtains by taking the limit $z \to 0$ in Eq. (4.67) and applying the expressions given in Eq. (4.47). From the figure, the importance of the non-Markovian contributions to the second and third cumulants is obvious. In Ref. [162] it was stated that the higher order cumulants are sensitive to quantum coherence, which is also clear from the results presented here, since the non-Markovian dynamics resulted from tracing out the off-diagonal elements of the reduced density matrix. However, non-Markovian dynamics does not necessarily have to occur due to parts of a system with a clear quantum nature (like the off-diagonal elements in the example above) being traced out. In Paper **N** we considered a purely classical model of real-time electron counting with a finite-bandwidth detector coupled to the charge states of a quantum dot. By tracing out the charge states of the quantum dot, an effective two-state model with non-Markovian dynamics was obtained, and the second cumulant for this two-state model was shown to differ significantly compared to the corresponding result for a Markovian two-state system given in Eq. (4.30). Therefore, we generalize the statement concerning the effects of quantum coherence on the counting statistics from Ref. [162], and conclude that the higher order current cumulants are sensitive to non-Markovian effects, which may (or may not) be caused by quantum coherence within the system. This statement may be of relevance in connection with the measured noise enhancement in transport through double quantum dots reported in Ref. [165], and, in particular, the recent interpretation of these results given in Ref. [166], where it was stated that the measured noise is a direct indicator of quantum coherent coupling between the quantum dots.

It is worth noting that while the examples of non-Markovian systems considered here were obtained in a somewhat artificial way by tracing out a finite number of states of an otherwise Markovian system, it is not difficult to find systems, where only a non-Markovian description is feasible. One example is the dissipative spin-boson model studied in Refs. [147, 163], where the current noise spectrum of the charge transport through a double quantum dot coupled to a dissipative boson bath was evaluated. For such a system, it is typically not feasible (nor necessarily interesting) to keep track of the

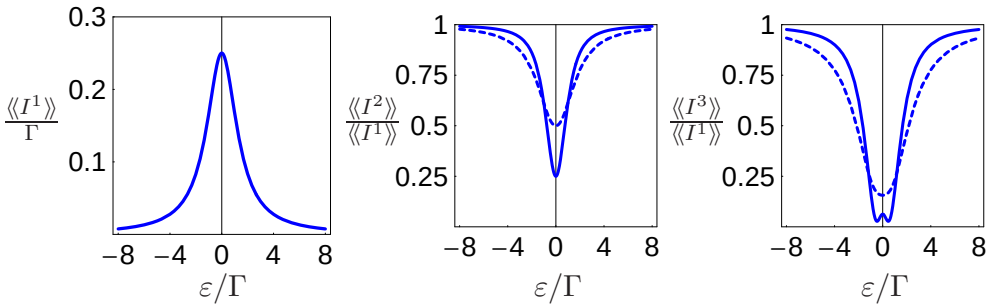

Figure 4.6: First three current cumulants of the transport through the double dot model. Here, without Coulomb interactions between the two quantum dots, such that double occupancy of the double dot is allowed. Full lines correspond to the full non-Markovian dynamics, while the dashed lines only include the Markovian contributions. The cumulants are shown as functions of the level dealignment $\varepsilon = \varepsilon_L - \varepsilon_R$, while other parameters are $\Gamma_L = \Gamma_R = \Gamma$ and $\Omega = 0.5\Gamma$.

infinitely many states associated with the heat bath, which is consequently traced out, leading to possible non-Markovian effects in the resulting dynamics. In Paper **Q** (not included) the zero-frequency noise of a very similar model was calculated using the approach for systems with non-Markovian systems described in this section.

We end this chapter by discussing a purely numerical approach to the calculation of the current cumulants given a non-Markovian rate equation. While it may be highly cumbersome to extend the analytic expressions in Eq. (4.59) beyond the first three cumulants, the recursive approach described below allows for relatively easy calculations of higher order cumulants. As starting point we take the formal expressions

$$\Lambda_0(z,x) = \langle\langle\tilde{0}|\overline{\mathcal{W}}(z,x)|0(z,x)\rangle\rangle \tag{4.68}$$

and

$$|0(x,z)\rangle\rangle = |0\rangle\rangle + \mathcal{R}[\Lambda_0(x,z) - \overline{\mathcal{W}}(x,z)]|0(x,z)\rangle\rangle, \tag{4.69}$$

which both follow easily using an approach similar to that described in Section 4.2. In order to simplify the notation we have used the substitution $i\chi \to x$. The eigenvalue $\Lambda_0(x,z)$, the right eigenvector $|0(x,z)\rangle\rangle$, and the

perturbation $\overline{\mathcal{W}}(x,z)$, are expanded in x and z, such that

$$\begin{aligned}\Lambda_0(x,z) &= \sum_{k=1,l=0}^{\infty} \frac{x^k}{k!}\frac{z^l}{l!} c^{(k,l)},\\ |0(x,z)\rangle\!\rangle &= \sum_{k=0,l=0}^{\infty} \frac{x^k}{k!}\frac{z^l}{l!} |0^{(k,l)}\rangle\!\rangle,\\ \overline{\mathcal{W}}(x,z) &= \sum_{k=1,l=0}^{\infty} \frac{x^k}{k!}\frac{z^l}{l!} \overline{\mathcal{W}}^{(k,l)}.\end{aligned} \tag{4.70}$$

Inserting these expansions into Eqs. (4.68) and (4.69) and collecting terms to same order in x and z, we find the following recursive expressions with $K = 1, 2, 3\ldots$, $L = 0, 1, 2\ldots$,

$$|0^{(K,L)}\rangle\!\rangle = \sum_{k=1}^{K}\binom{K}{k}\sum_{l=0}^{L}\binom{L}{l}\mathcal{R}\left[c^{(k,l)} - \overline{\mathcal{W}}^{(k,l)}\right]|0^{(K-k,L-l)}\rangle\!\rangle, \tag{4.71}$$

and

$$c^{(K,L)} = \sum_{k=1}^{K}\binom{K}{k}\sum_{l=0}^{L}\binom{L}{l}\langle\!\langle\tilde{0}|\overline{\mathcal{W}}^{(k,l)}|0^{(K-l,L-l)}\rangle\!\rangle, \tag{4.72}$$

where $\binom{N}{n} = N!/[n!(N-n)!]$. We note that $c^{(K,0)}$, $K = 1, 2, 3\ldots$, is the K'th current cumulant *without* the non-Markovian contributions.

Having determined the expansion coefficients $c^{(K,L)}$ in the expression for $\Lambda_0(z,x)$ in Eq. (4.70), we proceed with the solution of Eq. (4.57) by insertion of $z^*(x) = \sum_{n=1}^{\infty}\frac{x^n}{n!}c^{(n)}$, where $c^{(N)}$, $N = 1, 2, 3\ldots$, is the N'th current cumulant that we are seeking, yielding

$$\sum_{n=1}^{\infty}\frac{x^n}{n!}c^{(n)} = \sum_{k=1,l=0}^{\infty}\frac{x^k}{k!}\frac{1}{l!}\left[\sum_{n=1}^{\infty}\frac{x^n}{n!}c^{(n)}\right]^l c^{(k,l)}. \tag{4.73}$$

Collecting terms to order $N = 1, 2, 3, \ldots$ in x, we find the current cumulants

$$\langle\!\langle I^N\rangle\!\rangle = c^{(N)} = N!\sum_{k=1,l=0}^{N}\frac{1}{k!}\frac{1}{l!}P^{(N-k,l)}c^{(k,l)}, \tag{4.74}$$

with

$$P^{(K,L)} \equiv \left\{\sum_{n_1=1,\ldots,n_L=1}^{K}\frac{c^{(n_1)}}{n_1!}\cdots\frac{c^{(n_L)}}{n_L!}\right\}\Big|_{n_1+\ldots+n_L=K}, \tag{4.75}$$

where we have indicated that only terms in the sums for which $n_1+\ldots+n_L = K$ should be included. The $P^{(K,L)}$'s can be calculated recursively by noting that

$$P^{(K,L)} = \sum_{n=1}^{K} \frac{c^{(n)}}{n!} P^{(K-n,L-1)} \tag{4.76}$$

with $P^{(K,0)} = \delta_{K,0}$, $K = 1, 2, 3, \ldots$. Together with Eqs. (4.71) and (4.72), Eqs. (4.74) and (4.76) form a recursive scheme for numerical calculations of the current cumulants for a non-Markovian system. In order to apply the method it is necessary to implement the pseudo-inverse $\mathcal{R}$ and the expansion of the perturbation $\overline{\mathcal{W}}(z, x)$, as expressed in Eq. (4.70), must be known. In a numerical implementation it is worth exploiting the matrix product structure of Eqs. (4.74) and (4.76).

In order to illustrate the method we again consider the double dot model described above, however, now with strong Coulomb interaction between the two quantum dots, such that double occupation of the double dot is excluded. In that case, we only need to consider the three diagonal elements contained in the vector $\mathbf{P}(x,t) = [\rho_{00}(x,t), \rho_{LL}(x,t), \rho_{RR}(x,t)]^T$, whose equation of motion in Laplace space reads $\mathbf{P}(\chi, z) = [z - \mathbf{W}(\chi, z)]^{-1}\mathbf{P}(\chi, t = 0)$, where [compare with Eq. (4.67)]

$$\mathbf{W}(\chi, z) = \begin{pmatrix} -\Gamma_L & 0 & \Gamma_R e^{i\chi} \\ \Gamma_L & -\Gamma_\Omega(z) & \Gamma_\Omega(z) \\ 0 & \Gamma_\Omega(z) & -[\Gamma_\Omega(z) + \Gamma_R] \end{pmatrix}. \tag{4.77}$$

The function $\Gamma_\Omega(z)$ was defined in Eq. (4.66), however, here with $\Gamma = (\Gamma_L + \Gamma_R)/2$ replaced by $\Gamma_R/2$. The perturbation $\overline{\mathcal{W}}(x, z)$ can easily be expanded in z and x, enabling us to apply the recursive method described above. Numerical results for the first 16 cumulants are shown in Fig. 4.7. We have checked that the first three cumulants are identical to the results obtained using the expressions in Eq. (4.59), but we underline again that an extension of these expressions to higher orders would most likely be highly cumbersome, and the recursive approach presented here consequently provides a much more convenient method to the evaluation of higher order cumulants. The results presented in Fig. 4.7 serve only as an illustration of the method, and we shall here refrain from going into an analysis of the underlying physics.

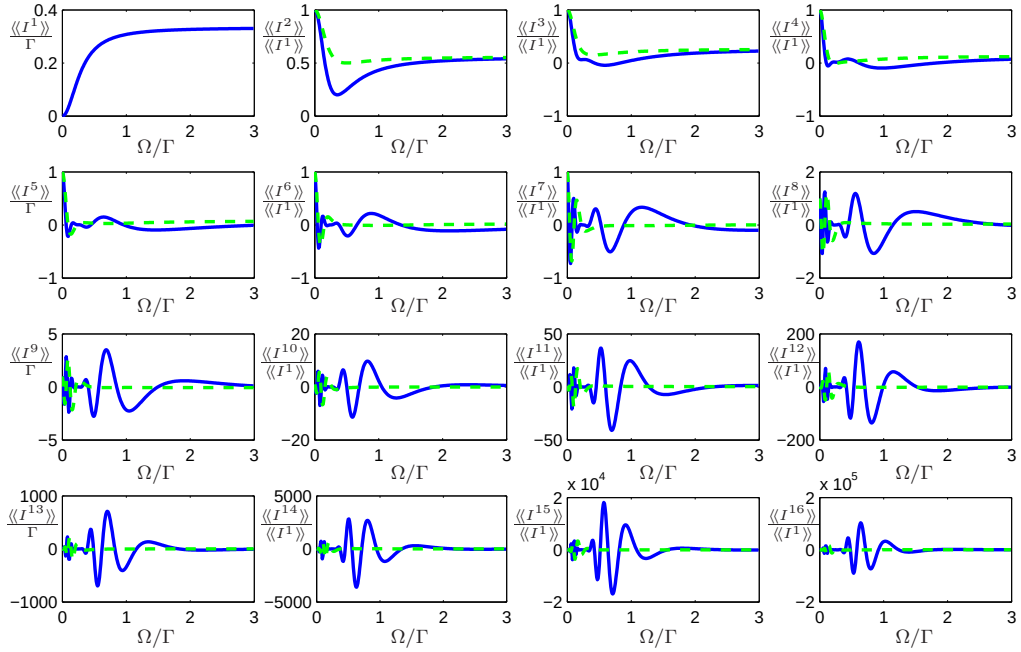

Figure 4.7: First 16 current cumulants of the transport through the double dot model. Here, with strong Coulomb interactions between the two quantum dots, such that double occupancy of the double dot is excluded. Full lines correspond to the full non-Markovian dynamics, while the dashed lines only include the Markovian contributions. The cumulants are shown as functions of the tunnel coupling Ω, while other parameters are $\Gamma_L = \Gamma_R = \Gamma$ and $\varepsilon = \varepsilon_L - \varepsilon_R = 0$.

Chapter 5

Summary

In this thesis we have considered various theoretical aspects of electrons in man-made nanostructures. The two focal points have been the coherent manipulation of electron spins in coupled quantum dots, aimed at future solid-state devices for large-scale quantum information processing, and full counting statistics, the stochastic theory of charge transport through nanoscale devices. The most important scientific contributions of the thesis have been (here neither in chronological order nor order of significance):

1. The proposal of a scalable method for trapping electrons in a solid-state structure based on designed defects in an otherwise periodic potential modulation of a two-dimensional electron gas (Papers **I** and **R**).

2. The numerical study of the exchange coupling between two electron spins in tunnel coupled quantum dots (Paper **O**). In the experimentally relevant regime, where the two electrons have a large wavepacket overlap, the results showed that a number of analytic approximations only have limited predictive powers.

3. The proposal to use the strong spin-orbit coupling in InAs nanowires as a general means to manipulate the spins of electrons in gate-defined quantum dots (Paper **J** and **K**). The proposal included ideas for single spin rotations as well as a two-spin coupling mechanism.

4. The proposal for an opto-electronic device that would enable electrically controlled generation of single photons which are frequency-entangled with the spin states of two electrons trapped in the device (Paper **M**). The photons can be used to generate entanglement between the spin states of electrons in remote devices with high fidelity.

5. The development of a general theory and method for the calculation of the current cumulants for transport systems described by Markovian (generalized) master (or rate) equations (Paper **D**). The method was extended to include also the finite-frequency noise of such systems (Paper **G**).

6. The study of current fluctuations in quantum electromechanical systems (Papers **D**, **G**, and **F**). The first three current cumulants were used to detect mechanical bistabilities occurring in two systems, while the finite-frequency noise was used to detect frequency shifts and internal energy scales.

7. The extension of the method for calculating current cumulants to the non-Markovian case. Analytic expressions were derived for the first three current cumulants, while a recursive method was developed for the calculation of higher order cumulants. The results showed that it may be difficult to distinguish between signatures in the counting statistics arising due to quantum coherence and classical, non-Markovian effects, respectively (Paper **N**).

These contributions were described in Chapters 2, 3, and 4 of this thesis, and in Papers **D**, **F**, **G**, **I**, **J**, **K**, **M**, **N**, **O**, and **R**, which are included. Below, we give a short summary of the thesis.

In Chapter 2 we briefly introduced a number of different types of quantum dots and discussed the important concept of Coulomb blockade which is essential in order to understand the charging dynamics of quantum dots. We next introduced a class of transport systems which combine electronic and mechanical degrees of freedom at the nano-scale, namely nanoelectromechanical systems, or NEMS. In particular, we considered two models of so-called charge shuttles, whose mechanical degrees of freedom were assumed quantized. Finally, we discussed our proposal for trapping electrons at designed defects in an otherwise periodic potential modulation of a two-dimensional electron gas.

In Chapter 3 we focused on the spins of electrons in coupled quantum dots, which are relevant in the context of future solid-state devices for quantum information processing. We first gave a brief introduction to quantum computing, providing the necessary background needed to understand the following sections and the included papers. We then focused on a certain spin-spin interaction, the so-called exchange interaction, discussed its origin and various approaches to the calculation of the coupling strength. Our numerical results showed that a number of analytic approximations only have limited predictive powers in the experimentally relevant regime, where the

two-electron system has a large wavepacket overlap. In the following section we discussed our proposal for using the strong spin-orbit coupling in, e.g., InAs nanowires as a general means to manipulate spins in gate-defined quantum dots. We described a scheme for carrying out single-spin rotations and found an effective spin-orbit induced spin-spin coupling. Finally, we discussed our proposal for an opto-electronic device that would allow for electrically controlled generation of single photons that are frequency-entangled with the spin states of two electrons in the device. We discussed a protocol for high-fidelity entanglement generation between electron spins in remote devices based on two-photon interference at a beam splitter.

In Chapter 4 we introduced the theory of full counting statistics within the framework of rate equations. We first considered a number of simple examples in order to gain an intuitive understanding of various aspects of the theory. In particular, we considered a simple, well-studied Markovian two-state model, which we, in a fairly unconventional manner, transformed into a non-Markovian problem for which we showed how a number of well-known results can be obtained, however, within the non-Markovian formulation. The following section was concerned with the development of a general approach to the calculation of the cumulants of the current through systems described by Markovian rate equations of arbitrary dimensions. The methods were applied to the charge shuttle systems introduced in Chapter 2, and it was shown how the first three current cumulants can be used to detect mechanical bistabilities in these systems. The finite-frequency noise of the systems was used to detect frequency shifts of the mechanical oscillations and internal energy scales of the systems. The last section dealt with the inclusion of non-Markovian effects in the calculations of current cumulants. The analytic results obtained in the previous section were extended with non-Markovian contributions, and a novel, purely numerical recursive approach was developed and shown to allow for calculations of current cumulants of higher order than the first few ones. It was shown that it may be non-trivial to distinguish between signatures in the counting statistics arising due to quantum coherence and non-Markovian, classical dynamics, respectively.

5.1 Outlook

Projects of a limited duration are bound to leave a number of questions unanswered and ideas untouched. This is also the case for the work described in this thesis, which to some extent should be considered more as a status report on the different projects at the time of writing rather than a finalized piece of work. We thus conclude the thesis by listing a series of possible

future directions and questions to be addressed.

In our proposal for the use of antidot lattices as a scalable spin qubit platform both spin and charge degrees of freedom were considered to be completely coherent and only the effects of static lattice disordered were briefly touched upon. It would be interesting to study the effects of the environment, e.g., on electron transport via the resonant coupling mechanism. This could in practice be implemented by combining the numerical wavepacket propagations with stochastic quantum jumps that account for fluctuations and dissipation due to the surrounding environment. This approach to non-unitary time evolution is described in Refs. [167] and [168].

While we only studied the exchange coupling between electron spins in two-dimensional double quantum dots, it might be possible also to include the effects of spin-orbit coupling in the numerical calculations. This would allow for numerical studies of the spin-orbit induced spin-spin coupling in closely situated, two-dimensional quantum dots, which could be compared with the analytic results reported in Ref. [121]. Further comparative studies of the spin-orbit induced spin-spin coupling and the exchange coupling for closely situated quantum dots would also be interesting, since both couplings increase in magnitude at shorter distances, making that regime most relevant for experiments. Further theoretical modeling of an actual experiment on spin manipulation using the spin-orbit coupling in a nanowire would of course be highly interesting.

The proposal for an opto-electrical device for spin-photon entanglement generation was based on a relatively simple modeling of the proposed device, and it would be obvious to invoke more sophisticated methods that would allow for more detailed modeling and design and material optimization. First principles calculations could for example provide precise band structures of the nanowire diode, which, among other things, would be necessary in order to understand its optical properties in detail. A different question concerns the coupling of electron spins in optically active quantum dots, as those considered in relation to the nanowire diode, and electron spins in gate-defined quantum dots, which were used in the experiments on coherent spin manipulation that we described. Proposals for coupling between electrons in these two types of quantum dots already exist (see Ref. [169]), but further extensions of these ideas could be interesting. Again, a collaboration with experimentalists on the fabrication and testing of an actual device would be highly interesting.

While we, except for the finite-frequency noise, only studied zero-frequency current cumulants, it would be relevant to seek an extension of the analytic results, both in the Markovian and the non-Markovian case, to finite frequencies. Finite-frequency cumulants in the Markovian case have recently

been studied in Ref. [170] and it might be possible to express some of the results reported there in a general superoperator notation. Also, the extension to non-Markovian dynamics would be of high relevance. Concerning non-Markovian systems, we have so far only studied a few, relatively simple systems, and it would be obvious to study more complicated models, where the memory effects would be clearly outspelled. One evident candidate would be the dissipative spin-boson model studied in Refs. [147, 163]. Concerning the finite-frequency noise, it is worth noting that also unsymmetrized noise (in contrast to the symmetrized current-current correlators studied in this thesis) can be measured in experiments, revealing energy quanta being transferred between the measurement apparatus and the measured system [171, 172]. Could one somehow consider similarly unsymmetrized current cumulants of higher order?

On a more general level, the question concerning the information contained in the higher order cumulants also deserves further investigation. We have seen how bistabilities can be detected in the first three cumulants, but it would be desirable to have a more clear picture of the information which is available in the higher order cumulants. This would surely lead to an increased experimental interest in the field of full counting statistics. It has been suggested that the full counting statistics can be useful for characterizing entanglement between electrons [173, 174], which would provide an interesting link to the field of quantum information processing. Finally, the approach to full counting statistics presented in this thesis, based on rate equations, makes the developed methods applicable well outside the field of nanophysics. Rate equations similar to the ones studied have, for example, found use within the fields of medicine [175], cell physiology [176], and network traffic [177]. Could the results presented in this thesis find use in similar fields outside physics?

Bibliography

[1] L. P. Kouwenhoven, D. G. Austing, and S. Tarucha, 'Few-electron quantum dots', Rep. Prog. Phys. **64**, 701 (2001).

[2] W. van der Wiel, S. de Franceschi, J. Elzerman, T. Fujisawa, S. Tarucha, and L. Kouwenhoven, 'Electron transport through double quantum dots', Rev. Mod. Phys. **75**, 1 (2003).

[3] R. Hanson, L. Kouwenhoven, J. Petta, S. Tarucha, and L. Vandersypen, 'Spins in few-electron quantum dots', Rev. Mod. Phys. **79**, 1217 (2007).

[4] Y. Ono, A. Fujiwara, K. Nishiguchi, H. Inokawa, and Y. Takahashi, 'Manipulation and detection of single electrons for future information processing', J. Appl. Phys. **97**, 031101 (2005).

[5] L. L. Sohn, L. P. Kouwenhoven, and G. Schön, editors, *Mesoscopic Electron Transport* (Kluwer Academic Publishers, 1996).

[6] J. R. Petta, A. C. Johnson, J. M. Taylor, E. A. Laird, A. Yacoby, M. D. Lukin, C. M. Marcus, M. P. Hanson, and A. C. Gossard, 'Coherent manipulation of coupled electron spins in semiconductor quantum dots', Science **309**, 2180 (2005).

[7] F. H. L. Koppens, J. A. Folk, J. M. Elzerman, R. Hanson, L. H. W. van Beveren, I. T. Vink, H. P. Tranitz, W. Wegscheider, L. P. Kouwenhoven, and L. M. K. Vandersypen, 'Control and detection of singlet-triplet mixing in a random nuclear field', Science **309**, 1346 (2005).

[8] T. Hatano, M. Stopa, and S. Tarucha, 'Single-electron delocalization in hybrid vertical-lateral double quantum dots', Science **309**, 268 (2005).

[9] M. T. Björk, A. Fuhrer, A. E. Hansen, M. W. Larsson, L. E. Fröberg, and L. Samuelson, 'Tunable effective g factor in InAs nanowire quantum dots', Phys. Rev. B **72**, 201307 (2005).

[10] C. Fasth, A. Fuhrer, M. T. Björk, and L. Samuelson, 'Tunable double quantum dots in InAs nanowires defined by local gate electrodes', Nano Lett. **5**, 1487 (2005).

[11] A. E. Hansen, M. T. Björk, C. Fasth, C. Thelander, and L. Samuelson, 'Spin relaxation in InAs nanowires studied by tunable weak antilocalization', Phys. Rev. B **71**, 205328 (2005).

[12] I. Shorubalko, A. Pfund, R. Leturcq, M. T. Borgström, F. Gramm, E. Möller, E. Gini, and K. Ensslin, 'Tunable few-electron quantum dots in InAs nanowires', Nanotech. **18**, 44014 (2007).

[13] S. Sapmaz, C. Meyer, P. Beliczynski, P. Jarillo-Herrero, and L. P. Kouwenhoven, 'Excited state spectroscopy in carbon nanotube double quantum dots', Nano Lett. **6**, 1350 (2006).

[14] H. I. Jørgensen, K. Grove-Rasmussen, J. R. Hauptmann, and P. E. Lindelof, 'Single wall carbon nanotube double quantum dot', Appl. Phys. Lett. **89**, 232113 (2006).

[15] P. M. Petroff, A. Lorke, and A. Imamoglu, 'Epitaxially self-assembled quantum dots', Phys. Today **54**, 46 (2001).

[16] M. Kroutvar, Y. Ducommun, D. Heiss, M. Bichler, D. Schuh, G. Abstreiter, and J. J. Finley, 'Optically programmable electron spin memory using semiconductor quantum dots', Nature **432**, 81 (2004).

[17] M. Atatüre, J. Dreiser, A. Badolato, A. Högele, K. Karrai, and A. Imamoglu, 'Quantum-dot spin-state preparation with near-unity fidelity', Science **312**, 551 (2006).

[18] E. A. Stinaff, M. Scheibner, A. S. Bracker, I. V. Ponomarev, V. L. Korenev, M. E. Ware, M. F. Doty, T. L. Reinecke, and D. Gammon, 'Optical signatures of coupled quantum dots', Science **311**, 636 (2006).

[19] J. Berezovsky, M. H. Mikkelsen, O. Gywat, N. G. Stoltz, L. A. Coldren, and D. D. Awschalom, 'Nondestructive optical measurements of a single electron spin in a quantum dot', Science **314**, 1916 (2006).

[20] E. D. Minot, F. Kelkensberg, M. van Kouwen, J. A. van Dam, L. P. Kouwenhoven, V. Zwiller, M. T. Borgström, O. Wunnicke, M. A. Verheijen, and E. P. A. M. Bakkers, 'Single quantum dot nanowire LEDs', Nano Lett. **7**, 367 (2007).

[21] H. Bruus and K. Flensberg, *Many-Body Quantum Theory in Condensed Matter Physics, An Introduction* (Oxford University Press, 2004).

[22] T. Fujisawa, T. Hayashi, R. Tomita, and Y. Hirayama, 'Bidirectional counting of single electrons', Science **312**, 1634 (2006).

[23] A. Naik, O. Buu, M. D. LaHaye, A. D. Armour, A. A. Clerk, M. P. Blencowe, and K. C. Schwab, 'Cooling a nanomechanical resonator with quantum back-action', Nature **443**, 193 (2006).

[24] H. Park, J. Park, A. K. L. Lim, E. H. Anderson, A. P. Alivisatos, and P. L. McEuen, 'Nanomechanical oscillations in a single-C_{60} transistor', Nature **407**, 57 (2000).

[25] M. Blencowe, 'Quantum electromechanical systems', Phys. Rep. **395**, 159 (2004).

[26] L. Y. Gorelik, A. Isacsson, M. V. Voinova, B. Kasemo, R. I. Shekhter, and M. Jonson, 'Shuttle Mechanism for Charge Transfer in Coulomb Blockade Nanostructures', Phys. Rev. Lett. **80**, 4526 (1998).

[27] A. Erbe, C. Weiss, W. Zwerger, and R. H. Blick, 'Nanomechanical Resonator Shuttling Single Electrons at Radio Frequencies', Phys. Rev. Lett. **87**, 096106 (2001).

[28] D. V. Scheible and R. H. Blick, 'Silicon nanopillars for mechanical single-electron transport', Appl. Phys. Lett. **84**, 4632 (2004).

[29] D. Fedorets, L. Y. Gorelik, R. I. Shekhter, and M. Jonson, 'Spintronics of a Nanoelectromechanical Shuttle', Phys. Rev. Lett. **95**, 057203 (2005).

[30] L. Y. Gorelik, S. I. Kulinich, R. I. Shekhter, M. Jonson, and V. M. Vinokur, 'Mechanically assisted spin-dependent transport of electrons', Phys. Rev. B **71**, 035327 (2005).

[31] L. Y. Gorelik, D. Fedorets, R. I. Shekhter, and M. Jonson, 'Spin-controlled nanoelectromechanics in magnetic NEM-SET systems', New J. Phys. **7**, 242 (2005).

[32] N. Nishiguchi, 'Shot-Noise-Induced Random Telegraph Noise in Shuttle Current', Phys. Rev. Lett. **89**, 066802 (2002).

[33] A. Isacsson and T. Nord, 'Low-frequency current noise of the single-electron shuttle', Europhys. Lett. **66**, 708 (2004).

[34] F. Pistolesi, 'Full counting statistics of a charge shuttle', Phys. Rev. B **69**, 245409 (2004).

[35] F. Pistolesi and R. Fazio, 'Dynamics and current fluctuations in an ac-driven charge shuttle', New J. Phys. **8**, 113 (2006).

[36] L. Y. Gorelik, A. Isacsson, Y. M. Galperin, R. I. Shekhter, and M. Jonson, 'Coherent transfer of Cooper pairs by a movable grain', Nature **411**, 454 (2001).

[37] A. Romito, F. Plastina, and R. Fazio, 'Decoherence in a Cooper pair shuttle', Phys. Rev. B **68**, 140502 (2003).

[38] A. Romito and Yu. V. Nazarov, 'Full counting statistics of Cooper pair shuttling', Phys. Rev. B **70**, 212509 (2004).

[39] C. Huldt and J. M. Kinaret, 'Multiscale modelling of a nanoelectromechanical shuttle', New J. Phys. **9**, 51 (2007).

[40] M. N. Kiselev, K. Kikoin, R. I. Shekhter, and V. M. Vinokur, 'Kondo shuttling in a nanoelectromechanical single-electron transistor', Phys. Rev. B **74**, 233403 (2006).

[41] M. D. LaHaye, O. Buu, B. Camarota, and K. C. Schwab, 'Approaching the Quantum Limit of a Nanomechanical Resonator', Science **304**, 74 (2004).

[42] A. D. Armour and A. MacKinnon, 'Transport via a quantum shuttle', Phys. Rev. B **66**, 035333 (2002).

[43] T. Novotný, A. Donarini, and A.-P. Jauho, 'Quantum Shuttle in Phase Space', Phys. Rev. Lett. **90**, 256801 (2003).

[44] D. Fedorets, 'Quantum description of shuttle instability in a nanoelectromechanical single-electron transistor', Phys. Rev. B **68**, 033106 (2003).

[45] D. Fedorets, L. Y. Gorelik, R. I. Shekhter, and M. Jonson, 'Quantum Shuttle Phenomena in a Nanoelectromechanical Single-Electron Transistor', Phys. Rev. Lett. **92**, 166801 (2004).

[46] A. Donarini and A.-P. Jauho, 'Shuttle instabilities: semiclassical phase analysis', Physica E **22**, 721 (2004).

[47] H. Haug and A.-P. Jauho, *Quantum Kinetics in Transport and Optics of Semi-conductors* (Springer-Verlag, 1998).

[48] S. A. Gurvitz and Ya. S. Prager, 'Microscopic derivation of rate equations for quantum transport', Phys. Rev. B **53**, 15932 (1996).

[49] A. Donarini, *Dynamics of Shuttle Devices*, Ph.D. thesis, Technical University of Denmark (2004).

[50] Sh. Kogan, *Electronic Noise and Fluctuations in Solids* (Cambridge University Press, 1996).

[51] E. Yablonovitch, 'Inhibited Spontaneous Emission in Solid-State Physics and Electronics', Phys. Rev. Lett. **58**, 2059 (1987).

[52] S. John, 'Strong Localization of Photons in Certain Disordered Dielectric Superlattices', Phys. Rev. Lett. **58**, 2486 (1987).

[53] J. C. Knight, T. A. Birks, P. S. Russell, and D. M. Atkin, 'All-silica single-mode optical fiber with photonic crystal cladding', Opt. Lett. **21**, 1547 (1996).

[54] K. Ensslin and P. M. Petroff, 'Magnetotransport Through an Antidot Lattice in GaAs-$Al_xGa_{1-x}As$ Heterostructures', Phys. Rev. B **41**, 12307 (1990).

[55] D. Weiss, K. Richter, A. Menschig, R. Bergmann, H. Schweizer, K. von Klitzing, and G. Weimann, 'Quantized Periodic-Orbits in Large Antidot Arrays', Phys. Rev. Lett. **70**, 4118 (1993).

[56] R. Schuster, K. Ensslin, D. Wharam, S. Kuhn, J. P. Kotthaus, G. Bohm, W. Klein, G. Trankle, and G. Weimann, 'Phase-coherent electrons in a finite antidot lattice', Phys. Rev. B **49**, 8510 (1994).

[57] A. Dorn, T. Ihn, K. Ensslin, W. Wegscheider, and M. Bichler, 'Electronic transport through a quantum dot network', Phys. Rev. B **70**, 205306 (2004).

[58] A. Dorn, E. Bieri, T. Ihn, K. Ensslin, D. D. Driscoll, and A. C. Gossard, 'Interplay between the periodic potential modulation and random background scatterers in an antidot lattice', Phys. Rev. B **71**, 035343 (2005).

[59] J. Pedersen, *Modelling Nanoscale Devices for Coherent Spin Manipulation*, Master's thesis, Technical University of Denmark (2007).

[60] J. Gorman, D. Hasko, and D. Williams, 'Charge-Qubit Operation of an Isolated Double Quantum Dot', Phys. Rev. Lett. **95**, 90502 (2005).

[61] G. M. Nikolopoulos, D. Petrosyan, and P. Lambropoulos, 'Coherent electron wavepacket propagation and entanglement in array of coupled quantum dots', Europhys. Lett. **65**, 297 (2004).

[62] G. M. Nikolopoulos, D. Petrosyan, and P. Lambropoulos, 'Electron wavepacket propagation in a chain of coupled quantum dots', J. Phys. C **16**, 4991 (2004).

[63] M. Skorobogatiy, K. Saitoh, and M. Koshiba, 'Transverse light guides in microstructured optical fibers', Opt. Lett. **31**, 314 (2006).

[64] M. Skorobogatiy, K. Saitoh, and M. Koshiba, 'Transverse lightwave circuits in microstructured optical fibers: resonator arrays', Opt. Express **14**, 1439 (2006).

[65] K. S. Novoselov, A. K. Geim, S. V. Morozov, D. Jiang, Y. Zhang, S. V. Dubonos, I. V. Grigorieva, and A. A. Firsov, 'Electric field effect in atomically thin carbon films', Science **306**, 666 (2004).

[66] K. S. Novoselov, A. K. Geim, S. V. Morozov, D. Jiang, M. I. Katsnelson, I. V. Grigorieva, S. V. Dubonos, and A. A. Firsov, 'Two-dimensional gas of massless Dirac fermions in graphene', Nature **438**, 197 (2005).

[67] Y. B. Zhang, Y. W. Tan, H. L. Stormer, and P. Kim, 'Experimental observation of the quantum Hall effect and Berry's phase in graphene', Nature **438**, 201 (2005).

[68] B. Trauzettel, D. V. Bulaev, D. Loss, and G. Burkard, 'Spin qubits in graphene quantum dots', Nat. Phys. **3**, 192 (2007).

[69] R. P. Feynman, 'Simulating Physics with Computers', Int. J. Theo. Phys. **21**, 467 (1982).

[70] R. P. Feynman, 'Quantum-Mechanical Computers', Found. Phys. **16**, 507 (1986).

[71] D. Deutsch, 'Quantum-Theory, the Church-Turing Principle and the Universal Quantum Computer', Proc. Roy. Soc. Lon. Ser. A **400**, 97 (1985).

[72] P. W. Shor, 'Polynomial-time algorithms for prime factorization and discrete logarithms on a quantum computer', Siam J. Comp. **26**, 1484 (1997).

[73] L. K. Grover, 'Quantum Mechanics Helps in Searching for a Needle in a Haystack', Phys. Rev. Lett. **79**, 325 (1997).

[74] D. P. DiVincenzo, 'The physical implementation of quantum computation', Prog. Phys. **48**, 771 (2000).

[75] D. P. DiVincenzo, '2-Bit Gates are Universal for Quantum Computation', Phys. Rev. A **51**, 1015 (1995).

[76] J. I. Cirac and P. Zoller, 'Quantum Computations with Cold Trapped Ions', Phys. Rev. Lett. **74**, 4091 (1995).

[77] A. S. Sørensen and K. Mølmer, 'Quantum Computation with Ions in Thermal Motion', Phys. Rev. Lett. **82**, 1971 (1999).

[78] N. A. Gershenfeld and I. L. Chuang, 'Bulk spin-resonance quantum computation', Science **275**, 350 (1997).

[79] I. L. Chuang, L. M. K. Vandersypen, X. L. Zhou, D. W. Leung, and S. Lloyd, 'Experimental realization of a quantum algorithm', Nature **393**, 143 (1998).

[80] L. M. K. Vandersypen, M. Steffen, G. Breyta, C. S. Yannoni, M. H. Sherwood, and I. L. Chuang, 'Experimental realization of Shor's quantum factoring algorithm using nuclear magnetic resonance', Nature **414**, 883 (2001).

[81] B. E. Kane, 'A silicon-based nuclear spin quantum computer', Nature **393**, 133 (1998).

[82] A. Shnirman, G. Schön, and Z. Hermon, 'Quantum Manipulations of Small Josephson Junctions', Phys. Rev. Lett. **79**, 2371 (1997).

[83] J. E. Mooij, T. P. Orlando, L. Levitov, L. Tian, C. H. van der Wal, and S. Lloyd, 'Josephson persistent-current qubit', Science **285**, 1036 (1999).

[84] L. Childress, M. V. G. Dutt, J. M. Taylor, A. S. Zibrov, F. Jelezko, J. Wrachtrup, P. R. Hemmer, and M. D. Lukin, 'Coherent dynamics of coupled electron and nuclear spin qubits in diamond', Science **314**, 281 (2006).

[85] M. V. G. Dutt, L. Childress, L. Jiang, E. Togan, J. Maze, F. Jelezko, A. S. Zibrov, P. R. Hemmer, and M. D. Lukin, 'Quantum register based on individual electronic and nuclear spin qubits in diamond', Science **316**, 1312 (2007).

[86] D. Loss and D. P. DiVincenzo, 'Quantum computation with quantum dots', Phys. Rev. A **57**, 120 (1998).

[87] G. Burkard, D. Loss, and D. P. DiVincenzo, 'Coupled quantum dots as quantum gates', Phys. Rev. B **59**, 2070 (1999).

[88] F. H. L. Koppens, C. Buizert, K. J. Tielrooij, I. T. Vink, K. C. Nowack, T. Meunier, L. P. Kouwenhoven, and L. M. K. Vandersypen, 'Driven coherent oscillations of a single electron spin in a quantum dot', Nature **442**, 766 (2006).

[89] J. M. Elzerman, R. Hanson, L. H. W. van Beveren, B. Witkamp, L. M. K. Vandersypen, and L. P. Kouwenhoven, 'Single-shot read-out of an individual electron spin in a quantum dot', Nature **430**, 431 (2004).

[90] J. M. Taylor, H.-A. Engel, W. Dür, A. Yacoby, C. M. Marcus, P. Zoller, and M. D. Lukin, 'Fault-tolerant architecture for quantum computation using electrically controlled semiconductor spins', Nat. Phys. **1**, 177 (2005).

[91] A. K. Ekert, 'Quantum Cryptography Based on Bell Theorem', Phys. Rev. Lett. **67**, 661 (1991).

[92] N. Gisin, G. G. Ribordy, W. Tittel, and H. Zbinden, 'Quantum cryptography', Rev. Mod. Phys. **74**, 145 (2002).

[93] N. W. Ashcroft and N. D. Mermin, *Solid State Physics* (Holt, Rinehart and Winston, 1976).

[94] W. Heitler and F. London, 'Reciprocal action of neutral atoms and homopolar combination according to quantum mechanics', Z. Phys. **44**, 455 (1927).

[95] X. Hu and S. Das Sarma, 'Charge Fluctuation Induced Dephasing of Exchange Coupled Spin Qubits', Phys. Rev. Lett. **96**, 100501 (2006).

[96] E. Lieb and D. Mattis, 'Theory of Ferromagnetism and Ordering of Electronic Energy Levels', Phys. Rev. **125**, 164 (1962).

[97] M. J. Calderon, B. Koiller, and S. Das Sarma, 'Exchange coupling in semiconductor nanostructures: Validity and limitations of the Heitler-London approach', Phys. Rev. B **74**, 45310 (2006).

[98] D. V. Melnikov and J. P. Leburton, 'Single-particle state mixing in two-electron double quantum dots', Phys. Rev. B **73**, 155301 (2006).

[99] A. L. Saraiva, M. J. Calderon, and B. Koiller, 'Heitler-London treatment for exchange gates in semiconductor double-dot quantum computer architectures', arXiv:0706.3354 (2007).

[100] B. Szafran, F. M. Peeters, and S. Bednarek, 'Exchange energy tuned by asymmetry in artificial molecules', Phys. Rev. B **70**, 205318 (2004).

[101] M. Helle, A. Harju, and R. M. Nieminen, 'Two-electron lateral quantum-dot molecules in a magnetic field', Phys. Rev. B **72**, 205329 (2005).

[102] D. V. Melnikov, J. P. Leburton, A. Taha, and N. Sobh, 'Coulomb localization and exchange modulation in two-electron coupled quantum dots', Phys. Rev. B **74**, 41309 (2006).

[103] L. X. Zhang, D. V. Melnikov, and J. P. Leburton, 'Exchange interaction and stability diagram of coupled quantum dots in magnetic fields', Phys. Rev. B **74**, 205306 (2006).

[104] L. X. Zhang, D. V. Melnikov, and J. P. Leburton, 'Engineering exchange coupling in double elliptic quantum dots', IEEE Trans. Nanotech. **6**, 250 (2007).

[105] M. Helle, *Few-electron quantum dot molecules*, Ph.D. thesis, Helsinki University of Technology (2006).

[106] D. Stepanenko, N. E. Bonesteel, D. P. DiVincenzo, G. Burkard, and D. Loss, 'Spin-orbit coupling and time-reversal symmetry in quantum gates', Phys. Rev. B **68** (2003).

[107] D. Stepanenko and N. E. Bonesteel, 'Universal Quantum Computation through Control of Spin-Orbit Coupling', Phys. Rev. Lett. **93** (2004).

[108] S. Debald and C. Emary, 'Spin-Orbit-Driven Coherent Oscillations in a Few-Electron Quantum Dot', Phys. Rev. Lett. **94** (2005).

[109] A. V. Khaetskii and Yu. V. Nazarov, 'Spin relaxation in semiconductor quantum dots', Phys. Rev. B **61**, 12639 (2000).

[110] A. V. Khaetskii and Yu. V. Nazarov, 'Spin-flip transitions between Zeeman sublevels in semiconductor quantum dots', Phys. Rev. B **64**, 125316 (2001).

[111] Yu. A. Bychkov and E. I. Rashba, 'Properties of a 2d Electron-Gas with Lifted Spectral Degeneracy', JETP Lett. **39**, 78 (1984).

[112] Yu. A. Bychkov and E. I. Rashba, 'Oscillatory Effects and the Magnetic-Susceptibility of Carriers in Inversion-Layers', J. Phys. C **17**, 6039 (1984).

[113] G. Dresselhaus, 'Spin-Orbit Coupling Effects in Zinc Blende Structures', Phys. Rev. **100**, 580 (1955).

[114] C. Fasth, A. Fuhrer, L. Samuelson, V. N. Golovach, and D. Loss, 'Direct Measurement of the Spin-Orbit Interaction in a Two-Electron InAs Nanowire Quantum Dot', Phys. Rev. Lett. **98**, 266801 (2007).

[115] D. Grundler, 'Large Rashba Splitting in InAs Quantum Wells due to Electron Wave Function Penetration into the Barrier Layers', Phys. Rev. Lett. **84**, 6074 (2000).

[116] T. Koga, J. Nitta, T. Akazaki, and H. Takayanagi, 'Rashba Spin-Orbit Coupling Probed by the Weak Antilocalization Analysis in InAlAs/InGaAs/InAlAs Quantum Wells as a Function of Quantum Well Asymmetry', Phys. Rev. Lett. **89**, 046801 (2002).

[117] L. E. Ballentine, *Quantum Mechanics – A Modern Development* (World Scientific, 1998).

[118] E. I. Rashba and A. L. Efros, 'Orbital Mechanisms of Electron-Spin Manipulation by an Electric Field', Phys. Rev. Lett. **91**, 126405 (2003).

[119] V. N. Golovach, M. Borhani, and D. Loss, 'Electric-dipole-induced spin resonance in quantum dots', Phys. Rev. B **74**, 165319 (2006).

[120] K. C. Nowack, F. H. L. Koppens, Yu. V. Nazarov, and L. M. K. Vandersypen, 'Coherent control of a single spin with electric fields', arXiv:0707.3080 (2007).

[121] M. Trif, V. N. Golovach, and D. Loss, 'Spin-spin coupling in electrostatically coupled quantum dots', Phys. Rev. B **75**, 085307 (2007).

[122] J. Levy, 'Universal Quantum Computation with Spin-1/2 Pairs and Heisenberg Exchange', Phys. Rev. Lett. **89**, 147902 (2002).

[123] I. Zutic, J. Fabian, and S. Das Sarma, 'Spintronics: Fundamentals and applications', Rev. Mod. Phys. **76**, 323 (2004).

[124] M. O. Scully and M. S. Zubairy, *Quantum Optics* (Cambridge University Press, 1996).

[125] L. M. Duan, M. D. Lukin, J. I. Cirac, and P. Zoller, 'Long-distance quantum communication with atomic ensembles and linear optics', Nature **414**, 413 (2001).

[126] R. Loudon, *The Quantum Theory of Light* (Oxford University Press, 1994).

[127] H. J. Briegel, W. Dür, J. I. Cirac, and P. Zoller, 'Quantum Repeaters: The Role of Imperfect Local Operations in Quantum Communication', Phys. Rev. Lett. **81**, 5932 (1998).

[128] W. Dür, H. J. Briegel, J. I. Cirac, and P. Zoller, 'Quantum repeaters based on entanglement purification', Phys. Rev. A **59**, 169 (1999).

[129] Ya. M. Blanter and M. Büttiker, 'Shot noise in mesoscopic conductors', Phys. Rep. **336**, 1 (2000).

[130] Ya. M. Blanter, 'Recent Advances in Studies of Current Noise', arXiv:cond-mat/0511478 (2005).

[131] Yu. V. Nazarov, editor, *Quantum Noise in Mesoscopic Physics* (Kluwer, Dordrecht, 2003).

[132] S. Gustavsson, R. Leturcq, B. Simovic, R. Schleser, T. Ihn, P. Studerus, K. Ensslin, D. C. Driscoll, and A. C. Gossard, 'Counting Statistics of Single-Electron Transport in a Quantum Dot', Phys. Rev. Lett. **96**, 076605 (2006).

[133] S. Gustavsson, R. Leturcq, B. Simovic, R. Schleser, P. Studerus, T. Ihn, K. Ensslin, D. C. Driscoll, and A. C. Gossard, 'Counting statistics and super-Poissonian noise in a quantum dot: Time-resolved measurements of electron transport', Phys. Rev. B **74**, 195305 (2006).

[134] S. Gustavsson, R. Leturcq, T. Ihn, K. Ensslin, M. Reinwald, and W. Wegscheider, 'Measurements of higher-order noise correlations in a quantum dot with a finite bandwidth detector', Phys. Rev. B **75**, 75314 (2007).

[135] C. Fricke, F. Hohls, W. Wegscheider, and R. J. Haug, 'Bimodal Counting Statistics in Single Electron Tunneling through a Quantum Dot', arXiv:0705.2420 (2007).

[136] L. S. Levitov and G. B. Lesovik, 'Charge-Transport Statistics In Quantum Conductors', JETP Lett. **55**, 555 (1992).

[137] L. S. Levitov and G. B. Lesovik, 'Charge-Distribution In Quantum Shot-Noise', JETP Lett. **58**, 230 (1993).

[138] D. A. Bagrets and Yu. V. Nazarov, 'Full counting statistics of charge transfer in Coulomb blockade systems', Phys. Rev. B **67**, 85316 (2003).

[139] A. N. Jordan, E. V. Sukhorukov, and S. Pilgram, 'Fluctuation statistics in networks: A stochastic path integral approach', J. Math. Phys. **45**, 4386 (2004).

[140] S. Camalet, S. Kohler, and P. Hänggi, 'Shot-noise control in ac-driven nanoscale conductors', Phys. Rev. B **70**, 155326 (2004).

[141] C. Beenakker and C. Schönenberger, 'Quantum Shot Noise', Physics Today **56**, 37 (2003).

[142] F. Lefloch, C. Hoffmann, M. Sanquer, and D. Quirion, 'Doubled Full Shot Noise in Quantum Coherent Superconductor-Semiconductor Junctions', Phys. Rev. Lett. **90**, 067002 (2003).

[143] L. Saminadayar, D. C. Glattli, Y. Jin, and B. Etienne, 'Observation of the e/3 Fractionally Charged Laughlin Quasiparticle', Phys. Rev. Lett. **79**, 2526 (1997).

[144] R. dePicciotto, M. Reznikov, M. Heiblum, V. Umansky, G. Bunin, and D. Mahalu, 'Direct observation of a fractional charge', Nature **389**, 162 (1997).

[145] M. Reznikov, R. de Picciotto, T. G. Griffiths, M. Heiblum, and V. Umansky, 'Observation of quasiparticles with one-fifth of an electron's charge', Nature **399**, 238 (1999).

[146] D. K. C. MacDonald, *Noise and Fluctuations: An Introduction* (Wiley, New York, 1962).

[147] R. Aguado and T. Brandes, 'Shot Noise Spectrum of Open Dissipative Quantum Two-Level Systems', Phys. Rev. Lett. **92**, 206601 (2004).

[148] E. B. Saff and A. D. Snider, *Fundamentals of Complex Analysis for Mathematics, Science, and Engineering* (Prentice Hall (New Jersey), 1993).

[149] A. Braggio, J. König, and R. Fazio, 'Full Counting Statistics in Strongly Interacting Systems: Non-Markovian Effects', Phys. Rev. Lett. **96**, 26805 (2006).

[150] M. J. M. de Jong, 'Distribution of transmitted charge through a double-barrier junction', Phys. Rev. B **54**, 8144 (1996).

[151] G. H. Golub and C. F. V. Loan, *Matrix Computations* (The John Hopkins University Press, 1996), third edition.

[152] T. Eirola and O. Nevanlinna, 'Numerical linear algebra; iterative methods', Lecture notes, Helsinki University of Technology (2003).

[153] E. V. Sukhorukov, G. Burkard, and D. Loss, 'Noise of a quantum dot system in the cotunneling regime', Phys. Rev. B **63**, 125315 (2001).

[154] A. N. Jordan and E. V. Sukhorukov, 'Transport Statistics of Bistable Systems', Phys. Rev. Lett. **93**, 260604 (2004).

[155] A. N. Jordan and E. V. Sukhorukov, 'Mesoscopic threshold detectors: Telegraphing the size of a fluctuation', Phys. Rev. B **72**, 035335 (2005).

[156] A. D. Armour, 'Current noise of a single-electron transistor coupled to a nanomechanical resonator', Phys. Rev. B **70**, 165315 (2004).

[157] J. Koch, M. E. Raikh, and F. von Oppen, 'Full Counting Statistics of Strongly Non-Ohmic Transport through Single Molecules', Phys. Rev. Lett. **95**, 056801 (2005).

[158] A. Donarini, M. Grifoni, and K. Richter, 'Dynamical Symmetry Breaking in Transport through Molecules', Phys. Rev. Lett. **97**, 166801 (2006).

[159] F. Haupt, F. Cavaliere, R. Fazio, and M. Sassetti, 'Anomalous suppression of the shot noise in a nanoelectromechanical system', Phys. Rev. B **74**, 205328 (2006).

[160] D. A. Rodrigues, J. Imbers, and A. D. Armour, 'Quantum Dynamics of a Resonator Driven by a Superconducting Single-Electron Transistor: A Solid-State Analogue of the Micromaser', Phys. Rev. Lett. **98**, 67204 (2007).

[161] H. Huebener and T. Brandes, 'Vibrational Coherences in Nano-Elastic Tunneling', arXiv:0705.2728 (2007).

[162] G. Kiesslich, P. Samuelsson, A. Wacker, and E. Schöll, 'Counting statistics and decoherence in coupled quantum dots', Phys. Rev. B **73**, 033312 (2006).

[163] R. Aguado and T. Brandes, 'Current fluctuation spectrum in dissipative solid-state qubits', Euro. Phys. Jour. B **40**, 357 (2004).

[164] B. Elattari and S. A. Gurvitz, 'Shot noise in coupled dots and the "fractional charges"', Phys. Lett. A **292**, 289 (2002).

[165] P. Barthold, F. Hohls, N. Maire, K. Pierz, and R. J. Haug, 'Enhanced Shot Noise in Tunneling Through a Stack of Coupled Quantum Dots', Phys. Rev. Lett. **96**, 246804 (2006).

[166] G. Kiesslich, E. Schöll, T. Brandes, F. Hohls, and R. J. Haug, 'Noise enhancement due to quantum coherence in coupled quantum dots', arXiv:0706.1737 (2007).

[167] J. Dalibard, Y. Castin, and K. Mølmer, 'Wave-Function Approach to Dissipative Processes in Quantum Optics', Phys. Rev. Lett. **68**, 580 (1992).

[168] K. Mølmer, Y. Castin, and J. Dalibard, 'Monte-Carlo Wave-Function Method In Quantum Optics', J. Opt. Soc. Am. B **10**, 524 (1993).

[169] H.-A. Engel, J. M. Taylor, M. D. Lukin, and A. Imamoglu, 'Quantum optical interface for gate-controlled spintronic devices', arXiv:cond-mat/0612700 (2006).

[170] C. Emary, D. Marcos, R. Aguado, and T. Brandes, 'Frequency-dependent counting statistics in interacting nanoscale conductors', arXiv:cond-mat/0703781 (2007).

[171] R. Aguado and L. P. Kouwenhoven, 'Double Quantum Dots as Detectors of High-Frequency Quantum Noise in Mesoscopic Conductors', Phys. Rev. Lett. **84**, 1986 (2000).

[172] H.-A. Engel and D. Loss, 'Asymmetric Quantum Shot Noise in Quantum Dots', Phys. Rev. Lett. **93**, 136602 (2004).

[173] F. Taddei and R. Fazio, 'Counting statistics for entangled electrons', Phys. Rev. B **65**, 075317 (2002).

[174] L. Faoro, F. Taddei, and R. Fazio, 'Clauser-Horne inequality for electron-counting statistics in multiterminal mesoscopic conductors', Phys. Rev. B **69**, 125326 (2004).

[175] P. S. Albert and M. A. Waclawiw, 'A two-state Markov chain for heterogeneous transitional data: A quasi-likelihood approach', Stat. Med. **17**, 1481 (1998).

[176] E. Neher, 'The Charge Carried by Single-Channel Currents of Rat Cultured Muscle-Cells in the Presence Of Local-Anesthetics', J. Physiol. **339**, 663 (1983).

[177] A. Adas, 'Traffic models in broadband networks', IEEE Commun. Mag. **35**, 82 (1997).

Paper D

C. Flindt, T. Novotný, and A.-P. Jauho

Full counting statistics of nano-electromechanical systems

Europhys. Lett. **69**, 475 (2005)

The theory was developed by CF and TN in a joint effort. The numerical results are mainly due to CF. $P(E)$ results for the C_{60}-model are due to TN. APJ contributed in the analysis of the results and with general supervision. The writing of the manuscript was done by CF, TN, and APJ in a joint effort.

EUROPHYSICS LETTERS 1 February 2005

Europhys. Lett., **69** (3), pp. 475–481 (2005)
DOI: 10.1209/epl/i2004-10351-x

Full counting statistics of nano-electromechanical systems

C. Flindt[1](*), T. Novotný[1,2] and A.-P. Jauho[1]

[1] *MIC, Department of Micro and Nanotechnology, Technical University of Denmark DTU, Building 345east - DK-2800 Kongens Lyngby, Denmark*
[2] *Department of Electronic Structures, Faculty of Mathematics and Physics Charles University - Ke Karlovu 5, 121 16 Prague, Czech Republic*

received 14 October 2004; accepted 18 November 2004
published online 24 December 2004

PACS. 85.85.+j – Micro- and nano-electromechanical systems (MEMS/NEMS) and devices.
PACS. 72.70.+m – Noise processes and phenomena.
PACS. 73.23.Hk – Coulomb blockade; single-electron tunneling.

Abstract. – We develop a theory for the full counting statistics (FCS) for a class of nano-electromechanical systems (NEMS), describable by a Markovian generalized master equation. The theory is applied to two specific examples of current interest: vibrating C_{60}-molecules and quantum shuttles. We report a numerical evaluation of the first three cumulants for the C_{60} setup; for the quantum shuttle we use the third cumulant to substantiate that the giant enhancement in noise observed at the shuttling transition is due to a slow switching between two competing conduction channels. Especially the last example illustrates the power of the FCS.

Introduction. – The full counting statistics (FCS) of charge transport in mesoscopic systems is an active topic of recent research [1–5]. Calculation and measurement of the whole probability distribution of transmitted charge is motivated by the fact that FCS provides more information about a particular system than just the mean current or current noise which are the first two cumulants of the large-time asymptotics of the probability distribution. Very recently, a measurement of the third cumulant, which quantifies the skewness of the distribution, was reported [6]. The detailed nature of charge transport in nanoelectromechanical systems (NEMS), another modern field in mesoscopics, poses many challenges both to experiments and theory, and the computation of FCS for NEMS is an important task that needs to be addressed. The first steps were taken recently with a calculation of FCS for a *driven, classical* shuttle [7].

In this letter, we present a theory for the evaluation of cumulants in a wide class of NEMS encompassing the majority of systems considered thus far, namely those which can be described by a Markovian generalized master equation (GME). The current cumulants turn out to be fully determined by an extremal eigenvalue of the system evolution superoperator (Liouvillean) in analogy with previous studies [4,5]. Their evaluation is, however, more complicated since in NEMS there are generally many relevant states which need to be taken into account. We solve the problem by formulating a systematic perturbation theory, and using this, derive explicit formulas for the first three cumulants. The method is illustrated by two examples of NEMS —the C_{60} experiment [8] and the quantum shuttle [9–11]. To test the method we calculate the first three cumulants for the model of the C_{60} setup from [12]. In case the oscillator is equilibrated, the cumulants can be calculated alternatively using $P(E)$-theory which gives the same results. For the quantum shuttle we use the third cumulant to substantiate

(*) E-mail: cf@mic.dtu.dk

that the giant enhancement of the current noise in the transition region [10] is caused by a slowly fluctuating amplitude of the shuttle resulting in a slow switching between two current channels, *i.e.* tunneling and shuttling. This part complements [7], which considered a fixed driving amplitude, and [13] describing a related phenomenon in a different model.

Theory. – We consider a nanoelectromechanical system with discrete energy levels electronically coupled to two leads and mechanically coupled to a generic heat bath providing dissipation. The system is described by the reduced density operator $\hat{\rho}(t)$, which, we assume, evolves according to the Markovian GME,

$$\dot{\hat{\rho}}(t) = \mathcal{L}\hat{\rho}(t). \tag{1}$$

The Liouvillean $\mathcal{L}$ describes the dynamics of the system and we assume that the system tends exponentially to a stationary state $\hat{\rho}^{\rm stat}$. This implies that the Liouvillean, which is a non-Hermitian operator, has a single eigenvalue equal to zero with $\hat{\rho}^{\rm stat}$ being the corresponding (normalized and unique) right eigenvector which we denote by $|0\rangle\!\rangle$ [14]. The corresponding left eigenvector is the identity operator $\hat{1}$, denoted by $\langle\!\langle\tilde{0}|$, and we have $\langle\!\langle\tilde{0}|0\rangle\!\rangle \equiv {\rm Tr}(\hat{1}^\dagger\hat{\rho}^{\rm stat}) = 1$. The pair of eigenvectors allows us to define the projectors $\mathcal{P} \equiv |0\rangle\!\rangle\langle\!\langle\tilde{0}|$ and $\mathcal{Q} \equiv 1 - \mathcal{P}$ obeying the relations $\mathcal{P}\mathcal{L} = \mathcal{L}\mathcal{P} = 0$ and $\mathcal{Q}\mathcal{L}\mathcal{Q} = \mathcal{L}$. We also introduce the pseudoinverse of the Liouvillean $\mathcal{R} \equiv \mathcal{Q}\mathcal{L}^{-1}\mathcal{Q}$, which is well defined, since the inversion is performed only in the subspace spanned by $\mathcal{Q}$, where $\mathcal{L}$ is regular. The assumption of exponential decay to the stationary state is equivalent to the spectrum of $\mathcal{L}$ in the subspace spanned by $\mathcal{Q}$ having a finite negative real part.

In order to evaluate the FCS of the system, *i.e.* the probability $P_n(t)$ of n electrons being collected in, say, the right lead in the time span t, we resolve the density operator $\hat{\rho}(t)$ and the GME with respect to n. The GME is a continuity equation for the probability (charge) and, therefore, we can identify terms corresponding to charge transfer processes between the system and the right lead. Specifically, we introduce the superoperator $\mathcal{I}^+$ of the particle current of electrons tunneling from the system to the right lead, and the corresponding superoperator $\mathcal{I}^-$ of the reverse process, where electrons tunnel from the right lead to the system. In terms of these superoperators the n-resolved GME can be written as

$$\dot{\hat{\rho}}^{(n)}(t) = (\mathcal{L} - \mathcal{I}^+ - \mathcal{I}^-)\hat{\rho}^{(n)}(t) + \mathcal{I}^+\hat{\rho}^{(n-1)}(t) + \mathcal{I}^-\hat{\rho}^{(n+1)}(t) \tag{2}$$

with $n = \ldots, -1, 0, 1, \ldots$. From the n-resolved density operator we can obtain, at least in principle, the complete probability distribution $P_n(t) = {\rm Tr}[\hat{\rho}^{(n)}(t)]$.

It is practical first to evaluate the cumulant generating function $S(t,\chi)$ defined as

$$e^{S(t,\chi)} = \sum_{n=-\infty}^{\infty} P_n(t)e^{in\chi}. \tag{3}$$

From $S(t,\chi)$ we then find the m-th cumulant of the charge distribution (we take $e = 1$) by taking the m-th derivative with respect to the counting field χ at $\chi = 0$, *i.e.* $\langle\!\langle n^m\rangle\!\rangle(t) = \frac{\partial^m S}{\partial(i\chi)^m}|_{\chi=0}$, and from the knowledge of all cumulants we can reconstruct $P_n(t)$. The cumulants of the current in the stationary limit $t \to \infty$ are given by the time derivative of the charge cumulants, *i.e.* $\langle\!\langle I^m\rangle\!\rangle = \frac{\rm d}{{\rm d}t}\langle\!\langle n^m\rangle\!\rangle(t)\big|_{t\to\infty}$. The first two current cumulants give the average current and the zero-frequency current noise, respectively.

Using $\hat{\rho}^{(n)}(t)$ we may express $S(t,\chi)$ as $e^{S(t,\chi)} = {\rm Tr}[\sum_{n=-\infty}^{\infty}\hat{\rho}^{(n)}(t)e^{in\chi}] = {\rm Tr}[\hat{F}(t,\chi)]$, where we have introduced the auxiliary operator $\hat{F}(t,\chi)$ whose equation of motion follows

from the n-resolved GME,

$$\frac{\partial}{\partial t}\hat{F}(t,\chi) = \left[\mathcal{L} - \left(1-e^{i\chi}\right)\mathcal{I}^{+} - \left(1-e^{-i\chi}\right)\mathcal{I}^{-}\right]\hat{F}(t,\chi) \equiv \mathcal{L}_{\chi}\hat{F}(t,\chi) \tag{4}$$

with the formal solution $\hat{F}(t,\chi) = e^{\mathcal{L}_{\chi}t}\hat{F}(0,\chi)$. We assume adiabatic evolution of the spectrum of $\mathcal{L}_{\chi}$ with increasing χ, *i.e.* there is a unique eigenvalue $\Lambda_{\chi}^{\min}$ of $\mathcal{L}_{\chi}$ associated with the projector $\mathcal{P}_{\chi}$ which develops from the zero eigenvalue of $\mathcal{L}$ and which is the closest to zero for small enough χ. The rest of the spectrum still has a finite negative real part which ensures the damping of its contribution for large times. Thus, we have

$$e^{S(t,\chi)} = \langle\langle\tilde{0}|e^{\mathcal{L}_{\chi}t}|F(0,\chi)\rangle\rangle \longrightarrow e^{\Lambda_{\chi}^{\min}t}\langle\langle\tilde{0}|\mathcal{P}_{\chi}|F(0,\chi)\rangle\rangle = e^{\Lambda_{\chi}^{\min}t+C_{\chi}^{\text{init}}} \quad \text{for } t\to\infty, \tag{5}$$

where C_{χ}^{init} depends on the initial state of the system. However, the current cumulants in the stationary state do not depend on the initial conditions, but are totally determined by $\Lambda_{\chi}^{\min}$ in full analogy with previous studies [4, 5]. For NEMS in general $\mathcal{L}_{\chi}$ is of very large dimensions, and the numerical evaluation of higher-order derivatives of $\Lambda_{\chi}^{\min}$ may become a formidable numerical problem. In order to circumvent this problem, we determine $\Lambda_{\chi}^{\min}$ using Rayleigh-Schrödinger perturbation theory for $\mathcal{L}_{\chi} = \mathcal{L} + \mathcal{L}'_{\chi}$, treating $\mathcal{L}'_{\chi}$ as the perturbation. Since the Liouvillean is not Hermitian, we cannot assume that it has a spectral decomposition in terms of its eigenvectors, and one cannot use directly the standard formulas. However, it is possible to formulate the perturbation theory exclusively in terms of the projectors $\mathcal{P}$, $\mathcal{Q}$ and the pseudoinverse $\mathcal{R}$. As in standard Rayleigh-Schrödinger perturbation theory, the first-order correction is given by the average of the perturbation with respect to the unperturbed eigenstate. Taking the derivative of the first-order correction with respect to $i\chi$ and letting $\chi\to 0$, we find

$$\langle\langle I\rangle\rangle = \langle\langle\tilde{0}|\mathcal{I}\,|0\rangle\rangle, \tag{6}$$

where $\mathcal{I} \equiv \mathcal{I}^{+} - \mathcal{I}^{-}$. As expected, the first cumulant equals the average current. For the second cumulant, *i.e.* the zero-frequency current noise, one finds

$$\langle\langle I^2\rangle\rangle = \langle\langle\tilde{0}|\mathcal{J}|0\rangle\rangle - 2\langle\langle\tilde{0}|\mathcal{I}\mathcal{R}\mathcal{I}\,|0\rangle\rangle, \tag{7}$$

where $\mathcal{J} \equiv \mathcal{I}^{+} + \mathcal{I}^{-}$. In the high-bias limit (where $\langle\langle\tilde{0}|\mathcal{I}^{-}|0\rangle\rangle = 0$, since backward tunneling is blocked) this expression yields the result previously derived in [14]. The expression for the third cumulant

$$\langle\langle I^3\rangle\rangle = \langle\langle\tilde{0}|\mathcal{I}\,|0\rangle\rangle - 3\langle\langle\tilde{0}|\mathcal{I}\mathcal{R}\mathcal{J} + \mathcal{J}\mathcal{R}\mathcal{I}\,|0\rangle\rangle - 6\langle\langle\tilde{0}|\mathcal{I}\mathcal{R}(\mathcal{R}\mathcal{I}\mathcal{P} - \mathcal{I}\mathcal{R})\mathcal{I}\,|0\rangle\rangle \tag{8}$$

is the main result of this section, and below we evaluate it for two specific cases. Higher-order cumulants can be obtained in the same manner by calculating the corresponding higher-order corrections.

Model 1: The C_{60} *experiment.* – An experiment with a NEMS that has received much attention is the measurement of the IV-curves of a vibrating C_{60}-molecule [8]. The experiment has been modelled in several papers [12, 15, 16] using a model which will also be employed here. Calculations of IV-curves [12, 15] have been found to be in good agreement with the experiment, and the current noise has been predicted [16]. We calculate the third cumulant for this setup by applying our method to the model as described in [12].

In the model of [12] both the coupling to the leads and to the heat bath are treated in the weak-coupling approximation which reduces the full GME to an ordinary Pauli master

equation for the probabilities of occupation of the individual eigenstates of the system:

$$\frac{\mathrm{d}P_{m,\sigma,l}}{\mathrm{d}t} = -\left[W_{l+1\leftarrow l} + W_{l-1\leftarrow l} + \sum_{m',\sigma',l',s} \Gamma^{(s)}_{m',\sigma',l'\leftarrow m,\sigma,l}\right] P_{m,\sigma,l} + \\ + \sum_{m',\sigma',l',s} \left[\Gamma^{(s)}_{m,\sigma,l\leftarrow m',\sigma',l'} + W_{l\leftarrow l'}(\delta_{l+1,l'} + \delta_{l-1,l'})\delta_{\sigma,\sigma'}\delta_{m,m'}\right] P_{m',\sigma',l'}, \quad (9)$$

where m, σ, l denote the (extra) charge on the molecule ($m = 0, 1$), the spin, and the vibrational state, respectively, while s indicates whether an electron tunneled from/to the left ($s = -1$) or right ($s = 1$) lead. $P_{m,\sigma,l}$ is the probability of being in the eigenstate labelled by the subindices. Bath-mediated transitions between different vibrational states are given by the thermal rates

$$W_{l+1\leftarrow l} = W_{l\leftarrow l+1} e^{-\hbar\omega_0/k_\mathrm{B}T} = K\frac{l+1}{e^{\hbar\omega_0/k_\mathrm{B}T} - 1}\,, \quad (10)$$

where ω_0 is the natural oscillator frequency. The charge transfer rates are

$$\Gamma^{(s)}_{1,\sigma,l'\leftarrow 0,0,l} = \Gamma^{(0)} \left|\langle l'| e^{\gamma(\hat{a}^\dagger - \hat{a})} |l\rangle\right|^2 f\Big(E_\mathrm{C} + \frac{seV}{2} + \hbar\omega_0\big(l' - l - \gamma^2\big)\Big), \\ \Gamma^{(s)}_{0,0,l\leftarrow 1,\sigma,l'} = \Gamma^{(0)} \left|\langle l| e^{\gamma(\hat{a}^\dagger - \hat{a})} |l'\rangle\right|^2 \left[1 - f\Big(E_\mathrm{C} + \frac{seV}{2} + \hbar\omega_0\big(l' - l - \gamma^2\big)\Big)\right], \quad (11)$$

where f is the Fermi function, $\Gamma^{(0)}$ is the bare tunneling rate, E_C is the charging energy difference, and V is the symmetrically applied bias. The quantity γ describes the bias dependence of the electric field at the position of the molecule, and is assumed to have the form $\gamma = c_1 + \frac{eV}{\hbar\omega_0}c_2$ [12]. Here we do not consider the case where the rates depend on the position of the molecule, although this can easily be included.

The current superoperators are identified from the expression for the stationary current,

$$I^\mathrm{stat} = \underbrace{\sum_{\sigma,l,l'} \left[\Gamma^{(1)}_{0,0,l'\leftarrow 1,\sigma,l} P^\mathrm{stat}_{1,\sigma,l}\right]}_{\langle\langle\tilde{0}|\mathcal{I}^+|0\rangle\rangle} - \underbrace{\sum_{\sigma,l,l'} \left[\Gamma^{(1)}_{1,\sigma,l'\leftarrow 0,0,l} P^\mathrm{stat}_{0,0,l}\right]}_{\langle\langle\tilde{0}|\mathcal{I}^-|0\rangle\rangle}. \quad (12)$$

Here $|0\rangle\rangle$ is a diagonal density matrix containing the stationary probabilities $P^\mathrm{stat}_{m,\sigma,l}$. Due to this diagonal form of the density matrices the relevant superoperators needed for the cumulants can be represented by matrices of dimension $2N \times 2N$ (N is the number of vibrational modes) which makes the calculation of the cumulants numerically straightforward.

In fig. 1 we show the bias dependence of the first three cumulants for parameters corresponding to fig. 3 of [12]. Since $\Gamma^{(0)} \ll K$, the oscillator is in equilibrium and, therefore, the FCS of the model can also be calculated from a simple two-level model with 4 rates given by $P(E)$-theory. We have verified that the semi-analytical results coincide with numerics (not shown) which we view as a non-trivial test of our method. In non-equilibrium cases there are no simple alternatives to the numerics. We demonstrate the full power of the method in the second example.

Model 2: The quantum shuttle. – We consider the model of a quantum shuttle used in [9–11]. The system consists of an oscillating nanoscopic grain coupled to two leads (fig. 2). In the strong Coulomb blockade regime the grain effectively has just one electronic level. The oscillations of the grain are treated fully quantum-mechanically, and damping of the

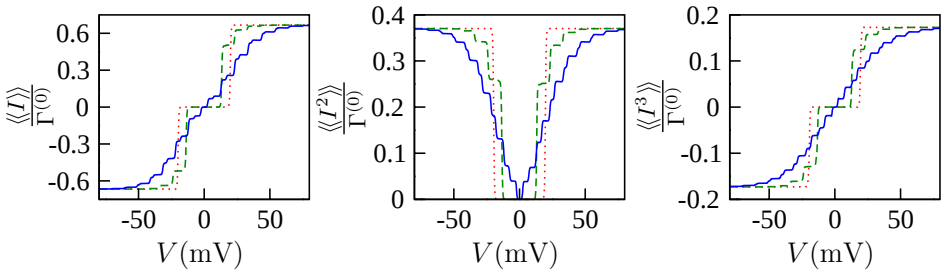

Fig. 1 – Results for the C_{60} setup. First three cumulants as a function of the bias V. The parameters, which correspond to fig. 3 of [12], are $E_c = 10\,\mathrm{meV}$, $\hbar\omega_0 = 5\,\mathrm{meV}$, $\hbar\Gamma^{(0)} = 1\,\mu\mathrm{eV}$, $k_BT = 0.15\,\mathrm{meV}$, $K = 0.1\omega_0$, and $c_1 = 0$ (dashed line), 0.8 (dotted line), 1.5 (full line), $c_2 = 0.005$.

oscillations is due to a surrounding heat bath. As in [10], we consider the n-resolved system density matrices $\hat{\rho}_{ii}^{(n)}(t)$, $i = 0, 1$, where n is the number of electrons that have tunneled into the right lead in the time span t. In the high-bias limit n is non-negative, and the $\hat{\rho}_{ii}^{(n)}(t)$ evolve according to the n-resolved GME,

$$\begin{aligned}
\dot{\hat{\rho}}_{00}^{(n)}(t) &= \frac{1}{i\hbar}\Big[\hat{H}_{\rm osc}, \hat{\rho}_{00}^{(n)}(t)\Big] + \mathcal{L}_{\rm damp}\hat{\rho}_{00}^{(n)}(t) - \frac{\Gamma_{\rm L}}{2}\Big\{e^{-\frac{2\hat{x}}{\lambda}}, \hat{\rho}_{00}^{(n)}(t)\Big\} + \Gamma_{\rm R}e^{\frac{\hat{x}}{\lambda}}\hat{\rho}_{11}^{(n-1)}(t)e^{\frac{\hat{x}}{\lambda}}, \\
\dot{\hat{\rho}}_{11}^{(n)}(t) &= \frac{1}{i\hbar}\Big[\hat{H}_{\rm osc} - eE\hat{x}, \hat{\rho}_{11}^{(n)}(t)\Big] + \mathcal{L}_{\rm damp}\hat{\rho}_{11}^{(n)}(t) - \frac{\Gamma_{\rm R}}{2}\Big\{e^{\frac{2\hat{x}}{\lambda}}, \hat{\rho}_{11}^{(n)}(t)\Big\} + \Gamma_{\rm L}e^{-\frac{\hat{x}}{\lambda}}\hat{\rho}_{00}^{(n)}(t)e^{-\frac{\hat{x}}{\lambda}}, \quad (13)
\end{aligned}$$

with $n = 0, 1, \ldots$ and $\hat{\rho}_{11}^{(-1)}(t) \equiv 0$. Here the commutators describe the coherent evolution of the charged (ρ_{11}) or empty (ρ_{00}) shuttle which is modelled by a quantum-mechanical harmonic oscillator of mass m and frequency ω. The electric field between the leads is denoted E. The terms proportional to $\Gamma_{\rm L/R}$ describe transfer processes from the left to the right lead with hopping amplitudes that depend exponentially on the position $\frac{\hat{x}}{\lambda}$, where λ is the electron tunneling length. The mechanical damping of the oscillator is described by the damping kernel (here $T = 0$) $\mathcal{L}_{\rm damp}\hat{\rho} = -\frac{i\gamma}{2\hbar}[\hat{x}, \{\hat{p}, \hat{\rho}\}] - \frac{\gamma m\omega}{2\hbar}[\hat{x}, [\hat{x}, \hat{\rho}]]$ [9, 10]. We identify the current superoperators from (13): $\mathcal{I}^+\hat{\rho} = \Gamma_{\rm R}e^{\frac{\hat{x}}{\lambda}}|0\rangle\langle 1|\hat{\rho}|1\rangle\langle 0|e^{\frac{\hat{x}}{\lambda}}$, $\mathcal{I}^- \equiv 0$.

In [9, 10] it was found that the quantum shuttle exhibits a crossover from tunneling to shuttling when the damping, starting above a certain threshold value, is decreased. This transition is clearly recorded both in the current [9] and the zero-frequency current noise [10]. The FCS in the tunneling and shuttling limit is to a first approximation captured by the re-

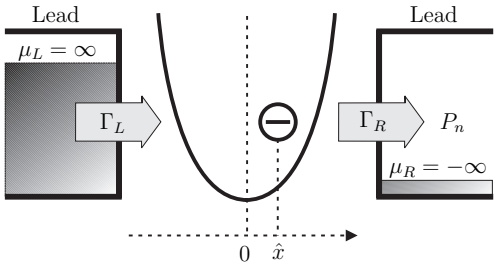

Fig. 2 – The quantum shuttle consists of a nanosized grain moving in a harmonic potential between two leads. A high bias between the leads drives electrons through the grain.

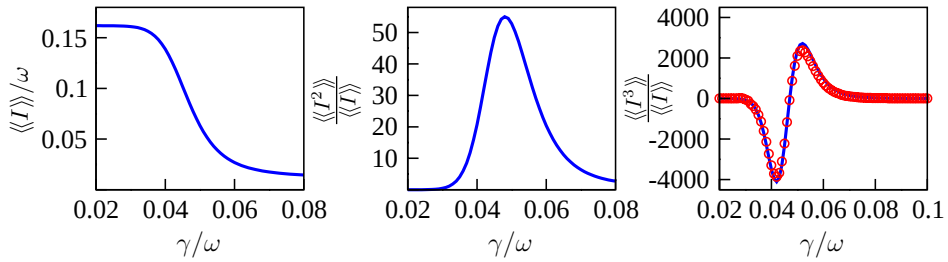

Fig. 3 – Results for the quantum shuttle. First three cumulants as a function of the damping γ. The parameters are $\Gamma_{\rm L} = \Gamma_{\rm R} = 0.01\omega$, $\lambda = 1.5x_0$, $d \equiv eE/m\omega^2 = 0.5x_0$, $x_0 = \sqrt{\hbar/m\omega}$. The full lines indicate numerical results, while the circles indicate the analytic expression for the third cumulant assuming that the shuttle in the transition region effectively behaves as a bistable system.

sults for the zero amplitude (with appropriately renormalized rates) and the large (shuttling) amplitude of a driven shuttle [7], respectively. When approaching the semi-classical regime, a giant enhancement of the noise was found in the transition region. This behavior was tentatively attributed to amplitude fluctuations in the spirit of [13]; however, a more quantitative explanation has been missing. The phase space representation of the stationary state of the shuttle in the transition region indicated that shuttling and tunneling processes coexist [10] leading to the conjecture that the giant noise enhancement is caused by switching between two current channels([1]) (tunneling and shuttling) induced by infrequent jumps between two discrete values of the shuttle amplitude. Very recently the FCS of such bistable systems has been studied [18], and it was found that the first three cumulants are (assuming that the individual channels are noiseless)

$$\langle\langle I\rangle\rangle = \frac{I_{\rm S}\Gamma_{\rm S\leftarrow T} + I_{\rm T}\Gamma_{\rm T\leftarrow S}}{\Gamma_{\rm T\leftarrow S} + \Gamma_{\rm S\leftarrow T}}\,, \tag{14a}$$

$$\langle\langle I^2\rangle\rangle = 2(I_{\rm S} - I_{\rm T})^2 \frac{\Gamma_{\rm S\leftarrow T}\Gamma_{\rm T\leftarrow S}}{(\Gamma_{\rm S\leftarrow T} + \Gamma_{\rm T\leftarrow S})^3}\,, \tag{14b}$$

$$\langle\langle I^3\rangle\rangle = 6(I_{\rm S} - I_{\rm T})^3 \frac{\Gamma_{\rm S\leftarrow T}\Gamma_{\rm T\leftarrow S}(\Gamma_{\rm T\leftarrow S} - \Gamma_{\rm S\leftarrow T})}{(\Gamma_{\rm S\leftarrow T} + \Gamma_{\rm T\leftarrow S})^5}\,. \tag{14c}$$

Here $I_{\rm S/T}$ denote the current associated with the shuttling/tunneling channel([2]), while $\Gamma_{\rm T\leftarrow S}$ is the transition rate from the shuttling to the tunneling channel and $\Gamma_{\rm S\leftarrow T}$ is the rate of the reverse transition.

The rates can be evaluated analytically in the limit $\lambda \to \infty$ and $E \to 0$ [19]. However, for other parameters an alternative approach is needed. First, one evaluates the first three cumulants numerically following the theory presented above. Then, one calculates the rates from the first two cumulants (eqs. (14a), (14b)) and compares the numerically calculated third cumulant from eq. (8) with the one obtained from eq. (14c). The numerical calculation of the cumulants is only possible by a truncation of the oscillator Hilbert space. By retaining the N lowest oscillator states the (non-sparse) matrix representations of the superoperators entering eqs. (6)-(8) are of dimension $2N^2 \times 2N^2$, which for the required values of $N \sim 100$ leaves us with non-trivial numerical matrix problems. However, using the iterative methods described in [14], the cumulants can be evaluated numerically.

([1])Such a behavior, referred to as the "whistle" effect, was first reported in [17].

([2])$I_{\rm S} = \omega/2\pi$, $I_{\rm T} = \frac{\tilde\Gamma_{\rm L}\tilde\Gamma_{\rm R}}{\tilde\Gamma_{\rm L}+\tilde\Gamma_{\rm R}}$, with $\tilde\Gamma_{\rm R} = \Gamma_{\rm R}e^{\hbar/m\omega\lambda^2}e^{2eE/m\omega^2\lambda}$, $\tilde\Gamma_{\rm L} = \Gamma_{\rm L}e^{\hbar/m\omega\lambda^2}$ [10,19].

In fig. 3 we show the γ-dependence of the first three cumulants for $\lambda = 1.5x_0$, where $x_0 = \sqrt{\hbar/m\omega}$. The first cumulant, the current, shows the transition from the tunneling to shuttling current with decreasing damping. The transition is also evident from the second cumulant, the zero-frequency current noise, which exhibits a giant enhancement in the transition region, before dropping to very low values in the shuttling region. Together with the numerical results for the third cumulant we show the analytic expression (eq. (14c)) with rates extracted from the first two cumulants. As can be seen, the two data sets coincide, which we take as evidence that the quantum shuttle in the transition region indeed behaves as a bistable system for which the FCS is known [18]. When approaching the deep quantum regime, $\lambda \sim x_0$ (not shown), the transition from tunneling to shuttling is smeared out and the distinct current channels cease to exist. In this limit the bistable system model is not valid.

Conclusion. – We have presented a method for computation of the FCS for typical nanoelectromechanical systems and applied it to two specific models. For the C_{60} setup with equilibrated oscillator we have calculated the first three cumulants and explained the results in terms of a simple two-level model. For the quantum shuttle we have used the first three cumulants as evidence that the shuttle in the transition region behaves as a bistable system. This example clearly illustrates the usefulness of the FCS in probing a microscopic system. Here we have only shown explicit expressions for the first three cumulants. Our method, however, can be extended to the calculation of cumulants of any order, and we believe that the method has a broad range of applicability.

* * *

The authors would like to thank A. Armour and A. Donarini for careful reading of the manuscript and fruitful discussions.

REFERENCES

[1] Nazarov Yu. V. (Editor), *Quantum Noise in Mesoscopic Systems* (Springer) 2003.
[2] Levitov L. S., Lee H.-W. and Lesovik G. B., *J. Math. Phys.*, **37** (1996) 4845.
[3] Pilgram S. *et al.*, *Phys. Rev. Lett.*, **90** (2003) 206801.
[4] Roche P. E., Derrida B. and Douçot B., cond-mat/0312659.
[5] Bagrets D. A. and Nazarov Yu. V., *Phys. Rev. B*, **67** (2003) 085316.
[6] Reulet B., Senzier J. and Prober D. E., *Phys. Rev. Lett.*, **91** (2003) 196601.
[7] Pistolesi F., *Phys. Rev. B*, **69** (2004) 245409.
[8] Park H. *et al.*, *Nature*, **407** (2000) 57.
[9] Novotný T., Donarini A. and Jauho A.-P., *Phys. Rev. Lett.*, **90** (2003) 256801.
[10] Novotný T., Donarini A., Flindt C. and Jauho A.-P., *Phys. Rev. Lett.*, **92** (2004) 248302.
[11] Fedorets D. *et al.*, *Phys. Rev. Lett.*, **92** (2004) 166801.
[12] McCarthy K. D., Prokof'ev N. and Tuominen M. T., *Phys. Rev. B*, **67** (2003) 245415.
[13] Isacsson A. and Nord T., *Europhys. Lett.*, **66** (2004) 708.
[14] Flindt C., Novotný T. and Jauho A.-P., to be published in *Phys. Rev. B*, cond-mat/0405512.
[15] Boese D. and Schoeller H., *Europhys. Lett.*, **54** (2001) 668.
[16] Mitra A., Aleiner I. and Millis A. J., *Phys. Rev. B*, **69** (2004) 245302.
[17] Sukhorukov E. V., Burkard G. and Loss D., *Phys. Rev. B*, **63** (2001) 125315.
[18] Jordan A. N. and Sukhorukov E. V., cond-mat/0406261.
[19] Donarini A., PhD Thesis, Technical University of Denmark, Kongens Lyngby (2004).

Paper F

C. Flindt, T. Novotný, and A.-P. Jauho

Noise and Bistabilities in Quantum Shuttles

AIP Conf. Proc. **780**, 442 (2005)

The work is mainly due to CF, while TN and APJ contributed in the analysis of the results, the writing, and with general supervision.

Noise and Bistabilities in Quantum Shuttles

Christian Flindt[*], Tomáš Novotný[†,**] and Antti-Pekka Jauho[*]

[*]*NanoDTU, MIC – Department of Micro and Nanotechnology, Technical University of Denmark, DTU - Building 345 East, DK - 2800 Kongens Lyngby, Denmark*
[†]*Nano-Science Center, University of Copenhagen - Universitetsparken 5, DK - 2100 Copenhagen Ø, Denmark*
[**]*Department of Electronic Structures, Faculty of Mathematics and Physics, Charles University - Ke Karlovu 5, 121 16 Prague, Czech Republic*

Abstract. We present a study of current fluctuations in two models proposed as quantum shuttles. Based on a numerical evaluation of the first three cumulants of the full counting statistics we have recently shown that a giant enhancement of the zero-frequency current noise in a single-dot quantum shuttle can be explained in terms of a bistable switching between two current channels. By applying the same method to a quantum shuttle consisting of a vibrating quantum dot array, we show that the same mechanism is responsible for a giant enhancement of the noise in this model, although arising from very different physics. The interpretation is further supported by a numerical evaluation of the finite-frequency noise. For both models we give numerical results for the effective switching rates.

Keywords: Current noise and fluctuations, bistabilities, quantum shuttles.
PACS: 85.85.+j, 72.70.+m, 73.23.Hk

Introduction – In 1998 Gorelik *et al.* proposed a nano-electromechanical system (NEMS), the charge shuttle, consisting of a movable nanoscopic grain coupled via tunnel barriers to source and drain electrodes [1]. Originally the motion of the grain was modelled using a classical harmonic oscillator. Here we present a study of current fluctuations in two models of (quantum) shuttles, where the oscillator is quantized.

Models – Two models have been proposed as quantum shuttles (the 1-dot shuttle [2] and the 3-dot shuttle [3]). The 1-dot shuttle consists of a single mechanically oscillating quantum dot situated between two leads. In the 3-dot shuttle the mechanically oscillating quantum dot is flanked by two static dots, thus making up an array of dots. Both devices are operated in the strong Coulomb blockade regime, and consequently only one excess electron at a time is allowed in the device. In the 1-dot (3-dot) model the coupling to the leads (the interdot coupling) depends exponentially on the position of the vibrating dot. For detailed descriptions of the models we refer to Refs. [2, 3, 4].

Both models are described using the language of quantum dissipative systems [5]. As the "system" we take in the 1-dot model (3-dot model) the single (three) electronic state(s) of the occupied dot (array) and the unoccupied state plus the quantum harmonic oscillator with natural frequency ω_0. In the limit of a high bias between the leads [6], and assuming that the oscillator is damped due to a weak coupling to a heat bath, the time evolution of the reduced density matrix of the system $\hat{\rho}(t)$ is governed by a Markovian generalized master equation (GME) of the form [2, 3, 4]

$$\dot{\hat{\rho}}(t) = \mathscr{L}\hat{\rho}(t) = (\mathscr{L}_{\rm coh} + \mathscr{L}_{\rm damp} + \mathscr{L}_{\rm driv})\hat{\rho}(t). \tag{1}$$

Here $\mathscr{L}_{\rm coh}$ describes the internal coherent dynamics of the system, while $\mathscr{L}_{\rm damp}$ and

CP780, *Noise and Fluctuations: 18th International Conference on Noise and Fluctuations-ICNF 2005,*
edited by T. González, J. Mateos, and D. Pardo

$\mathscr{L}_{\rm driv}$ give the damping and the coupling to the leads, respectively. In the following we consider the stationary state defined by $\hat{\rho}^{\rm stat}(t) = \mathscr{L}\hat{\rho}^{\rm stat}(t) = 0$. The GME is only valid in the high-bias limit, and hence we cannot use the applied bias as a control parameter. Instead, we vary in the 1-dot model the strength of the damping, denoted γ, and in the 3-dot model the difference between the energy levels corresponding to the outer dots, referred to as the *device bias* and denoted ε_b.

Theory – We have recently developed a systematic theory for the calculation of the n'th cumulant of the current $\langle\langle I^n \rangle\rangle$ for NEMS described by a Markovian GME of the form given in Eq. (1) [7]. In Ref. [7] a numerical evaluation of the first three cumulants showed that the 1-dot model in a certain parameter regime behaves as a bistable system switching slowly between two current channels. The first three cumulants of a bistable system switching slowly (compared to the electron transfer rates) with rates $\Gamma_{1\leftarrow 2}$ and $\Gamma_{2\leftarrow 1}$ between two current channels 1 and 2 with corresponding currents I_1 and I_2, respectively, are [8]

$$\begin{aligned}
\langle\langle I \rangle\rangle &= \frac{I_1\Gamma_{1\leftarrow 2} + I_2\Gamma_{2\leftarrow 1}}{\Gamma_{2\leftarrow 1} + \Gamma_{1\leftarrow 2}} \,, \\
\langle\langle I^2 \rangle\rangle &= 2(I_1 - I_2)^2 \frac{\Gamma_{1\leftarrow 2}\Gamma_{2\leftarrow 1}}{(\Gamma_{1\leftarrow 2} + \Gamma_{2\leftarrow 1})^3} \,, \\
\langle\langle I^3 \rangle\rangle &= 6(I_1 - I_2)^3 \frac{\Gamma_{1\leftarrow 2}\Gamma_{2\leftarrow 1}(\Gamma_{2\leftarrow 1} - \Gamma_{1\leftarrow 2})}{(\Gamma_{1\leftarrow 2} + \Gamma_{2\leftarrow 1})^5} \,.
\end{aligned} \tag{2}$$

As pointed out by Jordan and Sukhorukov [8, 9] these expressions are very general, *i. e.* they do not depend on the microscopic origin of the rates or the current channels. For the 1-dot model the two current channels were identified from phase space plots of the oscillating dot as a *shuttling* and a *tunneling* channel, respectively, with known analytic expressions for the corresponding two currents [7, 11]. By comparing the numerical results for the first two cumulants with the corresponding analytic expressions given above, the two rates $\Gamma_{1\leftarrow 2}$ and $\Gamma_{2\leftarrow 1}$ could be extracted, and finally a comparison of the numerical results for the third cumulant and the analytic expression given above (with the extracted rates[1] $\Gamma_{1\leftarrow 2}$ and $\Gamma_{2\leftarrow 1}$) confirmed the conjecture about the bistable behavior (see Fig. 1). This in turn explained a giant enhancement of the zero-frequency current noise (the second cumulant) found in Ref. [11].

A similar enhancement of the zero-frequency current noise was found in a study of the 3-dot model [4]. Also in this case, the enhancement was tentatively attributed to a switching behavior, however, neither the number nor the nature of the individual current channels were clarified, and no quantitative explanation could be given. Phase space plots of the oscillating dot seem to indicate the existence of two current channels [4]: One channel, where electrons tunnel *sequentially* through the array of dots, and one channel, where electrons *co-tunnel* between the static dots. The current corresponding to each of the two channels can be read off from the numerical results obtained in Ref. [4]. By proceeding along the lines outlined above, the conjecture that the enhanced noise is due to a slow switching between the sequential and co-tunneling channel can be scrutinized.

[1] In a certain limit the rates may even be found analytically, see Ref. [10].

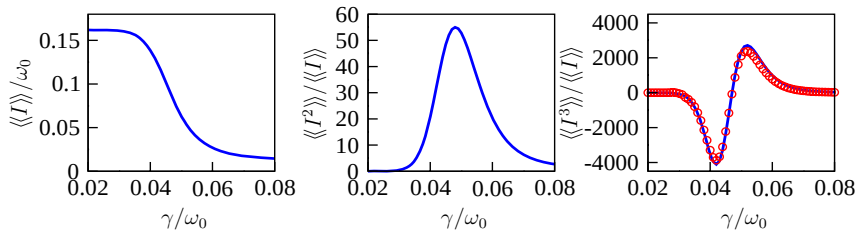

FIGURE 1. First three cumulants for the 1-dot model as a function of the damping strength γ (model parameters correspond to Fig. 3 in Ref. [7]). The shuttling channel current is $I_{\rm shut} = \omega_0/2\pi$ and the tunneling channel current $I_{\rm tun} = 0.0082\omega_0$ ($e = 1$). Full lines indicate numerical results, while circles show the (semi-) analytic results for the third cumulant. The central panel shows the giant enhancement of the zero-frequency noise. (Reproduced from Ref. [7]).

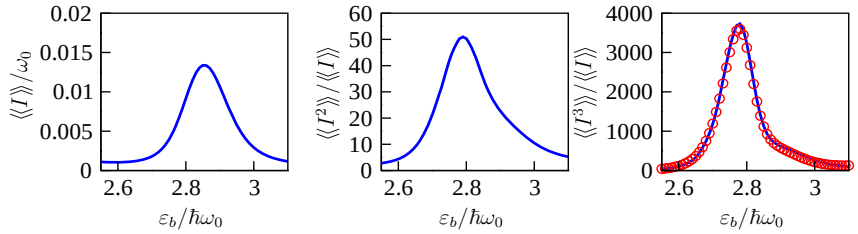

FIGURE 2. First three cumulants for the 3-dot model as a function of the device bias ε_b (model parameters correspond to Fig. 4 in Ref. [4]). The sequential tunneling channel current is $I_{\rm seq} = 0.043\omega_0$ and the co-tunneling channel current $I_{\rm cot} = 0.0008\omega_0$ ($e = 1$). Full lines indicate numerical results, while circles show the (semi-) analytic results for the third cumulant. The central panel shows the giant enhancement of the zero-frequency noise. (Left and central panel reproduced from Ref. [4]).

Results – In Figs. 1, 2 we show numerical results for the first three cumulants for the two models together with the analytic expression for the third cumulant of a bistable system with rates extracted from the first two cumulants. We take the agreement between the numerical and (semi-) analytic results as evidence that both models exhibit a bistable behavior. In Ref. [12] this interpretation was further supported by numerical studies of the finite-frequency current noise in the 1-dot model. Correspondingly, we show in Fig. 3 the agreement between the numerical results for the finite-frequency noise in the 3-dot model and semi-analytic results for a slow bistable switching process [12]. In Fig. 4 we show the extracted rates for both models. Most noteworthy is the crossing of the two rates in the 1-dot case, which results in the change of sign of the third cumulant seen in Fig. 1. On each side of the crossing one of the current channels dominates. In the 3-dot case, the two rates close in, however, without crossing each other. Consequently one of the current channels, the sequential tunneling channel, never dominates. It should also be noted that in both models one of the currents is comparable to one of the rates, which implies that some corrections to Eq. 2 are expected [9]. However, we have found that these corrections do not contribute significantly.

Conclusion – We have presented a study of noise in two models of quantum shuttles. By evaluating numerically the first three cumulants of the full counting statistics, we

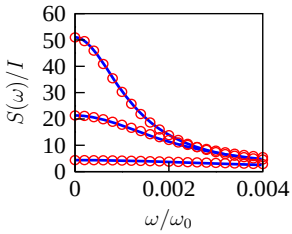

FIGURE 3. Finite-frequency current noise $S(\omega)$ (normalized with respect to the current I) for the 3-dot model. Circles indicate numerical results, while full lines are the corresponding (semi-)analytic results for a slow bistable switching process [12]. The results correspond to Fig. 2 with $\varepsilon_b = 2.60\hbar\omega_0$ (lower curve), $2.70\hbar\omega_0$, $2.79\hbar\omega_0$ (upper curve).

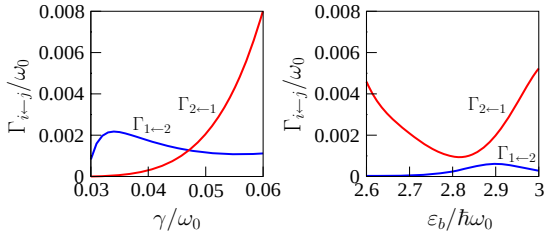

FIGURE 4. Left panel: The two switching rates for the 1-dot model as a function of the damping strength γ. Here the two current channels are the shuttling channel (1) and the tunneling channel (2). The rates correspond to the results shown in Fig. 1. Right panel: The two switching rates for the 3-dot model as a function of the device bias ε_b. Here the two current channels are the sequential tunneling channel (1) and the co-tunneling channel (2). The rates correspond to the results shown in Fig. 2.

have shown that a giant enhancement of the zero-frequency current noise in both models can be explained in terms of a slow bistable switching behavior. For both models, this interpretation is supported further by a numerical evaluation of the finite-frequency current noise. We underline that although the two models behave very differently, it is the same mechanism that is responsible for the giant enhancement of the noise.

REFERENCES

1. L. Y. Gorelik *et al.*, *Phys. Rev. Lett.*, **80**, 4526 (1998).
2. T. Novotný, A. Donarini, and A.-P. Jauho, *Phys. Rev. Lett.*, **90**, 256801 (2003).
3. A. D. Armour, and A. MacKinnon, *Phys. Rev. B*, **66**, 035333 (2002).
4. C. Flindt, T. Novotný, and A.-P. Jauho, *Phys. Rev. B*, **70**, 205334 (2004).
5. U. Weiss, *Quantum Dissipative Systems*, 2nd ed. (World Scientific, Singapore, 1999).
6. S. A. Gurvitz and Ya. S. Prager, *Phys. Rev. B*, **53**, 15392 (1996).
7. C. Flindt, T. Novotný, and A.-P. Jauho, *Europhys. Lett.*, **69**, 475 (2005).
8. A. N. Jordan, and E. V. Sukhorukov, *Phys. Rev. Lett.*, **93**, 260604 (2004).
9. A. N. Jordan, and E. V. Sukhorukov, cond-mat/0503751.
10. A. Donarini, *Dynamics of Shuttle Devices*, PhD thesis, MIC, DTU, cond-mat/0501242 (2004).
11. T. Novotný, A. Donarini, C. Flindt, and A.-P. Jauho, *Phys. Rev. Lett.*, **92**, 248302 (2004).
12. C. Flindt, T. Novotný, and A.-P. Jauho, to appear in *Physica E*, cond-mat/0412425.

Paper G

C. Flindt, T. Novotný, and A.-P. Jauho

Current noise spectrum of a quantum shuttle

Physica E **29**, 411 (2005)

The theory was developed by CF and TN in a joint effort. The numerical results are due to CF. The derivation of MacDonalds formula is due to TN. APJ contributed in the analysis of the results and with general supervision. The writing of the manuscript was done by CF, TN, and APJ in a joint effort.

Available online at www.sciencedirect.com
SCIENCE DIRECT®
ELSEVIER
Physica E 29 (2005) 411–418
PHYSICA E
www.elsevier.com/locate/physe

Current noise spectrum of a quantum shuttle

Christian Flindt[a,*], Tomáš Novotný[b,c], Antti-Pekka Jauho[a]

[a]*NanoDTU, MIC — Department of Micro and Nanotechnology, Technical University of Denmark, DTU, Building 345 east, DK-2800 Kongens Lyngby, Denmark*
[b]*Nano-Science Center, University of Copenhagen, Universitetsparken 5, DK-2100 Copenhagen Ø, Denmark*
[c]*Department of Electronic Structures, Faculty of Mathematics and Physics, Charles University, Ke Karlovu 5, 12116 Prague, Czech Republic*

Available online 1 July 2005

Abstract

We present a method for calculating the full current noise spectrum $S(\omega)$ for the class of nano-electromechanical systems (NEMS) that can be described by a Markovian generalized master equation. As a specific example we apply the method to a quantum shuttle. The noise spectrum of the shuttle has peaks at integer multiples of the mechanical frequency, which is slightly renormalized. The renormalization explains a previously observed small deviation of the shuttle current compared to the expected value given by the product of the natural mechanical frequency and the electron charge. For a certain parameter range the quantum shuttle exhibits a coexistence regime, where the charges are transported by two different mechanisms: shuttling and sequential tunneling. In our previous studies we showed that characteristic features in the zero-frequency noise could be quantitatively understood as a slow switching process between the two current channels, and the present study shows that this interpretation holds also qualitatively at finite frequency.

PACS: 85.85.+j; 72.70.+m; 73.23.Hk

Keywords: NEMS; Quantum shuttles; Current noise

1. Introduction

A decade of advances in microfabrication technology has pushed the typical length scales of electromechanical systems to the limit, where quantum mechanical effects of the mechanical motion must be taken into account [1]. Such nano-electromechanical systems (NEMS) exhibit a strong interplay between mechanical and electronic (or magnetic) degrees of freedom, and their electronic transport properties reflect this interplay in an intricate manner.

A modern trend in transport studies of mesoscopic systems has been to not only consider the current–voltage characteristics of a given device,

*Corresponding author.
E-mail address: cf@mic.dtu.dk (C. Flindt).

1386-9477/$ - see front matter © 2005 Elsevier B.V. All rights reserved.
doi:10.1016/j.physe.2005.05.040

but also to examine the noise properties, or even the higher cumulants (i.e. the full counting statistics (FCS)) of the current distribution [2,3]. The current noise, either its zero-frequency component or the whole frequency spectrum, provides more information than just the mean current and can be used to discern among different possible mechanisms resulting in the same mean current. While the noise spectra in generic mesoscopic systems have been studied well over a decade, it is only very recently that the study of noise spectra of NEMS has been initiated [4–6].

The aforementioned three studies deal with the noise spectra of a classical shuttle, a classical nanomechanical resonator coupled to a single electron transistor (SET), and the C_{60}-SET in a strong electromechanical coupling regime, respectively. The first two studies [4,5] found peaks in the current noise spectra at the first two multiples of the mechanical frequency. For low bias voltages and strong electromechnical coupling the third study [6] found a power-law frequency dependence of the noise spectrum attributed to scale-free avalanche charge transfer processes. In all three cases the noise spectra revealed interesting details about the systems. From the technical point of view, two of the studies [4,6] used Monte Carlo simulations, whereas [5] used a model-specific numerical evaluation of the MacDonald formula (see below).

In this work, we present a study of the full frequency spectrum of the current noise of a quantum shuttle [7–9]. We extend the general formalism developed for the zero-frequency noise [10,11] and the FCS [12] calculations for NEMS described by a Markovian generalized master equation (GME). The presented formalism applies not only to the shuttle studied here but could equally well be used for all three systems from the previous studies [4–6] for the determination of the noise spectra.

We apply the developed theory to compute numerically the noise spectrum of the shuttle in the deep quantum regime[1] as function of the damping coefficient. The spectrum has peaks at integer multiples of the slightly *renormalized* mechanical frequency. The renormalization of the bare oscillator frequency as read off from the current spectrum explains a small but observable deviation from the expected value of the current in the shuttling regime $I_{\rm shut} = e\omega_0/2\pi$ [8]. It turns out that it is the renormalized oscillator frequency $\tilde{\omega}_0$ which should enter this relation. Finally, we focus on the low-frequency part of the spectrum when approaching the semi-classical regime for intermediate values of the damping, i.e. in the coexistence regime, where both shuttling and tunneling are effective. We use the frequency dependence of the spectrum for $\omega \ll \omega_0$ to identify additional qualitative evidence for the bistable behavior of the shuttle in this regime described by a simple analytical theory of a slow switching between two current channels (compare with Refs. [12,13]).

2. Model

We consider the model of a quantum shuttle described in Refs. [7–10]. The shuttle consists of a mechanically oscillating nanoscale grain situated between two leads (see Fig. 1). In the strong Coulomb blockade regime the grain can be treated as having a single electronic level only. A high bias between the leads drives electrons through the grain and exerts an electrostatic force on the grain, when charged. The grain is assumed to move in a harmonic potential, and the oscillations of the grain are treated fully quantum mechanically. Damping of the oscillations is described by interactions with a surrounding heat bath.

From the Hamiltonian of the model one can derive a generalized master equation resolved with respect to the number of electrons n that have been collected in the right lead during the time span 0 to t. The n-resolved GME describes the time evolution of the n-resolved system density matrix $\hat{\rho}^{(n)}(t)$, where the 'system' consists of the electronic level of the grain and the quantized oscillations. In the following we only need the n-resolved GME for the part of $\hat{\rho}^{(n)}(t)$ that is diagonal in the electronic

[1] In this regime $\lambda \simeq x_0$, where λ is the tunneling length (see also Eq. (1)) and $x_0 = \sqrt{\hbar/m\omega_0}$ sets the length scale for the quantum mechanical zero-point motion.

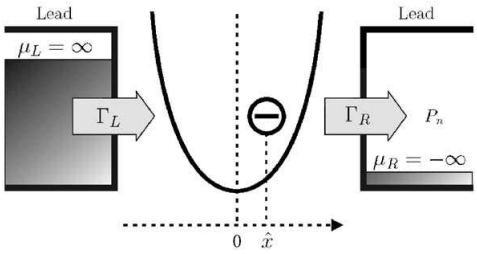

Fig. 1. The quantum shuttle consists of a nanosized grain moving in a harmonic potential between two leads. A high bias between the leads drives electrons through the grain.

components, which reads [10]

$$\dot{\hat{\rho}}_{00}^{(n)}(t) = \frac{1}{\mathrm{i}\hbar}[\hat{H}_{\mathrm{osc}}, \hat{\rho}_{00}^{(n)}(t)] + \mathscr{L}_{\mathrm{damp}}\hat{\rho}_{00}^{(n)}(t) - \frac{\Gamma_{\mathrm{L}}}{2}\{\mathrm{e}^{-2\hat{x}/\lambda}, \hat{\rho}_{00}^{(n)}(t)\} + \Gamma_{\mathrm{R}}\mathrm{e}^{\hat{x}/\lambda}\hat{\rho}_{11}^{(n-1)}(t)\mathrm{e}^{\hat{x}/\lambda},$$

$$\dot{\hat{\rho}}_{11}^{(n)}(t) = \frac{1}{\mathrm{i}\hbar}[\hat{H}_{\mathrm{osc}} - eE\hat{x}, \hat{\rho}_{11}^{(n)}(t)] + \mathscr{L}_{\mathrm{damp}}\hat{\rho}_{11}^{(n)}(t) - \frac{\Gamma_{\mathrm{R}}}{2}\{\mathrm{e}^{2\hat{x}/\lambda}, \hat{\rho}_{11}^{(n)}(t)\} + \Gamma_{\mathrm{L}}\mathrm{e}^{-\hat{x}/\lambda}\hat{\rho}_{00}^{(n)}(t)\mathrm{e}^{-\hat{x}/\lambda} \tag{1}$$

with $n = 0, 1, 2, \ldots$ and $\hat{\rho}_{11}^{(-1)}(t) \equiv 0$. The commutators describe the coherent evolution of the charged ($\hat{\rho}_{11}^{(n)} \equiv \langle 1|\hat{\rho}^{(n)}|1\rangle$) or empty ($\hat{\rho}_{00}^{(n)} \equiv \langle 0|\hat{\rho}^{(n)}|0\rangle$) shuttle with mass m and natural frequency ω_0. The electric field[2] between the leads is denoted E. The terms proportional to $\Gamma_{\mathrm{L(R)}}$ describe transfer processes from the left (to the right) lead with hopping amplitudes that depend exponentially on the ratio between position $\hat{x}$ and the electron tunneling length λ. The mechanical damping of the oscillator is described by the damping kernel (here at zero temperature) $\mathscr{L}_{\mathrm{damp}}\hat{\rho}_{jj}^{(n)} = -\frac{\mathrm{i}\gamma}{2\hbar}[\hat{x}, \{\hat{p}, \hat{\rho}_{jj}^{(n)}\}] - \frac{\gamma m\omega_0}{2\hbar}[\hat{x}, [\hat{x}, \hat{\rho}_{jj}^{(n)}]], j = 0, 1$ [8,10].

The n-resolved GME can be recast into the compact form [11]

$$\dot{\hat{\rho}}^{(n)} = (\mathscr{L} - \mathscr{I}_{\mathrm{R}})\hat{\rho}^{(n)} + \mathscr{I}_{\mathrm{R}}\hat{\rho}^{(n-1)}, \hat{\rho}^{(-1)} \equiv 0, \tag{2}$$

where we have introduced the Liouvillean $\mathscr{L}$, describing the evolution of the system density matrix $\hat{\rho}(t) = \sum_n \hat{\rho}^{(n)}(t)$, i.e. $\dot{\hat{\rho}}(t) = \mathscr{L}\hat{\rho}(t)$, and the superoperator for the tunnel current through the right junction (taking $e = 1$), defined by its action on the density operator

$$\mathscr{I}_{\mathrm{R}}\hat{\rho} = \Gamma_{\mathrm{R}}\mathrm{e}^{\hat{x}/\lambda}|0\rangle\langle 1|\hat{\rho}|1\rangle\langle 0|\mathrm{e}^{\hat{x}/\lambda}. \tag{3}$$

Assuming that the system tends exponentially to a stationary state $\hat{\rho}^{\mathrm{stat}}$ the Liouvillean has a single eigenvalue equal to zero with $\hat{\rho}^{\mathrm{stat}}$ being the (unique and normalized) right eigenvector which we denote by $|0\rangle\rangle$ [11]. The corresponding left eigenvector is the identity operator $\hat{1}$ which we denote by $\langle\langle\tilde{0}|$, and from the definition of the inner product[3] we have $\langle\langle\tilde{0}|0\rangle\rangle = \mathrm{Tr}(\hat{1}^{\dagger}\hat{\rho}^{\mathrm{stat}}) = 1$. In terms of $\mathscr{I}_{\mathrm{R}}$ the average tunnel current in the stationary state can be expressed as

$$\langle\hat{I}_{\mathrm{R}}\rangle = \mathrm{Tr}(\mathscr{I}_{\mathrm{R}}\hat{\rho}^{\mathrm{stat}}) = \langle\langle\tilde{0}|\mathscr{I}_{\mathrm{R}}|0\rangle\rangle. \tag{4}$$

We define the projectors $\mathscr{P} = |0\rangle\rangle\langle\langle\tilde{0}|$ and $\mathscr{Q} = 1 - \mathscr{P}$ obeying the relations $\mathscr{P}\mathscr{L} = \mathscr{L}\mathscr{P} = 0$ and $\mathscr{Q}\mathscr{L}\mathscr{Q} = \mathscr{L}$. In terms of the two projectors we can express the resolvent of the Liouvillean $\mathscr{G}(-\mathrm{i}\omega) = (-\mathrm{i}\omega - \mathscr{L})^{-1}$ as

$$\mathscr{G}(-\mathrm{i}\omega) = -\frac{1}{\mathrm{i}\omega}\mathscr{P} - \mathscr{Q}\frac{1}{\mathrm{i}\omega + \mathscr{L}}\mathscr{Q} = -\frac{1}{\mathrm{i}\omega}\mathscr{P} - \mathscr{R}(\omega), \tag{5}$$

where we have introduced the frequency dependent superoperator $\mathscr{R}(\omega)$, which is well-defined even for $\omega = 0$, since the inversion in that case is performed only in the subspace where $\mathscr{L}$ is regular.

3. Theory

We consider the current autocorrelation function defined as

$$C_{II}(t', t'') = \tfrac{1}{2}\langle\{\Delta\hat{I}(t'), \Delta\hat{I}(t'')\}\rangle, \tag{6}$$

where $\Delta\hat{I}(t) = \hat{I}(t) - \langle\hat{I}(t)\rangle$. In the stationary state $C_{II}(t', t'')$ can only be a function of the time difference $t = t' - t''$, and we thus write

$$C_{II}(t) = \tfrac{1}{2}\langle\{\Delta\hat{I}(t), \Delta\hat{I}(0)\}\rangle. \tag{7}$$

[2] In order to obtain a Markovian GME it is necessary to assume that the bias applied between the leads is the highest energy scale of the system [8]. Nevertheless, we consider the electric field between the leads as a free parameter of the model.

[3] We define the inner product of two supervectors as $\langle\langle a|b\rangle\rangle = \mathrm{Tr}(\hat{A}^{\dagger}\hat{B})$ with the identification $|o\rangle\rangle \leftrightarrow \hat{O}$, where $\hat{O}$ is a quantum mechanical operator and $|o\rangle\rangle$ is the corresponding supervector.

The current noise spectrum is the Fourier transform of $C_{II}(t)$, i.e.

$$S_{II}(\omega) \equiv \int_{-\infty}^{\infty} \mathrm{d}t C_{II}(t) \mathrm{e}^{\mathrm{i}\omega t}. \tag{8}$$

In order to calculate the current noise measurable in, say, the right lead one must recognize that the current running in the lead is a sum of two contributions, namely the tunnel current through the right junction and a displacement current induced by electrons tunneling between leads and grain. This is reflected in the Ramo–Shockley theorem [2]

$$\hat{I} = c_{\mathrm{L}} \hat{I}_{\mathrm{R}} + c_{\mathrm{R}} \hat{I}_{\mathrm{L}}. \tag{9}$$

Here $\hat{I}$ is the current operator for the current running in the lead, whereas $\hat{I}_{\mathrm{L(R)}}$ is the operator for the tunnel current through the left (right) junction, and $c_{\mathrm{L(R)}}$ is the relative capacitance of the left (right) junction in the sense $c_{\mathrm{L}} + c_{\mathrm{R}} = 1$. Combining the Ramo–Shockley theorem with charge conservation leads to an expression for the current noise measured in the lead [14]

$$S_{II}(\omega) = c_{\mathrm{L}} S_{I_{\mathrm{R}} I_{\mathrm{R}}}(\omega) + c_{\mathrm{R}} S_{I_{\mathrm{L}} I_{\mathrm{L}}}(\omega) - c_{\mathrm{L}} c_{\mathrm{R}} \omega^2 S_{NN}(\omega), \tag{10}$$

where $\hat{N} = |1\rangle\langle 1|$ is the occupation number operator of the electronic level of the grain. In the following we neglect any dependence of the capacitances on the position of the grain and consider the symmetric case $c_{\mathrm{L}} = c_{\mathrm{R}} = \frac{1}{2}$.

The two first terms of Eq. (10) can be evaluated using the methods developed by MacDonald [15]. The starting point of the derivation is the property $C_{II}(t) = C_{II}(-t)$, which immediately leads to

$$S_{I_{\mathrm{R}} I_{\mathrm{R}}}(\omega) = \int_0^{\infty} \mathrm{d}t C_{I_{\mathrm{R}} I_{\mathrm{R}}}(t) (\mathrm{e}^{\mathrm{i}\omega t} + \mathrm{e}^{-\mathrm{i}\omega t}). \tag{11}$$

Let us consider the first term

$$S^{+}_{I_{\mathrm{R}} I_{\mathrm{R}}}(\omega) \equiv \int_0^{\infty} \mathrm{d}t C_{I_{\mathrm{R}} I_{\mathrm{R}}}(t) \mathrm{e}^{\mathrm{i}\omega t}, \tag{12}$$

the second term, $S^{-}_{I_{\mathrm{R}} I_{\mathrm{R}}}(\omega)$, follows analogously. Defining $\hat{Q}_{\mathrm{R}}(t)$ as the operator of charge collected in the right lead in the time span 0 to t we have

$$\Delta\hat{Q}_{\mathrm{R}}(t) = \hat{Q}_{\mathrm{R}}(t) - \langle \hat{Q}_{\mathrm{R}}(t) \rangle = \int_0^t \mathrm{d}t' \Delta\hat{I}_{\mathrm{R}}(t'), \tag{13}$$

and we can express the current autocorrelation function as

$$C_{I_{\mathrm{R}} I_{\mathrm{R}}}(t) = \frac{1}{2} \frac{\mathrm{d}}{\mathrm{d}t} \langle \{ \Delta\hat{Q}_{\mathrm{R}}(t), \Delta\hat{I}_{\mathrm{R}}(0) \} \rangle. \tag{14}$$

Introducing the convergence factor $\varepsilon \to 0^+$ and performing the integration by parts in Eq. (12) we get

$$S^{+}_{I_{\mathrm{R}} I_{\mathrm{R}}}(\omega) = \int_0^{\infty} \mathrm{d}t \langle \{ \Delta\hat{Q}_{\mathrm{R}}(t), \Delta\hat{I}_{\mathrm{R}}(0) \} \rangle \times \frac{\omega + \mathrm{i}\varepsilon}{2\mathrm{i}} \mathrm{e}^{\mathrm{i}(\omega + \mathrm{i}\varepsilon)t}. \tag{15}$$

Since $\langle \{ \Delta\hat{Q}_{\mathrm{R}}(t), \Delta\hat{I}_{\mathrm{R}}(0) \} \rangle = \langle \{ \Delta\hat{Q}_{\mathrm{R}}(t), \Delta\hat{I}_{\mathrm{R}}(t) \} \rangle = \frac{\mathrm{d}}{\mathrm{d}t} \langle \Delta\hat{Q}^2_{\mathrm{R}}(t) \rangle$ in the stationary state[4] we can write

$$S^{+}_{I_{\mathrm{R}} I_{\mathrm{R}}}(\omega) = \int_0^{\infty} \mathrm{d}t \frac{\mathrm{d}}{\mathrm{d}t} \langle \Delta\hat{Q}^2_{\mathrm{R}}(t) \rangle \frac{\omega + \mathrm{i}\varepsilon}{2\mathrm{i}} \mathrm{e}^{\mathrm{i}(\omega + \mathrm{i}\varepsilon)t}. \tag{16}$$

Similarly, we find

$$S^{-}_{I_{\mathrm{R}} I_{\mathrm{R}}}(\omega) = -\int_0^{\infty} \mathrm{d}t \frac{\mathrm{d}}{\mathrm{d}t} \langle \Delta\hat{Q}^2_{\mathrm{R}}(t) \rangle \frac{\omega - \mathrm{i}\varepsilon}{2\mathrm{i}} \mathrm{e}^{-\mathrm{i}(\omega - \mathrm{i}\varepsilon)t}, \tag{17}$$

and consequently

$$S_{I_{\mathrm{R}} I_{\mathrm{R}}}(\omega) = \int_0^{\infty} \mathrm{d}t \frac{\mathrm{d}}{\mathrm{d}t} \langle \Delta\hat{Q}^2_{\mathrm{R}}(t) \rangle \times (\omega \sin \omega t + \varepsilon \cos \omega t) \mathrm{e}^{-\varepsilon t}. \tag{18}$$

We now make use of the fact that

$$\langle \Delta\hat{Q}^2_{\mathrm{R}}(t) \rangle = \langle \hat{Q}^2_{\mathrm{R}}(t) \rangle - \langle \hat{Q}_{\mathrm{R}}(t) \rangle^2 = \langle n^2(t) \rangle - \langle n(t) \rangle^2 \tag{19}$$

with $\langle n^{\alpha}(t) \rangle \equiv \sum_{n=0}^{\infty} n^{\alpha} P_n(t), \alpha = 1, 2$, where $P_n(t)$ is the probability of having collected $n = 0, 1, 2, \ldots$ electrons in the right lead during the time span 0 to t. This finally leads us to the commonly used form of the MacDonald formula (cf. Refs. [5,14,15])

$$S_{I_{\mathrm{R}} I_{\mathrm{R}}}(\omega) = \omega \int_0^{\infty} \mathrm{d}t \, \sin(\omega t) \frac{\mathrm{d}}{\mathrm{d}t} [\langle n^2(t) \rangle - \langle n(t) \rangle^2], \tag{20}$$

[4] The first equality follows from a simple substitution $\tau \to t - \tau$ in the chain $\langle \{ \Delta\hat{Q}_{\mathrm{R}}(t), \Delta\hat{I}_{\mathrm{R}}(0) \} \rangle = \int_0^t \mathrm{d}\tau \langle \{ \Delta\hat{I}_{\mathrm{R}}(\tau), \Delta\hat{I}_{\mathrm{R}}(0) \} \rangle = \int_0^t \mathrm{d}\tau \langle \{ \Delta\hat{I}_{\mathrm{R}}(t), \Delta\hat{I}_{\mathrm{R}}(\tau) \} \rangle = \langle \{ \Delta\hat{Q}_{\mathrm{R}}(t), \Delta\hat{I}_{\mathrm{R}}(t) \} \rangle$.

where the regularization

$$\omega\sin(\omega t)\to\frac{1}{2\mathrm{i}}((\omega+\mathrm{i}\varepsilon)\mathrm{e}^{\mathrm{i}(\omega+\mathrm{i}\varepsilon)t}-(\omega-\mathrm{i}\varepsilon)\mathrm{e}^{-\mathrm{i}(\omega-\mathrm{i}\varepsilon)t})$$
$$=(\omega\sin\omega t+\varepsilon\cos\omega t)\mathrm{e}^{-\varepsilon t},\varepsilon\to 0^{+} \quad (21)$$

is implied. Only the proper treatment of the regularization ensures correct results including the $\omega=0$ case where the zero-frequency noise MacDonald formula is recovered (by using the Laplace transform identity for $\varepsilon\to 0^{+}$)

$$S_{I_\mathrm{R}I_\mathrm{R}}(0)=\varepsilon\int_0^\infty \mathrm{d}t\,\mathrm{e}^{-\varepsilon t}\frac{\mathrm{d}}{\mathrm{d}t}[\langle n^2(t)\rangle-\langle n(t)\rangle^2]$$
$$=\frac{\mathrm{d}}{\mathrm{d}t}[\langle n^2(t)\rangle-\langle n(t)\rangle^2]|_{t\to\infty}. \quad (22)$$

In order to evaluate the current noise spectrum we now introduce the quantity

$$\tilde{S}(\omega)=\omega\int_0^\infty \mathrm{d}t\mathrm{e}^{\mathrm{i}\omega t}\left[\frac{\mathrm{d}}{\mathrm{d}t}\langle n^2(t)\rangle-2\langle n(t)\rangle\frac{\mathrm{d}}{\mathrm{d}t}\langle n(t)\rangle\right] \quad (23)$$

with either $S(\omega)=\mathrm{Im}\,\tilde{S}(\omega)$ or $S(\omega)=(\tilde{S}(\omega)+\tilde{S}(-\omega))/2\mathrm{i}$ and evaluate it along the lines of Ref. [11]. Since $P_n(t)=\mathrm{Tr}(\hat{\rho}^{(n)}(t))$, Eq. (2) leads to (keeping in mind that $\mathrm{Tr}(\mathscr{L}\bullet)=0$)

$$\dot{P}_n(t)=\mathrm{Tr}[\mathscr{I}_\mathrm{R}(\hat{\rho}^{(n-1)}(t)-\hat{\rho}^{(n)}(t))], \quad (24)$$

and as shown in Ref. [11]

$$\frac{\mathrm{d}}{\mathrm{d}t}\langle n(t)\rangle=\mathrm{Tr}(\mathscr{I}_\mathrm{R}\hat{\rho}(t))=\langle\langle\tilde{0}|\mathscr{I}_\mathrm{R}|0\rangle\rangle, \quad (25)$$

$$\frac{\mathrm{d}}{\mathrm{d}t}\langle n^2(t)\rangle=2\mathrm{Tr}\left[\mathscr{I}_\mathrm{R}\sum_n n\hat{\rho}^{(n)}(t)\right]+\langle\langle\tilde{0}|\mathscr{I}_\mathrm{R}|0\rangle\rangle, \quad (26)$$

where we have used $\hat{\rho}(t)=\hat{\rho}^{\mathrm{stat}}$, since we are considering the stationary limit. The sum entering Eq. (26) is evaluated by introducing an operator-valued generating function defined as $\hat{F}(t,z)=\sum_{n=0}^\infty\hat{\rho}^{(n)}(t)z^n$, from which we get

$$\frac{\partial}{\partial z}\hat{F}(t,z)|_{z=1}=\sum_n n\hat{\rho}^{(n)}(t). \quad (27)$$

From the definition of the Laplace transform, $\tilde{\hat{F}}(s,z)=\int_0^\infty \mathrm{d}t\hat{F}(t,z)\mathrm{e}^{-st}$, we see that the integration in Eq. (23) can be considered as a Laplace transform evaluated at $s=-\mathrm{i}\omega+\varepsilon$ (remember the proper regularization; from now on we skip explicitly mentioning the ε-factors). In Ref. [11] it was shown that

$$\frac{\partial}{\partial z}\tilde{\hat{F}}(s=-\mathrm{i}\omega,z)|_{z=1}=\mathscr{G}(-\mathrm{i}\omega)\mathscr{I}_\mathrm{R}\mathscr{G}(-\mathrm{i}\omega)\hat{\rho}(0)$$
$$+\mathscr{G}(-\mathrm{i}\omega)\sum_n n\hat{\rho}^{(n)}(0). \quad (28)$$

Again, we have $\hat{\rho}(0)=\hat{\rho}^{\mathrm{stat}}$, and moreover we assume the factorized initial condition [14,16] $\hat{\rho}^{(n)}(0)=\delta_{0n}\hat{\rho}^{\mathrm{stat}}$, i.e. we start counting the charge passing through the right junction at $t=0$ and the system is in its stationary state. Now, combining Eqs. (5), (23)–(28) and having in mind that $\mathscr{P}\hat{\rho}^{\mathrm{stat}}=\hat{\rho}^{\mathrm{stat}},\mathscr{Q}\hat{\rho}^{\mathrm{stat}}=0$, straightforward algebra leads to

$$\tilde{S}(\omega)=\mathrm{i}\big(\langle\langle\tilde{0}|\mathscr{I}_\mathrm{R}|0\rangle\rangle-2\langle\langle\tilde{0}|\mathscr{I}_\mathrm{R}\mathscr{R}(\omega)\mathscr{I}_\mathrm{R}|0\rangle\rangle\big). \quad (29)$$

We thus arrive at

$$S_{I_\mathrm{R}I_\mathrm{R}}(\omega)=\langle\langle\tilde{0}|\mathscr{I}_\mathrm{R}|0\rangle\rangle-2\mathrm{Re}[\langle\langle\tilde{0}|\mathscr{I}_\mathrm{R}\mathscr{R}(\omega)\mathscr{I}_\mathrm{R}|0\rangle\rangle]$$
$$=\langle\langle\tilde{0}|\mathscr{I}_\mathrm{R}|0\rangle\rangle$$
$$-2\langle\langle\tilde{0}|\mathscr{I}_\mathrm{R}\left[\frac{\mathscr{L}}{\mathscr{L}^2+\omega^2}\right]\mathscr{I}_\mathrm{R}|0\rangle\rangle. \quad (30)$$

For the left junction one similarly finds

$$S_{I_\mathrm{L}I_\mathrm{L}}(\omega)=\langle\langle\tilde{0}|\mathscr{I}_\mathrm{L}|0\rangle\rangle-2\mathrm{Re}[\langle\langle\tilde{0}|\mathscr{I}_\mathrm{L}\mathscr{R}(\omega)\mathscr{I}_\mathrm{L}|0\rangle\rangle] \quad (31)$$

with

$$\mathscr{I}_\mathrm{L}\hat{\rho}=\Gamma_\mathrm{L}\mathrm{e}^{-\hat{x}/\lambda}|1\rangle\langle 0|\hat{\rho}|0\rangle\langle 1|\mathrm{e}^{-\hat{x}/\lambda}. \quad (32)$$

For the evaluation of the charge-charge correlation function $S_{NN}(\omega)$ we note that $\hat{N}$ is a system operator, and the quantum regression theorem thus applies [17]. Following [11] we immediately get

$$S_{NN}(\omega)=-2\mathrm{Re}[\langle\langle\tilde{0}|\mathscr{N}\mathscr{R}(\omega)\mathscr{N}|0\rangle\rangle], \quad (33)$$

having introduced the superoperator $\mathscr{N}$ corresponding to $\hat{N}$, defined as

$$\mathscr{N}\hat{\rho}=|1\rangle\langle 1|\hat{\rho}|1\rangle\langle 1|. \quad (34)$$

Collecting all terms in Eq. (10) we finally obtain the expression for the current noise measured

in the leads for the symmetric setup ($c_L = c_R = \frac{1}{2}$)

$$S_{II}(\omega) = \langle\langle\tilde{0}|\mathscr{I}_R|0\rangle\rangle + \frac{\omega^2}{2}\mathrm{Re}[\langle\langle\tilde{0}|\mathscr{N}\mathscr{R}(\omega)\mathscr{N}|0\rangle\rangle] - \mathrm{Re}[\langle\langle\tilde{0}|\mathscr{I}_R\mathscr{R}(\omega)\mathscr{I}_R + \mathscr{I}_L\mathscr{R}(\omega)\mathscr{I}_L|0\rangle\rangle]. \quad (35)$$

We notice that for $\omega = 0$ we get the previous result [10–12]

$$S_{II}(0) = \langle\langle\tilde{0}|\mathscr{I}_R|0\rangle\rangle - 2\langle\langle\tilde{0}|\mathscr{I}_R\mathscr{R}(0)\mathscr{I}_R|0\rangle\rangle, \quad (36)$$

since the zero-frequency tunnel current noise is the same at both junctions and the second term is real [11].

The numerical evaluation of Eq. (35) is only possible by truncating the number of oscillator states. As in previous studies [8,10,12] we retain the 100 lowest oscillator states, which however still leaves us with the task of dealing numerically with the matrix representations of the relevant superoperators, which are of size $20\,000 \times 20\,000$. As explained in Ref. [11] the stationary density matrix $\hat{\rho}^{\mathrm{stat}}$ (or $|0\rangle\rangle$) can be found using the Arnoldi iteration scheme, and $\mathscr{R}(\omega)$ can be evaluated using the generalized minimum residual method (GMRes). Both methods are iterative and rely crucially on an appropriate choice of preconditioner to ensure that the iterations converge and to speed up the computation. It should be stressed that finding a suitable preconditioner for a given problem is by no means simple. For finding $\hat{\rho}^{\mathrm{stat}}$ and $\mathscr{R}(0)$ it turns out that the Sylvester part of the Liouvillean, which is the part that can be written $\mathscr{L}_{\mathrm{sylv}}\hat{\rho} = \hat{A}\hat{\rho} + \hat{\rho}\hat{A}^{\dagger}$, is well-suited for preconditioning [11]. This preconditioner separates the zero eigenvalue from the rest of the spectrum of $\mathscr{L}$ leading to a decrease in computation time.

For finding $\mathscr{R}(\omega)$ the original preconditioner must be modified in order to separate the relevant eigenvalue from the rest of the spectrum. A reasonable choice is the superoperator $\mathscr{M}$ defined as

$$\mathscr{M}\hat{\rho} = \left(\hat{A} + \frac{i\omega}{2}\right)\hat{\rho} + \hat{\rho}\left(\hat{A} - \frac{i\omega}{2}\right)^{\dagger}. \quad (37)$$

For the range of parameters discussed in the present paper this choice of preconditioner was sufficient for convergence, however the obtained computational speedup is considerably smaller than the speedup provided by $\mathscr{L}_{\mathrm{sylv}}$, when computing $\mathscr{R}(0)$. This observation combined with the fact that GMRes fails to converge for certain parameters in the semi-classical regime indicates that the identification of the optimal preconditioner for the problem at hand remains an open problem.

4. Results

In Fig. 2 we show results for the current noise spectrum of the quantum shuttle in the deep quantum regime. In accordance with previous studies [4,5] we find peaks at integer multiples of the mechanical frequency. A close look at the spectrum reveals a slight renormalization of the mechanical frequency with the peaks appearing at $\omega = \tilde{\omega}_0, 2\tilde{\omega}_0, 3\tilde{\omega}_0$, where $\tilde{\omega}_0 \simeq 1.03\omega_0$. In the shuttling regime the current is expected to saturate at a value expressed as one electron per cycle of the mechanical vibrations. For a shuttle with mechanical frequency ω_0 this implies that the saturated shuttle current is $I_{\mathrm{shut}} = \omega_0/2\pi \simeq 0.159\omega_0$. For the given parameters the numerical calculation yields a slightly higher value, namely $I_{\mathrm{shut}} = 0.164\omega_0 = 0.159 \times 1.03\omega_0 \simeq \tilde{\omega}_0/2\pi$, and this can now be understood in light of the observed renormalization of the mechanical frequency.

In Refs. [12,13] it was shown that an observed giant enhancement of the zero-frequency noise [10] in the coexistence regime of a shuttle approaching the semi-classical regime can be understood in terms of a simple model of a bistable system switching slowly between two current channels (shuttling and tunneling). Denoting the currents of the two channels[5] as I_S and I_T, respectively, and the switching rates $\Gamma_{S\leftarrow T}$ and $\Gamma_{T\leftarrow S}$, one can show (following Ref. [13]) that the ratio between the current noise spectrum and the current (in the zero-frequency limit known as the Fano factor) $F(\omega) = S(\omega)/I$ for the bistable system has the

[5] $I_S = \frac{\tilde{\omega}_0}{2\pi}$, and $I_T = \frac{\tilde{\Gamma}_L\tilde{\Gamma}_R}{\tilde{\Gamma}_L+\tilde{\Gamma}_R}$, with $\tilde{\Gamma}_R = \Gamma_R e^{\hbar/m\omega_0\lambda^2} e^{2eE/m\omega_0^2\lambda}$, $\tilde{\Gamma}_L = \Gamma_L e^{\hbar/m\omega_0\lambda^2}$ [10,13].

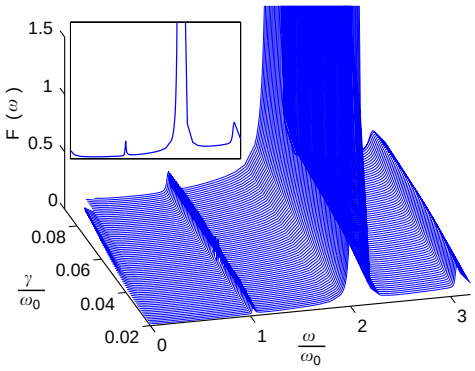

Fig. 2. The ratio between the current noise and the current $F(\omega) = S_{II}(\omega)/\langle \hat{I} \rangle$ as function of the damping γ and frequency ω. The other parameters are $\Gamma_L = \Gamma_R = 0.05\omega_0$, $\lambda = x_0$, $d \equiv eE/m\omega_0^2 = 0.5x_0$, where $x_0 = \sqrt{\hbar/m\omega_0}$. Peaks are seen at $\omega \simeq 1.03\omega_0$, $2.06\omega_0, 3.09\omega_0$. The peak at $\omega \simeq 2.06\omega_0$ reaches values of $F(\omega) \simeq 20$ (not shown) for $\gamma = 0.02$ and decreases monotonously with increasing γ to $F(\omega) \simeq 6$ for $\gamma = 0.09$. The insert shows a representative curve ($\gamma = 0.05$).

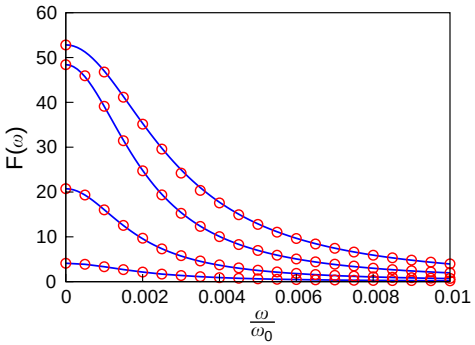

Fig. 3. The ratio between the current noise and the current $F(\omega) = S_{II}(\omega)/\langle \hat{I} \rangle$ for low frequencies ($\omega \ll \omega_0$). The parameters are $\gamma = 0.035\omega_0$ (lowest curve), $0.04\omega_0, 0.045\omega_0, 0.05\omega_0$ (topmost curve), $\Gamma_L = \Gamma_R = 0.01\omega_0$, $\lambda = 1.5x_0$, $d \equiv eE/m\omega_0^2 = 0.5x_0$, where $x_0 = \sqrt{\hbar/m\omega_0}$. The circles indicate numerical results, while the full lines indicate the analytic results for the current noise spectrum of a bistable system. It should be noted that in order to obtain the agreement between the numerical and analytic results it is necessary to assume that the shuttling current for the given values of γ is not fully saturated to the value $I_{\text{shut}} = 1.03\omega_0/2\pi$. Corresponding to the different values of γ we have used $I_{\text{shut}} = 1.01\omega_0/2\pi$ (for $\gamma = 0.03\omega_0$), $1.00\omega_0/2\pi$, $0.98\omega_0/2\pi$, $0.94\omega_0/2\pi$ (for $\gamma = 0.05\omega_0$), respectively.

Lorentzian form

$$F(\omega) = \frac{2}{I}\frac{\Gamma_{S\leftarrow T}\Gamma_{T\leftarrow S}}{\Gamma_{S\leftarrow T}+\Gamma_{T\leftarrow S}}\frac{(I_S - I_T)^2}{(\Gamma_{S\leftarrow T}+\Gamma_{T\leftarrow S})^2+\omega^2}, \tag{38}$$

where

$$I = \frac{I_S\Gamma_{S\leftarrow T} + I_T\Gamma_{T\leftarrow S}}{\Gamma_{S\leftarrow T}+\Gamma_{T\leftarrow S}}. \tag{39}$$

The two switching rates, $\Gamma_{S\leftarrow T}$ and $\Gamma_{T\leftarrow S}$, can be extracted from the numerical values of current and zero-frequency noise, and by comparing Eq. (38) with the noise spectrum obtained numerically, one can perform another independent test of the hypothesis that the shuttle behaves as a bistable system in the coexistence regime.

In Fig. 3 we show numerical results for the low-frequency current noise of the quantum shuttle in the coexistence regime. Together with the numerical results we show the analytic expression for the current noise of the bistable system (Eq. (38)) with rates extracted from the numerical values of current and zero-frequency noise. It should be noted that the agreement between the numerical and analytic results could only be obtained by assuming that the shuttling current for the given values of the damping is not fully saturated to the value $I_{\text{shut}} = \tilde{\omega}_0/2\pi$. The current noise spectrum thus provides us with qualitative evidence for the shuttle behaving as a bistable system in the coexistence regime, while it, however, leaves us with an open question concerning the saturation of the shuttling current.

5. Conclusion

We have presented a theory for the calculation of the current noise spectrum of a large class of nano-electromechanical systems, namely those that can be described by a Markovian generalized master equation. As a specific example we have applied the theory to a quantum shuttle. For the quantum shuttle numerical calculations of the current noise spectrum in the deep quantum regime revealed a slight renormalization of the

mechanical frequency—this, in turn, explains an observed small deviation of the shuttle current compared to the expected value given by the product of the natural mechanical frequency and the electron charge. When approaching the semi-classical regime the low-frequency noise served as another evidence for the quantum shuttle behaving as a bistable system, switching slowly between two current channels, thus supporting this claim, previously based on the calculation of the full counting statistics of the quantum shuttle. The theory presented here has a broad range of applicability, encompassing the few previous studies of the current noise spectra of nano-electromechanical systems.

Acknowledgements

The authors would like to thank A. Donarini, A.D. Armour, and A. Isacsson for stimulating discussions.

References

[1] M. Blencowe, Phys. Rep. 395 (2004) 159.
[2] Ya.M. Blanter, M. Büttiker, Phys. Rep. 336 (2000) 1.
[3] Quantum Noise in Mesoscopic Systems, NATO Science Series II, vol. 97, Yu.V. Nazarov (Eds.), Kluwer, Dordrecht, 2003.
[4] A. Isacsson, T. Nord, Europhys. Lett. 66 (2004) 708.
[5] A.D. Armour, Phys. Rev. B 70 (2004) 165315.
[6] J. Koch, F. von Oppen, Phys. Rev. Lett. 94 (2005) 206804.
[7] L.Y. Gorelik, A. Isacsson, M.V. Voinova, B. Kasemo, R.I. Shekhter, M. Jonson, Phys. Rev. Lett. 80 (1998) 4526.
[8] T. Novotný, A. Donarini, A.-P. Jauho, Phys. Rev. Lett. 90 (2003) 256801.
[9] D. Fedorets, L.Y. Gorelik, R.I. Shekhter, M. Jonson, Phys. Rev. Lett. 92 (2004) 166801.
[10] T. Novotný, A. Donarini, C. Flindt, A.-P. Jauho, Phys. Rev. Lett. 92 (2004) 248302.
[11] C. Flindt, T. Novotný, A.-P. Jauho, Phys. Rev. B 70 (2004) 205334.
[12] C. Flindt, T. Novotný, A.-P. Jauho, Europhys. Lett. 69 (2005) 475.
[13] A. Donarini, Ph.D. Thesis, Technical University of Denmark, Lyngby, 2004.
[14] R. Aguado, T. Brandes, Phys. Rev. Lett. 92 (2004) 206601.
[15] D.K.C. MacDonald, Noise and Fluctuations: An Introduction, Wiley, New York, 1962.
[16] R. Ruskov, A.N. Korotkov, Phys. Rev. B 67 (2003) 075303.
[17] C.W. Gardiner, P. Zoller, Quantum Noise, second ed., Springer, New York, 2000.

Paper I

C. Flindt, N. A. Mortensen, and A.-P. Jauho

Quantum Computing via Defect States in Two-Dimensional Anti-Dot Lattices

Nano Lett. **5**, 2515 (2005)

The initial idea was developed by CF and NAM in a joint effort, while the implementation is mainly due to CF. Eqs. (3) and (4) are due to NAM. The writing is due to CF, NAM, and APJ in a joint effort.

NANO LETTERS

2005
Vol. 5, No. 12
2515−2518

Quantum Computing via Defect States in Two-Dimensional Antidot Lattices

Christian Flindt,* Niels Asger Mortensen, and Antti-Pekka Jauho

MIC −Department of Micro and Nanotechnology, NanoDTU, Technical University of Denmark, Building 345east, DK-2800 Kongens Lyngby, Denmark

Received September 15, 2005; Revised Manuscript Received October 14, 2005

ABSTRACT

We propose a new structure suitable for quantum computing in a solid-state environment: designed defect states in antidot lattices superimposed on a two-dimensional electron gas at a semiconductor heterostructure. State manipulation can be obtained with gate control. Model calculations indicate that it is feasible to fabricate structures whose energy level structure is robust against thermal dephasing.

At present an intensive search is taking place for solid-state structures which are suitable for quantum computing; a typical example consists of gate-defined double-dot systems studied by several groups.[1−6] A necessary requirement for a practical application is scalability,[7] and many of the existing structures do not immediately offer this possibility. Here we propose an alternative scheme: quantum-mechanical bound states which form at defects in an antidot superlattice defined on a semiconductor heterostructure. Scalability is not a critical issue for the suggested structures, which enable the fabrication of a large number of solid-state qubits with no particular extra effort. The flexibility offered by e-beam or local oxidation techniques allows the sample designer to optimize the samples for many different purposes with a very high degree of control.

Antidot lattices on semiconductor heterostructures have been a topic of intense research due to their interesting transport properties. In the semiclassical regime novel oscillatory features in magnetoresistance have been discovered,[8] and as the lattice spacing is diminished and the quantum regime is approached, exotic energy spectra, such as the Hofstadter butterfly[9] may become experimentally accessible. The fabrication of antidot lattices with lattice constants as small as 75 nm has been demonstrated in experiments.[10] Smaller lattice constants are however expected to be within experimental reach[11] leading to a further enhancement of quantum effects. We shall in this paper demonstrate that state-of-the-art antidot lattices may have important practical applications in quantum information processing.

Consider a two-dimensional electron gas (2DEG) at a GaAs heterostructure[12] superimposed with a triangular lattice of antidots with lattice constant Λ. In the effective-mass approximation the two-dimensional single-electron Schrödinger equation reads

$$\left[-\frac{\hbar^2}{2m^*}\nabla_{\mathbf{r}}^2 + \sum_i V(\mathbf{r}-\mathbf{R}_i)\right]\psi_n(\mathbf{r}) = E_n\psi_n(\mathbf{r}) \qquad (1)$$

where the sum runs over all antidots i, positioned at $\mathbf{R}_i$. Each antidot is modeled as a circular potential barrier of height V_0 and diameter d, i.e., $V(\mathbf{r}) = V_0$ for $r < d/2$, and zero elsewhere. It is convenient to express all energies in terms of the length scale Λ. Assuming that V_0 is so large that the eigenfunctions ψ_n do not penetrate into the antidots, i.e., $\psi_n = 0$ in the antidots, eq 1, simplifies to[13]

$$-\Lambda^2\nabla_{\mathbf{r}}^2\psi_n(\mathbf{r}) = \epsilon_n\psi_n(\mathbf{r}) \qquad (2)$$

where we have introduced the dimensionless eigenenergies $\epsilon_n \equiv E_n\Lambda^2 2m^*/\hbar^2$. For GaAs $\hbar^2/2m^* \simeq 0.6$ eV nm^2.

We first consider the perfectly periodic structure defined by the Wigner−Seitz cell shown in the left inset of Figure 1. For definiteness, we now take $d/\Lambda = 0.5$. Imposing periodic boundary conditions leaves us with the problem of solving eq 2 on a finite-size domain. This class of problems is well-suited for finite-element calculations, and the available software packages make the required computations simple, convenient, and fast.[14] Figure 1 shows finite-element calculations of the band structure along the high-symmetry axes indicated in the right inset of the figure. For state-of-the-art samples, $\Lambda \simeq 75$ nm, implying a band splitting of the order of 3 meV between the two lowest bands at the Γ-point. On the figure we have also indicated the gap ϑ_{eff} below which no states exist for the periodic structure.

* Corresponding author. E-mail: cf@mic.dtu.dk.

10.1021/nl0518472 CCC: $30.25
Published on Web 11/01/2005

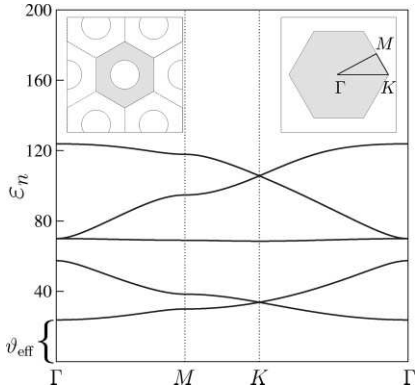

Figure 1. Band structure for the periodic structure. The ratio between the diameter of the antidots and the lattice constant is $d/\Lambda = 0.5$. Only the five lowest bands are shown. On the (dimensionless) energy axis we have indicated the gap $\vartheta_{\rm eff}$ which can be considered as the height of an effective potential (see text). Left inset: Wigner−Seitz cell (gray area) for the periodic structure. Circles indicate antidots. Right inset: First Brillouin zone (gray area) with indications of the three high-symmetry axes along which the band structure was calculated.

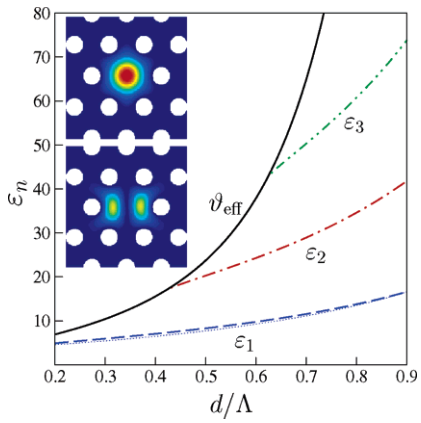

Figure 2. Energy spectrum for a single quantum dot. The three lowest dimensionless eigenvalues, ϵ_1, ϵ_2, ϵ_3, (corresponding to localized states) as a function of the ratio between the antidot diameter d and the lattice constant Λ. The full line indicates the height $\vartheta_{\rm eff}$ of the effective potential giving an upper limit to the existence of bound states (see text). The thin dotted line is the semianalytic expression given in eq 3. Inset: Localized eigenfunctions $\psi_1(\mathbf{r})$ (upper panel) and $\psi_2(\mathbf{r})$ corresponding to the eigenvalues ϵ_1 and ϵ_2, respectively, for $d/\Lambda = 0.5$. The absolute square $|\psi_i(\mathbf{r})|^2$, $i = 1, 2$, is shown.

Next, we turn to the case where a single antidot has been left out of the lattice. Relying on the analogy with photonic crystal fibers, where similar ideas have been used to design confined electromagnetic waves,[15] we expect one or several localized states to form at the location of the "defect". The eigenfunctions ψ_n corresponding to localized states decay to zero within a finite distance from the defect, and it is again sufficient to solve eq 2 on a finite-size domain. The inset in Figure 2 shows finite-element calculations of eigenfunctions corresponding to the two lowest eigenvalues for the geometrical ratio $d/\Lambda = 0.5$. The computed energy eigenvalues are converged with respect to an increase of the size of the domain on which eq 2 is solved. The two lowest eigenvalues correspond to localized states, whereas higher eigenvalues correspond to delocalized states (not shown). The second lowest eigenvalue is 2-fold degenerate, and we only show one of the corresponding eigenstates. One observes that the shown eigenstate does not exhibit the underlying 6-fold rotational symmetry of the lattice. This can be traced back to the fact that the mesh on which eq 2 was solved also lacked this symmetry. However, as recently shown by Mortensen et al.[16] even weak disorder in the lattice leads to a significant deformation of the higher-order eigenstates, and the shown eigenstate is thus likely to bear a closer resemblance to the states occurring in experimental structures, rather than the one found for an ideal lattice. Similarly, we note that the formation of defect states does not rely crucially on perfect periodicity of the antidot lattice, which thus allows for a certain tolerance in the fabrication of the antidot lattice.

Figure 2 also shows finite-element calculations of the lowest eigenvalues corresponding to localized states as a function of the geometrical ratio d/Λ. In addition, the gap $\vartheta_{\rm eff}$ as indicated on Figure 1 is plotted as a function of d/Λ. The gap gives an upper limit to the existence of bound states and can be considered as the height of an effective two-dimensional spherical potential well in which the localized states reside. For GaAs with $d/\Lambda = 0.5$ and $\Lambda = 75$ nm the energy splitting of the two levels is $\Delta E = E_2 - E_1 \simeq 1.1$ meV, which is much larger than $k_{\rm B}T$ at subkelvin temperatures. Thus, a missing single antidot in the lattice leads to the formation of a quantum dot with two levels at the location of the defect with an energy level structure suitable for a charge (orbital) qubit. As d/Λ is increased, the confinement becomes stronger and the eigenvalues and their relative separations increase. Moreover, the number of levels in the quantum dot can be controlled by adjusting d/Λ, allowing for $n = 1, 2, 3, \ldots$, levels in the quantum dot. In particular, for any $d/\Lambda < 0.42$ a single-level quantum dot is formed.

For sample optimizing purposes it is convenient to have simple expressions for the eigenvalues. In the limit of d/Λ approaching 1, the problem can be approximated with that of a two-dimensional spherical infinite potential well with radius $\Lambda - d/2$. For this problem the lowest eigenvalue is $\epsilon_1^{(\infty)} = \Lambda^2\alpha_{0,1}^2/(\Lambda - d/2)^2$, where $\alpha_{0,1} \simeq 2.405$ is the first zero of the zeroth order Bessel function. Although this expression yields the correct scaling with d, the approximation obviously breaks down for small values of d/Λ. In that limit we follow the ideas of Glazman et al.[17] who studied quantum conductance through narrow constrictions. The effective one-dimensional energy barrier for transmission through two neighboring antidots has a maximum value of π^2, and we thus approximate the problem with that of a two-dimensional spherical potential well of height π^2 and radius Λ. The lowest eigenvalue $\epsilon_1^{(\pi^2)}$ for this problem can be

determined numerically, and we find $\epsilon_1^{(\pi^2)} \simeq 3.221$. Correcting for the low-d/Λ behavior we find

$$\epsilon \simeq \epsilon_1^{(\infty)} - \lim_{d/\Lambda \to 0} \epsilon_1^{(\infty)} + \epsilon_1^{(\pi^2)} = \epsilon_1^{(\pi^2)} + \frac{(4 - d/\Lambda)d/\Lambda}{(2 - d/\Lambda)^2} \alpha_{0,1}{}^2 \quad (3)$$

In Figure 2 we show this expression together with the results for the lowest eigenvalue determined by finite element calculations. As can be seen on the figure, the expression given above captures to a very high degree the results obtained from finite-element calculations. For the higher-order eigenvalues, similar expressions can be found.

The leakage (transmission probability for penetrating the effective potential) due to a finite size of the antidot lattice can be found in the WKB approximation.[18] Multiplying by a characteristic attempt frequency we get the following estimate for the inverse lifetime

$$\frac{1}{\tau_d(E)} = \left(\frac{E}{2m^*\Lambda^2}\right)^{1/2} e^{-2N\Lambda(2m^*(V_{\text{eff}}-E)/\hbar^2)^{1/2}} \quad (4)$$

where N is the number of rings of antidots surrounding the defect, and $V_{\text{eff}} = \vartheta_{\text{eff}}\hbar^2/2m^*\Lambda^2$. For GaAs with $\Lambda = 75$ nm, $d/\Lambda = 0.4$, and $N = 1, 2, 3, 4, 5$, respectively, we find $\tau_d \simeq$ 0.8 ns, 0.3 μs, 90 μs, 30 ms, 10 s. We see that even relatively small "superlattices" offer nearly perfect confinement.

We next consider the case where an antidot and one of its next-nearest neighbors have been left out of the lattice. Due to the close proximity of the resulting quantum dots, the different states of the two quantum dots couple with a coupling determined by the overlap of the corresponding single-dot wavefunctions. In particular, for two single-level quantum dots, L and R, with corresponding states $|L\rangle$ and $|R\rangle$, respectively, a bonding $|-\rangle = (|L\rangle - |R\rangle)/\sqrt{2}$ and an antibonding state $|+\rangle = (|L\rangle + |R\rangle)/\sqrt{2}$ form. The corresponding eigenenergies are $E_\pm = E \pm |t|$, with E being the eigenenergy corresponding to each of the states $|L\rangle$ and $|R\rangle$ and t being the tunnel matrix element. From the eigenenergy splitting we easily obtain the tunnel matrix element as $|t| = (E_+ - E_-)/2$.

The coupling of the two levels can be tuned using a metallic split gate defined on top of the 2DEG in order to control the opening connecting the two quantum dots. By increasing the applied gate voltage, one squeezes the opening, thereby decreasing the overlap of the two states $|L\rangle$ and $|R\rangle$. In the following we model the split gate with an infinite potential barrier shaped as shown on the inset in Figure 3. Changing the applied gate voltage effectively leads to a change of the width w of the opening, which we in the following take as a control parameter.

In Figure 3 we show finite-element calculations of the dimensionless tunnel matrix element $|\tau| \equiv |t|\Lambda^2 2m^*/\hbar^2$ as a function of the geometrical ratio w/Λ for a number of different values of d/Λ in the single-level regime, i.e., $d/\Lambda < 0.42$. For GaAs with $\Lambda = 75$ nm and $d/\Lambda = 0.4$, $w/\Lambda =$ 0.6, the tunnel matrix element is $|t| = 0.015$ meV. With this coupling an electron initially prepared in the state $|L\rangle$ is expected to oscillate coherently between $|L\rangle$ and $|R\rangle$ with a period of $T = h/2|t| = 0.14$ ns. We note that the period agrees well with the time scale set by the lifetime obtained from eq 4 with $N = 1$. According to the figure the coupling varies over several orders of magnitude, thus clearly indicating that the coupling of the two quantum dots can be controlled via the applied gate voltage.

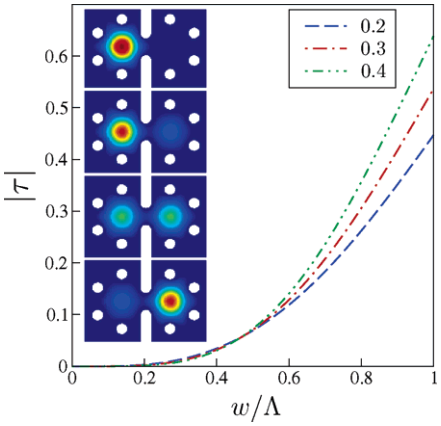

Figure 3. Coupling between two single-level quantum dots. The dimensionless tunnel matrix element $|\tau|$ as a function of the ratio between the width w of the opening defined by the split gates and the lattice constant Λ for different values of d/Λ (0.2, 0.3, 0.4) in the single-level regime. The width w is defined as the shortest distance between the split gates. Inset: Time propagation of an electron initially prepared in the state $|L\rangle$ (uppermost panel). Parameters are $d/\Lambda = 0.4$ and $w/\Lambda = 0.6$ which for GaAs with $\Lambda = 75$ nm implies as oscillation period of $T = 0.14$ ns (see text). The following panels show the state of the electron after a time span of $T/8$, $2T/8$, $3T/8$ (lowest panel), respectively. The absolute square $|\psi(\mathbf{r})|^2$ of the electron wavefunction is shown.

We have performed a numerical time propagation of an electron initially prepared in the state $|L\rangle$. In the inset of Figure 3 we show a number of snapshots at different points in time as the electron propagates from the left to the right quantum dot. Once located in the right quantum dot, the electron starts propagating back to the left quantum dot (not shown), confirming the expected oscillatory behavior.

Considering the double-dot as a charge qubit, one-qubit operations may be performed by controlling the tunnel matrix element as described above. Alternatively, one may consider the spin of two electrons, each localized on one of the quantum dots, as qubits. In that case the qubits (the spins) couple due to the exchange coupling, which again depends on the amplitude for tunneling between the two quantum dots. In this manner one may perform two-qubit operations as originally proposed in ref 1.

In this work we have carried out a number of model calculations showing that an implementation of qubits using defect states in an antidot lattice is feasible. While we have here only considered the most basic building blocks of a

quantum computer, a single charge qubit or two spin-qubits, we believe that the suggested structure can readily be scaled to a larger number of qubits. It is not difficult to imagine large architectures consisting of an antidot lattice with several coupled defect states and/or linear arrays of defect states constituting quantum channels along which coherent and controllable transport of electrons can take place.[19] We believe that the suggested structure, when compared to conventional gate-defined quantum dots, has the advantage that less wiring is needed. The individual antidots need not be electrically contacted, which in the case of conventional gate-defined structures may be a critical issue for large structures consisting of many quantum dots.

In conclusion, we have suggested a new structure which seems to offer many attractive features in terms of flexibility, scalability, and operation in the pursuit of achieving solid-state quantum computation.

Acknowledgment. The authors thank D. Graf, P. E. Lindelof, and T. Novotný for valuable advice during the preparation of the manuscript and T. Markussen for sharing his numerical codes with them.

References

(1) Loss, D.; DiVincenzo, D. P. *Phys. Rev. A* **1998**, *57* (1), 120−126.
(2) Fujisawa, T.; Oosterkamp, T. H.; van der Wiel, W. G.; Broer, B. W.; Aguado, R.; Tarucha, S.; Kouwenhoven, L. P. *Science* **1998**, *282* (5390), 932−935.
(3) Elzerman, J. M.; Hanson, R.; Greidanus, J. S.; van Beveren, L. H. W.; de Franceschi, S.; Vandersypen, L. M. K.; Tarucha, S.; Kouwenhoven, L. P. *Phys. Rev. B* **2003**, *67* (16).
(4) Hayashi, T.; Fujisawa, T.; Cheong, H. D.; Jeong, Y. H.; Hirayama, Y. *Phys. Rev. Lett.* **2003**, *91*(22).
(5) Gorman, J.; Hasko, D. G.; Williams, D. A. *Phys. Rev. Lett.* **2005**, *95*, 090502.
(6) Johnson, A. C.; Petta, J. R.; Taylor, J. M.; Yacoby, A.; Lukin, M. D.; Marcus, C. M.; Hanson, M. P.; Gossard, A. C. *Nature* **2005**, *435* (7044), 925−928.
(7) DiVincenzo, D. P. *Fortschr. Phys.* **2000**, *48* (9-11), 771−783.
(8) Gerhardts, P. R.; Weiss, D.; von Klitzing, K. *Phys. Rev. Lett.* **1989**, *62* (10), 1173−1176.
(9) Hofstadter, D. R. *Phys. Rev. B* **1976**, *14* (6), 2239−2249.
(10) Stadelmann, T. O.; Nicholas, R. J. In *Microscopy of Semiconducting Materials 2003*: *Proceedings of the Institute of Physics Conference*; Cullis, A. G., Midgley, P. A., Eds.; Institute of Physics Conference Series 180; Institute of Physics Publications: Philadelphia and Bristol, 2003; pp 661−664.
(11) Cavallini, M.; Mei, P.; Biscarini, F.; Garcia, R. *Appl. Phys. Lett.* **2003**, *83* (25), 5286−5288.
(12) The choice of material is not crucial for the conclusions reached below, and other choices of material, e.g., materials with a lower effective mass, may be preferable.
(13) This assumption corresponds to taking the limit $V_0 \rightarrow \infty$. We believe that our results do not change qualitatively for a large but finite value of V_0. The appealing and convenient form of eq 2 can however only be obtained in the limit $V_0 \rightarrow \infty$.
(14) Femlab, http://www.comsol.com.
(15) Mortensen, N. A. *Opt. Lett.* **2005**, *30* (12), 1455−1457.
(16) Mortensen, N. A.; Nielsen, M. D.; Folkenberg, J. R.; Hansen, K. P.; Lægsgaard, J. *J. Opt. A*: *Pure Appl. Opt.* **2004**, *6* (2), 221−223.
(17) Glazman, L. I.; Lesovik, G. K.; Khmelnitskii, D. E.; Shekter, R. I. *JETP Lett.* **1988**, *48* (4), 238−241.
(18) Koshiba, M.; Saitoh, K. *Opt. Commun.* **2005**, *253*, 95−98.
(19) Nikolopoulos, G. M.; Petrosyan, D.; Lambropoulos, P. *Europhys. Lett.* **2004**, *65* (3), 297−303.

NL0518472

Paper J

C. Flindt, A. S. Sørensen, and K. Flensberg

Spin-Orbit Mediated Control of Spin Qubits

Phys. Rev. Lett. **97**, 240501 (2006)

The initial idea behind the work is due to KF. The numerical work is due to CF, while the idea for one-qubit rotations is due to ASS. The analytic result for the effective two-qubit interaction (Eqs. 7-8) was obtained by CF, ASS, and KF in a joint effort. The writing of the manuscript was done by CF, ASS, and KF in a joint effort.

PRL **97,** 240501 (2006) PHYSICAL REVIEW LETTERS week ending 15 DECEMBER 2006

Spin-Orbit Mediated Control of Spin Qubits

Christian Flindt,[1,2] Anders S. Sørensen,[1] and Karsten Flensberg[1]
[1]*Niels Bohr Institute, Universitetsparken 5, DK-2100 Copenhagen, Denmark*
[2]*MIC — Department of Micro and Nanotechnology, NanoDTU, Technical University of Denmark, Building 345east, DK-2800 Kongens Lyngby, Denmark*
(Received 21 March 2006; published 11 December 2006)

We propose to use the spin-orbit interaction as a means to control electron spins in quantum dots, enabling both single-qubit and two-qubit operations. Very fast single-qubit operations may be achieved by temporarily displacing the electrons. For two-qubit operations the coupling mechanism is based on a combination of the spin-orbit coupling and the mutual long-ranged Coulomb interaction. Compared to existing schemes using the exchange coupling, the spin-orbit induced coupling is less sensitive to random electrical fluctuations in the electrodes defining the quantum dots.

DOI: 10.1103/PhysRevLett.97.240501 PACS numbers: 03.67.Lx, 71.70.Ej, 73.21.La

It is believed that solid-state systems could facilitate large-scale quantum computing [1] due to the well-developed fabrication techniques that allow for a high degree of scalability. On the other hand, solid-state systems are inherently more noisy than, e.g., quantum optical systems, and, in particular, several sources of low-frequency noise are typically present in a solid-state environment. One prominent candidate for solid-state quantum computing uses electron spins in semiconductor quantum dots as carriers of the fundamental unit of information, the qubit [2]. Electron spins have the advantage that they are weakly coupled to the surroundings and therefore weakly sensitive to noise. At the same time, however, this weak coupling makes the electron spin hard to control experimentally. To couple two spin qubits, it was proposed to use the exchange coupling between electron spins in neighboring quantum dots [3], and this was recently demonstrated experimentally [4]. Here the triplet and singlet spin states have different charge profiles, thereby enabling electrical control of the coupling. Unfortunately, this spin-charge coupling also makes the qubits sensitive to electrical noise and, in particular, to low-frequency noise [5]. In this setting the spin-orbit interaction is also considered as a source of decoherence [6], because it mixes spin and charge. Recently, however, it has been proposed that it could also play a role in the coherent interaction of qubits [7]. In this Letter we take these ideas further and propose to use the spin-orbit interaction as a general means to manipulate electron spins. The spin-orbit interaction allows for electrical control of both single- and two-qubit operations, but unlike the exchange interaction, the spin-orbit interaction generates dressed states of spin and charge where the mixing happens at a high frequency, making the interaction less susceptible to low-frequency noise.

While the general methods we propose in this Letter are applicable in a wide range of situations, we only consider a simplified one-dimensional model where the electrons are localized in quantum dots by an external potential $V(x)$. Physically, we may think of a structure like the one shown schematically in Fig. 1 which was recently realized experimentally [8], and we give realistic parameters corresponding to such a system. In our model we include a perpendicular magnetic field B (defining the z direction) and a spin-orbit coupling of the form $p\sigma^y$, where p denotes the momentum in the x direction [9]. With two electrons trapped in a double-dot potential the Hamiltonian of the system reads

$$H = H_1 + H_2 + \frac{e^2}{4\pi\varepsilon_r\varepsilon_0|x_2 - x_1|},$$
$$H_i = \frac{p_i^2}{2m} + V(x_i) + \frac{1}{2}g\mu_B B\sigma_i^z + \alpha p_i\sigma_i^y, \qquad i = 1, 2. \tag{1}$$

Here α denotes the strength of the spin-orbit coupling, while m is the effective electron mass. Below, we first consider how the spin-orbit interaction allows us to control the spin state of a single electron and then move on to discuss how the combination of the spin-orbit interaction and the Coulomb interaction enables two-qubit operations in a manner analogous to the method used for trapped ions [11].

First, we consider a single electron, and for our analytical calculation we assume that the potential is harmonic, but has a time varying equilibrium position denoted $\bar{x}(t)$,

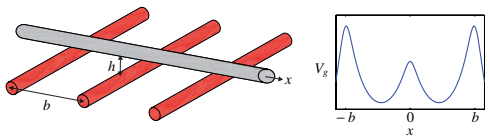

FIG. 1 (color online). A nanowire (light gray) placed above three electrodes. The electrodes are used to define electrostatically a double quantum dot within the nanowire. The electrodes are placed at a distance b apart, while the nanowire is situated at a distance h above the plane of the electrodes. The inset shows a representative curve for the potential $V_g(x)$ along the nanowire (the x axis) with the electrodes placed at positions $x = -b, 0, b$, respectively. The shown setup resembles the one used in the experiment in Ref. [8].

$V(x) = m\omega_0^2[x - \bar{x}(t)]^2/2$. We have omitted the subscript i, since we are considering a single electron. Physically the time varying equilibrium position can be induced with time varying potentials on the electrodes. We proceed by performing a unitary transformation $H \rightarrow UHU^\dagger$ with $U = \exp(i\sigma^y[x - \bar{x}(0)]/\ell_{so})$, where we have introduced the spin-orbit length $\ell_{so} = \hbar/m\alpha$, which characterizes the length scale of the spin-orbit interaction, i.e., in the absence of a magnetic field, a spin along the x or z directions is flipped after traveling a distance $\pi\ell_{so}/2$. With this transformation the Hamiltonian becomes

$$H = \frac{p^2}{2m} + \frac{1}{2}m\omega_0^2[x - \bar{x}(t)]^2 + \frac{1}{2}g\mu_B B \times \left[\cos\left(\frac{2[x - \bar{x}(0)]}{\ell_{so}}\right)\sigma^z - \sin\left(\frac{2[x - \bar{x}(0)]}{\ell_{so}}\right)\sigma^x\right]. \quad (2)$$

We further assume that the renormalized Zeeman splitting $\Delta_z \equiv \tilde{g}\mu_B B$ ($\tilde{g}$ defined below) is much smaller than the oscillator energy $\hbar\omega_0$, and that the equilibrium position is changed adiabatically with respect to the oscillator frequency $\omega_0 \gg (1/\ell_o)[d\bar{x}(t)/dt]$, where $\ell_o = \sqrt{\hbar/m\omega_0}$ is the characteristic oscillator length. In this limit, we can trace out the motional degrees of freedom and obtain

$$H_{spin} = \frac{1}{2}\tilde{g}\mu_B B\left[\cos\left(\frac{2[\bar{x}(t) - \bar{x}(0)]}{\ell_{so}}\right)\sigma^z - \sin\left(\frac{2[\bar{x}(t) - \bar{x}(0)]}{\ell_{so}}\right)\sigma^x\right], \quad (3)$$

with the renormalized g factor [12] given by

$$\tilde{g} = g\langle e^{2i(x - \bar{x}(0))/\ell_{so}}\rangle = g\exp[-(\ell_o/\ell_{so})^2]. \quad (4)$$

The renormalization of the g factor reflects that the qubits states are not pure states of the electron spin, but dressed states of spin and position [13]. Normally, such admixture of spin and position introduces decoherence because the position is coupled to charge fluctuations, but in this case the charge distribution is independent of the spin state, and produces no decoherence in the absence of a magnetic field. With a magnetic field the dressed states are still insensitive to slowly varying electric fields (slow compared to the Zeeman frequency $\Delta_z/\hbar$), which only shift the equilibrium position, while the spin state follows adiabatically. The dressed states will, however, be sensitive to slowly varying gradients of the electric fields which change the trap frequency ω_0. Because of the dependence of $\tilde{g}$ on ℓ_o in Eq. (4) such fluctuations in ω_0 will affect the Zeeman splitting and thereby cause decoherence of the spin states. As we shall see below this is one of the major limitations for the coupling of two qubits, but it will not significantly affect the fast single-qubit operations, provided that the ground state width is reasonably well defined.

Remarkably, the coupling of spin and position can be used to perform single-qubit operations if one applies an electric field with a sufficiently fast variation in time. If we consider the Hamiltonian in Eq. (3) there are two distinct principles for such single-qubit operations. One was considered in Ref. [14], where small amplitude oscillations of the equilibrium position ($|\delta\bar{x}(t)| \ll \ell_{so}$) at the Zeeman frequency produced spin-orbit induced electron spin resonance (ESR) oscillations between the two spin states. The second possibility, similar to Ramsey spectroscopy, for producing spin reversals is to first perform a large rapid change of the equilibrium position for a very short duration. In particular, if we change $\bar{x}(t)$ by $\pi\ell_{so}/4$ on a time scale much shorter than $\hbar/\Delta_z$, the effective Hamiltonian becomes $H_{spin} = \Delta_z\sigma^x/2$. Consequently, after a time $\hbar\pi/\Delta_z$ the spin state has been flipped and we can then change $\bar{x}(t)$ back to the original position. The second procedure has the advantage that it does not rely on any resonance conditions and allows for very rapid manipulation of the spin. Since the time scale can be changed by changing the magnetic field, the spin flip time will in practice only be limited by how fast one can change the voltage on the electrodes. As a particular example of material parameters, we take parameters typical for InAs, i.e., $m = 0.027m_e$, $\hbar\alpha = 3 \times 10^{-8}$ meV m and $g = 14.8$, giving $\ell_{so} = 94$ nm. With $B = 40$ mT and $\hbar\omega_0 = 0.5$ meV, we get $\ell_o = 75$ nm, so that the Zeeman frequency is $\Delta_z/\hbar = (2\pi)4.4$ GHz. The required displacement of the electron spin can be achieved by applying an electric field $E = \pi\ell_{so}m\omega_0^2/4e = 6.6\ \mu$V/nm, which for a setup like in Fig. 1 with an electrode spacing of $b = 500$ nm corresponds to a voltage of roughly 3 mV, and the entire spin flip process can be achieved in approximately 0.1 ns.

In addition to being important for performing logical operations in a quantum computer, the ability to perform rapid spin flips also allows the reduction of the leading kinds of decoherence due to the presence of magnetic impurities and the hyperfine coupling to nuclear spins. For electron spins in GaAs a dephasing time on the order of 10 ns has been reported [4], and we expect a similar time scale for InAs. This dephasing can, however, be reversed by applying pulses, which flip the spin on a much shorter time scale [4].

The spin-orbit interaction can also mediate *two-qubit interactions* in a very effective way. Returning to the setup shown in Fig. 1 described by the Hamiltonian in Eq. (1), we consider next the possibility of using the dipole moment associated with displacements of the electron charges to couple the two spins. In this one-dimensional geometry the two dots holding each one spin are separated by a distance $d = \bar{x}_2 - \bar{x}_1 > 0$. We consider the limit where the two electrons are well separated, allowing us to expand the Coulomb interaction term as $1/|x_2 - x_1| \simeq 1/d - \delta/d^2 + \delta^2/d^3$, while using $d \gg \delta \equiv (x_2 - \bar{x}_2) - (x_1 - \bar{x}_1)$. The first term in this expansion gives a constant contribution to the energy, the second term corresponds to constant forces, which redefine the two equilibrium positions. The last term

PRL **97,** 240501 (2006) PHYSICAL REVIEW LETTERS week ending 15 DECEMBER 2006

has diagonal terms, x_i^2, which provide a small renormalization of the trapping frequencies. Finally, the interesting term is the cross term $-2(x_1 - \bar{x}_1)(x_2 - \bar{x}_2)/d^3$, which results in a coupling of the two orbitals degrees of freedom, and hence also, via the spin-orbit interaction, between the two spin degrees of freedom.

To calculate this coupling we go back to Eq. (2) (for each electron) with time independent equilibrium positions $\bar{x}_i(t) = \bar{x}_i(0)$, and perform perturbation theory in the magnetic field. To second order in B the effective Hamiltonian for a single electron spin is still given by Eq. (3), i.e., $H_i = \tilde{g}\mu_B B\sigma_i^z/2$ (for $i = 1, 2$) plus a spin independent contribution. The cross term that couples the two spins gives rise to an effective spin coupling term given by

$$H_{\text{spin},12} = -\frac{e^2}{2\pi\varepsilon_0\varepsilon_r d^3}\langle x_1 - \bar{x}_1\rangle\langle x_2 - \bar{x}_2\rangle, \tag{5}$$

where the brackets only refer to a trace over the vibrational state, *not* the spin state. Because the two orbital degrees to this order are decoupled the expectation value separates. To leading order in B, the displacement of the electrons can be found from Eq. (2) by first order perturbation theory, and we obtain

$$\langle x_i - \bar{x}_i\rangle = \sigma_i^x \frac{\tilde{g}\mu_B B\ell_o^2}{\hbar\omega_0\ell_{\text{so}}}. \tag{6}$$

Combining this with the single particle contributions, we arrive at the final effective Hamiltonian for the two spins

$$H_{\text{spin}} = \tau\sigma_1^x\sigma_2^x + \frac{1}{2}\tilde{g}\mu_B B(\sigma_1^z + \sigma_2^z), \tag{7}$$

where the coupling constant τ is given by

$$\tau = -\frac{e^2}{4\pi\varepsilon_0\varepsilon_r}\frac{2\ell_o^4(\tilde{g}\mu_B B)^2}{\ell_{\text{so}}^2(\hbar\omega_0)^2 d^3}. \tag{8}$$

We stress that this effective Hamiltonian is correct to all orders in the spin-orbit coupling, but only to second order in the B field and first order in the Coulomb interaction between the two electrons. The last approximation can, however, be relaxed *without* changing the form of the Hamiltonian, but at the expense of a more complicated expression for τ.

To characterize the stability of the proposed coupling mechanism to slowly varying perturbations, such as fluctuations in the gate electrodes, we develop a more realistic model for the double-dot potential $V(x)$. We are having in mind an experimental setup like the one shown in Fig. 1 [8], and, consequently, we consider the electrostatic potential $V_g(x)$ created by three parallel electrodes with spacing b, each modeled as an infinite line charge, along the x axis running perpendicular to the electrodes at a distance h above the plane of the electrodes. The ratio of the charge density on the left (central) electrode $\lambda_{l(c)}$ and the right electrode λ_r is denoted $\beta_{l(c)}$, i.e., $\beta_{l(c)} \equiv \lambda_{l(c)}/\lambda_r$, which we assume can be controlled via the voltages applied to the electrodes. Moreover, we define $\hbar\omega_g \equiv e\lambda_r/4\pi\varepsilon_r\varepsilon_0$ and $x_g \equiv \sqrt{\hbar/m\omega_g}$, in terms of which we express the electrostatic potential as

$$V_g(x) = V_e(x + b, \beta_l) + V_e(x, \beta_c) + V_e(x - b, 1) \tag{9}$$

with $V_e(x, \beta) = -\beta\hbar\omega_g \ln[(x^2 + h^2)/x_g^2]$. A representative curve for $V_g(x)$ is shown the inset of Fig. 1.

We have implemented numerically on a finite-size real-space grid the two-particle Hamiltonian in Eq. (1) using $V_g(x)$ in Eq. (9) as the potential $V(x)$. With $N \sim 100$–500 grid points, the resulting matrix representation of the Hamiltonian is large (dimension $4N^2 \times 4N^2$), but sparse, allowing for computationally cheap calculations of the low-energy spectrum from which we can extract the coupling of the various spin states. In the left panel of Fig. 2 we show numerical calculations of the coupling τ as a function of the applied B field. The renormalized Zeeman splitting due to the applied B field is much smaller than the spacing of the orbital levels, and we thus expect Eq. (8) to hold. The numerical results show excellent agreement with the analytic expression. For the parameters used in the figure typical interaction strengths are $\tau/\hbar = (2\pi)f$, with $f \sim 0.1$ GHz, corresponding to gate times on the order of $1/(2f) \sim 5$ ns.

In the right panel of Fig. 2 we show numerical results for the coupling τ as a function of the voltage applied to the central electrode parametrized by β_c. In order to determine the contribution arising from the bare exchange coupling (due to the Pauli principle and the Coulomb interaction), we also show numerical results for the splitting of the spin states without the spin-orbit coupling. Compared to the bare exchange coupling J, which is clearly exponentially dependent on the applied voltage, the spin-orbit induced coupling shows a weaker voltage dependence.

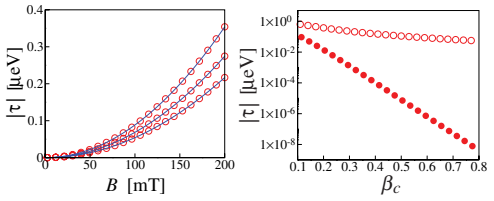

FIG. 2 (color online). Numerical calculation of the coupling τ. Material parameters correspond to InAs and we use $\hbar\omega_g = 1$ meV, $\beta_l = 1$, $x_g = 53$ nm, $h = 0.5x_g$, $b = 10x_g$. Left panel: The coupling τ as function of applied magnetic field B for $\beta_c = 0.6$ (upper circles), 0.7, 0.8 (lower circles). Solid lines show Eq. (8) with the orbital energy spacing $\hbar\omega_0$ extracted from the low-energy spectrum and d being the only fitting-parameter. Corresponding to $\beta_c = 0.6$, 0.7, 0.8, we have $\hbar\omega_0 = 0.39$, 0.40, 0.42 meV, and $d = 8.3x_g$, $8.7x_g$, $9.1x_g$, respectively. Right panel: Open circles show the coupling τ as a function of the applied voltage on the central electrode parametrized by β_c with $B = 40$ mT. Solid circles show the contribution from the bare exchange coupling J.

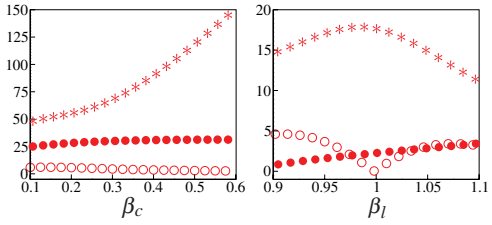

FIG. 3 (color online). Numerical calculations of the sensitivity to fluctuations in the gate electrodes. The sensitivity of the spin-orbit induced coupling τ and the Zeeman splitting Δ_z are quantified by $|(1/\tau)(\partial\tau/\partial\beta_i)|$, $i = c, l$ (open circles) and $|(1/\tau)(\partial\Delta_z/\partial\beta_i)|$, $i = c, l$ (stars), respectively. Material parameters correspond to InAs. The other parameters are $B = 80$ mT, $\hbar\omega_g = 1$ meV, $x_g = 53$ nm, $h = 0.5x_g$, and $b = 10x_g$. In both panels solid circles show the sensitivity of the bare exchange coupling $|(1/J)(\partial J/\partial\beta_i)|$, $i = c, l$. Left panel: Sensitivity to fluctuations in the central electrode. The electrostatic potential is symmetric, i.e., $\beta_l = 1$. Right panel: Sensitivity to fluctuations in the left electrode with $\beta_c = 0.7$.

Fluctuations in the electrostatic environment cause fluctuations of the orbital level splitting $\hbar\omega_0$ and the distance d. Typically these fluctuations have the form of $1/f$ noise and concentrating on the dominating low-frequency component, we characterize in the following the sensitivity of the coupling to electrical fluctuations using a purely static calculation by taking derivatives with respect to β_c and β_l. For the spin-orbit induced coupling τ given in Eq. (8), we have $|(1/\tau)(\partial\tau/\partial\omega_0)\delta\omega_0| = 4|\delta\omega_0/\omega_0|$ and $|(1/\tau)\times(\partial\tau/\partial d)\delta d| = 3|\delta d/d|$. In order to perform reliable two-qubit operations, both of these quantities must be much smaller than unity, which for the fluctuations imply $|\delta\omega_0/\omega_0|$, $|\delta d/d| \ll 0.1$. In Fig. 3, we show $|(1/\tau)\times(\partial\tau/\partial\beta_i)|$ as a function of β_i, $i = c, l$. The coupling is stable for $|(1/\tau)(\partial\tau/\partial\beta_i)\delta\beta_i| \ll 1$, $i = c, l$, implying $|\delta\beta_i| < 0.1$, $i = l, c$ according to the numerical results. This does not impose any unrealistic requirements on the experimental setup. For comparison we also show $|(1/J)\times(\partial J/\partial\beta_i)|$, $i = c, l$ for the exchange interaction J, which for fluctuations in β_c is an order of magnitude more sensitive.

As discussed previously, electrical fluctuations also cause fluctuations of the renormalized Zeeman splitting, Δ_z. For Δ_z, we have $|(1/\tau)(\partial\Delta_z/\partial\omega_0)\delta\omega_0| = (4\pi\varepsilon_r\varepsilon_0\hbar m d^3\omega_0^3/e^2\tilde{g}\mu_B B)|\delta\omega_0/\omega_0|$. For InAs with $d = 500$ nm, $\hbar\omega_0 = 0.3$ meV, $B = 80$ mT, $|(1/\tau)\times(\partial\Delta_z/\partial\omega_0)\delta\omega_0| \simeq 50|\delta\omega_0/\omega_0|$, implying the stricter condition $|\delta\omega_0/\omega_0| \ll 0.01$. In Fig. 3, we show numerical results for $|(1/\tau)(\partial\Delta_z/\partial\beta_i)|$ as a function of β_i, $i = c, l$. The results indicate that we must require $|\delta\beta_i| < 0.01$, $i = l, c$ for the renormalized Zeeman splitting to be stable. If this requirement cannot be met in experiments, the problem may be circumvented by encoding a single qubit in a singlet-triplet pair as recently discussed in Refs. [4,15] or alternatively by combining the gate with fast spin-echo pulses implemented by rapidly shifting the position of the electrons.

In conclusion, we have presented a spin-orbit induced mechanism for coherent control of spin qubits in quantum dots. The spin-orbit coupling allows for fast single-qubit operations, and the two-qubit operations are robust against electrical fluctuations in the electrodes defining the double dot. We emphasize that although some of the above conclusions have been made in connection with a specific experimental setup in mind, they also hold at a more general level.

The authors thank G. Burkard, X. Cartoixa, W. A. Coish, A. Fuhrer, A.-P. Jauho, M. D. Lukin, J. Nygård, and J. M. Taylor for valuable discussions and comments. This work was supported by the Danish Natural Science Research Council.

[1] For a recent special issue on solid-state quantum computing, we refer to New J. Phys. **7**, 1 (2005).
[2] D. Loss and D. P. DiVincenzo, Phys. Rev. A **57**, 120 (1998).
[3] G. Burkard, D. Loss, and D. P. DiVincenzo, Phys. Rev. B **59**, 2070 (1999).
[4] J. R. Petta *et al.*, Science **309**, 2180 (2005).
[5] X. Hu and S. Das Sarma, Phys. Rev. Lett. **96**, 100501 (2006).
[6] A. V. Khaetskii and Yu. V. Nazarov, Phys. Rev. B **61**, 12 639 (2000); A. V. Khaetskii and Yu. V. Nazarov, Phys. Rev. B **64**, 125316 (2001).
[7] D. Stepanenko *et al.*, Phys. Rev. B **68**, 115306 (2003); D. Stepanenko and N. E. Bonesteel, Phys. Rev. Lett. **93**, 140501 (2004); L.-A. Wu and D. A. Lidar, Phys. Rev. A **66**, 062314 (2002); S. Debald and C. Emary, Phys. Rev. Lett. **94**, 226803 (2005).
[8] C. Fasth, A. Fuhrer, M. T. Björk, and L. Samuelson, Nano Lett. **5**, 1487 (2005).
[9] By a suitable alignment of the magnetic field and definition of the spin operators this form of the coupling applies to any type of spin-orbit interaction linear in p and may have contributions from both bulk and structure inversion asymmetry [10].
[10] L. S. Levitov and E. I. Rashba, Phys. Rev. B **67**, 115324 (2003).
[11] J. I. Cirac and P. Zoller, Nature (London) **404**, 579 (2000).
[12] S. Debald and B. Kramer, Phys. Rev. B **71**, 115322 (2005).
[13] L.-A. Wu and D. A. Lidar, Phys. Rev. Lett. **91**, 097904 (2003).
[14] E. I. Rashba and A. L. Efros, Phys. Rev. Lett. **91**, 126405 (2003); V. N. Golovach, M. Borhani, and D. Loss, Phys. Rev. B **74**, 165319 (2006).
[15] J. M. Taylor *et al.*, Nature Phys. **1**, 177 (2005).

Paper K

C. Flindt, A. S. Sørensen, and K. Flensberg

Spin-orbit induced spin-qubit control in nanowires

J. Phys.: Conf. Ser. **61**, 302 (2007)

The work contains results that were not published in the paper Phys. Rev. Lett. **97** (2006) 240501 by CF, ASS, and KF. The work is mainly due to CF.

IOP Publishing Journal of Physics: Conference Series **61** (2007) 302–306
doi:10.1088/1742-6596/61/1/061 International Conference on Nanoscience and Technology (ICN&T 2006)

Spin-orbit induced spin-qubit control in nanowires

Christian Flindt[1,2], Anders S Sørensen[1] and Karsten Flensberg[1]

[1] Niels Bohr Institute, Universitetsparken 5, DK-2100 Copenhagen, Denmark
[2] MIC – Department of Micro and Nanotechnology, NanoDTU, Technical University of Denmark, Building 345 East, DK-2800 Kongens Lyngby, Denmark

Abstract. We elaborate on a number of issues concerning our recent proposal for spin-qubit manipulation in nanowires using the spin-orbit coupling. We discuss the experimental status and describe in further detail the scheme for single-qubit rotations. We present a derivation of the effective two-qubit coupling which can be extended to higher orders in the Coulomb interaction. The analytic expression for the coupling strength is shown to agree with numerics.

1. Introduction

Gate-defined quantum dots containing only a few electrons have been promoted as a possible candidate for solid state quantum information processing [1]. Qubits are envisioned to be encoded in the spin degree of freedom of the trapped electrons, which are manipulated individually using local electron spin resonance (ESR). Two-qubit gates are carried out by pulsing electrically the exchange coupling between electrons in neighboring tunnel-coupled quantum dots [2]. Experimentally, electric control of the exchange coupling between two electrons in a double quantum dot was recently reported in Ref. [3]. A review of the current status of quantum computing with spins in solid state systems can be found in Ref. [4].

We have recently proposed to use the spin-orbit (SO) coupling in nanostructures as a general means to manipulate electron spins in a coherent and controllable manner [5]. More specifically, we have shown how single-spin flips may be achieved by combining the SO coupling with fast gate-induced displacements of the electron(s), and how the SO coupling together with the Coulomb interaction gives rise to an effective spin-spin coupling, which is less sensitive to charge fluctuations compared to the exchange coupling [6].

Here, we elaborate on a number of issues related to our proposal. First, we discuss a relevant experimental setup consisting of a gate-defined double-dot in an InAs nanowire [7]. This type of setup is of particular interest to us due to the strong SO coupling measured in InAs nanowires [8]. We discuss in further detail our scheme for single-spin flips and present a derivation of the two-spin interaction, which can be extended to arbitrary order in the Coulomb interaction. Finally, we show that the analytic expression for the two-spin interaction agrees with numerics.

2. Quantum dots in nanowires

In the work described in Ref. [7] a setup consisting of an InAs nanowire placed above a number of gold electrodes was successfully fabricated. The gold electrodes were used to define electrostatically a double quantum dot within the InAs nanowire, which was characterized using low-temperature transport measurements, and electrostatic control of the tunnel coupling between the two quantum dots was demonstrated. The setup is shown schematically in Fig. 1.

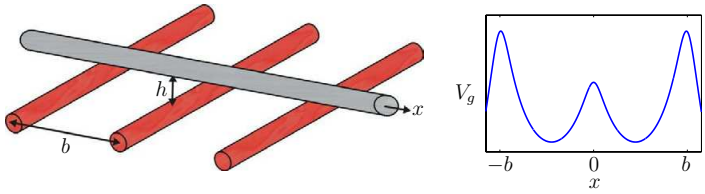

Figure 1. An InAs nanowire (light gray) placed above three gold electrodes. The three electrodes are used to define electrostatically a double quantum dot along the InAs nanowire. A representative curve for the electrostatic potential $V_g(x)$ along the wire is shown on the inset to the right. The gold electrodes are placed at positions $x = -b, 0, b$, respectively. Typical length scales are $h \simeq 25$ nm and $b \simeq 200$ nm. In the experiment of Ref. [7] two additional gold electrodes were used as plunger gates (not shown).

The choice of material is interesting due to the strong SO coupling and the large g-factor in InAs compared to GaAs. In Ref. [8] measurements of a positive correction to the conductivity of InAs nanowires were attributed to weak antilocalization arising from spin relaxation of electrons propagating through the nanowires. This interpretation was supported further by applying a magnetic field that was sufficiently strong to break time-reversal symmetry, thereby suppressing the weak antilocalization correction to the conductivity. A spin relaxation length on the order of 200 nm was reported, but no definitive microscopic theory for the underlying spin-orbit coupling mechanism could be given. The exact nature of the SO coupling in InAs nanowires is still to be fully understood and deserves further experimental and theoretical investigation. We expect, however, that the allowed type and strength of the SO coupling in InAs nanowires are highly dependent on various experimentally controllable parameters, *e.g.*, the growth direction of the nanowire.

3. Single-spin manipulation

We now describe how the SO coupling can be used to flip the spin of an electron in a controllable manner. Motivated by the structure described above we consider a one-dimensional system[1] consisting of a single electron trapped in a gate-defined quantum dot which we approximate with the harmonic potential $V(x,t) = \frac{1}{2}m\omega_0^2(x - \bar{x}(t))^2$ along the x-axis. We assume that the minimum position of the harmonic potential, denoted $\bar{x}(t)$, can be varied by changing the voltages on the gate electrodes. A static B-field perpendicular to the x-axis splits the spin states and determines the z-axis. The x-, y-, and z-axis define the lab frame in which the Hamiltonian reads

$$H_{\rm lab} = \frac{p_x^2}{2m} + \frac{1}{2}m\omega_0^2(x - \bar{x}(t))^2 + \frac{1}{2}g\mu_B B\sigma_z + \alpha p_x\sigma_y. \qquad (1)$$

Here α denotes the strength of the SO coupling. The particular form of the SO coupling is assumed to arise from lack of inversion symmetry in the yz-plane [9]. In order to get a feeling for the SO coupling it is useful to introduce the SO length $l_{\rm so} \equiv \hbar/m\alpha$: Without an applied B-field, a spin along the z-axis is flipped after having traveled the distance $\pi l_{\rm so}/2$ along the x-axis. Another important length scale is the oscillator length defined as $l_0 \equiv \sqrt{\hbar/m\omega_0}$.

It is convenient to work in a frame that follows the SO induced rotation of the spin. We shall refer to this frame as the rest frame. The Hamiltonian in the rest frame $H_{\rm rest}$ is obtained by the

[1] The following results are not only valid for InAs nanowires, but more generally for gate-defined quantum dots in one-dimensional systems with strong SO coupling.

unitary transformation $H_{\rm rest} = UH_{\rm lab}U^\dagger$, where $U = \exp\left(i\sigma_y(x-\bar{x}(0))/l_{\rm so}\right)$, and we find

$$H_{\rm rest} = \frac{p_x^2}{2m} + \frac{1}{2}m\omega_0^2(x-\bar{x}(t))^2 + \frac{1}{2}g\mu_B B\left[\cos\left(\frac{2(x-\bar{x}(0))}{l_{\rm so}}\right)\sigma_z - \sin\left(\frac{2(x-\bar{x}(0))}{l_{\rm so}}\right)\sigma_x\right]. \quad (2)$$

The static B-field in the lab frame is rotating in the rest frame of the spin as it travels along the x-axis. In the following we work in a regime, where the equilibrium position $\bar{x}(t)$ is slowly changed on the time-scale of the orbital degree of freedom, while fast on the time-scale of the spin, *i.e.*, $g\mu_B B/\hbar \ll (1/l_0)d\bar{x}(t)/dt \ll \omega_0$. This allows us to trace out the orbital degree of freedom by projecting $H_{\rm rest}$ onto the oscillator ground state, whereby we arrive at an effective spin Hamiltonian reading

$$H_{\rm spin} = \frac{1}{2}\tilde{g}\mu_B B\left[\cos\left(\frac{2(\bar{x}(t)-\bar{x}(0))}{l_{\rm so}}\right)\sigma_z - \sin\left(\frac{2(\bar{x}(t)-\bar{x}(0))}{l_{\rm so}}\right)\sigma_x\right] \quad (3)$$

with the renormalized g-factor given by

$$\tilde{g} = g\left\langle e^{2i(x-\bar{x}(0))/l_{\rm so}}\right\rangle = ge^{-(l_0/l_{\rm so})^2}. \quad (4)$$

Here the brackets denote an average with respect to the oscillator ground state.

Using the spin Hamiltonian given in Eq. (4) we can manipulate the spin by changing the equilibrium position $\bar{x}(t)$. Below we describe a scheme for spin flips, which does not rely on any resonance conditions as in previous studies [10, 11]. Instead, our scheme relies on fast (on the time scale of the spin) and large (on the order of $l_{\rm so}$) changes of $\bar{x}(t)$ obtained by controlling the potentials on the gate electrodes. Considering a spin being in an eigenstate of the spin Hamiltonian at $t = 0$, *i.e.*, $H_{\rm spin} = \frac{1}{2}\tilde{g}\mu_B B\sigma_z$, the scheme reads:

(i) Fast displacement of $\bar{x}(t)$: $\bar{x}(0) \to \bar{x}(0) + \pi l_{\rm so}/4$. This rotates the B-field into the x-axis of the rest frame.

(ii) Free evolution of the spin now governed by the spin Hamiltonian $H_{\rm spin} = -\frac{1}{2}\tilde{g}\mu_B B\sigma_x$ for a time span $\Delta t = \hbar\pi/\tilde{g}\mu_B B$. This rotates the spin in the rest frame by π around the x-axis.

(iii) Fast return of $\bar{x}(t)$: $\bar{x}(0) + \pi l_{\rm so}/4 \to \bar{x}(0)$. This returns the B-field to the initial position in the rest frame, pointing along the z-axis.

After the three steps, a spin initially prepared in an eigenstate of $H_{\rm spin} = \frac{1}{2}\tilde{g}\mu_B B\sigma_z$ has been flipped into the other eigenstate. For realistic experimental parameters one finds an estimated time for the spin flip process on the order of 0.1 ns [5]. A graphical interpretation of the spin flip process (as seen in the lab frame) is given in Fig. 2. We note that the spin Hamiltonian given in Eq. (4) allows for rotations of the spin to any point on the Bloch sphere.

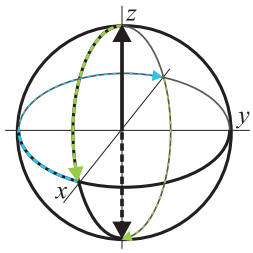

Figure 2. Bloch sphere in the lab frame with the full black arrow denoting the initial spin state. The three colored dashed lines indicate the rotations of the spin during the spin flip scheme. The green lines correspond to the fast displacements of $\bar{x}(t)$, while the blue line in the xy-plane corresponds to the rotation around the static B-field. The dashed black arrow denotes the final spin state.

4. Two-spin manipulation

The SO coupling also couples spins in neighboring quantum dots. The form and the strength of the coupling can be found by considering two electrons, each described by a (rest frame) Hamiltonian $H^{(i)}_{\rm rest}$ of the form given in Eq. (2) with different values of $\bar{x}_i$, $i = 1, 2$, for each of the two quantum dots. The orbital degrees of freedom are coupled due to the Coulomb interaction between the electrons, which we expand using $1/|x_2 - x_1| \simeq 1/d - \delta/d^2 + \delta^2/d^3$, where we have introduced the distance between the quantum dots $d \equiv \bar{x}_2 - \bar{x}_1 > 0$ and assumed that $d \gg \delta \equiv (x_2 - \bar{x}_2) - (x_1 - \bar{x}_1)$. Retaining only the term in the expansion of the Coulomb interaction that couples the positions of the electrons, the two-particle Hamiltonian reads

$$H = H^{(1)}_{\rm rest} + H^{(2)}_{\rm rest} - \frac{e^2}{2\pi\varepsilon_0\varepsilon_r d^3}(x_1 - \bar{x}_1)(x_2 - \bar{x}_2). \tag{5}$$

For the two-spin coupling temporal variations of $\bar{x}_i$, $i = 1, 2$, are not necessary.

An effective two-spin Hamiltonian $H_{\rm eff}$ can be found using imaginary time formalism. The two-particle Hamiltonian given in Eq. (5) is written $H = H_0 + H'$, where H_0 denotes the Hamiltonian of the two oscillators and $H' \equiv H - H_0$. We define $e^{-\beta H_{\rm eff}} \equiv {\rm Tr}_{\rm osc}(e^{-\beta H})/Z_0$, $Z_0 \equiv {\rm Tr}_{\rm osc}(e^{-\beta H_0})$, where ${\rm Tr}_{\rm osc}$ denotes a (partial) trace over the two oscillators. Introducing the operator $\hat{U}(\beta) \equiv e^{\beta H_0}e^{-\beta H}$, and the thermal average of an operator A with respect to H_0, $\langle A\rangle_0 \equiv {\rm Tr}_{\rm osc}(Ae^{-\beta H_0})/Z_0$, we write $e^{-\beta H_{\rm eff}} = \langle\hat{U}(\beta)\rangle_0$. Using the formal expression $\hat{U}(\beta) = T_\tau \exp\left(-\int_0^\beta d\tau \hat{H}'(\tau)\right)$, where T_τ denotes the (imaginary) time-ordering operator and $\hat{H}'(\tau) \equiv e^{\tau H_0/\hbar}H'e^{-\tau H_0/\hbar}$ is the interaction picture representation of H' (in imaginary time), we can in principle calculate the effective two-spin Hamiltonian $H_{\rm eff}$ to any order in H'. The first non-vanishing term that couples the two spins arises from the expansion of $\hat{U}(\beta)$ to third order in H' and has the form $\tau_{xx}\sigma^{(1)}_x\sigma^{(2)}_x$, where τ_{xx} is to be determined. Concentrating on this term, we find

$$e^{-\beta H_{\rm eff}} \simeq \ldots + \frac{(eg\mu_B B)^2}{8\pi\varepsilon_0\varepsilon_r d^3}\int_0^\beta\int_0^\beta\int_0^\beta d\tau_1 d\tau_2 d\tau_3 \mathcal{G}(x_1 - \bar{x}_1, \tau_1 - \tau_2)\mathcal{G}(x_2 - \bar{x}_2, \tau_2 - \tau_3)\sigma^{(1)}_x\sigma^{(2)}_x + \ldots, \tag{6}$$

where we have assumed that the spin degrees of freedom evolve much slower than the orbital part, and $\hat{\sigma}^{(1)}_x$ and $\hat{\sigma}^{(2)}_x$ are thus taken to be time-independent. The correlation function $\mathcal{G}(x_i, \tau)$ is defined as

$$\mathcal{G}(x_i, \tau) \equiv \left\langle T_\tau \sin\left(\frac{2\hat{x}_i(\tau)}{l_{\rm so}}\right) x_i \right\rangle_0, \tag{7}$$

and can be evaluated using linked cluster theory. We find

$$\mathcal{G}(x_i, \tau) = \frac{l_0^2}{l_{\rm so}} e^{-(l_0/l_{\rm so})^2}\Big[\Theta(\tau)\Big(n_B(\beta\hbar\omega_0)e^{\omega_0\tau} + (1 + n_B(\beta\hbar\omega_0))e^{-\omega_0\tau}\Big) + (\tau \to -\tau)\Big], \tag{8}$$

where $\Theta(\tau)$ is the Heaviside step function and $n_B(x) = 1/(e^x - 1)$. Collecting all terms and carrying out the triple integral, we find

$$e^{-\beta H_{\rm eff}} = \ldots + \frac{e^2}{4\pi\varepsilon_0\varepsilon_r}\frac{2l_0^4(g\mu_B B)^2}{l_{\rm so}^2(\hbar\omega_0)^3 d^3} e^{-2(l_{\rm so}/l_0)^2(1 + n_B(\beta\hbar\omega_0))} F(\beta\hbar\omega_0)\sigma^{(1)}_x\sigma^{(2)}_x + \ldots \tag{9}$$

with $F(x) = [x(\cosh(x) - 2) + \sinh(x)]/2\sinh^2(x/2)$. Having solved the finite-temperature ($\beta < \infty$) problem, we let $\beta \to \infty$, and identify

$$\tau_{xx} = -\frac{e^2}{4\pi\varepsilon_0\varepsilon_r}\frac{2l_0^4(\tilde{g}\mu_B B)^2}{l_{\rm so}^2(\hbar\omega_0)^2 d^3} \tag{10}$$

in agreement with our previous work [5]. The imaginary time formalism outlined here allows for calculation of the coupling to higher order in the Coulomb interaction and corrections due to a finite temperature.

5. Numerics

In Ref. [5] we used a numerical implementation of the two-particle Hamiltonian in Eq. (5) to study the coupling τ_{xx} in case of non-harmonic confining potentials. Here we use the numerical implementation to calculate τ as a function of the SO coupling strength α. In Fig. 3 we show a comparison of numerical results for τ_{xx} using nearly harmonic confining potentials and Eq. (10). The numerical results agree well with the analytic results, and as expected the coupling depends quadratically on α, *i.e.*, $\tau_{xx} \propto \alpha^2$ for small values of α (corresponding to $l_{\rm so} \gg l_0$), while it for large values of α is dominated by the renormalized g-factor which drops off exponentially with increasing α.

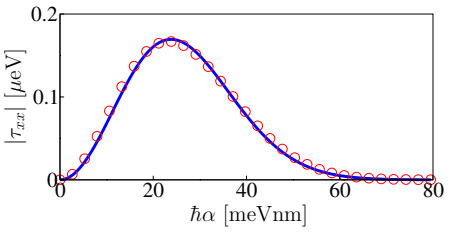

Figure 3. Two-qubit coupling τ_{xx} as a function of the SO coupling α. Parameters are $\varepsilon_r = 15.15$, $m = 0.027m_e$, $g = 14.8$, $B = 160$ mT, $l_0 = 80$ nm ($\hbar\omega_0 \simeq 0.4$ meV) and $d \simeq 0.75$ μm. Circles indicate numerical results, while the full line shows Eq. (10).

6. Conclusion

We have elaborated on our recent proposal for spin-qubit manipulation using the SO coupling in nanostructures. We have discussed an experimental setup with strong SO coupling which may be relevant for realizing our proposal. We have described in detail how single-spin rotations may be carried out using fast displacements of the electron(s), and we have derived an expression for the effective two-spin interaction using imaginary-time formalism. Finally, we have shown that the analytic result for the two-spin interaction agrees with numerics.

Acknowledgments

The authors thank G Burkard, X Cartoixa, W A Coish, A Fuhrer and J M Taylor for illuminating discussions during the preparation of this manuscript.

References

[1] Loss D and DiVincenzo D P 1998 *Phys. Rev.* A **57** 120
[2] Burkard G, Loss D and DiVincenzo D P 1999 *Phys. Rev.* B **59** 2070
[3] Petta J R *et al.* 2005 *Science* **309** 2180
[4] Coish W A and Loss D 2006 cond-mat/0606550
[5] Flindt C, Sørensen A S and Flensberg K 2006 cond-mat/0603559
[6] Hu X and Das Sarma S 2006 *Phys. Rev. Lett.* **96** 100501
[7] Fasth C, Fuhrer A, Björk M T and Samuelson L 2005 *Nano Lett.* **5** 1487
[8] Hansen A E *et al.* 2005 *Phys. Rev.* B **71** 205328
[9] Levitov L S and Rashba E I 2003 *Phys. Rev.* B **67** 115324
[10] Rashba E I and Efros A L 2003 *Phys. Rev. Lett.* **91** 126405
[11] Golovach V N, Borhani M and Loss D 2006 cond-mat/0601674

Paper M

C. Flindt, A. S. Sørensen, M. D. Lukin, and J. M. Taylor

Spin-Photon Entangling Diode

Phys. Rev. Lett. **98**, 240501 (2007)

The initial idea behind the work is due to JMT, while the actual implementation is mainly due to CF. ASS and MDL contributed with several important comments, corrections, and physical insights. The writing of the manuscript was done by all authors in a joint effort.

PRL **98,** 240501 (2007) PHYSICAL REVIEW LETTERS week ending 15 JUNE 2007

Spin-Photon Entangling Diode

Christian Flindt,[1,2,3] Anders S. Sørensen,[2] Mikhail D. Lukin,[3] and Jacob M. Taylor[3,4]

[1]*MIC—Department of Micro and Nanotechnology, Technical University of Denmark, Kongens Lyngby 2800, Denmark*
[2]*QUANTOP and the Niels Bohr Institute, University of Copenhagen, Copenhagen 2100, Denmark*
[3]*Department of Physics, Harvard University, Massachusetts 02138, USA*
[4]*Department of Physics, Massachusetts Institute of Technology, Massachusetts 02139, USA*

(Received 28 February 2007; published 14 June 2007)

We propose a semiconductor device that can electrically generate entangled electron spin-photon states, providing a building block for entanglement of distant spins. The device consists of a *p-i-n* diode structure that incorporates a coupled double quantum dot. We show that electronic control of the diode bias and local gating allow for the generation of single photons that are entangled with a robust quantum memory based on the electron spins. Practical performance of this approach to controlled spin-photon entanglement is analyzed.

DOI: 10.1103/PhysRevLett.98.240501 PACS numbers: 03.67.Mn, 71.35.−y, 73.40.Ty

Many practical approaches to quantum communication and computation rely upon interfacing stable quantum systems, which provide a good quantum memory, with carriers of quantum information (optical photons) at the level of single quanta. One promising approach to quantum memory uses electron spins confined in semiconductor quantum dots [1]. Quantum dots in diode structures can also be used for creating devices with novel electronic and optical properties. In particular, the Coulomb blockade exhibited by quantum dots is being used in experiments involving single charge and spin transport and manipulation [2–4] as well as for optical experiments such as generation of single-photons [5–8]. Application of these systems for quantum communication and computation protocols is a vibrant area of research [9–16].

In this Letter, we propose and analyze a novel semiconductor device in which an electrically pumped diode structure can combine controlled photonic interface with stable quantum memory. Such a device features purely electrical control over photonic and spin degrees of freedom. Specifically, we show that it can be used for controlled generation of entangled states between the frequency of an outgoing photon and the spin state of the electrons in a double quantum dot in the insulating layer of the diode similar to recent laser-driven experiments in atomic systems [17–19]. Using recently demonstrated techniques [20], the double-dot spin states can provide a robust quantum memory for long-term information storage, while outgoing photons can be used for probabilistic generation of long-distance entanglement in direct analogy to approaches being explored for atomic systems [21]. Finally, when integrated with gate-controlled quantum dot systems [22], this device could also form a building block for scalable quantum computation.

The basic idea of our approach can be understood by considering the semiconductor nanowire shown in Fig. 1(a), in which a Coulomb-blockade double quantum dot is sandwiched between the positively and negatively doped semiconductor regions, forming a *p-i-n* diode. By manipulating the bias across the diode and the local gate, we can control the injection of electrons and holes into the double dot at the level of single charges. This allows us to electrically prepare a metastable exciton complex that

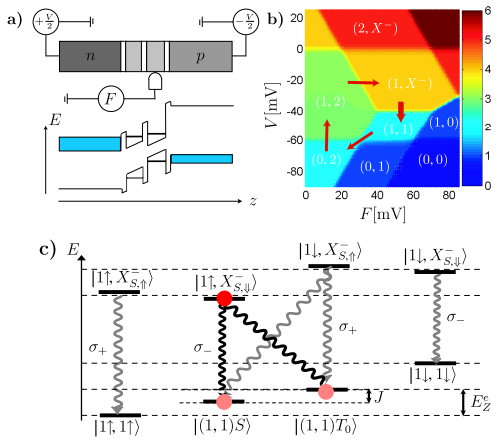

FIG. 1 (color online). Diode structure, charge stability diagram, and decay paths. (a) The device consists of a double quantum dot within the intrinsic region of a *p-i-n* diode structure. A schematic band-edge diagram is shown below. The left hole state (gray) is assumed to be energetically out of reach. (b) The stable charge configuration of the double quantum dot as a function of the bias V and the local gate F. The scale bar indicates the total number of charges, while the labeling (n, m) corresponds to the number of electrons on the left (n) and right (m) dot, replaced by X^- for dots containing a negatively charged exciton consisting of two electrons and a hole. As discussed in the text, the charging sequence indicated by arrows preferentially initializes the dots in the state $|1\uparrow, X^-_{S,\Downarrow}\rangle$. (c) Initial and final states for excitonic recombination together with the polarization of the emitted photon. The desired decay processes (shown in black) are selected by filtering σ_- polarization.

decays by electron-hole recombination to a charge configuration with a single electron in each of the two dots. When the two-electron spin states are split by the exchange coupling [1], the left circularly polarized photon that is emitted under the electron-hole recombination process will be frequency-entangled with the spin state of the remaining electrons [Fig. 1(c)].

Double dots can be grown inside *p-i-n* junctions with techniques similar to those recently used to fabricate single quantum dot nanowire LEDs [23,24]. Alternatively, self-assembled dots on wafers can be used [25]. As illustrated in Fig. 1(a), the chemical potentials of the p and n regions on each side of the intrinsic region can be controlled by applying a bias across the device, while a gate electrode nearby the double dot can be used to tune the levels inside the dots independently of the applied bias. In what follows, we focus on III-V semiconductors, but in practice, other optically active materials can be used.

The electrostatic properties of the device can be visualized by using a charge stability diagram [26]. We describe the charge degrees of freedom of the double quantum dot using the Hamiltonian

$$\hat{H}_{\mathrm{DQD}} = \hat{H}^{l}_{ee} + \hat{H}^{r}_{ee} + \hat{H}^{r}_{hh} + \hat{H}^{r}_{eh} + \hat{H}_{\tau} + \hat{H}_{F}, \quad (1)$$

where the Coulomb repulsion between similar charges ($q = e, h$) on the left or right dot reads $\hat{H}^{s}_{qq} = U_{qq}\hat{n}^{s}_{q}(\hat{n}^{s}_{q} - 1)/2$, $s = l, r$, while the Coulomb attraction between electrons and hole in the right dot reads $\hat{H}^{r}_{eh} = -U_{eh}\hat{n}^{r}_{e}\hat{n}^{r}_{h}$. Here, $\hat{n}^{l\{r\}}_{e(h)}$ is the operator for the number of electrons (holes) in the left {right} dot. Tunneling of electrons between the dots with tunnel coupling τ is contained in the term $\hat{H}_{\tau}$, while $\hat{H}_{F} = -eF(\hat{n}^{r}_{h} - \hat{n}^{r}_{e})$ incorporates the shift of the electron and hole states in the right dot due to the local gate F. Electrons with spin $\sigma = \pm 1/2$ on the left and right dots are created by $\hat{c}^{\dagger}_{l,\sigma}$ and $\hat{c}^{\dagger}_{r,\sigma}$, respectively, while heavy holes in the right dot are described by $\hat{d}^{\dagger}_{r,\Sigma}$, with $\Sigma = \pm 3/2$. In order for the scheme we consider to work ideally, we assume in the following that the hole states of the left dot remain unoccupied. This could occur due to the substantial band gap differences (0.1 eV or more) between the two dots, due, e.g., to strain and dot size differences. Electrons are injected into the left dot from the electron Fermi sea in the n-region at chemical potential μ_n, while holes are injected into the right dot from the hole Fermi sea in the p-region at chemical potential μ_p. Assuming weak coupling to the electron and hole Fermi seas, we solve numerically the master equation for the probability of occupying the different many-body eigenstates of the double dot and find the stable charge configurations for the chosen parameter range.

In Fig. 1(b), we show the resulting charge stability diagram, where the total number of charges on the double quantum dot is given as function of the bias across the device V and the local gate F. Here, $\mu_n = \mu^{0}_{n} + eV/2$ and $\mu_p = \mu^{0}_{p} - eV/2$, where μ^{0}_{n} and μ^{0}_{p}, given by the doping levels of the n and p regions, respectively, determine the filling of the double dot without applied voltages. In the numerical calculations, the values of μ^{0}_{n} and μ^{0}_{p} were used to fix the occupations of the dots at V, $F = 0$. For the shown charge stability diagram we have used the parameters $U_{ee} \simeq 30$ meV, $U_{hh} \simeq 50$ meV, $U_{eh} \simeq 40$ meV, $\tau = 1$ meV, and the tunnel couplings to the electron and hole Fermi seas being identical and much smaller than the temperature $T = 4$ K. With a given setting of V and F, the system rapidly reaches the corresponding stable charge configuration. On the figure, we also indicate the charge configuration of each of the two dots, where the labeling (n, m) refers to the charges on the left dot (n) and the right dot (m), respectively. For configurations with no holes, the two labels correspond to the number of electrons in the left and right dot, respectively, while the symbol X^{-} denotes a negatively charged exciton consisting of two electrons and a hole. Such excitonic states have previously successfully been generated and controlled optically [27,28], but the procedure presented here works all electrically and thereby does not require any laser control. An external magnetic field B is applied to the system parallel to the light emission and growth axis [the z-axis on Fig. 1(a)], i.e., in a Faraday configuration. In order to have reliable electron spin state preparation, we will require the Fermi seas to be sufficiently cold: $k_B T \ll |g^{*}\mu_B B|$ (see below).

We now describe the charge injection sequence indicated by arrows in Fig. 1(b). The sequence allows us repeatedly to prepare a desired spin and charge configuration, by injecting charges one at a time, and to direct its decay and corresponding photon emission process. We assume that single charges may be injected faster than the spontaneous decay time (~ 1 ns for GaAs self-assembled dots). By controlling the bias V and the local gate F, the system is first put in the charge configuration (0, 2). The expected ground state spin configuration of this state is a singlet due to the tight confinement of the electrons to a single dot: $|0, 2S\rangle = \hat{c}^{\dagger}_{r,\uparrow}\hat{c}^{\dagger}_{r,\downarrow}|0\rangle$. By increasing the bias, an additional spin-$\uparrow$ electron is added to the left dot, taking $|0, 2S\rangle$ to $|1\uparrow, 2S\rangle = \hat{c}^{\dagger}_{l,\uparrow}\hat{c}^{\dagger}_{r,\uparrow}\hat{c}^{\dagger}_{r,\downarrow}|0\rangle$. A spin-$\Downarrow$ heavy hole is now added to the right dot by control of the local gate, yielding the state $|1\uparrow, X^{-}_{S,\Downarrow}\rangle = \hat{d}^{\dagger}_{r,\Downarrow}\hat{c}^{\dagger}_{l,\uparrow}\hat{c}^{\dagger}_{r,\uparrow}\hat{c}^{\dagger}_{r,\downarrow}|0\rangle$, which we expect to decay to $|1\uparrow, 1\downarrow\rangle = \hat{c}^{\dagger}_{l,\uparrow}\hat{c}^{\dagger}_{r,\downarrow}|0\rangle$ via excitonic recombination ($\hat{d}_{r,\Downarrow}\hat{c}_{r,\uparrow}$). However, before recombination takes place, we rapidly (faster than the decay rate) move to the region, where (1, 1) is the stable charge configuration, hereby preventing emission of more than one photon (by refilling of an electron and a hole) in each cycle of the sequence.

The exciton decay couples the state $|1\uparrow, X^{-}_{S,\Downarrow}\rangle$ to $|1\uparrow, 1\downarrow\rangle$. With finite tunnel coupling between the left and right dots, this may be written as a superposition $|1\uparrow, 1\downarrow\rangle = [|(1, 1)S\rangle + |(1, 1)T_0\rangle]/\sqrt{2}$, of the exchange-split singlet and triplet eigenstates $|(1, 1)S(T_0)\rangle = 2^{-1/2}(\hat{c}^{\dagger}_{l,\uparrow}\hat{c}^{\dagger}_{r,\downarrow} \pm \hat{c}^{\dagger}_{l,\downarrow}\hat{c}^{\dagger}_{r,\uparrow})|0\rangle$. Since S and T_0 have different energies, the

PRL 98, 240501 (2007) PHYSICAL REVIEW LETTERS week ending 15 JUNE 2007

frequency of the outgoing photon will be entangled with the spin state [see Fig. 1(c) and Eq. (2) below]. These S-T_0 spin states were used in recent double-dot experiments where it was shown that they form a decoherence free subspace when manipulated with fast spin-echo pulses [3,29,30]. With the system in Faraday configuration, the spin of the hole determines the polarization of the emitted photon. While a spin-$\Downarrow$ heavy-hole recombines with a spin-$\uparrow$ electron under emission of a left-hand circularly polarized (σ_-) photon, a spin-$\Uparrow$ heavy-hole recombines with a spin-$\downarrow$ electron under emission of a right-hand circularly polarized (σ_+) photon. With temperature being comparable to or larger than the (small) hole Zeeman energy, the injected hole has a random spin state. With suitable polarization filtering, it is, however, possible to exclude photons that have been emitted with the heavy-hole incorrectly in the spin-$\Uparrow$ state; thus, in practice when the hole g-factor is substantially smaller than the electronic g-factor or has the opposite sign, the possibility of incorrect hole spin states does not limit our approach. However, we still require $k_bT \ll |g^*\mu_B B|$ for the reliable preparation of the desired electron spin state in the left dot as this electron spin has no effect on the final polarization of the photon.

The resulting spin-photon entangled state can be used for generating spin-spin entanglement between two remote devices by interfering the emitted photons on a beam splitter as shown in Fig. 2(a) [31]. If the spin state in both devices are identical, both incoming photons can be mode matched in space, frequency, and time, so that Hong-Ou-Mandel bunching will occur, leading to photon detection in only one arm of the beam splitter. On the other hand, if the spin states are different, the photons are distinguishable, and no "bunching" will occur. A photon detection in each arm of the beam splitter therefore leads to an entangled state of the spins in the spatially separated devices $|\Psi_{12}\rangle = (|S\rangle_1|T_0\rangle_2 - |T_0\rangle_1|S\rangle_2)/\sqrt{2}$, where we have omitted the charge labeling (1, 1). In the following, we consider the distinguishability of our outgoing photons to determine the requirements for such entanglement generation.

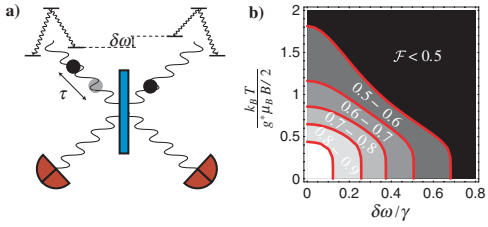

FIG. 2 (color online). Beam splitter setup and entanglement fidelity. (a) Photon interference leading to entanglement between two devices. The entanglement fidelity may be reduced due to different arrival times τ at the beam splitter, mismatch $\delta\omega$ between energy splittings in the two devices, and incorrect spin initialization (not indicated). (b) Entanglement fidelity $\mathcal{F}$ as function of temperature T and energy mismatch $\delta\omega$. For the calculations, we have used $\gamma \times \bar{\tau} = 0.03$. In the white region, $\mathcal{F} > 0.9$.

We first consider spontaneous decay associated with electron-hole recombination in a single device. The process can be described within the framework of Wigner-Weisskopf theory yielding a characteristic decay rate γ. We note that the ground state charge configuration (1, 1) may also be reached by the electron-hole pair tunneling back into the Fermi seas with rate Γ_o rather than recombining. This does not impact the fidelity of entanglement, since no photon is emitted and we always condition on two clicks in the detectors, but it does reduce the success probability. After spontaneous decay has taken place the combined state $|\Phi\rangle$ (conditioned on electron-hole recombination) of the charges and the photon field reads

$$|\Phi\rangle = \frac{1}{\sqrt{2}}[|S\rangle \otimes \hat{\xi}^\dagger(\omega_S)|0\rangle + |T_0\rangle \otimes \hat{\xi}^\dagger(\omega_{T_0})|0\rangle], \quad (2)$$

where $\hat{\xi}^\dagger(\omega) = \sum_k \xi(\omega, k)\hat{a}_k^\dagger$ with $\xi(\omega, k) = \frac{1}{\sqrt{2\pi}} \times \frac{\sqrt{\gamma}e^{-ikz_0}}{(\omega_k - \omega) + i\gamma/2}$ and $\hat{a}_k^\dagger$ being the creation operator for photons of mode k. Here, $|0\rangle$ is the vacuum state of the photon field, while the position of the double quantum dot is z_0, and ω_S and ω_{T_0} denote the splittings between the excited state and the singlet and triplet ground states, respectively, so that $|\omega_S - \omega_{T_0}|$ equals the exchange coupling J. The width of the photon wave packet is given by $\gamma = \gamma_S + \gamma_{T_0} + \Gamma_o$, and above we have taken the same rates, $\gamma_S = \gamma_{T_0}$, resulting in equal branching ratios for the two processes.

We now consider the beam splitter setup depicted in Fig. 2(a) and consider two photons emitted by similar devices. With probability $1/2$, the two photons are in states corresponding to the same spin state of the electrons in the two devices (both singlet or both triplet). The probability of detecting two photons, in states $|\Psi_L\rangle = \xi_L^\dagger(\omega_L)|0\rangle$ and $|\Psi_R\rangle = \xi_R^\dagger(\omega_R)|0\rangle$, respectively, at different detectors (denoted L and R) after they have scattered on the 50/50 beam splitter is $P(1_L, 1_R) = (1 - |\mathcal{J}|^2)/2$, where $\mathcal{J} \equiv \sum_k \xi_L(\omega_L, k)\xi_R^*(\omega_R, k)$ is the overlap of the wave packet amplitudes. With $\omega_L = \omega_S$ and $\omega_R = \omega_{T_0}$, we find

$$P(1_L, 1_R) = \frac{1}{2}\left(1 - \frac{\gamma^2}{\gamma^2 + J^2}\right). \quad (3)$$

Typical electron-hole recombination rates are on the order of GHz, and the width of the wave packets γ therefore is on the order of μeVs, which is smaller than the exchange coupling J between tunnel-coupled quantum dots, which is in the range 10 μeV to 1 meV. Thus, we expect $P(1_L, 1_R) \sim 1/2$ and a corresponding success rate of $\eta^2/4$ for detecting the two photons at different detectors, where η is the combined single photon emission and detection probability.

Besides the success rate, we need to consider the fidelity $\mathcal{F} = \langle\Psi_{12}|\hat{\rho}_s|\Psi_{12}\rangle$ of the entangling procedure, where $|\Psi_{12}\rangle$ is the desired state, and $\hat{\rho}_s$ is the reduced density

matrix for the spins in the two devices. Possible error processes include wrong initialization of the spin states, jitter in the hole injection and path length differences leading to different arrival times at the beam splitter, and different energy splittings between the excited state and the ground states in the two devices. We remark that the specific device details could be tuned, e.g., with dc Stark shifts, to minimize these errors. To evaluate the effect of jitter and the different energy splittings, we write the full density matrix of the spins and photons as $\hat{\rho} = |\Phi\rangle_1|\tilde{\Phi}\rangle_{22}\langle\tilde{\Phi}|_1\langle\Phi|$ where both $|\Phi\rangle_1$ and $|\tilde{\Phi}\rangle_2$ are of the form given in Eq. (2), but $|\tilde{\Phi}\rangle_2$ has a component on a field mode perpendicular to the field mode emitted by device number 1; i.e., for $|\tilde{\Phi}\rangle_2$, $\hat{\xi}^\dagger$ is replaced by $\mathcal{J}\hat{\xi}^\dagger + \sqrt{1-|\mathcal{J}|^2}\hat{\xi}^\dagger_{\rm err}$. Here, $\hat{\xi}^\dagger_{\rm err}$ creates a photon in an undesired mode due to the jitter and energy shifts, and $\mathcal{J}$ denotes the corresponding wave packet overlap. Conditioned on clicks in different detectors after the beam splitter, we find that the erroneous field component generates the spin states $|T_0\rangle_1|T_0\rangle_2$, $|S\rangle_1|S\rangle_2$, $|T_0\rangle_1|S\rangle_2$, and $|S\rangle_1|T_0\rangle_2$ with equal probability $(1-|\mathcal{J}|^2)/(4-3|\mathcal{J}|^2)$. The fidelities corresponding to these states are 0, 0, 1/2, and 1/2, respectively. The desired state $(|S\rangle_1|T_0\rangle_2 - |T_0\rangle_1|S\rangle_2)/\sqrt{2}$ (with fidelity 1) is generated with probability $|\mathcal{J}|^2/(4-3|\mathcal{J}|^2)$. Combining these numbers, we find the fidelity $1/(4-3|\mathcal{J}|^2)$, which, however, does not yet include the possibility of wrong spin initialization.

In thermal equilibrium, the probability of initializing the wrong spin state $|\downarrow\rangle$ in the left dot is given by the Boltzmann factor $p_\downarrow \propto e^{-g^*\mu_B B/2k_B T}$. Wrong initialization of the spin in one or both of the devices leads to states with fidelity 0. For the probability of detection at different detectors due to a wrong spin in one or both of the devices, we use the upper bound $\eta^2(2p_\downarrow - p_\downarrow^2)/2$. Including this estimate for the effect of wrong spin initialization in the above expression for the fidelity, we find

$$\mathcal{F} = \frac{1}{4-3|\mathcal{J}|^2}\,\frac{1}{1+2(2p_\downarrow - p_\downarrow^2)}. \qquad (4)$$

Two photons created by $\hat{\xi}^\dagger(\omega)$ and $\hat{\xi}^\dagger(\omega+\delta\omega)$ with a time difference τ have the wave packet overlap $|\mathcal{J}|^2 = \frac{\gamma^2 e^{-\gamma|\tau|}}{\delta\omega^2+\gamma^2}$. For the time difference, we assume a Gaussian probability distribution with width $\bar{\tau}$, $\mathcal{P}(\tau) \propto e^{-(\tau/\bar{\tau})^2/2}$. This distribution is relevant when noise in the gates controlling the hole injection is responsible for the photons being created at different times or when the optical paths do not have exactly the same length. When evaluating the fidelity, we average the expression in Eq. (4) with respect to the Gaussian distribution. In Fig. 2(b), we show the fidelity as function of temperature and energy mismatch. We see that with realistic parameters, it is possible to obtain a high degree of fidelity, $\mathcal{F} > 0.9$, and even with temperatures comparable to the Zeeman energy, the fidelity may be larger than 0.5, the lower bound for the use of entanglement purification protocols [32]. Furthermore, the loss of fidelity due to time jitter or energy mismatch may be suppressed by gating the detectors in time, thereby improving the shown results.

In conclusion, we have presented a proposal for an all-electrically controlled device for long-range electron spin entanglement and shown that entanglement can be generated with a high degree of fidelity using available experimental techniques. When combined with existing quantum optical methods and solid-state technologies for spin manipulation and detection, our proposed device may form an important building block in future quantum communication and information processing architectures.

We thank M. V. G. Dutt, K. Flensberg, A. Imamoglu, and M. Stopa for helpful conversations. The work was supported by the Denmark-America Foundation, Pappalardo, the Danish Natural Science Research Council, NSF, DTO, and the Packard Foundation.

[1] D. Loss and D. P. DiVincenzo, Phys. Rev. A **57**, 120 (1998); G. Burkard, D. Loss, and D. P. DiVincenzo, Phys. Rev. B **59**, 2070 (1999).
[2] M. Kroutvar *et al.*, Nature (London) **432**, 81 (2004).
[3] J. R. Petta *et al.*, Science **309**, 2180 (2005).
[4] F. H. L. Koppens *et al.*, Nature (London) **442**, 766 (2006).
[5] A. Imamoglu and Y. Yamamoto, Phys. Rev. Lett. **72**, 210 (1994).
[6] J. Kim *et al.*, Nature (London) **397**, 500 (1999).
[7] P. Michler *et al.*, Science **290**, 2282 (2000).
[8] A. J. Bennett *et al.*, Phys. Status Solidi B **243**, 3730 (2006).
[9] G. Chen *et al.*, Science **289**, 1906 (2000).
[10] O. Gywat, G. Burkard, and D. Loss, Phys. Rev. B **65**, 205329 (2002).
[11] W. Yao, R.-B. Liu, and L. J. Sham, Phys. Rev. Lett. **95**, 030504 (2005).
[12] E. Waks *et al.*, Nature (London) **420**, 762 (2002).
[13] A. Badolato *et al.*, Science **308**, 1158 (2005).
[14] H. J. Krenner *et al.*, Phys. Rev. Lett. **97**, 076403 (2006).
[15] E. A. Stinaff *et al.*, Science **311**, 636 (2006).
[16] R. M. Stevenson *et al.*, Nature (London) **439**, 179 (2006).
[17] B. B. Blinov *et al.*, Nature (London) **428**, 153 (2004).
[18] J. Volz *et al.*, Phys. Rev. Lett. **96**, 030404 (2006).
[19] W. Rosenfeld *et al.*, Phys. Rev. Lett. **98**, 050504 (2007).
[20] J. M. Taylor *et al.*, Phys. Rev. Lett. **94**, 236803 (2005).
[21] L. M. Duan *et al.*, Nature (London) **414**, 413 (2001).
[22] H. A. Engel *et al.*, arXiv:cond-mat/0612700.
[23] M. T. Borgstrom *et al.*, Nano Lett. **5**, 1439 (2005).
[24] E. D. Minot *et al.*, Nano Lett. **7**, 367 (2007).
[25] G. S. Solomon *et al.*, Phys. Rev. Lett. **76**, 952 (1996).
[26] W. G. van der Wiel *et al.*, Rev. Mod. Phys. **75**, 1 (2003).
[27] M. V. G. Dutt *et al.*, Phys. Rev. Lett. **94**, 227403 (2005).
[28] M. Atatüre *et al.*, Science **312**, 551 (2006).
[29] J. Levy, Phys. Rev. Lett. **89**, 147902 (2002).
[30] J. M. Taylor *et al.*, Nature Phys. **1**, 177 (2005).
[31] L. M. Duan *et al.*, Phys. Rev. A **73**, 062324 (2006).
[32] H. J. Briegel *et al.*, Phys. Rev. Lett. **81**, 5932 (1998).

Paper N

C. Flindt, A. Braggio, and T. Novotný

Non-Markovian dynamics in the theory of full counting statistics

AIP Conf. Proc. **922**, 531 (2007)

The work is part of a joint project involving CF, AB, and TN, on non-Markovian dynamics in the theory of full counting statistics. While the general theoretical framework was developed in a joint effort of CF, AB, and TN, this particular work is mainly due to CF.

Non-Markovian dynamics in the theory of full counting statistics

Christian Flindt*, Alessandro Braggio† and Tomáš Novotný**

*MIC – Department of Micro and Nanotechnology, NanoDTU, Technical University of Denmark, Building 345east, DK-2800 Kongens Lyngby, Denmark
†LAMIA-INFM-CNR, Dipartimento di Fisica, Via Dodecaneso 33, I-16146, Genova, Italy
**Department of Condensed Matter Physics, Faculty of Mathematics and Physics, Charles University, Ke Karlovu 5, 121 16 Prague, Czech Republic

Abstract. We consider the theoretical description of real-time counting of electrons tunneling through a Coulomb-blockade quantum dot using a detector with finite bandwidth. By tracing out the quantum dot we find that the dynamics of the detector effectively is non-Markovian. We calculate the cumulant generating function corresponding to the resulting non-Markovian rate equation and find that the measured current cumulants behave significantly differently compared to those of a Markovian transport process. Our findings provide a novel interpretation of noise suppression found in a number of systems.

Keywords: Full counting statistics, detectors, non-Markovian dynamics
PACS: 72.70.+m, 73.23.Hk, 73.23.-b

The theory of full counting statistics concerns the probability $P(n,t)$ of having transferred n charges through a mesoscopic system at time t, when starting counting at $t=0$ [1]. Rather than the probability distribution $P(n,t)$, it is often more convenient to consider the cumulant generating function $S(\chi,t)$ defined as

$$e^{S(\chi,t)} \equiv P(\chi,t) = \sum_n P(n,t)e^{in\chi}, \tag{1}$$

from which the zero-frequency cumulants of the current can be found in the long-t limit by deriving with respect to the counting field χ at zero, i.e.,

$$\langle\langle I^n \rangle\rangle = \frac{d}{dt}\frac{d^n S(\chi,t)}{d(i\chi)^n}\bigg|_{\chi=0,t\to\infty}, n=1,2,3,\ldots \tag{2}$$

In this work we consider the effects of a finite bandwidth of the apparatus detecting charge transfers on the *measured* counting statistics. In particular, we show that the finite bandwidth makes the effective dynamics of the detector *non-Markovian*, and we discuss how non-Markovian dynamics in general can make the counting statistics and the corresponding current cumulants behave significantly differently compared to Markovian transport processes. Although, the conclusions reached below are obtained for a specific setup, we argue that they are valid for a large class of systems.

We consider a model of real-time counting with a finite-bandwidth detector [2] recently employed in order to explain experimental counting statistics results on electron transport through a Coulomb-blockade quantum dot [3]. In the experiment a quantum

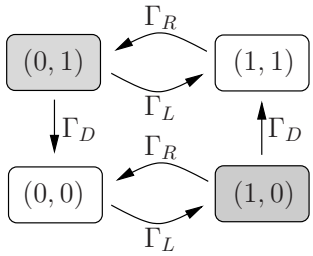

FIGURE 1. Detector-dot model. The system switches with rates Γ_L, Γ_R, and Γ_D between the states (i,j), where $i = 0,1$ denotes the charge state of the quantum dot and $j = 0,1$ the charge state as *measured* by the detector. Each switching event between the states $(1,0)$ and $(1,1)$ corresponds to the measurement of a single electron having entered the quantum. In the ideal detector limit $\Gamma_D \to \infty$, the system effectively switches between the states $(0,0)$ and $(1,1)$ with rates Γ_L and Γ_L, while the other states essentially remain unoccupied. We note that similar figures can be found in Refs. [2, 3].

point contact was used to monitor the two charge states participating in transport through a nearby quantum dot weakly coupled to source and drain electrodes and each switching event between the two charge states was associated with an electron either entering the quantum dot from the source electrode or leaving it via the drain. Rather than just considering the two charge states of the quantum dot, while keeping track of the number of electrons n that have tunneled through the quantum dot, the model also takes into account the state of the detector that counts the electrons. In the following $P_{ij}(n,t)$ denotes the probability that the system at time t is in a state, where the quantum dot is occupied by $i = 0,1$ extra electrons, while the detector indicates $j = 0,1$ extra electrons on the quantum dot, and n electrons *according to the detector* have been transferred through the quantum dot. We collect these four probabilities in the vector $\mathbf{P} = (P_{00}, P_{10}, P_{11}, P_{01})^T$ and note that $P(n,t) = P_{00}(n,t) + P_{10}(n,t) + P_{11}(n,t) + P_{01}(n,t)$. The counting field is now introduced via a Fourier transformation as in Eq. (1) and the Markovian equation of motion for $\mathbf{P}(\chi,t)$ then reads

$$\frac{d}{dt}\mathbf{P}(\chi,t) = \mathbf{M}(\chi)\mathbf{P}(\chi,t), \tag{3}$$

where

$$\mathbf{M}(\chi) = \begin{pmatrix} -\Gamma_L & \Gamma_R & 0 & \Gamma_D \\ \Gamma_L & -(\Gamma_D+\Gamma_R) & 0 & 0 \\ 0 & \Gamma_D e^{i\chi} & -\Gamma_R & \Gamma_L \\ 0 & 0 & \Gamma_R & -(\Gamma_D+\Gamma_L) \end{pmatrix}. \tag{4}$$

Here, Γ_L and Γ_R denote the rates at which electrons are injected and leave the quantum dot, respectively, while Γ_D is the rate (or the bandwidth) at which the detector reacts to changes of the charge state of the quantum dot (see Fig. 1). An ideal detector ($\Gamma_D \to \infty$) is able to count every electron that is transported through the quantum dot. On the other hand, when Γ_D is comparable to the electron tunneling rates Γ_L and Γ_R, the finite bandwidth of the detector reduces the ability of the detector to count every electron transfer event. This, of course, affects the measured counting statistics.

In the following, we trace out the quantum dot and show that the resulting dynamics of the detector is non-Markovian. The quantum dot is traced out by defining $P_j \equiv \sum_{i=0,1} P_{ij}$, $j=0,1$, whose equations of motion read $\dot{P}_0 = \Gamma_D(P_{01}-P_{10})$ and $\dot{P}_1 = \Gamma_D(e^{i\chi}P_{10}-P_{01})$, respectively. The probabilities $P_j(\chi,t)$, $j=0,1$, only contain information about the state of the detector and the number of electrons counted by the detector. By observing that $\dot{P}_{10} = \Gamma_L P_{00} - (\Gamma_D+\Gamma_R)P_{10} = \Gamma_L P_0 - (\Gamma_D+\Gamma_L+\Gamma_R)P_{10}$ and $\dot{P}_{01} = \Gamma_R P_{11} - (\Gamma_D+\Gamma_L)P_{01} = \Gamma_R P_1 - (\Gamma_D+\Gamma_L+\Gamma_R)P_{01}$, we find

$$P_{10}(\chi,t) = \Gamma_L \int_0^t d\tau e^{-(\Gamma_D+\Gamma_L+\Gamma_R)(t-\tau)} P_0(\chi,\tau) + e^{-(\Gamma_D+\Gamma_L+\Gamma_R)t} P_{10}(\chi,t=0), \tag{5}$$

and a similar expression for $P_{01}(\chi,t)$. In the following, we focus on the long-t limit, where the initial condition $P_{10}(\chi,t=0)$ (and $P_{01}(\chi,t=0)$) may safely be neglected.[1] This leads to a *non-Markovian* rate-equation for $\mathbf{p}(\chi,t) = (P_0,P_1)^T$, reading

$$\frac{d}{dt}\mathbf{p}(\chi,t) = \int_0^t \mathbf{W}(\chi,t-\tau)\mathbf{p}(\chi,\tau), \tag{6}$$

where

$$\mathbf{W}(\chi,t-\tau) = \Gamma_D e^{-(\Gamma_D+\Gamma_L+\Gamma_R)(t-\tau)} \begin{pmatrix} -\Gamma_L & \Gamma_R \\ \Gamma_L e^{i\chi} & -\Gamma_R \end{pmatrix}. \tag{7}$$

In Laplace space this translates to the algebraic equation

$$z\mathbf{p}(\chi,z) - \mathbf{p}(\chi,t=0) = \mathbf{W}(\chi,z)\mathbf{p}(\chi,z) \tag{8}$$

or

$$\mathbf{p}(\chi,z) = \frac{1}{z-\mathbf{W}(\chi,z)}\mathbf{p}(\chi,t=0) \tag{9}$$

with

$$\mathbf{W}(\chi,z) = D(z) \begin{pmatrix} -\Gamma_L & \Gamma_R \\ \Gamma_L e^{i\chi} & -\Gamma_R \end{pmatrix}, \tag{10}$$

having introduced $D(z) = \Gamma_D/(z+\Gamma_D+\Gamma_L+\Gamma_R)$. We note that in the limit $\Gamma_D \to \infty$, $D(z) \to 1$, and the detector follows the *Markovian* dynamics of the quantum dot.

One can show (see e.g. Refs. [4, 5]) that the cumulant generating function in the long-t limit is given as $S(\chi,t) = z^*(\chi)t$, where $z^*(\chi)$ solves the equation

$$z^*(\chi) - \Lambda_0[\chi, z^*(\chi)] = 0. \tag{11}$$

Here $\Lambda_0[\chi,z]$ is the eigenvalue of $\mathbf{W}(\chi,z)$ which for $\chi=0$ is zero, i.e., $\Lambda_0[0,z]=0$, and the solution $z^*(\chi)$ must be chosen such that $z^*(0)=0$. We find $\Lambda_0[\chi,z] = D(z)\lambda_0(\chi)$ with $\lambda_0(\chi) = -(\Gamma_L+\Gamma_R)/2 + \sqrt{(\Gamma_L+\Gamma_R)^2/4 + \Gamma_L\Gamma_R(e^{i\chi}-1)}$, and

$$z^*(\chi) = -\frac{\Gamma_D+\Gamma_L+\Gamma_R}{2} + \sqrt{\left(\frac{\Gamma_D+\Gamma_L+\Gamma_R}{2}\right)^2 + \Gamma_D\lambda_0(\chi)}. \tag{12}$$

---

[1] We note that the initial condition plays a crucial role when studying finite-frequency fluctuations.

For large matrices, in general, it may be non-trivial to find $z^*(\chi)$ and more sophisticated methods, as the one we describe in Ref. [5], may be needed. Having found the cumulant generating function in the long-t limit, $S(\chi,t) = z^*(\chi)t$, we may calculate the current cumulants, and here we just give the results for the first two current cumulants, although it, in principle, is possible to obtain any cumulant having found $S(\chi,t)$,

$$\begin{aligned} \langle\langle I^1 \rangle\rangle &= \Gamma_R \left[\frac{1+a}{2}\right] \times \left[\frac{k}{1+k}\right], \\ \langle\langle I^2 \rangle\rangle &= \left[\frac{1+a^2}{2} - \frac{k(1-a^2)}{2(1+k)^2}\right] \langle\langle I^1 \rangle\rangle. \end{aligned} \tag{13}$$

These are the results also found in Ref. [3] using the model in its Markovian formulation given by Eq. (4), and following that work we have also introduced the asymmetry $a = (\Gamma_R - \Gamma_L)/(\Gamma_R + \Gamma_L)$ and the relative bandwidth $k = \Gamma_D/(\Gamma_R + \Gamma_L)$.

It is interesting to consider the so-called Fano factor $F \equiv \langle\langle I^2 \rangle\rangle / \langle\langle I^1 \rangle\rangle$. In the ideal detector limit $\Gamma_D \to \infty$, we find the well-known result $F = (1+a^2)/2$ for a *Markovian* two-state model with uni-directional transport where $1/2 \leq F \leq 1$. For finite bandwidths, the Fano factor may, however, be suppressed below $1/2$, and for the given model, we find that the Fano factor is bounded from below by the value 3/8 ($a = 0, k = 1$). In a number of papers, the sensitivity of the counting statistics to coherent versus sequential tunneling has been discussed [6], and particularly, it has been conjectured that a suppression of the Fano factor below $1/2$ for transport through a double barrier resonant diode could be an indication of coherent tunneling rather than sequential [7]. The results found in the present work show that a suppression below $1/2$ can occur due to non-Markovian dynamics, which is not necessarily induced by quantum coherence, but in general arises from tracing out parts of a system. We believe that a similar interpretation can explain the recently calculated Fano factor suppression of incoherent transport through a single electron transistor (SET) coupled to a nano-mechanical resonator [8]. There, we believe that the dynamics of the SET effectively is non-Markovian due to the coupling to the resonator, which in turn can explain the suppression of the Fano factor below $1/2$.

In conclusion, we have presented a study of the full counting statistics of electron transport through a Coulomb-blockade quantum dot as measured by a detector with finite bandwidth. In particular, we have calculated the current cumulants of the measured charge transport described by a non-Markovian rate equation obtained by tracing out the quantum dot and only considering the dynamics of the detector. Our results show that non-Markovian effects may strongly effect the charge transport statistics.

REFERENCES

1. *Quantum Noise in Mesoscopic Physics*, edited by Yu. V. Nazarov (Kluwer, Dordrecht, 2003)
2. O. Naaman and J. Aumentado, *Phys. Rev. Lett.* **96** (2006) 100201
3. S. Gustavsson *et al.*, *Phys. Rev. B* **75** (2007) 075314
4. A. Braggio, J. König, and R. Fazio, *Phys. Rev. Lett.* **96** (2006) 026805
5. C. Flindt *et al.*, in preparation (2007)
6. G. Kiesslich *et al.*, *Phys. Rev. B* **73** (2006) 033312
7. V. Ya. Aleshkin *et al.*, *Phys. Rev. B* **70** (2004) 115321
8. F. Haupt *et al.*, *Phys. Rev. B* **74** (2006) 205328

Paper O

J. Pedersen, C. Flindt, N. A. Mortensen, and A.-P. Jauho

Failure of standard approximations of the exchange coupling in nanostructures

Phys. Rev. B **76**, 125323 (2007)

The work is a result of the M.Sc. thesis by JP, supervised by CF and APJ. The idea behind the work is mainly due to CF, while the actual implementation is due to JP. NAM contributed with several physical insights. The writing was done in a joint effort by all authors, with CF being the main contributor to the main text, while JP was responsible for the appendices.

PHYSICAL REVIEW B **76**, 125323 (2007)

Failure of standard approximations of the exchange coupling in nanostructures

Jesper Pedersen,[1] Christian Flindt,[1] Niels Asger Mortensen,[1] and Antti-Pekka Jauho[1,2]
[1]*MIC—Department of Micro and Nanotechnology, NanoDTU, Technical University of Denmark, Building 345E, DK-2800 Kongens Lyngby, Denmark*
[2]*Laboratory of Physics, Helsinki University of Technology, P.O. Box 1100, FI-02015 HUT, Finland*
(Received 30 May 2007; revised manuscript received 23 July 2007; published 28 September 2007)

We calculate the exchange coupling for a double dot system using a numerically exact technique based on finite-element methods and an expansion in two-dimensional Gaussians. Specifically, we evaluate the exchange coupling both for a quasi-one- and a two-dimensional system, also including an applied magnetic field. Our numerical results provide a stringent test of standard approximation schemes (e.g., Heitler-London, Hund-Mulliken, Hubbard), and they show that the standard methods do not have reliable predictive power even for simple model systems. Their value in modeling more realistic quantum-dot structures is thus cast in serious doubt.

DOI: 10.1103/PhysRevB.76.125323 PACS number(s): 73.21.La, 75.30.Et, 02.70.Dh

I. INTRODUCTION

The possibility of coherent manipulation of electron spins in low-dimensional nanostructures, aimed at future large-scale quantum information processing,[1] calls for a thorough understanding of the spin interactions at play. In the proposal for quantum computing with quantum dots by Loss and DiVincenzo, the exchange coupling between the spins of electrons in tunnel-coupled quantum dots was envisioned as the controllable mechanism for coherent manipulation of spin qubits.[1,2] Recently, this fundamental building block of a possible future solid-state quantum computing architecture was realized in an experiment, demonstrating electrostatic control of the exchange coupling.[3]

In this paper, we present numerically exact finite-element methods for calculations of the exchange coupling between electron spins in tunnel-coupled quasi-one- and two-dimensional quantum dots. Such structures have already been under intensive theoretical investigation using various numerical methods, e.g., based on an exact diagonalization of the underlying Hamiltonian[4–10] or using quantum-chemical approaches such as self-consistent Hartree-Fock methods.[11] Such numerical approaches often require extensive numerical work. Therefore, much attention has been devoted to simple approximations which lead to closed-form analytic expressions for the exchange coupling.[2,12,13] It is, however, not immediately obvious to what extent these approximations yield correct predictions, and where they break down. For example, in a recent work,[12] the validity criterion for such approximations was the requirement that the exchange coupling at zero magnetic field must always be positive. A criterion like this can only provide a necessary condition for an approximate scheme to be acceptable.

The aim of this work is to provide a quantitative comparison of the Heitler-London, the Hund-Mulliken, and the Hubbard approximations, applied to a simple model potential of a double quantum dot, with numerically exact results. In particular, we focus on the case, where the distance between the two quantum dots is short, such that the single-dot electron wave functions have a large overlap. For short distances, the exchange coupling can reach values on the order of several meV, making it sufficiently large to exploit and observe in experiments, and our comparative study is thus highly relevant for on-going experimental activities within the field. The finite-element methods used here allow an easy implementation using available numerical packages,[14] also when finite magnetic fields are included, which strongly influence the exchange coupling in two-dimensional geometries. We find that the approximative schemes may provide reasonable predictions of the exchange coupling for certain parameter ranges, while they fail, also qualitatively, for short distances, even for the simple model potential considered here. Their value in modeling more realistic quantum-dot structures used in experiments is thereby cast in serious doubt.

II. DOUBLE QUANTUM-DOT MODEL

Experimentally, electrons can be confined in double quantum dots using metallic gates on top of a semiconductor heterostructure[3,15,16] or across a nanowire[17,18] or a nanotube.[19,20] By suitable electrostatic gating, such

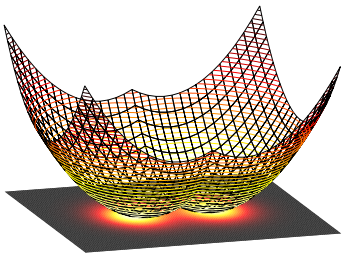

FIG. 1. (Color online) Double quantum dot and numerically calculated charge density. The double quantum dot is described by the potential $V(\mathbf{r})$ given in Eq. (4) (here with $\alpha=1$, $\hbar\omega_0=4$ meV and $d/r_0=1$). The two-dimensional contour plot shows how the charge of two electrons in a singlet spin state is distributed within the double quantum dot. With finite tunnel coupling between the two quantum dots, the spins of the electrons interact due to the exchange interaction.

Coulomb-blockade double quantum dots can be brought into a few-electron regime,[21] where only a single electron occupies each of the two quantum dots. In this regime, the spin and charge dynamics are described by a two-electron Hamiltonian of the form

$$H(\mathbf{r}_1,\mathbf{r}_2) = h(\mathbf{r}_1) + h(\mathbf{r}_2) + C(|\mathbf{r}_1 - \mathbf{r}_2|), \tag{1}$$

where

$$C(|\mathbf{r}_1 - \mathbf{r}_2|) = \frac{e^2}{4\pi\varepsilon_r\varepsilon_0|\mathbf{r}_1 - \mathbf{r}_2|} \tag{2}$$

is the Coulomb interaction and the single-particle Hamiltonians are

$$h(\mathbf{r}) = \frac{\mathbf{p}^2}{2m} + V(\mathbf{r}), \tag{3}$$

with $V(\mathbf{r})$ denoting the confining potential. As in many realizations of double quantum dots, we assume that the motion of the electrons is restricted to maximally two dimensions, i.e., $\mathbf{r}=(x,y)$. The inclusion of a magnetic field is discussed below.

As an illustrative example,[22] we consider a simple double dot potential reading[6,23]

$$V(\mathbf{r}) = \frac{m\omega_0^2}{2}[\min\{(x-d)^2,(x+d)^2\} + (\alpha y)^2]. \tag{4}$$

Here, m is the effective electron mass, $\hbar\omega_0$ is the characteristic confinement energy, $2d$ measures the center to center distance between the quantum dots, and α denotes the ratio of the confinement strengths in the x and y directions. Moreover, we introduce the characteristic oscillator length $r_0 = \sqrt{\hbar/m\omega_0}$. The potential is shown in Fig. 1 together with a numerically calculated charge density. In the limit $d\to 0$, the potential reduces to that of a single quantum dot. In our calculations we use material parameters typical of GaAs ($m = 0.067m_e$, $\varepsilon_r = 12.9$). We consider both the quasi-one-dimensional limit $\alpha \gg 1$ and the two-dimensional case $\alpha = 1$.

The exchange coupling between the two electrons is a purely orbital effect which arises as a consequence of the Pauli principle and the Coulomb interaction which lead to a splitting $J = E_A - E_S$ of the lowest eigenvalue E_S corresponding to a symmetric orbital wave function of the two electrons, $\Psi_S(\mathbf{r}_1,\mathbf{r}_2) = \Psi_S(\mathbf{r}_2,\mathbf{r}_1)$, and the lowest eigenvalue E_A corresponding to an antisymmetric orbital wave function, $\Psi_A(\mathbf{r}_1,\mathbf{r}_2) = -\Psi_A(\mathbf{r}_2,\mathbf{r}_1)$. Due to the Pauli principle, the orbital part of a singlet state must be symmetric, while the orbital part of a triplet state must be antisymmetric. The splitting of the orbital wave functions may thereby be mapped onto an effective spin Hamiltonian, $\mathcal{H} = J\mathbf{S}_1\cdot\mathbf{S}_2$.[25] The task is to calculate the exchange coupling J as a function of various parameters, e.g., the distance between the quantum dots and the applied magnetic field. A magnetic field only affects the exchange coupling significantly in two-dimensional geometries and we consequently concentrate on the inclusion of a magnetic field in the two-dimensional case $\alpha = 1$.

III. VALIDITY OF APPROXIMATE METHODS

A. Quasi-one-dimensional limit

We first consider the quasi-one-dimensional limit $\alpha \gg 1$, which may be relevant, e.g., for describing confined electrons in nanowires. In this limit, we integrate out the motion in the y direction and consider an effective one-dimensional model reading

$$H = h(x_1) + h(x_2) + \tilde{C}_\alpha(|x_1 - x_2|), \tag{5}$$

where the single-electron Hamiltonian is

$$h(x) = \frac{p_x^2}{2m} + V(x), \tag{6}$$

$$V(x) = \frac{m\omega_0^2}{2}[\min\{(x-d)^2,(x+d)^2\}], \tag{7}$$

and we have introduced

$$\tilde{C}_\alpha(|x|) = \frac{e^2}{4\pi\varepsilon_r\varepsilon_0}\sqrt{\frac{\alpha}{2\pi r_0^2}}e^{\alpha x^2/4r_0^2}K_0(\alpha x^2/4r_0^2) \tag{8}$$

as the (regularized) Coulomb interaction in one dimension. Here, K_0 is the zeroth-order modified Bessel function of the second kind. The exchange coupling can now be calculated using finite elements by mapping the one-dimensional two-particle problem onto an effective two-dimensional single-particle problem: We consider the two-particle wave function $\Psi(x_1,x_2)$ as describing a single fictitious particle with spatial coordinates $\tilde{\mathbf{r}} = (x_1,x_2)$ and momentum $\tilde{\mathbf{p}} = (p_{x_1},p_{x_2})$. Mathematically, the corresponding single-particle-like Hamiltonian then reads

$$H = \tilde{\mathbf{p}}^2/2m + W(\tilde{\mathbf{r}}), \tag{9}$$

where

$$W(\tilde{\mathbf{r}}) = V(x_1) + V(x_2) + \tilde{C}_\alpha(|x_1 - x_2|) \tag{10}$$

is the effective external potential that the fictitious particle experiences.

In this reformulation of the problem, the symmetry of the original two-particle wave function enters via the boundary condition along the diagonal $x_2 = x_1$. Symmetric wave functions fulfill $\Psi_S(x_1,x_2) = \Psi_S(x_2,x_1)$ and consequently $\partial_{x_1}\Psi_S(x_1,x_2)|_{x_2=x_1} = \partial_{x_2}\Psi_S(x_1,x_2)|_{x_2=x_1}$ (Neumann condition), while antisymmetric wave functions fulfill $\Psi_A(x_1,x_2) = -\Psi_A(x_2,x_1)$ and thus $\Psi_A(x_1,x_2)|_{x_2=x_1} = 0$ (Dirichlet condition).[26] Since $W(\tilde{\mathbf{r}})$ is a confining potential, eigenfunctions go to zero in the limit $|\tilde{\mathbf{r}}|\to\infty$. In the numerical calculations, we assume that the eigenfunctions are zero outside a certain finite range, and we check that the results converge with respect to an increase of this range. Thus, we only need to solve a one-particle problem on a finite-size two-dimensional domain with well-defined boundary conditions. This class of problems is computationally cheap with available finite-element method packages.[14]

Before discussing the numerical results, we briefly review the standard approximations.[2] In the Heitler-London approxi-

mation, the exchange splitting is calculated as $J_{\mathrm{HL}}=\langle -|H|-\rangle - \langle +|H|+\rangle$ with the Heitler-London wave functions $|\pm\rangle = (|L\rangle_1|R\rangle_2 \pm |R\rangle_1|L\rangle_2)/\sqrt{2(1\pm|\langle L|R\rangle|^2)}$, where H is the full two-particle Hamiltonian, and $|L\rangle$ and $|R\rangle$ are the single-particle Fock-Darwin ground states of a single quantum dot centered at $\mathbf{r}_L=(-d,0)$ and $\mathbf{r}_R=(d,0)$, respectively. The Heitler-London approximation can be improved by including doubly occupied spin singlet states and diagonalizing the Hamiltonian in the resulting Hilbert space. This is known as the Hund-Mulliken approach and yields the expression $J_{\mathrm{HM}} = V - U_r/2 + \frac{1}{2}\sqrt{U_r^2+16t_r^2}$. Here, U_r and t_r are the on-site Coulomb interaction and the tunnel coupling, respectively, renormalized by the interdot Coulomb interaction as described in Ref. 2, while V (not to be confused with the confinement potential) is the difference in Coulomb energy between the singly occupied singlet and triplet states. Additional details about the approximative methods are given in Appendix A.

If the interdot Coulomb interaction is negligible, the renormalized quantities U_r and t_r reduce to their bare values, U and t, while $V=0$, and if moreover $t/U \ll 1$, the Hund-Mulliken expression reduces to the standard Hubbard expression $J_H=4t^2/U$. The Hubbard approximation, which always predicts a positive exchange energy, obviously cannot explain that the exchange energy with an applied magnetic field can be negative. This failure can be corrected by retaining the interdot Coulomb interaction, and in the limit $t_r/U_r \ll 1$, the Hund-Mulliken approximation then yields the extended Hubbard approximation: $J_H^*=4t_r^2/U_r+V$. The energy difference V is important for the prediction of the exchange coupling at finite magnetic fields, where it allows for the predicted exchange coupling to become negative.

In Fig. 2, we show numerical results for the exchange coupling as a function of the interdot distance with different values of the confinement energy $\hbar\omega_0$ for the quasi-one-dimensional case $\alpha=10 \gg 1$. Together with the numerical results, we show the Heitler-London, the Hund-Mulliken, and different variations of the Hubbard approximations. The validity of the Heitler-London approximation is strongly dependent on dimensionality due to the increasingly dominating Coulomb interaction in lower-dimensional systems,[12] and for the quasi-one-dimensional case J_{HL} is negative in the entire range considered for $\hbar\omega_0 \leqslant 8$ meV. The standard Hubbard approximation predicts reasonably well the d dependence, while both the Hund-Mulliken and extended Hubbard approaches lead to (unphysical) negative values of the exchange coupling for a wide range of system parameters. We discuss these discrepancies in more details when we consider the two-dimensional case below. Confinement energies larger than 18 meV are required for these approximations to yield positive exchange couplings for all interdot distances. For higher values of α, corresponding to stronger confinement in the y direction, the range of validity of these approximations is further reduced.

B. Two-dimensional case

We next consider the two-dimensional case $\alpha=1$. In two dimensions, the exchange coupling is strongly dependent on applied magnetic fields, and we include a magnetic field perpendicular to the motion of the electrons by the substitution $\mathbf{p} \to \mathbf{p}+e\mathbf{A}$, where $\mathbf{A}=B_z(-y,x)/2$ is a vector potential corresponding to the applied magnetic field $B_z\hat{\mathbf{z}}$. The Zeeman term does not affect the exchange coupling and is trivial to include in final total energy calculations.

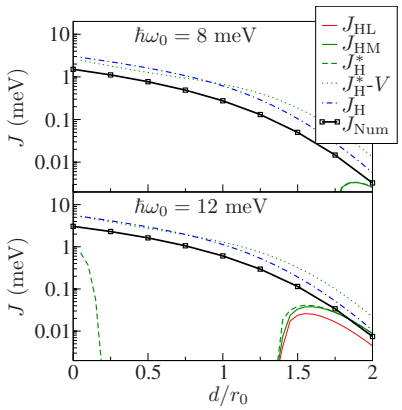

FIG. 2. (Color online) Exchange coupling as function of interdot distance in a quasi-one-dimensional double quantum dot, $\alpha=10$. The distance d is measured in units of $r_0 \equiv \sqrt{\hbar/m\omega_0}$. Together with the numerical results, we show the exchange couplings obtained with the Heitler-London J_{HL}, the Hund-Mulliken J_{HM}, the extended Hubbard J_H^*, and the standard Hubbard J_H approximations. We also show J_H^*-V, where V is the Coulomb energy difference between the singly occupied singlet and triplet states.

Rather than mapping the two-dimensional two-particle problem onto an effective four-dimensional one-particle problem, we construct a two-particle basis from single-particle eigenstates $\phi_i(\mathbf{r})$ with eigenenergies ε_i found by diagonalizing the single-particle Hamiltonian $h(\mathbf{r})=\frac{(\mathbf{p}+e\mathbf{A})^2}{2m} + V(\mathbf{r})$, again using finite-element methods.[14] The (unsymmmetrized) two-particle basis functions are then $\Psi_{i,j}(\mathbf{r}_1,\mathbf{r}_2)=\phi_i(\mathbf{r}_1)\phi_j(\mathbf{r}_2)$, in terms of which the matrix elements of the two-particle Hamiltonian read

$$[\mathbf{H}]_{ij,i'j'} = \langle \Psi_{i,j}|H|\Psi_{i',j'}\rangle = (\varepsilon_i+\varepsilon_j)\delta_{i,i'}\delta_{j,j'} + \langle \Psi_{i,j}|C|\Psi_{i',j'}\rangle. \tag{11}$$

The Coulomb matrix elements are evaluated by inserting a set of two-particle states constructed from orthonormalized Gaussian single-particle wave functions. From the low-energy spectrum of $\mathbf{H}$, we then obtain the exchange coupling J. The details of this procedure are described in Appendix B.

In Fig. 3, we show the results for the two-dimensional case $\alpha=1$. While the standard Hubbard approximation predicts well the d dependence of the exchange coupling, the Heitler-London and the Hund-Mulliken approximations yield predictions that in certain parameter ranges deviate significantly from the numerical results. In particular, in the case $\hbar\omega_0=4$ meV, a range of distances exists around $d=r_0$, where both approximations predict negative exchange couplings. It

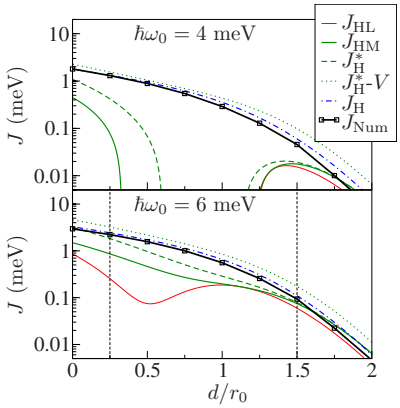

FIG. 3. (Color online) Exchange coupling as function of interdot distance in a two-dimensional double dot, α=1. See Fig. 2 for details. The vertical lines denote the two values of d/r_0 for which the dependence on the magnetic field is shown in Fig. 4.

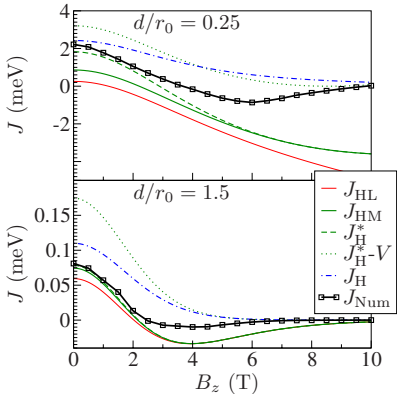

FIG. 4. (Color online) Exchange coupling as function of magnetic field in a two-dimensional double dot. Results were obtained with $\hbar\omega_0$=6 meV. See Fig. 2 for details.

is well known that the Heitler-London approximation fails at short distances, when the overlap of the Heitler-London wave functions becomes large, and that the range of validity is reduced as the ratio between the Coulomb and confinement energy is increased.[12] This explains why the discrepancies are less pronounced in the case $\hbar\omega_0$=6 meV. We conjecture that the poor predictions by the Hund-Mulliken and the extended Hubbard approximations are mainly due to the Coulomb energy difference between the singly occupied singlet and triplet states, denoted V, overestimating the effects of the interdot Coulomb interaction at short distances ($d \sim r_0$), leading to a too low (or even negative) exchange energy. For large distances ($d \sim 2r_0$), this overestimation decreases and a better agreement with the full numerics is obtained. In the figure, we also show $J^*_H - V$ which predicts well the exchange coupling, indicating that the effects of the interdot Coulomb interaction indeed seem to be overestimated. With larger confinement energies, this overestimation becomes less significant, and a better agreement with the numerically exact results is found.

In Fig. 4, we show numerical results for the exchange coupling as function of the magnetic field B with different interdot distances d. Together with the numerical results, we again show the Heitler-London, the Hund-Mulliken, and different variations of the Hubbard approximations. The results show that *none* of the approximations predicts well the dependence of the exchange coupling over the full range of magnetic fields for short distances $d < r_0$. For the Hund-Mulliken and the extended Hubbard approximations, we again attribute the discrepancy to an overestimation of the effects of the interdot Coulomb interaction. For large distances, this overestimation is less pronounced, and a good prediction of the qualitative features is obtained.

IV. CONCLUSIONS

We have presented numerically exact finite-element calculations of the exchange coupling between electron spins confined in low-dimensional nanostructures. We have tested a number of approximations often encountered in the literature by applying them to a simple double dot potential and found that they only predict well the exchange coupling in restricted parameter regimes, when compared to numerical exact results. While the approximative schemes may yield some insight into the qualitative features of the exchange coupling, we find it unlikely that they would suffice in the exchange coupling calculations for actual experimental structures and experiments, having seen how they may fail even in the case of a simple model potential.

ACKNOWLEDGMENTS

We thank A. Braggio, K. Flensberg, L. H. Olsen, A. S. Sørensen, and J. M. Taylor for fruitful discussions. In particular, we thank A. Harju for helpful advice during the development of our numerical routines. A.P.J. is grateful to the FiDiPro program of the Finnish Academy for support during the final stages of this work.

APPENDIX A: APPROXIMATIVE METHODS

In the quasi-one-dimensional limit $\alpha \gg 1$, we have evaluated the approximative methods numerically using MATHEMATICA, ensuring convergence of the results with respect to a screening length $\delta \to 0$ of the regularized Coulomb interaction. In the following, we list analytical expressions obtained for the various approximative methods presented in the paper for the two-dimensional case α=1.

The single-dot potentials corresponding to the double dot potential in Eq. (4) are those of a harmonic oscillator centered at $(\pm d, 0)$. The single-dot orbitals are thus the Fock-

Darwin states shifted to $(\pm d,0)$. For $d=0$, the Fock-Darwin ground state is

$$\varphi(x,y) = \sqrt{\frac{m\omega}{\pi\hbar}} e^{-m\omega(x^2+y^2)/2\hbar}, \tag{A1}$$

where $\omega=\omega_0\sqrt{1+\omega_L^2/\omega_0^2}$ with ω_L denoting the Larmor frequency $\omega_L=eB/2mc$. In the presence of a magnetic field given by the vector potential $\mathbf{A}=B_z(-y,x)/2$, shifting the ground state to $(\pm d,0)$ adds a phase factor of $e^{\pm iyd/2l_B^2}$, where l_B is the magnetic length $l_B=\sqrt{\hbar c/eB}$. We thus obtain the single-dot orbitals $\varphi_{\pm d}(x,y)=e^{\pm iyd/2l_B^2}\varphi(x\mp d,y)$, where $\varphi_{\pm d}(x,y)$ then denotes the single-dot orbital centered at $(\pm d,0)$.

Using these single-dot orbitals, we obtain for the exchange coupling in the Heitler-London approximation

$$J_{\mathrm{HL}} = \frac{\hbar\omega_0}{\sinh[2d^2(2b-1/b)]}\left[c_s\frac{\sqrt{\pi b}}{2}\{e^{-bd^2}I_0(bd^2)\} + \frac{2d}{\sqrt{b\pi}}\{1-e^{-bd^2}\} + 2d^2\{1-\mathrm{erf}(\sqrt{b}d)\}\right], \tag{A2}$$

where b is the magnetic compression factor $b=\omega/\omega_0$, I_0 is the zeroth-order Bessel function, $\mathrm{erf}(x)$ is the error function, and we have introduced the dimensionless distance $d\rightarrow d/r_0$. The prefactor c_s is the ratio between the Coulomb and confining energy, $c_s=\frac{e^2}{4\pi\epsilon_r\epsilon_0 r_0}\frac{1}{\hbar\omega_0}$.

In the Hund-Mulliken approximation, the exchange coupling is calculated by diagonalizing the two-electron Hamiltonian in the space spanned by $\Psi^D_{\pm d}(\mathbf{r}_1,\mathbf{r}_2)=\Phi_{\pm d}(\mathbf{r}_1)\Phi_{\pm d}(\mathbf{r}_2)$ and $\Psi^S_{\pm}(\mathbf{r}_1,\mathbf{r}_2)=[\Phi_{+d}(\mathbf{r}_1)\Phi_{-d}(\mathbf{r}_2)\pm\Phi_{-d}(\mathbf{r}_1)\Phi_{+d}(\mathbf{r}_2)]/\sqrt{2}$, where $\Phi_{\pm d}$ are the orthonormalized single-particle states $\Phi_{\pm d}=(\varphi_{\pm d}-g\varphi_{\mp d})/\sqrt{1-2Sg+g^2}$, with $g=(1-\sqrt{1-S^2})/S$. This leads to the expression $J_{\mathrm{HM}}=V-U_r/2+\frac{1}{2}\sqrt{U_r^2+16t_r^2}$, where[2]

$$t_r = t-w = \langle\Phi_{\pm d}|h|\Phi_{\mp d}\rangle - \langle\Psi^S_+|C|\Psi^D_{\pm d}\rangle/\sqrt{2},$$

$$V = V_- - V_+ = \langle\Psi^S_-|C|\Psi^S_-\rangle - \langle\Psi^S_+|C|\Psi^S_+\rangle,$$

$$U_r = U - V_+ + X = \langle\Psi^D_{\pm d}|C|\Psi^D_{\pm d}\rangle - \langle\Psi^S_+|C|\Psi^S_+\rangle + \langle\Psi^D_{\pm d}|C|\Psi^D_{\mp d}\rangle. \tag{A3}$$

The Coulomb matrix elements are given by Burkard *et al.* in Ref. 2 and are applicable to any model potential for which the corresponding single-dot potential is a simple harmonic oscillator. Thus, only the matrix element t is different for our model potential. We find

$$\frac{t}{\hbar\omega_0} = \frac{S}{1-S^2}\left[\frac{d}{\sqrt{\pi b}}(1-e^{-bd^2}) + d^2\,\mathrm{erfc}(d\sqrt{b})\right], \tag{A4}$$

where $\mathrm{erfc}(x)$ is the complementary error function.

APPENDIX B: NUMERICAL METHODS

Here, we discuss the numerical method used in the two-dimensional case $\alpha=1$. We use finite-element methods to solve the single-electron problem given by the single-particle Hamiltonian h in Eq. (1).[14] The full two-electron problem is then solved by expressing the two-electron Hamiltonian in Eq. (1) in a basis of product states of single-electron solutions $|\psi_n\rangle$, in terms of which the matrix elements are given by Eq. (11). To evaluate the Coulomb elements, the single-electron eigenstates are expanded in an orthonormalized basis of two-dimensional (2D) Gaussians $\phi_{n_x,n_y}(x,y)=x^{n_x}y^{n_y}e^{-r^2/2}$, where n_x and n_y are positive integers or zero. The Coulomb matrix elements between product states of 2D Gaussians can be determined analytically, and we state the result here for convenience[27]

$$C_{ijkl} = \frac{e^2}{4\pi\epsilon_0\epsilon_r}\frac{\pi}{2}\left(-\frac{1}{4}\right)^{n/2}\sum_{s_1=0}^{\lfloor n_1/2\rfloor}\cdots\sum_{s_4=0}^{\lfloor n_4/2\rfloor}(-1)^{n_3+n_4+s_1+s_2-s_3-s_4}\frac{\Gamma(n_1+1)}{\Gamma(s_1+1)\Gamma(n_1-2s_1+1)}\cdots\frac{\Gamma(n_4+1)}{\Gamma(s_4+1)\Gamma(n_4-2s_4+1)} \times\frac{\Gamma[(n_1+n_3-2s_1-2s_3+1)/2]\Gamma[(n_2+n_4-2s_2-2s_4+1)/2]}{\Gamma[(n-2s)/2+1]}2^{(n-2s+1)/2}\Gamma[(n-2s+1)/2],$$

for n_1+n_3 and n_2+n_4 even and zero otherwise. Here, $C_{ijkl}=\langle\phi_{n_{x,i},n_{y,i}}\phi_{n_{x,j},n_{y,j}}|C|\phi_{n_{x,k},n_{y,k}}\phi_{n_{x,l},n_{y,l}}\rangle$ while $\Gamma(x)$ is the gamma function and $\lfloor n/2\rfloor$ indicates flooring of half-integers. Above, we have introduced $n_1=n_{x,i}+n_{x,k}$, $n_2=n_{y,i}+n_{y,k}$, $n_3=n_{x,j}+n_{x,l}$, and $n_4=n_{y,j}+n_{y,l}$, while $n=\Sigma_i n_i$ and $s=\Sigma_i s_i$. The two-particle Hamiltonian matrix resulting from this procedure may then be diagonalized in the subspaces spanned by the symmetric and antisymmetric product states, respectively, to yield the exchange coupling. Because the expansion in 2D Gaussians becomes increasingly inaccurate as the interdot distance is increased, we are limited to interdot distances of the order of the characteristic oscillator length r_0. The accuracy of the 2D Gaussian expansion at larger interdot distances could be greatly improved by using an expansion in relative coordinates.[6]

The finite-element calculations of the single-particle states can be carried out with very high efficiency using existing finite-element packages[14] and are not a limiting factor in

terms of computational time or convergence. Also, the Coulomb matrix elements C_{ijkl} may be precalculated and saved in a lookup table, such that the largest portion of the computational time is spent assembling the two-electron Hamiltonian matrix. For each matrix element, a total of N^2 lookups in the C_{ijkl} table are required, where N is the number of 2D Gaussians included in the expansion set. A significant reduction in computational time is accomplished by utilizing the symmetry of the Hamiltonian in the product state basis, limiting the calculation to matrix elements which differ by more than a simple complex conjugation. For the results presented in this paper, a total of 100 2D Gaussians were used to ensure that the results obtained may essentially be considered exact. With this basis set and a total of $7^2=49$ single-particle product states, the calculation of the exchange coupling takes approximately 2.5 h on a standard computer equipped with an Intel Core2 Duo 1.86 MHz CPU. As few as 25 Gaussians are in many cases sufficient to produce results that are within 10% of the exact results, and in that case a single calculation only takes about 5 min.

The use of finite-element methods for solving the single-electron problem makes it easy to construct the two-electron Hamiltonian, even if analytic expressions for the matrix elements of the single-electron Hamiltonian in the basis of 2D Gaussians cannot be easily obtained. This makes the method very flexible, and only little work is required to solve problems with different choices of potentials. We have verified our numerical implementation against the results in Ref. 6 as well as for the simple problem of two opposite spin particles in a two-dimensional parabolic potential, which can be solved analytically.

[1] D. Loss and D. P. DiVincenzo, Phys. Rev. A **57**, 120 (1998).
[2] G. Burkard, D. Loss, and D. P. DiVincenzo, Phys. Rev. B **59**, 2070 (1999).
[3] J. R. Petta, A. C. Johnson, J. M. Taylor, E. A. Laird, A. Yacoby, M. D. Lukin, C. M. Marcus, M. P. Hanson, and A. C. Gossard, Science **309**, 2180 (2005).
[4] B. Szafran, F. M. Peeters, and S. Bednarek, Phys. Rev. B **70**, 205318 (2004).
[5] D. Bellucci, M. Rontani, F. Troiani, G. Goldoni, and E. Molinari, Phys. Rev. B **69**, 201308(R) (2004).
[6] M. Helle, A. Harju, and R. M. Nieminen, Phys. Rev. B **72**, 205329 (2005).
[7] L. X. Zhang, D. V. Melnikov, and J. P. Leburton, Phys. Rev. B **74**, 205306 (2006).
[8] D. V. Melnikov and J. P. Leburton, Phys. Rev. B **73**, 155301 (2006).
[9] D. V. Melnikov, J. P. Leburton, A. Taha, and N. Sobh, Phys. Rev. B **74**, 041309(R) (2006).
[10] L. X. Zhang, D. V. Melnikov, and J. P. Leburton, IEEE Trans. Nanotechnol. **6**, 250 (2007).
[11] X. D. Hu and S. Das Sarma, Phys. Rev. A **61**, 062301 (2000).
[12] M. J. Calderon, B. Koiller, and S. Das Sarma, Phys. Rev. B **74**, 045310 (2006).
[13] A. L. Saraiva, M. J. Calderon, and B. Koiller, arXiv:0706.3354 (unpublished).
[14] We have used the COMSOL MULTIPHYSICS 3.2 package for all finite-element calculations. See www.comsol.com. Convergence with respect to the mesh size has been ensured.
[15] F. Koppens, J. Folk, J. Elzerman, R. Hanson, L. van Beveren, I. Vink, H. Tranitz, W. Wegscheider, L. Kouwenhoven, and L. Vandersypen, Science **309**, 1346 (2005).
[16] T. Hatano, M. Stopa, and S. Tarucha, Science **309**, 268 (2005).
[17] C. Fasth, A. Fuhrer, M. T. Björk, and L. Samuelson, Nano Lett. **5**, 1487 (2005).
[18] I. Shorubalko, A. Pfund, R. Leturcq, M. T. Borgström, F. Gramm, E. Müller, E. Gini, and K. Ensslin, Nanotechnology **18**, 44014 (2007).
[19] S. Sapmaz, C. Meyer, P. Beliczynski, P. Jarillo-Herrero, and L. P. Kouwenhoven, Nano Lett. **6**, 1350 (2006).
[20] H. Jørgensen, K. Grove-Rasmussen, J. Hauptmann, and P. Lindelof, Appl. Phys. Lett. **89**, 232113 (2006).
[21] W. van der Wiel, S. de Franceschi, J. Elzerman, T. Fujisawa, S. Tarucha, and L. Kouwenhoven, Rev. Mod. Phys. **75**, 1 (2003).
[22] We have applied our methods to other double dot potentials encountered in the literature (Refs. 2 and 4) and found that the reliability of the approximative schemes analyzed in this work are highly sensitive to the details of the confining potential.
[23] M. Helle, Ph.D. thesis, Helsinki University of Technology, 2006.
[24] J. M. Leinaas and J. Myrheim, Nuovo Cimento Soc. Ital. Fis., B **37**, 1 (1977).
[25] N. W. Ashcroft and N. D. Mermin, *Solid State Physics* (Saunders, Philadelphia, 1976), Chap. 32.
[26] Similar boundary conditions have been used in discussions on the fundamental understanding of identical particles (Ref. 24).
[27] J. Pedersen, Master's thesis, Technical University of Denmark, 2007.

Paper R

J. Pedersen, C. Flindt, N. A. Mortensen, and A.-P. Jauho

Spin qubits in antidot lattices

Phys. Rev. B, submitted to

The work is a result of the M.Sc. thesis by JP, supervised by CF and APJ. The numerical approach to density of states calculations and the resonant tunneling phenomenon were developed by JP, CF, and NAM, while the analytic model of the level-structure is due to NAM and the exchange coupling calculations are mainly due to JP and CF. All numerical implementations are due to JP. The writing was done in a joint effort by all authors, with JP being the main contributor, and CF responsible for the introductory and concluding sections.

Spin qubits in antidot lattices

Jesper Pedersen,[1] Christian Flindt,[1] Niels Asger Mortensen,[1] and Antti-Pekka Jauho[1,2]
[1] *MIC – Department of Micro and Nanotechnology, NanoDTU, Technical University of Denmark, Building 345east, DK-2800 Kongens Lyngby, Denmark*
[2] *Laboratory of Physics, Helsinki University of Technology, P. O. Box 1100, FI-02015 HUT, Finland*
(Dated: September 24, 2007)

We suggest and study designed defects in an otherwise periodic potential modulation of a two-dimensional electron gas as an alternative approach to electron spin based quantum information processing in the solid-state using conventional gate-defined quantum dots. We calculate the band structure and density of states for a periodic potential modulation, referred to as an antidot lattice, and find that localized states appear, when designed defects are introduced in the lattice. Such defect states may form the building blocks for quantum computing in a large antidot lattice, allowing for coherent electron transport between distant defect states in the lattice and tunnel coupling of neighboring defect states with corresponding electrostatically controllable exchange coupling between different electron spins.

PACS numbers: 73.21.Cd, 75.30.Et, 73.22.-f

I. INTRODUCTION

Localized electrons spins in a solid state structure have been suggested as a possible implementation of a future device for large-scale quantum information processing.[1] Together with single spin rotations, the exchange coupling between spins in tunnel coupled electronic levels would provide a universal set of quantum gate operations.[2] Recently, both of these operations have been realized in experiments on electron spins in double quantum dots, demonstrating electron spin resonance (ESR) driven single spin rotations[3] and electrostatic control of the exchange coupling between two electron spins.[4] Combined with the long coherence time of the electron spin due to its weak coupling to the environment, and the experimental ability to initialize a spin and reading it out,[5] four of DiVincenzo's five criteria[6] for implementing a quantum computer may essentially be considered fulfilled. This leaves only the question of scalability experimentally unaddressed.

While large-scale quantum information processing with conventional gate-defined quantum dots is a topic of ongoing theoretical research,[7] we here suggest and study an alternative approach based on so-called defect states that form at designed defects in a periodic potential modulation of a two-dimensional electron gas (2DEG) residing at the interface of a semiconductor heterostructure.[8] One way of implementing the potential modulation would be similar to the periodic antidot lattices[9,10] that are now routinely fabricated. Such lattices can be fabricated on top of a semiconductor heterostructure using local oxidation techniques that allow for a precise patterning of arrays of insulating islands, with a spacing on the order of 100 nm, in the underlying 2DEG.[11] Even though the origin of these depletion spots is not essential for our proposal, we refer to them as antidots, and a missing antidot in the lattice as a defect. Alternative fabrication methods include electron beam and photo lithography. In Ref. 11 a square lattice consisting of $20 \times 20 = 400$ antidots was patterned on an approximately 2.5 μm $\times$ 2.5 μm area, and the available fabrication methods suggest that even larger antidot lattices with more than 1000 antidots and many defect states may be within experimental reach.

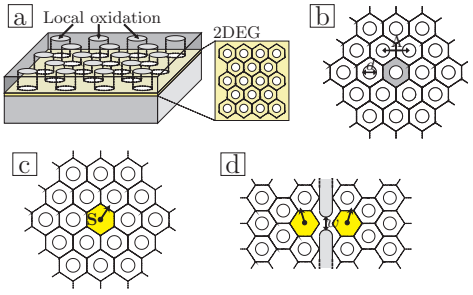

FIG. 1: (Color online) (a) Schematic illustration of a periodic antidot lattice; antidots may, e.g., be fabricated using local oxidation of a Ga[Al]As heterostructure. (b) Geometry of the periodic antidot lattice with the Wigner–Seitz cell marked in gray and the antidot diameter d and lattice constant Λ indicated. (c) A designed defect leads to the formation of defect states in which an electron with spin **S** can reside. (d) Tunnel coupled defects. The coupling can be controlled using a split-gate with an effective opening denoted w.

The idea of using designed defects in antidot lattices as a possible quantum computing architecture was originally proposed by some of us in Ref. 8, where we presented simple calculations of the single-particle level structure of an antidot lattice with one or two designed defects. Here, we take these ideas further and present detailed band structure and density of states calculations for a periodic lattice, describe a resonant tunneling phenomenon allowing for electron transport between distant defects in the lattice, and calculate numerically the exchange coupling between spins in two neighboring de-

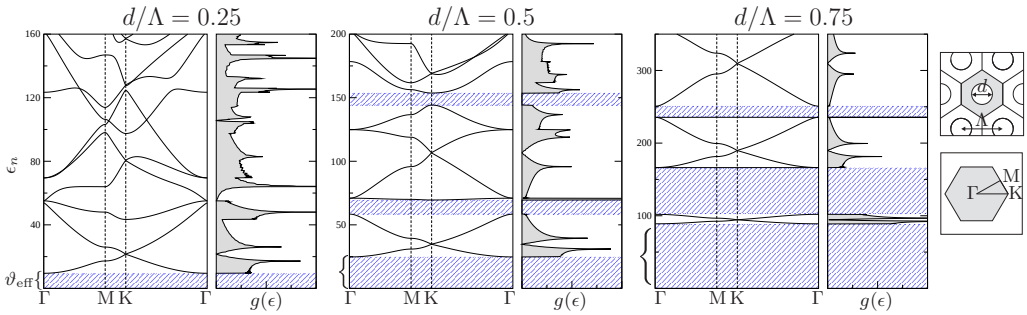

FIG. 2: (Color online) Band structures and densities of states $g(\epsilon)$ of the periodic antidot lattice for three different values of the relative antidot diameter d/Λ. Notice the different energy scales for the three cases. On each band structure the gap $\vartheta_{\rm eff}$ is indicated, below which no states exist for the periodic lattice. The band gaps and the gap below $\vartheta_{\rm eff}$ are highlighted as hatched blue regions. Also shown is the periodic lattice structure with the Wigner–Seitz cell indicated in gray, as well as the first Brillouin zone (FBZ) with the three high-symmetry points and the irreducible FBZ indicated.

fects, showing that the suggested architecture could be useful for spin-based quantum information processing. The envisioned structure and the basic building blocks are shown schematically in Fig. 1.

The paper is organized as follows: In Section II we introduce our model of the antidot lattice and present numerical results for the band structure and density of states of a periodic antidot lattice. In particular, we show that the periodic potential modulation gives rise to band gaps in the otherwise parabolic free electron band structure. In Section III we introduce a single missing antidot, a defect, in the lattice and calculate numerically the eigenvalue spectrum of the localized defect states that form at the location of the defect. We develop a semi-analytic model that explains the level-structure of the lowest-lying defect states. In Section IV we consider two neighboring defect states and calculate numerically the tunnel coupling between them. In Section V we describe a principle for coherent electron transport between distant defect states in the antidot lattice, and illustrate this phenomenon by wavepacket propagations. In Section VI we present numerically exact results for the exchange coupling between electron spins in tunnel coupled defect states, before we finally in Section VII present our conclusions.

II. PERIODIC ANTIDOT LATTICE

We first consider a triangular lattice of antidots with lattice constant Λ superimposed on a two-dimensional electron gas (2DEG). The structure is shown schematically together with the Wigner-Seitz cell in Fig. 1(b). While experiments on antidot lattices are often performed in a semi-classical regime, where the typical feature sizes and distances, e.g., the lattice constant Λ, are much larger than the electron wavelength, we here consider the opposite regime, where these length scales are comparable, and a full quantum mechanical treatment consequently is necessary. In the effective-mass approximation we thus model the periodic lattice with a two-dimensional single-electron Hamiltonian reading

$$H = -\frac{\hbar^2}{2m^*}\nabla^2_{\mathbf{r}} + \sum_i V\left(\mathbf{r}-\mathbf{R}_i\right),\ \mathbf{r}=(x,y), \quad (1)$$

where m^* is the effective mass of the electron and $V(\mathbf{r}-\mathbf{R}_i)$ is the potential of the i'th antidot positioned at $\mathbf{R}_i$. We model each antidot as a circular potential barrier of diameter d so that $V(\mathbf{r}-\mathbf{R}_i)=V_0$ for $|\mathbf{r}-\mathbf{R}_i|\le d/2$ and zero otherwise. In the limit $V_0\to\infty$ the eigenfunctions do not penetrate into the antidots, and the Schrödinger equation may be written as

$$-\Lambda^2\nabla^2_{\mathbf{r}}\psi_n(\mathbf{r}) = \epsilon_n\psi_n(\mathbf{r}), \quad (2)$$

with the boundary condition $\psi_n=0$ in the antidots, and where we have introduced the dimensionless eigenvalues

$$\epsilon_n = E_n\Lambda^2 2m^*/\hbar^2. \quad (3)$$

In the following we use parameter values typical of GaAs, for which $\hbar^2/2m^*\simeq 0.6$ eV nm^2 with $m^*=0.067m_e$, although the choice of material is not essential. We have checked numerically that our results are not critically sensitive to the approximation $V_0\to\infty$, so long as the height is significantly larger than any energies under consideration. All results presented in this work have thus been calculated in this limit, for which the simple form of the Schrödinger equation Eq. (2) applies. In this limit, the band structures presented below are of a purely geometrical origin. The band structure can be calculated by imposing periodic boundary conditions and solving

Eq. (2) on the finite domain of the Wigner–Seitz cell. We solve this problem using a finite-element method.[12] The corresponding density of states is calculated using the linear tetrahedron method in its symmetry corrected form.[13–15]

In Fig. 2 we show the band structure and density of states of the periodic antidot lattice for three different values of the relative antidot diameter d/Λ. We note that an increasing antidot diameter raises the kinetic energy of the Bloch states due to the increased confinement and that several band gaps open up. We have indicated the gap ϑ_{eff} below which no states exist for the periodic structure. We shall denote as *band gaps* only those gaps occurring between two bands, and thus we do not refer to the gap below ϑ_{eff} as a band gap in the following. This is motivated by the difference in the underlying mechanisms responsible for the gaps: While the band gaps rely on the periodicity of the antidot lattice, similar to Bragg reflection in the solid state, the gap below ϑ_{eff} represents an averaging of the potential landscape generated by the antidots, and is thus robust against lattice disorder as we have also checked numerically.[16] The lowest band gap is thus present for $d/\Lambda > 0.35$ while the higher-energy band gap only develops for $d/\Lambda > 0.45$. As the antidot diameter is increased, several flat bands appear with $\nabla_{\mathbf{k}}\epsilon_n(\mathbf{k}) \simeq 0$, giving rise to Van Hove singularities in the corresponding density of states.

III. DEFECT STATES

We now introduce a defect in the lattice by leaving out a single antidot. Topologically, this structure resembles a planar 2D photonic crystal, and relying on this analogy we expect one or more localized defect states to form inside the defect.[17] The gap ϑ_{eff} indicated in Fig. 2 may be considered as the height of an effective two-dimensional potential surrounding the defect, and thus gives an upper limit to the existence of defect states in this gap. Similar states are expected to form in the band gaps of the periodic structure, which are highlighted in Fig. 2. As defect states decay to zero far from the location of the defect, we have a large freedom in the way we spatially truncate the problem at large distances. For simplicity we use a super-cell approximation, but with $\psi = 0$ imposed on the edge, thus leaving Eq. (2) a Hermitian eigenvalue problem which we may conveniently solve with a finite-element method.[12] Other choices, such as periodic boundary conditions, do not influence our numerical results. The size of the super-cell has been chosen sufficient large, such that the results are unaffected by a further increase in size.

In the insets of Fig. 3(a) we show the calculated eigenfunctions corresponding to the two lowest energy eigenvalues for a relative antidot diameter $d/\Lambda = 0.5$. As expected, we find that defect states form that to a high degree are localized within the defect. The second-lowest eigenvalue is two-fold degenerate and we only show one of the corresponding eigenstates. The figure shows the energy eigenvalues of the defect states as a function of the relative antidot diameter together with the gap ϑ_{eff}. As this effective potential is increased, additional defect states become available and we may thus tune the number of levels in the defect by adjusting the relative antidot diameter. In particular, we note that for $d/\Lambda \lesssim 0.42$ only a single defect state forms. As the size of the antidots is increased, the confinement of the defect states becomes stronger, leading to an increase in their energy eigenvalues. For GaAs with $d/\Lambda = 0.5$ and $\Lambda = 75$ nm the energy splitting of the two lowest defect states is approximately 1.1 meV, which is much larger than $k_B T$ at subkelvin temperatures, and the level structure is thus robust against thermal dephasing.

In Fig. 3(b) we show similar results for defect states residing in the lowest band gap of the periodic structure. While the states residing below ϑ_{eff} resemble those occurring due to the confining potential in conventional gate-defined quantum dots, these higher-lying states are of a very different nature, being dependent on the periodicity of the surrounding lattice. For the band gaps, the existence of bound states is limited by the relevant band edges as indicated in the figure. As the size of the band gap is increased, additional defect states become available and we may thus also tune the number of levels residing in the band gaps by adjusting the relative antidot diameter.

Because the formation of localized states residing below ϑ_{eff} depends only on the existence of the effective potential surrounding the defect, the formation of such states is not critically dependent on perfect periodicity of the surrounding lattice, which we have checked numerically.[16] Also, the lifetimes of the states due to the finite size of the antidot lattice are of the order of seconds even for a relatively small number of rings of antidots surrounding the defect.[8] However, the localized states residing in the band gaps are more sensitive to lattice disorder, since they rely more crucially on the periodicity of the surrounding lattice. Introducing disorder may induce a finite density of states in the band gaps of the periodic structure and thus significantly decrease the lifetimes of the localized states residing in this region.

In order to gain a better understanding of the level-structure of the defect states confined by ϑ_{eff} we develop a semi-analytic model for ϑ_{eff} and the corresponding defect states. We first note that the effective potential ϑ_{eff} is given by the energy of the lowest Bloch state at the Γ point of the periodic lattice. At this point $\mathbf{k} = \mathbf{0}$ and Bloch's theorem reduces to an ordinary Neumann boundary condition on the edge of the Wigner–Seitz cell. This problem may be solved using a conformal mapping, and we obtain the expression[18]

$$\vartheta_{\text{eff}} \simeq \left(\mathcal{C}_1 + \frac{\mathcal{C}_2}{\mathcal{C}_3 - d/\Lambda}\right)^2, \tag{4}$$

where $\mathcal{C}_1 \simeq -0.2326$, $\mathcal{C}_2 \simeq 2.7040$ and $\mathcal{C}_3 \simeq 1.0181$ are given by expressions involving the Bessel functions Y_0

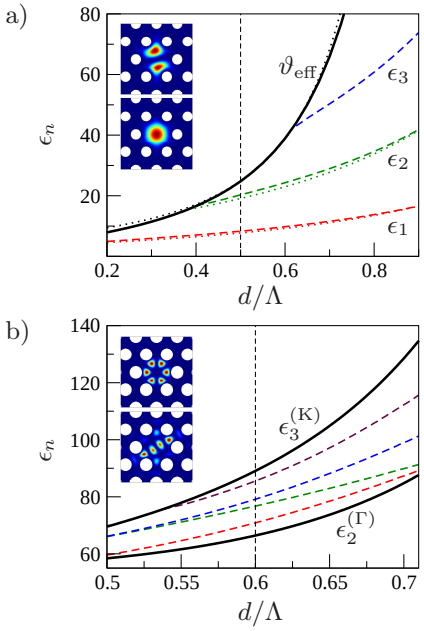

FIG. 3: (Color online) Energy spectrum for a single defect. The (dimensionless) eigenvalues corresponding to localized states are shown as a function of the relative antidot diameter d/Λ. For a given choice of Λ, the eigenvalues can be converted to meV using Eq. (3). (a) Energy spectrum for defect states residing in the gap below $\vartheta_{\rm eff}$. The full line indicates the height $\vartheta_{\rm eff}$ of the effective potential in which the localized states reside. The dotted lines are the approximate expressions given by Eqs. (4), (6) and (7). The approximate results for ϵ_1 are in almost perfect agreement with the numerical calculations. (b) Energy spectrum for the defect states residing in the lowest band gap region. The full lines indicate the band gap edges of the periodic structure, $\epsilon_3^{(\rm K)}$ and $\epsilon_2^{(\Gamma)}$, giving upper and lower limits to the existence of bound states. The inset in both figures show the localized states corresponding to the two lowest energy eigenvalues indicated by the dashed vertical lines. The absolute square is shown.

and Y_1.[18] We now consider the limit of $d/\Lambda \to 1$ and note that in this case the defect states residing below $\vartheta_{\rm eff}$ are subject to a potential which we may approximate as an infinite two-dimensional spherical potential well with radius $\Lambda - d/2$. The lowest eigenvalue for this problem is $\epsilon_1^{(\infty)} = \Lambda^2\alpha_{0,1}^2/(\Lambda - d/2)^2$, where $\alpha_{0,1} \simeq 2.405$ is the first zero of the zeroth order Bessel function. This expression yields the correct scaling with d/Λ, but is only accurate in the limit of $d/\Lambda \to 1$. We correct for this by considering the limit of $d/\Lambda \to 0$, in which we may solve the problem using ideas developed by Glazman *et al.* in studies of quantum conductance through narrow constrictions.[19] The problem may be approximated as a two-dimensional spherical potential well of height π^2 and radius Λ. The lowest eigenvalues $\epsilon_1^{(\pi^2)}$ of this problem is the first root of the equation

$$\sqrt{\epsilon_1^{(\pi^2)}}\frac{J_1\left(\sqrt{\epsilon_1^{(\pi^2)}}\right)}{J_0\left(\sqrt{\epsilon_1^{(\pi^2)}}\right)} = \sqrt{\pi^2-\epsilon_1^{(\pi^2)}}\frac{K_1\left(\sqrt{\pi^2-\epsilon_1^{(\pi^2)}}\right)}{K_0\left(\sqrt{\pi^2-\epsilon_1^{(\pi^2)}}\right)}, \tag{5}$$

where $J_i(K_i)$ is the i'th order Bessel function of the first (second) kind. If the height of the potential well π^2 is much larger than the energy eigenvalues, the first root would simply be $\alpha_{0,1}^2$. Lowering the confinement must obviously shift down the eigenvalue, and in the present case we find that $\epsilon_1^{(\pi^2)} \simeq \pi$. By expanding the equation to first order in $\sqrt{\epsilon_1^{(\pi^2)}}$ around $\sqrt{\pi}$ we may solve the equation to obtain $\epsilon_1^{(\pi^2)} \simeq 3.221$, which is in excellent agreement with a full numerical solution of Eq. (5). Correcting for the low-d/Λ behavior we thus find the approximate expression for the lowest energy eigenvalue[8]

$$\begin{aligned}\epsilon_1 &\simeq \epsilon_1^{(\infty)} - \lim_{d/\Lambda\to 0}\epsilon_1^{(\infty)} + \epsilon_1^{(\pi^2)} \\ &= \epsilon_1^{(\pi^2)} + \frac{(4-d/\Lambda)\,d/\Lambda}{(2-d/\Lambda)^2}\alpha_{0,1}^2. \end{aligned} \tag{6}$$

A similar analysis leads to an approximate expression for the first excited state ϵ_2. This mode has a finite angular momentum of ± 1 and a radial J_1 solution yields

$$\epsilon_2 \simeq \epsilon_2^{(\pi^2)} + \frac{(4-d/\Lambda)\,d/\Lambda}{(2-d/\Lambda)^2}\alpha_{1,1}^2, \tag{7}$$

where $\epsilon_2^{(\pi^2)} \simeq 7.673$ is the second-lowest eigenvalue of the two-dimensional spherical potential well of height π^2 and radius Λ, which can be found from an equation very similar to Eq. (5). The first root of the first-order Bessel function is $\alpha_{1,1} \simeq 3.832$. The scaling of the two lowest eigenvalues with d/Λ is thus approximately the same. The approximate expressions are indicated by the dotted lines in Fig. 3, and we note an excellent agreement with the numerical results. We remark that the filling of the defect states can be controlled using a metallic back gate that changes the electron density and thus the occupation of the different defect states.[27]

IV. TUNNEL COUPLED DEFECT STATES

Two closely situated defect states can have a finite tunnel coupling, leading to the formation of hybridized defect states. The coupling between the two defects may be tuned via a metallic split gate defined on top of the 2DEG in order to control the opening between the two defects. As the voltage is increased the opening is squeezed,

leading to a reduced overlap between the defect states. We model such a split gate as an infinite potential barrier shaped as shown in Fig. 1(d). Changing the applied voltage effectively leads to a change in the relative width w/Λ of the opening, which we take as a control parameter in the following. If we consider just a single level in each defect we can calculate the tunnel matrix element as $|\tau| = (\epsilon_+ - \epsilon_-)/2$ where $\epsilon_\pm$ are the eigenenergies of the bonding and anti-bonding states, respectively, of the double defect. In the following, we calculate the tunnel coupling between two defect states lying below $\vartheta_{\rm eff}$, but the analysis applies equally well to defect states lying in the band gaps.

In Fig. 4 we show the tunnel matrix element $|\tau|$ as a function of the relative gate constriction width w/Λ for three different values of d/Λ in the single-level regime of each defect, i.e., $d/\Lambda \lesssim 0.42$. As expected, the tunnel coupling grows with increasing constriction width due to the increased overlap between the defect states. A saturation point is reached when the constriction width is on the order of the diameter of the defect states, after which the overlap is no longer increased significantly. An electron prepared in one of the defect states will oscillate coherently between the two defect states with a period given as $T = \pi\hbar/|\tau|$, which for GaAs with $\Lambda = 75$ nm, $d/\Lambda = 0.4$ and $w/\Lambda = 0.6$ implies an oscillation time of $T \simeq 0.14$ ns. A numerical wavepacket propagation of an electron initially prepared in the left defect state is shown in Fig. 4(b), confirming the expected oscillatory behavior. With a finite tunnel coupling between two defect states, two electron spins trapped in the defects will interact due to the exchange coupling, to which we return in Section VI.

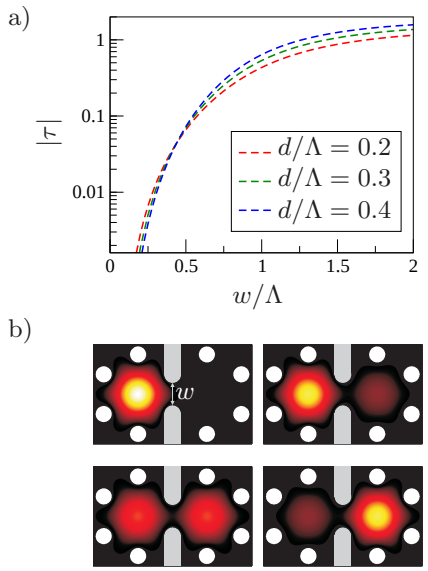

FIG. 4: (Color online) (a) The (dimensionless) tunnel coupling $|\tau|$ as a function of the relative split gate constriction width w/Λ for three different values of d/Λ in the single-level regime. For a given choice of Λ, the tunnel couplings can be converted to meV using Eq. (3). (b) Time propagation of an electron initially prepared in the left defect state for $d/\Lambda = 0.4$ and $w/\Lambda = 0.6$. The absolute square of the initial wavefunction is shown in the upper left panel. The following panels show the state after a time span of $T/8$, $2T/8$ and $3T/8$, respectively, where T is the oscillation period.

V. RESONANT COUPLING OF DISTANT DEFECT STATES

With a large antidot lattice and several defect states it may be convenient with quantum channels along which coherent electron transport can take place, connecting distant defect states. In Refs. 20 and 21 it was suggested to use arrays of tunnel coupled quantum dots as a means to obtain high-fidelity electron transfer between two distant quantum dots. We have applied this idea to an array of tunnel coupled defect states and confirmed that this mechanism may be used for coherent electron transport between distant defects in an antidot lattice.[16] This approach, however, relies on precise tunings of the tunnel couplings between each defect in the array, which may be difficult to implement experimentally. Instead, we suggest an alternative approach based on a resonant coupling phenomenon inspired by similar ideas used to couple light between different fiber cores in a photonic crystal fiber.[23,24]

We consider two defects separated by a central line of N antidots and a central back gate V_g in the region between the defects, as shown in Fig. 5. Again, we consider

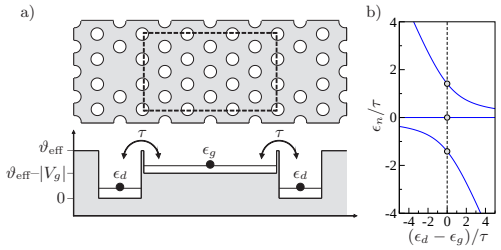

FIG. 5: (a) The structure considered for resonant coupling of distant defect states; two defects separated by a central line of $N = 3$ antidots, with a central back gate V_g controlling the potential square well in the region marked with dashed lines. A simple three-level model of the system is illustrated below. (b) The eigenvalue spectrum of the three-level model. The dashed line marks the point of resonance.

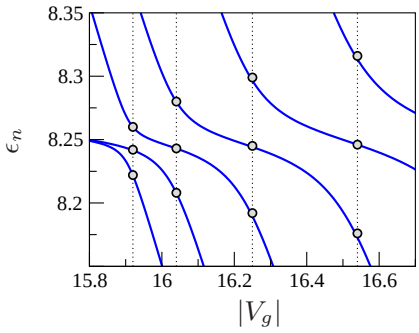

FIG. 6: (Color online) Energy eigenvalues as a function of the magnitude $|V_g|$ of the back gate for the structure illustrated in Fig. 5 for $d/\Lambda = 0.5$ and a central line of $N = 7$ antidots separating the two defects. The resonances are marked with dotted lines and characterized by a symmetric splitting of the eigenvalues.

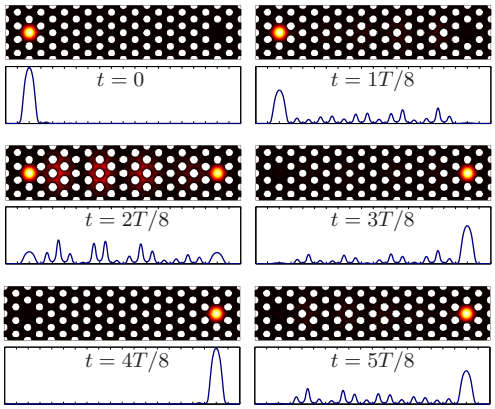

FIG. 7: (Color online) Numerical time propagation of an electron initially prepared in the left defect of the structure illustrated in Fig. 5(a) and corresponding to the results of Fig. 6 with $|V_g| \simeq 16.54$. The charge densities $\rho(x, y)$ are shown in the upper panels, while the lower panels show $\int dy \rho(x, y)$. The oscillation period is denoted T.

defect states residing below $\vartheta_{\rm eff}$, but the principle described here may equally well be applied to defect states in the band gaps. Using the back gate, the potential between the two defects can be controlled locally. If the potential is lowered below $\vartheta_{\rm eff}$, a discrete spectrum of standing-wave solutions form between the two defects. In the following we denoted the energy of one of these standing-wave solutions by ϵ_g, while the energy of the two defect states is assumed to be identical and is denoted ϵ_d. A simple three-level analysis of this system, as illustrated in Fig. 5, reveals that by tuning the back gate so that the levels are aligned, $\epsilon_g = \epsilon_d$, a resonant coupling between the two distant defects occurs, characterized by a symmetric splitting of the three lowest eigenvalues into $\epsilon_0 = \epsilon_d$ and $\epsilon_\pm = \epsilon_d \pm \sqrt{2}|\tau|$, where $|\tau|$ is the tunnel coupling between the defects and the standing-wave solution in the central back gate region. If an electron is prepared in one of the defects states, it will oscillate coherently between the two defects with an oscillation period of $T = \sqrt{2}\pi\hbar/|\tau|$. By turning off the back gate at time $t = T/2$ we may thereby trap the electron in the opposite defect which may by situated a distance an order of magnitude larger than the lattice constant away from the other defect.

In Fig. 6 we show the numerically calculated eigenvalues as a function of the depth $|V_g|$ of the central potential square well of the structure illustrated in Fig. 5 for $d/\Lambda = 0.5$ and a central line of $N = 7$ antidots separating the two defects. Contrary to the simple three-level model, several resonances now occur as the back gate is lowered, corresponding to coupling to different standing-wave solutions in the multi-leveled central region. The energy splitting at resonance is larger when the defect states couple to higher-lying central states due to a large overlap between the defect states and the central standing-wave solution. In Fig. 7 we show a numerical time propagation of an electron initially prepared in the left defect, confirming the oscillatory behavior expected from the simple model. For GaAs and $\Lambda = 75$ nm the results indicate an oscillation period of $T \simeq 0.16$ ns for the time propagation illustrated. The resonant phenomenon relies solely on the level alignment $\epsilon_g = \epsilon_d$ and on the symmetry condition that both defect states have the same energy and magnitude of tunnel coupling to the standing wave solution in the central region. It is in principle independent of the number of antidots N separating the two defects, but in practice this range is limited by the coherence length of the sample and the fact that the levels of the central region grow too dense if N becomes large.[28] We have checked numerically that resonant coupling of defect levels below $\vartheta_{\rm eff}$ is robust against lattice disorder.[16]

VI. EXCHANGE COUPLING

So far we have only considered the single-particle electronic level-structure of the antidot lattice. However, as mentioned in the introduction, the exchange coupling between electron spins is a crucial building block for spin based quantum computing architecture, and in fact suffices to implement a universal set of quantum gates.[25] The exchange coupling is a result of the Pauli principle for identical fermions, which couples the symmetries of the orbital and spin degrees of freedom. If the orbital wavefunction of the two electrons is symmetric (i.e. preserves sign under particle-exchange), the spins must be in

the antisymmetric singlet state, while an antisymmetric orbital wavefunction means that the spins are in a symmetric triplet state. One may thereby map the splitting between the ground state energy E_S of the symmetric orbital subspace and the ground state energy E_A of the antisymmetric orbital subspace onto an effective Heisenberg spin Hamiltonian $\mathcal{H} = J\mathbf{S}_1 \cdot \mathbf{S}_2$, where $J = E_A - E_S$ is the exchange coupling between the two spins, $\mathbf{S}_1$ and $\mathbf{S}_2$. The implementation of quantum gates based on the exchange coupling requires that J can be varied over several orders of magnitude in order to effectively turn the coupling on and off. In this section we present numerically exact results for the exchange coupling between two electron spins residing in tunnel coupled defects as those illustrated in Fig. 1(d).

The Hamiltonian of two electrons in two tunnel coupled defects may be written as

$$H(\mathbf{r}_1, \mathbf{r}_2) = h(\mathbf{r}_1) + h(\mathbf{r}_2) + C(\mathbf{r}_1, \mathbf{r}_2), \tag{8}$$

where

$$C(\mathbf{r}_1, \mathbf{r}_2) = \frac{e^2}{4\pi\epsilon_r\epsilon_0} \frac{1}{|\mathbf{r}_1 - \mathbf{r}_2|} \tag{9}$$

is the Coulomb interaction and the single-electron Hamiltonians are

$$h(\mathbf{r}_i) = \frac{(\mathbf{p}_i + e\mathbf{A})^2}{2m^*} + V(\mathbf{r}_i) + \frac{1}{2} g\mu_B B S_{z,i}\,,\ i = 1, 2, \tag{10}$$

where $V(\mathbf{r})$ is the potential due to the antidots and the coupled defects. As previously, we model the antidots and the split gate as potential barriers of infinite height, and use finite-element methods to solve the single-electron problem defined by Eq. (10). A Zeeman field $B\hat{\mathbf{z}}$ applied perpendicularly to the electron gas splits the spin states, and we choose a corresponding vector potential reading $\mathbf{A} = B(-y\hat{\mathbf{x}} + x\hat{\mathbf{y}})/2$.

In order to calculate the exchange coupling J we employ a recently developed method for numerically exact finite-element calculations of the exchange coupling:[22] The full two-electron problem is solved by expressing the two-electron Hamiltonian in a basis of product states of single-electron solutions obtained using a finite element method.[12] The Coulomb matrix elements are evaluated by expanding the single-electron states in a basis of 2D Gaussians,[26] and the two-particle Hamiltonian matrix resulting from this procedure may then be diagonalized in the subspaces spanned by the symmetric and antisymmetric product states, respectively, to yield the exchange coupling. The details of the numerical method are described elsewhere.[16,22] The results presented below have all been obtained with a sufficient size of the 2D Gaussian basis set as well as the number of single-electron eigenstates, such that a further increase does not change the results.[29]

In Fig. 8 we show the calculated exchange coupling for a double defect structure. The exchange coupling varies by several orders of magnitude as the split gate

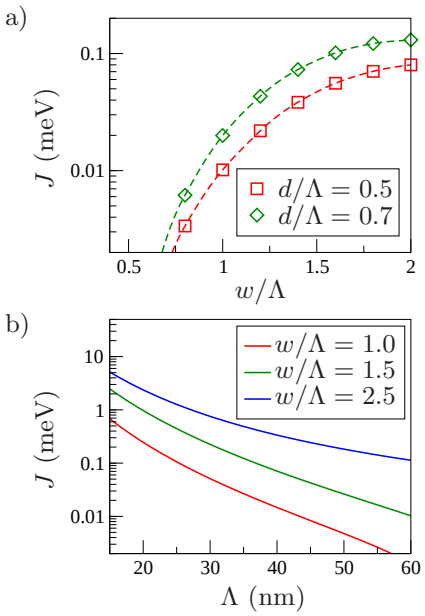

FIG. 8: (Color online) Exchange coupling J for a double defect structure. (a) Exchange coupling as a function of the relative split gate constriction width w/Λ for two different values of the relative antidot diameter and a lattice constant $\Lambda = 45$ nm. (b) Exchange coupling as a function of the lattice constant Λ for three different values of the relative split gate constriction width.

constriction width is increased, showing that electrostatic control of the exchange coupling in an antidot lattice is possible, similarly to the principles proposed[2] and experimentally realized[4] for double quantum dots. Just as the tunnel coupling, the exchange coupling reaches a saturation point when the split gate constriction width is on the order of the diameter of the defect states. This is to be expected since the exchange coupling in the Hubbard approximation is proportional to the square of the tunnel coupling.[2] As illustrated in Fig. 8(b), the exchange coupling is highly dependent on the lattice constant, increasing several orders of magnitude as the lattice constant is decreased from 60 nm to 20 nm. This is in part due to the overall increase in the energy levels and the splitting between them with increased confinement, but also due to a decrease in the ratio of the Coulomb interaction strength to the confinement strength. As the relative strength of the Coulomb interaction is decreased, the defect states are effectively moved closer together, resulting in an increase in the exchange coupling.

The exchange coupling is also highly dependent on

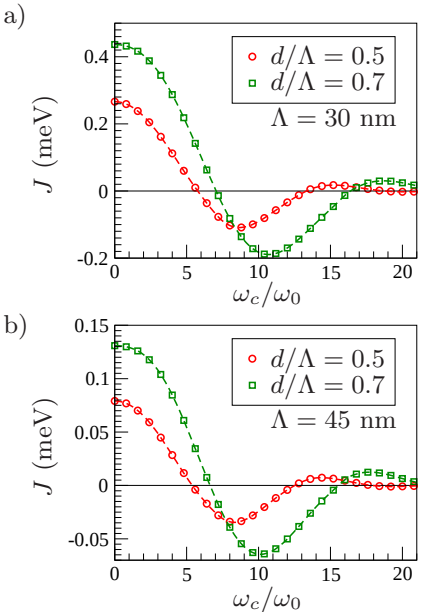

FIG. 9: (Color online) Exchange coupling J for a double defect structure as a function of ω_c/ω_0, where $\omega_c = eB/m^*c$ and $\omega_0 = \hbar/(2m^*\Lambda^2)$. Results are shown for a relative split gate constriction width $w/\Lambda = 2$, and two different values of the relative antidot diameter d/Λ. The lattice constant is (a) $\Lambda = 30$ nm and (b) $\Lambda = 45$ nm.

magnetic fields applied perpendicularly to the plane of the electrons.[2] In Fig. 9 we show the exchange coupling as a function of ω_c/ω_0 where $\omega_c = eB/m^*c$ and we define $\omega_0 = \frac{\hbar}{2m^*\Lambda^2}$. For GaAs $\omega_c/\omega_0 \simeq 0.00104\ \mathrm{T}^{-1}\mathrm{nm}^{-2}\cdot\Lambda^2 B$. As expected, the results of Fig. 9 are very similar to those obtained for double quantum dots.[2,26] In all cases we note an initial transition from the anti-ferromagnetic ($J > 0$) to the ferromagnetic ($J < 0$) regime of exchange coupling, followed by a return to positive values of the exchange coupling at higher magnetic fields. The initial transition to negative exchange coupling is caused by long-range Coulomb interactions.[2] As the magnetic field is increased further, magnetic confinement becomes dominant, compressing the orbits and thus reducing the overlap between the single-defect wave functions. This leads to a strong reduction of the magnitude of the exchange coupling. Due to the increased confinement strength for smaller lattice constants Λ, these transitions occur at larger magnetic fields. The same is the case for the larger relative antidot diameters, in which the ratio of magnetic confinement to confinement due to the antidots is reduced. We have only considered the case of a large constriction width $w/\Lambda = 2$, since this regime of relatively large exchange coupling is the most interesting for practical purposes. For small values of w/Λ we expect to find results similar to those obtained in the limit of large interdot distances for double quantum dot systems.[2]

VII. CONCLUSIONS

In conclusion, we have suggested and studied an alternative candidate for spin based quantum information processing in the solid-state, namely defect states forming at the location of designed defects in an otherwise periodic potential modulation of a two-dimensional electron gas, here referred to as an antidot lattice. We have performed numerical band structure and density of states calculations of a periodic antidot lattice, and shown how localized defect states form at the location of designed defects. The antidot lattice allows for resonant coupling of distant defect states, enabling coherent transport of electrons between distant defects. Finally, we have shown that electrostatic control of the exchange coupling between electron spins in tunnel coupled defect states is possible, which is an essential ingredient for spin based quantum computing. Altogether, we believe that designed defects in antidot lattices provide several prerequisites for a large quantum information processing device in the solid state.

Acknowledgments

We thank A. Harju for helpful advice during the development of our numerical routines, and T. G. Pedersen for fruitful discussions during the preparation of this manuscript. APJ is grateful to the FiDiPro program of the Finnish Academy for support during the final stages of this work.

[1] D. Loss and D. P. DiVincenzo, Phys. Rev. A **57**, 120 (1998).
[2] G. Burkard, D. Loss, and D. P. DiVincenzo, Phys. Rev. B **59**, 2070 (1999).
[3] F. H. L. Koppens, C. Buizert, K. J. Tielrooij, I. T. Vink, K. C. Nowack, T. Meunier, L. P. Kouwenhoven, and L. M. K. Vandersypen, Nature **442**, 766 (2006).
[4] J. R. Petta, A. C. Johnson, J. M. Taylor, E. A. Laird, A. Yacoby, M. D. Lukin, C. M. Marcus, M. P. Hanson, and A. C. Gossard, Science **309**, 2180 (2005).
[5] J. M. Elzerman, R. Hanson, L. H. W. van Beveren, B. Witkamp, L. M. K. Vandersypen, and L. P. Kouwen-

hoven, Nature **430**, 431 (2004).
[6] D. P. DiVincenzo, Fortschr. Phys. **48**, 771 (2000).
[7] J. M. Taylor, H. A. Engel, W. Dur, A. Yacoby, C. M. Marcus, P. Zoller, and M. D. Lukin, Nat. Phys. **1**, 177 (2005).
[8] C. Flindt, N. A. Mortensen, and A. P. Jauho, Nano Lett. **5**, 2515 (2005).
[9] K. Ensslin and P. M. Petroff, Phys. Rev. B **41**, 12307 (1990).
[10] D. Weiss, K. Richter, A. Menschig, R. Bergmann, H. Schweizer, K. von Klitzing, and G. Weimann, Phys. Rev. Lett. **70**, 4118 (1993).
[11] A. Dorn, E. Bieri, T. Ihn, K. Ensslin, D. D. Driscoll, and A. C. Gossard, Phys. Rev. B **71**, 035343 (2005).
[12] We have used the COMSOL Multiphysics 3.2 package for all finite-element calculations. See www.comsol.com. Convergence with respect to the mesh size has been ensured.
[13] G. Lehmann and M. Taut, Phys. Status Solidi B **54**, 469 (1972).
[14] J. Hama, M. Watanabe, and T. Kato, J. Phys. Cond. Matt. **2**, 7445 (1990).
[15] J. Pedersen, C. Flindt, N. A. Mortensen, and A.-P. Jauho, AIP Conf. Proc. **893**, 821 (2007).
[16] J. Pedersen, Master's thesis, Technical University of Denmark (2007).
[17] N. A. Mortensen, Opt. Lett. **30**, 1455 (2005).
[18] N. A. Mortensen, J. Eur. Opt. Soc., Rapid Publ. **1**, 06009 (2006).
[19] L. I. Glazman, G. K. Lesovik, D. E. Khmelnitskii, and R. I. Shekter, JEPT Lett. **48**, 238 (1988).
[20] G. M. Nikolopoulos, D. Petrosyan, and P. Lambropoulos, J. Phys. Cond. Matt. **16**, 4991 (2004).
[21] G. M. Nikolopoulos, D. Petrosyan, and P. Lambropoulos, Europhys. Lett. **65**, 297 (2004).
[22] J. Pedersen, C. Flindt, N. A. Mortensen, and A.-P. Jauho, under review (2007), arXiv:0706.1859v1.
[23] M. Skorobogatiy, K. Saitoh, and M. Koshiba, Opt. Lett. **31**, 314 (2006).
[24] M. Skorobogatiy, K. Saitoh, and M. Koshiba, Opt. Express **14**, 1439 (2006).
[25] D. P. DiVincenzo, D. Bacon, J. Kempe, G. Burkard, and K. B. Whaley, Nature **408**, 339 (2000).
[26] M. Helle, A. Harju, and R. M. Nieminen, Phys. Rev. B **72**, 205329 (2005).
[27] In practice, reliable single-electron filling may pose a serious experimental challenge which could require further optimization of the architecture presented here.
[28] Another experimental challenge relates to the RC switching time of the back gate which grows with length, making it harder to control on short time scales.
[29] Because we use an expansion in localized single-particle product states our method is most reliable for systems with several localized single-particle states. We consequently focus on relative antidot diameters above the single-level regime of the single defects ($d/\Lambda > 0.42$), see Fig. 3.